

Huong Thi Thanh Tong

**Boron Coordination and Co-incorporation of
Al, Ga in *BEA Borosilicate and
Dissolution of Zeolite Nanoparticles from
Large Particles in Organic Solvents**

2007

Physikalische Chemie

**Boron Coordination and Co-incorporation of
Al, Ga in *BEA Borosilicate and
Dissolution of Zeolite Nanoparticles from
Large Particles in Organic Solvents**

Inaugural-Dissertation
zur Erlangung des Doktorgrades der Naturwissenschaften
im Fachbereich Chemie und Pharmazie
der Mathematisch-Naturwissenschaftlichen Fakultät
der Westfälischen Wilhelms-Universität Münster

vorgelegt von
Huong Thi Thanh Tong
aus Hanoi, Vietnam

2007

Dekan:

Prof. Dr. F. E. Hahn

Erster Gutachter:

PD Dr. H. Koller

Zweiter Gutachter:

Prof. Dr. H. J. Galla

Tag der mündlichen Prüfung:

11.07.2007

Tag der Promotion:

11.07.2007

To Vinh, for always believing in me

And Tintin, to show him what is possible

Acknowledgements

This work was performed in the Institute of Physical Chemistry at the Westfälischen Wilhelms-Universität Münster, Germany.

I know, however, that I would not have been able to finish this thesis without the help and support of a number of people, whom I want to thank here.

First and foremost, I would like to deeply thank my advisor PD Dr. Hubert Koller for giving me the opportunity to work in his group for past four years. With his enthusiasm, his inspiration, and his great efforts to explain things clearly and simply, he has helped to make this work enjoyable for me. Throughout my work, he provided encouragement, good teaching and lots of good ideas.

I wish to thank Prof. Dr. Hans-Joachim Galla for mentoring me and many fruitful discussions in this thesis. I also thank Prof. Dr. Hans-Dieter Wiemhöfer for being my co-mentor and reviewing the thesis.

I am also grateful to Prof. Dr. Hellmut Eckert for so readily receiving me into his group, providing resources and fruitful suggestions in the group seminars. Many thanks go to Prof. Dr. Monika Schönhoff for valuable discussion and providing me the opportunity to work with the DLS.

I would like to express my gratitude for members of my doctoral committee for taking time out of their busy schedules to review this thesis, providing insightful suggestions and commentary on the manuscript.

I would like to acknowledge the Vietnamese Ministry of Education and Training (MOET) with project 322 and the Institute of Physical Chemistry for financial support.

This work would not have been possible without the assistance of the people, who help me to characterize the samples. I would like to thank Tobias Schuldt for the AFM images,

Wilma Pröbsting for the thermal analysis, Dr. Michael Wark and Falco Mark Schappacher for the SEM micrographs, Dr. Birgit Janza for providing dried DMF, and Katja Hoffmann for explaining the DLS measurement.

Many thanks go to Dr. Karin Meise-Gresch for scientific support. I also want to thank Jakob Kopp for his hardware support and teaching me to paint, Sebastian Wegner and Hendrik Feldhues for helping out with computer, Birgit Heying, Thomas Fickenscher and Dr. Marcus Eschen for XRD support.

Thanks to all members of AK Koller, AK Eckert, and AK van Wüllen for assistance and the pleasant atmosphere and working environment.

I would like to acknowledge Ansgar Bögershausen and Edgar Jordan for guidance and advice, especially at the beginning of my work in Münster. Many thanks go to Dr. Long Zhang for his scientific support and friendship. I am also grateful to my colleagues and friends Geo Paul, Simone Ulke, Nina Wichner and Jan Heimink for invaluable help in the work as well as in the life.

I would like to thank all my friends, who always encourage me when I was discouraged. All e-mail from them kept me thinking I would never be alone.

My deepest gratitude goes to my parents for their unwavering encouragement and believing in me throughout my life. Without their constant support and love, I would not be the person I am today. I wish to thank my parents-in-law, who have always supported in my life. I also want to thank to my brother, sisters- and brothers-in-law for always encouraging me.

Finally, this thesis is dedicated my husband, Vinh, for his assistance and sympathy to encourage me follow my dreams; and to my son, Tintin, to show him what is possible.

Contents

Acknowledgements	vii
Contents	ix
Abbreviations	xiii
1 Introduction	1
1.1 Zeolites	1
1.1.1 Zeolites and Historical Perspective.....	1
1.1.2 Zeolites and Molecular Sieve Materials	2
1.2 Beta Zeolites and Beta Borosilicates.....	4
1.2.1 Beta Zeolites	4
1.2.2 Beta Borosilicates	6
1.2.3 Applications	7
1.3 Zeolite Nanocrystals	9
1.4 Scope of this Thesis.....	10
2 Synthesis of Zeolites and Molecular Sieves	13
2.1 Organic Structure Directing Agents	14
2.1.1 Introduction.....	14
2.1.2 Removal of SDAs from the Zeotype Framework.....	15
2.1.3 SDAs for Beta Zeolite and Beta Borosilicate Synthesis.....	16
2.2 Hydrothermal Technique.....	17
2.2.1 Induction Period.....	18
2.2.2 Nucleation.....	19
2.2.3 Crystal Growth.....	19
2.3 Dry-Gel Conversion Technique	19
2.4 Post-Synthesis Modification.....	20
3 Colloidal Zeolite Nanocrystals	23

3.1 Synthesis of Zeolite Nanocrystals	24
3.1.1 Synthesis of Zeolite Nanocrystals from Clear Solution and Gel	24
3.1.2 Confined Space Synthesis	27
3.2 Application of Zeolite Nanocrystals	29
3.2.1 Preparation of Structure Materials	30
3.2.2 Tailored Synthesis of Porous Solids	33
3.2.3 Other Applications of Zeolite Nanocrystals	34
3.3 Zeolite Nanoparticles Prepared in Organic Solvents	35
3.3.1 Organic Solvent	35
3.3.2 Nanoparticles in Organic Solvents	36
4 Nuclear Magnetic Resonance	37
4.1 Fundamentals of Nuclear Magnetic Resonance Spectroscopy	37
4.2 Interactions in Nuclear Magnetic Resonance	39
4.2.1 The Zeeman	40
4.2.2 Radiofrequency Interaction	40
4.2.3 Chemical Shift Interaction	40
4.2.4 Spin-Spin Coupling Interaction	41
4.2.5 Direct Dipole-Dipole Interaction	41
4.2.6 Quadrupolar Interaction	43
4.3 NMR Techniques	45
4.3.1 Magic Angle Spinning (MAS)	45
4.3.2 Multiple Quantum Magic Angle Spinning (MQMAS)	46
5 Experimental	49
5.1 Synthesis	49
5.1.1 *BEA Hydrothermal Synthesis	49
5.1.2 *BEA Dry-Gel Synthesis	51
5.1.3 MFI Synthesis	52
5.2 Calcination and Dehydration	53
5.3 Ion Exchange	54
5.3.1 Ion Exchange with Na ⁺ , NH ₄ ⁺	54
5.3.2 Post Synthesis Modification	55
5.4 Zeolite Dissolution	56

5.5 X-Ray Diffraction.....	57
5.6 Raman Spectroscopy	57
5.7 Scanning Electron Microscopy (SEM).....	57
5.8 Atomic Force Microscopy (AFM)	58
5.9 Thermogravimetric and Differential Thermal Analyses (TGA-DTA).....	58
5.10 Dynamic Light Scattering (DLS)	58
5.11 Nuclear Magnetic Resonance (NMR) Spectroscopy.....	58
6 Synthesis and Characterization of *BEA-Borosilicate	61
6.1 Beta Borosilicate Structure.....	61
6.1.1 Synthesis Methods	61
6.1.2 Crystallization Time.....	64
6.2 Thermal Analysis	67
6.3 NMR Spectroscopy	69
6.3.1 ²⁹ Si MAS NMR Spectroscopy	69
6.3.2 ¹ H MAS NMR Spectroscopy	71
6.3.3 ¹¹ B MAS NMR Spectroscopy.....	74
7 Boron Coordination of *BEA-Borosilicate	79
7.1 Dehydration of *BEA-Borosilicate.....	80
7.1.1 ¹¹ B NMR Spectroscopy.....	80
7.1.2 ¹ H MAS NMR Spectroscopy	85
7.2 Hydration of *BEA-Borosilicate.....	88
7.2.1 ¹¹ B NMR Spectroscopy.....	88
7.2.2 ¹ H MAS NMR Spectroscopy	93
7.2.3 ²⁹ Si MAS NMR Spectroscopy	95
7.3 Dehydration of Borosilicate after Hydration.....	96
7.3.1 ¹¹ B NMR Spectroscopy.....	96
7.3.2 ¹ H MAS NMR Spectroscopy	100
7.3.3 ²⁹ Si MAS NMR Spectroscopy	100
7.4 Discussion	101
8 Post-Synthesis of *BEA-Borosilicate	107
8.1 Deboronation of *BEA-Borosilicate.....	108

8.1.1 Ion Exchange	108
8.1.2 Deboronation.....	112
8.1.3 Discussion	114
8.2 Post-Synthesis Exchange with Aluminum	115
8.2.1 Post-Synthesis Exchange in Aqueous Media.....	115
8.2.2 Post-Synthesis Exchange in Ethanol Solvent	118
8.2.3 Discussion	121
8.3 Post-Synthesis Exchange with Gallium	123
8.3.1 XRD Powder Patterns	124
8.3.2 MAS NMR Spectroscopy	124
8.3.3 Discussion	126
9 Dissolution of Zeolite Nanoparticles in Organic Solvents	129
9.1 Zeolite Nanoparticles in Organic Solvents.....	129
9.1.1 Microscale Zeolites	130
9.1.2 Zeolite Nanoparticles in Dimethylformamide (DMF).....	131
9.1.3 Nanoparticles in Dimethylsulfoxide (DMSO).....	136
9.2 Zeolite Nanoparticle Structure	137
9.2.1 X-Ray Diffraction	137
9.2.2 MAS NMR Spectroscopy	139
9.2.3 Raman Spectroscopy.....	141
9.3 Water and Cation Concentration Effects.....	142
9.3.1 Water Effect	142
9.3.2 Sodium Effect	144
9.4 Concluding Remarks	147
10 Summary and Outlook.....	149
Appendix	153
Bibliography	163
Lebenslauf.....	173

Abbreviations

AFM	Atomic Force Microscopy
ALPO	Aluminophosphates
*BEA	Zeolite Beta
BISPIP	Trimethylenebis (N-methyl, N-benzyl, piperidinium)
CT	Central Transition
CVD	Chemical Vapor Deposition
DGC	Dry Gel Conversion
DLS	Dynamic Light Scattering
DMF	Dimethylformamide
DMSO	Dimethylsulfoxide
DTA	Differential Thermal Analysis
FAU	Faujasite
FCC	Fluid Catalytic Cracking
IUPAC	International Union of Pure and Applied Chemistry
LbL	Layer-by-Layer
LTA	Zeolite A
MAS	Magic Angle Spinning
MFI	Zeolite ZSM-5
MOR	Zeolite Mordenite
MQMAS	Multiple Quantum Magic Angle Spinning
MRI	Magnetic Resonance Imaging
MTBE	Methyl Tert-Butyl-Ether
NMP	1-methyl-2-pyrrolidone
NMR	Nuclear Magnetic Resonance
NNSL	Non-Negatively Constrained Least Squares
RT	Room Temperature
SAC	Steam Assisted Conversion

SAPO	Silicaluminophosphates
SDA	Structure Directing Agent
SEM	Scanning Electron Microscopy
ST	Satellite Transition
TEA	Tetraethylammonium
TEABr	Tetraethylammonium Bromide
TEAOH	Tetraethylammonium Hydroxide
TEOS	Tetraethylorthosilicate
TG	Thermogravimetric
THF	Tetrahydrofuran
TPA	Tetrapropylammonium
TPAOH	Tetrapropylammonium Hydroxide
TS-1	Titanium Silicalite-1
VPT	Vapor Phase Transport
XRD	X-ray Diffraction
ZSM-12	Zeolite Secony Mobil 12
ZSM-5	Zeolite Secony Mobil 5

Chapter

1

Introduction

1.1 Zeolites

1.1.1 Zeolites and Historical Perspective

Zeolites are inorganic crystalline solids containing pores and cavities of molecular dimensions. The history of zeolite began with the discovery of A.F. Cronstedt in 1756.¹ The material was described by its behavior under fast heating conditions. The mineral seemed to boil because of the fast water loss. Therefore, it was named from the Greek: “zeo” and “lithos”, meaning “to boil” and “a stone”.

During the 19th century, not many investigations were carried out on zeolites. Some nice specimens were regarded as a curiosity of nature and zeolites did not attract the scientists' interest. Until 1940s, attempts to synthesize zeolites were made by mineralogists interested in the stability with other minerals. Union Carbide pioneered the synthetic molecular sieve zeolite business, initiating research in 1948 on adsorption for purification, separation and catalysis.

In the 1950s, zeolite A, B, C and X were synthesized one after another by the discovering of Barrer and Linde groups. The patents on zeolite A and X were filed in 1953. During this time, Milton and his co-worker had synthesized 20 zeolites including 14 unknown as natural mineral.² Following the foundations laid in the 1950s, the next decade saw many significant developments, both in terms of new discoveries and also in the beginnings of investigative work aimed at gaining an understanding of the synthesis process. The first high silica, beta zeolite was synthesized in this time. Since these starting positions, a huge investigation on zeolites has developed over last time.

1.1.2 Zeolites and Molecular Sieve Materials

In general, zeolites are inorganic frameworks of tetrahedral alumina (AlO_4^-) and silica (SiO_4) units, which were linked to each other by the sharing of oxygen ions. The SiO_4 unit is neutral while the net formal charge of (AlO_4^-) is -1, so that the zeolite framework is negatively charged. This charge is balanced by cations. The framework structure contains channels or interconnected voids that are occupied by the cations and water molecules. The cations are mobile and may usually be exchanged by other ions. On the other hand, the water might be removed reversibly, generally by the application of heat.

Besides the aluminosilicates, silicates with various heteroatoms, such as B, Ga, Ti, Ge, Ti, etc., aluminophosphates (AIPO), and silicaluminophosphates (SAPO) have been synthesized. When these materials have crystalline porous structures like zeolites, they are called as molecular sieve materials.

Based on variation of framework Si/Al composition, molecular sieve materials are categorized as: (i) low Si/Al zeolites (about 1 to 1.5, zeolite A, X); (ii) intermediate Si/Al zeolites (about 2 to 5, mordenite); (iii) high Si/Al zeolites (about 10 to 100, ZSM-5, beta); and (iv) silica molecular sieves.³ As the Si/Al ratio increases, the cation content decreases, the thermal stability increases and the surface selectivity changes from hydrophilic to hydrophobic. Silica molecular sieves which have a neutral framework are hydrophobic in nature and have no ion exchange or catalytic properties.

The framework structures of zeolites exhibit pore sizes from 0.3 to 0.8 nm. Generally, based on the pore openings, typical zeolite pore sizes using oxygen-packing models are referred to: (i) small pores with 8-member rings and free diameters of 0.30 to 0.45 nm, such

as zeolite A; (ii) medium pores formed by 10-member rings with 0.45 to 0.65 nm in free diameters, for instance ZSM-5; and (iii) large pores with 12-member rings, 0.60 to 0.80 nm in free diameter, for example zeolite X, Y, beta. Figure 1.1 illustrates the typical topology of several zeolites.

Each zeolite framework type is assigned a three-letter code (e.g MFI, *BEA, LTA...) according to the rules set out by the IUPAC Commission on Zeolite Nomenclature. At present, there are 176 zeolite framework types recognized by the Structure Commission of the International Zeolite Association.⁴ This work deals with the *BEA type zeotype which will be described more detail in succeeding sections.

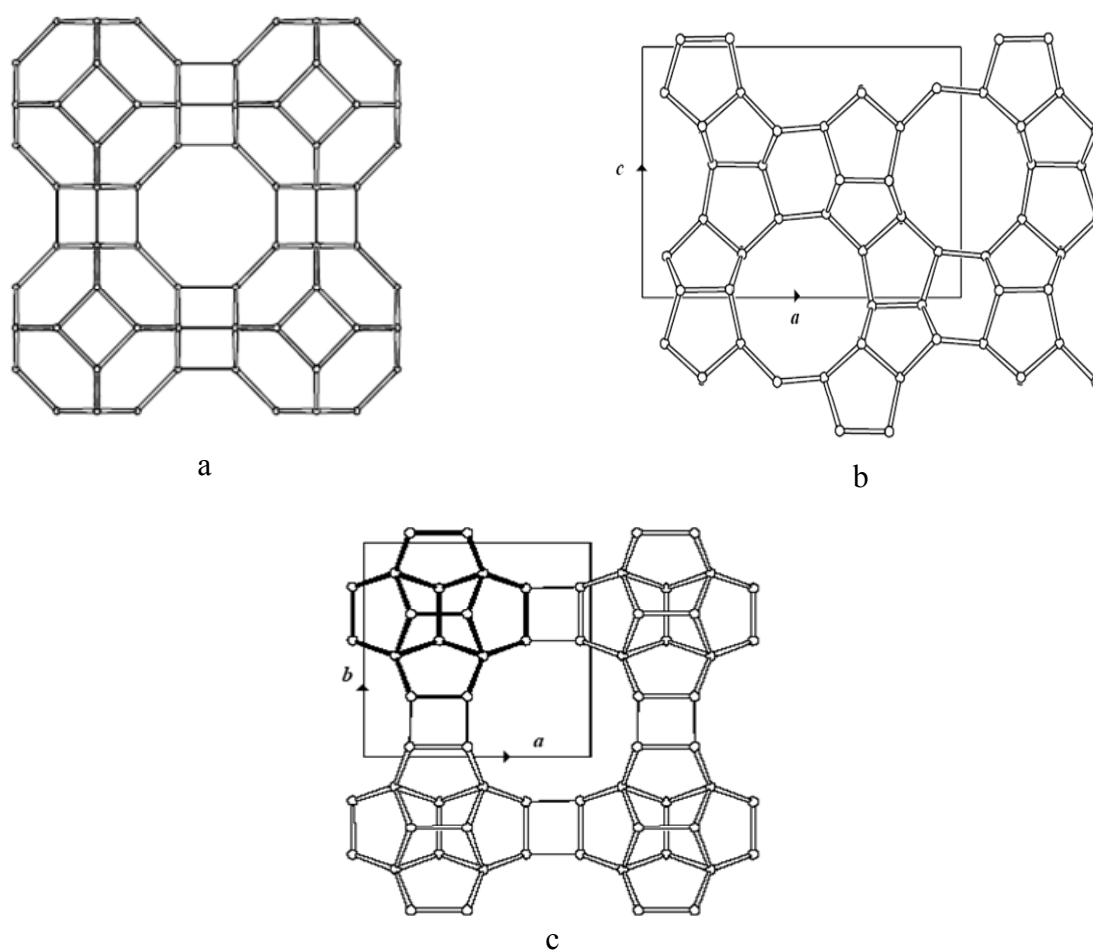


Figure 1.1: The Periodic Building Unit (PerBU) of (a): LTA, viewed along a axis, (b): MFI, viewed along b axis, (c): *BEA, viewed along c axis.

Zeolites with different structures display various characteristics

- The important characteristic is acid catalysis. The zeolites with protons for framework charge compensation display very strong Brønsted acid sites. These acid sites are capable of selective catalysis for special reactions, particularly in the petrolchemical industries such as cracking, isomeration, etc.
- Another interesting property is ability to adsorb molecules. On the other hand, Al rich zeolites have a strong affinity towards water. Therefore, zeolites can be utilized for purification the gaseous and liquid mixtures.
- In addition, zeolites show ion exchange properties. Therefore, zeolites can be used as a water softener in detergents due to the ability to remove Mg^{2+} and Ca^{2+} from water.

1.2 Beta Zeolites and Beta Borosilicates

1.2.1 Beta Zeolites

Beta zeolite (*BEA), a large pore was first synthesized in 1967 by Wadlinger et al. at the Mobil Research and Development Laboratories with tetraethylammonium hydroxide (TEAOH) as the templating agent.⁵ Afterwards the use of other templating agents such as TEAOH-diethanolamine, TEAOH-tetraethylammonium bromide (TEABr) – triethanolamine⁶ and TEABr-NH₃⁷ was also claimed. Further templating agents, for instance, 1,4-diazabicyclo[2,2,2]octane,⁸ dibenzyltrimethylammonium hydroxide,⁹ and dibenzyltrimethylammonium halide¹⁰ were also utilized for beta zeolite formation.

The most interesting property of beta zeolite is its highly disordered framework. The structure consists of layers formed by five- and six- rings that may be stacked in different sequences forming 12-ring pores.^{11,12} The crystallographic pore dimensions are about 7.3 x 6.4 Å for the straight channels along the a and b axes and about 5.6 x 5.6 Å for the pore along c. These channel schemes are illustrated in Figure 1.2.

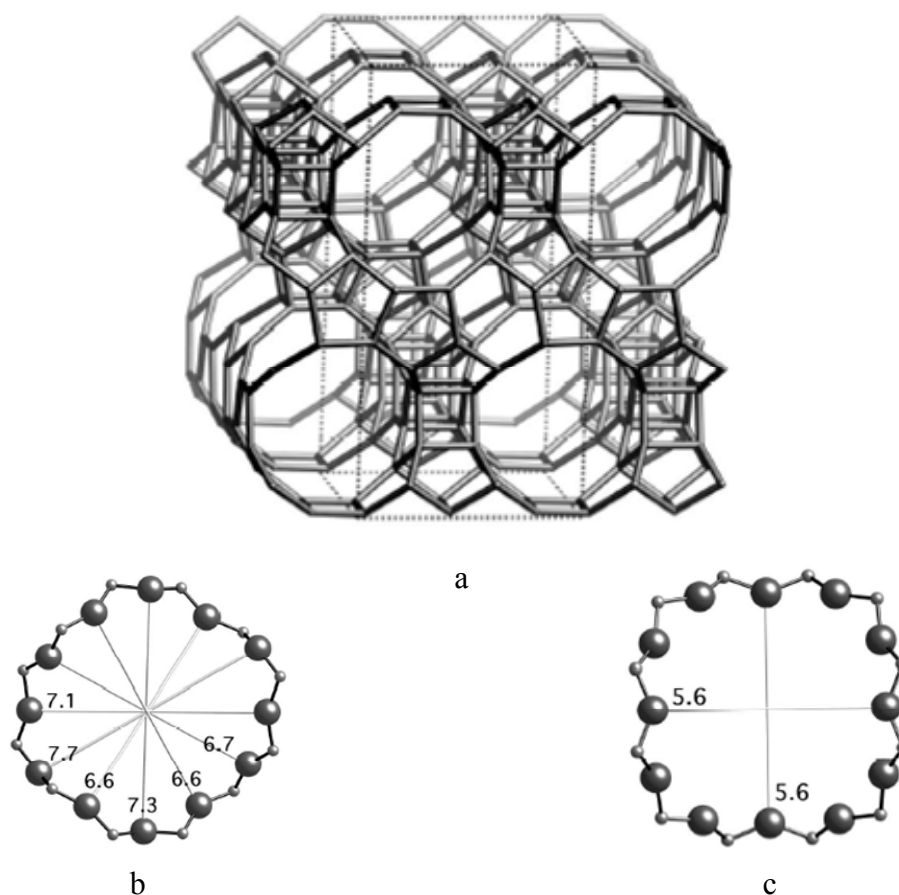


Figure 1.2: Beta zeolite: (a) framework viewed along $[010]$, (b) 12-ring viewed along $[100]$, (c) 12-ring viewed along $[001]$ ⁴

*BEA structure has been reported to be an intergrowth of two or more polymorphs.^{11, 13} One of these polymorphs shows chirality; and all of these features make beta zeolite an attractive material from the catalytic point of view. Newsam, Treacy^{14, 15} and Hingginis et al. reported that the crystal structure of beta zeolite was deduced and three distinct polytypes were identified as polytype A, B and C. Polymorph A is tetragonal and exists as an enantiomorphism pair of crystal structures. Polytype B is monoclinic and achiral. Polymorph C was suggested as a hypothetical structure and predicted to be an achiral tetragonal phase.^{16, 17}

Beta zeolite is easily synthesized in the $\text{SiO}_2/\text{Al}_2\text{O}_3$ range of 30-50. This lies between TEA^+ mordenite (typically, 10-30) and ZSM-12 (typically > 60). For almost 30 years, it

seemed to be not possible to obtain beta zeolite without alumina. Recently, the synthesis of pure silica, boron-beta zeolite or Ti-beta zeolite without aluminum was made possible by using deboronated or dealuminated zeolite beta seeds.^{9, 18}

Partial or complete substitution of aluminum by boron,¹⁹ titanium,²⁰ zirconium,²¹ gallium,^{22, 23} iron^{24, 25} could be prepared in the beta zeolite framework by direct synthesis from basic aqueous gel. On the other side, beta zeolite could be synthesized from near neutral fluoride-containing media with aluminum,²⁶ boron, and gallium²⁷ in the framework.

1.2.2 Beta Borosilicates

Boron containing silica with the *BEA structure was first synthesized by Taramasso et al., using tetraethylammonium hydroxide (TEAOH) as a structure directing agent and the Al content was below 100 ppm.²⁸ Degnan et al. synthesized [B-*BEA], using tetraethylammonium bromide (TEABr) as templating agent, but it contained Al ($\text{SiO}_2/\text{Al}_2\text{O}_3 = 264$) coming from the [Al]-Beta seeds ($\text{SiO}_2/\text{Al}_2\text{O}_3 = 40$) used and/or from low purity starting materials.^{10, 28} Zones et al. claimed the use of bis-1, 1'-diazabicyclo [2,2,2]-octane-1,4- butane dihydroxide as a structure directing agent in seeded reaction mixture for the synthesis of [B-*BEA] containing less than 0.1 wt % aluminum.

Ruite et al. synthesized [B,Al-*BEA] using TEAOH as the template and essentially Al free- [B-*BEA] was prepared without seeding or stirring. The conditions for obtaining Al free B-Beta ($\text{Si}/\text{Al} > 400$) were investigated in detail. Based on the results obtained, the $\text{SiO}_2\text{-BO}_2\text{-AlO}_2$ phase diagram was constructed (Figure 1.3). Pure [B,Al-*BEA] can be obtained with $(\text{B} + \text{Al})/(\text{B} + \text{Al} + \text{Si})$ ratios range 0.063-0.106, corresponding to 4.0-6.8 trivalent ions per unit cell.

Beta-borosilicate zeolite is one class of high silica material where aluminum is substituted by boron. Post synthesis treatment or substitution of [B-*BEA] could be useful for synthesizing other metallocilicate analogues, which are sometimes difficult to synthesize by direct hydrothermal methods. On the other hand, Zones and Nakagawa reported that [B-*BEA] could be used as the precursor (i.e. source of boron and silica) for the synthesis of other borosilicate-zeolites such as [B-SSZ-24], [B-SSZ-31], and [B-SSZ-33].

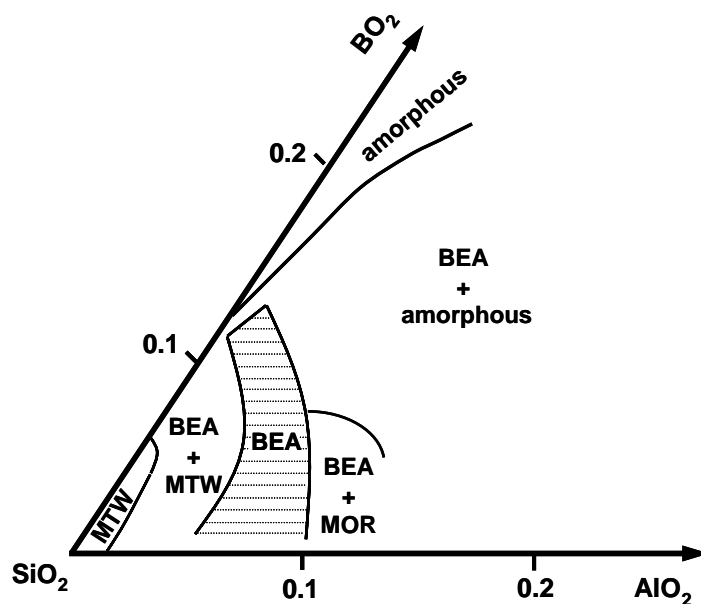


Figure 1.3: Phase diagram depicting the products obtained for the reaction mixture composition.¹⁰

Similar to other borosilicates, beta-borosilicate displays a lower acidic strength than the aluminosilicate analogue, a property which can be appropriately exploited for modulating the catalytic properties of acidic catalysts. The lack of strong Brønsted acid sites in borosilicates makes them weaker and less active than their aluminum counterparts.²⁹

1.2.3 Applications

In general, there are three properties from which zeolites have technologically important applications: (i) selective and strong adsorbent, (ii) selective ion exchanger and (iii) catalytic activity.

Beta zeolite, as a large pore zeolite has been demonstrated to be useful as a catalyst in several hydrocarbon conversion processes.

Freese et al. found that beta zeolite is the most active catalyst for Friedel-Crafts acylation reactions compared to Y- and ZSM-5 zeolites.³⁰

Fluid Catalytic Cracking (FCC) process converts heavy distillates like gas oil or residues to gasoline and middle distillates using cracking catalysts and FCC is one of

important units in refinery process industry.³¹ Beta zeolite has been indicated to present good cracking activity when used as catalyst or additive. Beta zeolite with crystal sizes of 0.40 μm has been claimed to present good cracking activity, when used as catalyst or additive with a higher production of light olefins than USY due to a low hydrogen transfer activity.³² Corma et al. claimed that beta zeolite, while used as catalyst for FCC process can be preferred for optimizing C₃–C₄ olefins and branched olefins in C₄–C₅ fractions.^{33, 34} Owing to the temperatures and steam concentrations prevailing in an FCC regenerator, hydrothermal stability is a prerequisite. The stabilization of beta zeolite for FCC application by embedding in amorphous matrix was recognized in investigation of N. Kubicek et al.³⁵

In the petroleum refining technique, isomerization and alkylation processes are the methods to improve octane-number without increasing the aromatic or olefin content. Baburek et al. investigated the isomerization of n-butane to iso-butane, the starting compound for the synthesis of methyl tert-butyl-ether (MTBE) over H-beta zeolite. The results indicated that the selectivity of n-butane to iso-butane over H-beta zeolite is 1.8 times higher than over H-Mordenite.³⁶ Goodwin et al. claimed that H-beta zeolite has an activity similar to the current commercial resin catalysts being used for MTBE synthesis.³⁷ Beta zeolite catalyst was studied over alkylation of isobutene with light olefine.³⁸ The sole presence of saturated hydrocarbons in products indicates the dominance of the alkylation over alkene oligomerization. For the alkylation of aromatic compounds, G. Bellussi et al. indicated that beta zeolite is active and selective in the alkylation with propylene and ethylene to cumene and ethylbenzene.³⁹

On the other hand, due to 12 member rings in the frameworks, beta-zeolite can accommodate benzene molecules.^{11, 16} Beta zeolite exhibits excellent activity, selectivity and stability in cumene disproportionation,^{40, 41} and in trimethyl benzene disproportionation.⁴² Ferino et al. claimed the disproportionation and isomerization products on conversion of sec-butylbenzene over H-beta zeolite are favored at low temperatures.⁴³ In addition, beta zeolite has been demonstrated to be useful as sorbent in separation of aromatics. The investigation of adsorption of benzene and ethylbenzene on beta zeolite indicated ethylbenzene interacts only with the cations, whereas benzene can interact with either cations, acidic sites or the oxygen in the ring window, basic sites.⁴⁴

1.3 Zeolite Nanocrystals

Zeolite nanocrystals have received much attention due to their great potential of applications in catalysis and adsorption. Interest in the synthesis and application of zeolite nanocrystals has grown continuously since colloidal suspensions of zeolite particles were first reported in the early 1970s.⁴⁵ Zeolite nanocrystals were often prepared by hydrothermal methods. Direct synthesis with clear solutions can provide nanosized zeolite crystals by controlling the gel composition and crystallization conditions. Another method using confined space can be applied for preparation of nanosized zeolite. For the aim to form the homogeneous nanoparticles and control the particle sizes, the inert matrix was utilized in this method. Besides the hydrothermal synthesis, several nanosized zeolites were successfully prepared by dry-gel synthesis with steam assisted conversion (SAC) technique where the crystallization occurs only under water steaming of a dry gel containing the structure directing agent.⁴⁶ In general, the zeolite nanocrystals could be stabilized in solvents such as water, ethanol, etc., with the solid concentration of the suspension in a range of 1 to 6 %.⁴⁷

Zeolite nanocrystals with small particles and large surface areas exhibit advantages in catalytic and sorption processes. The reduction of particle size to the nanometer scale can improve the mass- and heat-transfer in catalytic and sorption processes, thereby enhancing their catalytic selectivity and reducing coke formation in some petro-reactions.^{48, 49} Thus, as the zeolite particle size decreases, the external surface area increases and zeolite nanocrystals have a high surface activity. This is expected to be of significant importance in catalytic reaction. In addition, smaller zeolite crystals can reduce the diffusion path lengths relative to conventional micrometer zeolites and ultimately, the undesired diffusion limitations of heterogeneous reactions can be reduced or eliminated.^{50, 51} This feature is of great interests to heterogeneous catalysis.⁵² Besides the profits from small crystals, zeolite nanocrystals have an emerging application in preparation of structured materials. The use of preformed zeolite nanocrystals for the preparation of supported zeolite films, layers and membranes is one of the important applications of colloidal zeolites.^{53, 54} Due to their controlled host-sorbate interactions and their molecular sieving ability, the colloidal zeolite nanocrystals can be utilized as sensors, and as a medium for the separation of gaseous and/or liquid mixtures.⁵⁵

1.4 Scope of this Thesis

This thesis is composed of two separate projects. The first part concerns to the boron coordination in the beta borosilicate structure. The second part examines a novel method for the preparation of zeolite nanocrystals from larger particles through organic solvents.

Chapter 2 presents a general survey for preparation of zeolites. Besides the hydrothermal synthesis, which is a common technique applied for preparation the most of zeolites due to their convenience and the yield of products; dry-gel synthesis and post-synthesis modification are also mentioned in this chapter.

Chapter 3 gives a short overview of zeolite nanocrystals. General techniques which were usually applied for the synthesis of zeolite nanocrystals, such as synthesis from clear solution and gel or confined-space synthesis are indicated in this chapter. On the other hand, a proposed method based on the polarity of organic solvent is mentioned for preparation of colloidal zeolite nanocrystals.

In chapter 4, the fundamentals of nuclear magnetic resonance spectroscopy and several basic interactions are generally described. In addition, the principal techniques that are utilized to clarify the zeolite structure presented in this thesis are elementarily portrayed.

Chapter 5 is reserved for explaining the experiments. The conditions for preparing the samples as well as parameters for analyzing the materials are described in detail.

In chapter 6, structural properties of borosilicate materials as-synthesized by hydrothermal and dry-gel techniques are studied. Using the X-Ray diffraction and thermal analysis, the characterizations of beta borosilicates synthesized through different methods are initially recognized. Furthermore, the local structure of these materials can be studied by NMR technique.

In chapter 7, the coordination of boron in beta borosilicates are investigated. By applying the hydration/dehydration processes, boron coordinations in framework or extra-framework are clarified. The influences of the local environment on the conversion between trigonal and tetrahedral boron are discussed. In addition, the influence of cations on the coordination to transformation of boron is shown in this chapter.

Chapter 8 indicates the post-synthesis modification of beta borosilicate. The flexibility of boron coordination is applied to investigate the forming aluminum or gallium beta zeolites from beta borosilicate deboronated. Besides water as a common solvent for post-synthesis exchange, ethanol solvent is utilized for post-synthetic modification.

Chapter 9 presents a novel method for preparation of zeolite nanoparticles. The zeolite nanoparticles forming from microscale particles are examined in several organic solvents. Some parameters can influence to the size of nanoparticles, for instance water or cation concentrations.

Finally, chapter 10 presents conclusions and suggestions for future research.

Chapter

2

Synthesis of Zeolites and Molecular Sieves

The zeolite synthesis for commercial applications was introduced in the 1940s in the works of Barrer and Milton. The first synthetic zeolites were formed by imitating the formation process of natural zeolites under the action of strong salt solutions at fairly high temperatures (ca. 170-270°C).⁵⁶ In general, zeolitic materials are synthesized from a gel containing silica precursor, which can contain heteroatoms such as Al, B, Ti, Ga, etc., organic or inorganic cations, mineralizing agents, and water. The crystalline phase of the obtained zeotype depends mainly on the gel composition. The different crystalline structures with various pore sizes and pore structures can be synthesized by changing the organic or inorganic cations, heteroatoms, mineralizing agents, and the ratio of these compounds. In addition, reaction time, temperature, seeds, aging, and status of reaction vessel (static or rotating) can influence the final zeolite structure.

As other crystallizations, zeolith synthesis can be subdivided into three stages: supersaturation, nucleation and crystal growth.

2.1 Organic Structure Directing Agents

2.1.1 Introduction

During the development of zeolite science, a new family of zeotypes with different pore topologies has been synthesized by self-assembly of organic Structure Directing Agents (SDAs), silica and precursor compounds. The regular pore dimensions and microporous volume of these materials can be fine tuned by means of the SDAs. The conditions at which an organic guest will yield clathrasils have been summarized by Liebau and co-workers.⁵⁷ These conditions can be considered as requirements of SDAs for zeolite synthesis.

1. The molecule should have sufficient room within a particular cage or pore.

In the case of using bigger SDAs, steric forces inhibit the formation of the clathrasil; zeotypes with larger pore were formed. When the reactant gel contained no organic molecules, quartz was synthesized.

2. The molecule must be stable under the synthesis conditions.

This point indicated that if the SDAs were destroyed at harsh synthesis conditions, decomposed SDAs can easily affect to the structure of the product.

3. The molecule should fit the inner surface of the cage with as many van der Waals contacts as possible, but with the least deformation.

The SDAs may be deformed to accommodate inside a zeolite pore if they do not fit perfectly. If such distortion tension would be too high, the formation of a crystalline structure is hindered.

4. The molecule should have only a weak tendency to form complexes with the solvent.

The SDA should have intermediate hydrophobicity when the zeotype is synthesized in hydrothermal conditions with aqueous solution. Zones et al. claimed the C/N^+ of the SDA is a critical parameter in determining the ability of the organic additive. The various organic molecules with intermediate hydrophobicity of $C/N^+ = 9-15$ works well as SDAs yielding a variety of zeolitic materials.^{58, 59}

5. More rigid molecules will tend to form clathrasils easier than flexible molecules.

When the SDAs are flexible, they may fit many metastable states of inorganic-organic composites. This leads to the competition among those metastable states. In this case, the template effect of organic molecules is considered to be weak. On the contrary, the rigid organic molecules will have very limited conformational configurations and will produce the same crystalline phase across various synthesis conditions.

6. The tendency to form a clathrasil will increase with the basicity or polarizability of the guest molecule.

The organic-molecule basicity assists the silicate hydrolysis, and their polarizability stabilizes the whole system with the electric field caused by the partial ionic character of the Si-O bonds.

The zeotype structure depends more on the size and shape of the organic molecules rather than the chemical properties of SDA.⁶⁰ The thermal motion of SDA at high temperature influences the SDA shape. The change in the shape of organic molecules leads to different zeotype phases.

In addition, organic SDAs have been used as a controller for the crystal growth of zeotype. Wakihara et al. reported the heteroepitaxial growth of zeolite film with patterned surface-texture has been achieved by controlled use of SDA.⁶¹

2.1.2 Removal of SDAs from the Zeotype Framework

The SDA must be removed after zeotype synthesis in order to create the microporous void spaces that are needed for their applications. The factors such as pore size, the size of SDA, and interaction between SDA and zeotype framework can affect the removal of the SDA. The calcination and extraction are methods used for removing SDAs.

2.1.2.1 Calcination

Calcination is the most common method to remove the organic components from the pores. Due to the properties of organic molecules, they should be easily combusted at high

temperature; the calcination is carried out at high temperature in an oxygen or air atmosphere. During the calcination, high local temperature and water may occur, and therefore some extra-framework species may be formed.⁶² An exothermic reaction takes place when the organic compound is burned inside the pore. This may destroy the inorganic framework and it often occurs for less stable inorganic crystalline materials with open frameworks.

2.1.2.2 Extraction

The other method to remove the organic molecules from the framework is extraction. Many novel methods, such as microwave assisted template removal, extraction with supercritical CO₂, and ozone treatment have been used to remove templates from the framework without using of high temperatures.⁶³ Following these methods, the organic components can be easily removed due to large pore sizes and weak framework SDA interaction of mesoporous materials. However, successful extraction is limited to just a few cases, e.g. tetraethylammonium in *BEA. Jones et al. reported the amount of SDA removed by extraction depends on the size of the SDA and strength of interaction between SDA and the molecular sieve framework.⁶⁴ The effect of interaction strength was estimated by using *BEA with different heteroatoms such as Al, B, and Zn in framework. The result claimed that the SDA was only extracted partially, and heteroatoms were removed from the framework during extraction, too. To have a reasonable chance to extract the SDA, the SDA should have a smaller size than the pore opening of zeotype framework and the interaction between SDA and framework is weaker.⁶⁵

2.1.3 SDAs for Beta Zeolite and Beta Borosilicate Synthesis

As mentioned in Chapter 1, zeolites and molecular sieves could be synthesized by hydrothermal method in basic or fluoride medium. By using rigid polycyclic organo-cations as template, considerable selectivity towards the formation of 12 ring (large pore) zeolites can be achieved.¹⁹

Tetraethylammonium hydroxide (TEAOH) was used as SDA in the first preparation of *BEA zeolite. In basic medium, Tsuji et al. claimed that high concentrations of SDA and hydroxide are both necessary for the crystallization of *BEA.⁶⁶

Camblor and co-worker have synthesized *BEA pure silica in fluoride medium using organic quaternary ammonium cations as SDAs.^{67, 68} These organic molecules are various: for the size, shape, C/N⁺ ratio, and conformational rigidity.

Piccione et al. investigated the interactions between *BEA and the organic cations to determine the effect of variable cation sizes to select one structure over others. While investigating the quantitative characterization of *BEA/SDAs, TEOH and trimethylenebis (N-methyl, N-benzyl, piperidinium) (BISPIP), they claimed that the spatial fit of the organic guest inside the inorganic host is important.⁶⁹ Tsuji and Davis also claimed that the spacing and flexibility of methylenes between the piperidinium moieties is necessary for the preparation of *BEA.

2.2 Hydrothermal Technique

Hydrothermal synthesis is the most common method utilized for zeolite synthesis. A typical hydrothermal zeolite synthesis can be described as follows:⁷⁰

- Amorphous reactants containing silica and alumina are mixed together with a cation source, usually in a basic medium.
- The aqueous reaction mixture is heated in a sealed autoclave.
- For some time after rising to synthesis temperature, the reactants remain amorphous.
- After the “induction period”, crystalline zeolite product can be detected.
- Gradually, essentially all amorphous material is replaced by an approximately equal mass of zeolite crystals (which are recovered by filtration, washing and drying).

For synthesis mechanism, the pathways in zeolite formation are described in sequence: induction period, nucleation, and crystal growth to give the final zeotype crystals. To illustrate the zeolite formation process, Figure 2.1 shows an energetic diagram for steps occurring during the synthesis of Si-TPA-MFI.⁷¹

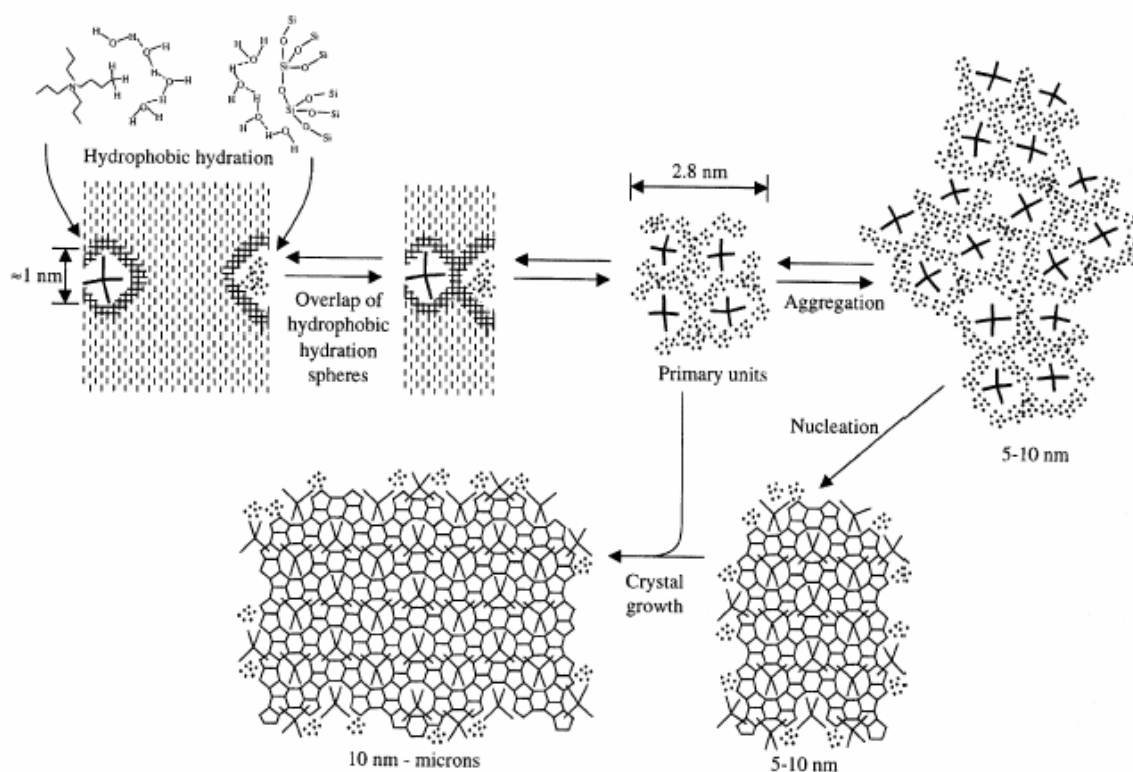


Figure 2.1: Scheme for the crystallization mechanism of Si-TPA-MFI⁷¹

2.2.1 Induction Period

The induction period is the time between the notional start of reaction and the point at which crystalline product is first observed. This is the time for the equilibration reactions taking place on mixing the reagents and allowing them to reach reaction temperature.⁷⁰ Apparently, the induction period encompasses all the significant events of zeolite formation. It is assumed that the interaction between the silica species and the SDA forms in this period.⁷² After the induction time, a myriad of small zeolite crystals forms from the reaction mixture. The induction period seems to consist of several steps in which an assembled organic-inorganic amorphous material is formed. At the point where the synthesis reactants are initially mixed, a gel is formed, and it is referred to as “primary amorphous phase”. The primary amorphous phase consists of the initial reactants and their immediate products after mixing. It is a non-equilibrium state and probably a heterogeneous product. After some time, under ambient conditions or more rapidly upon heating at reaction temperature, the mixture undergoes changes. The mixture is converted into a pseudo-steady-state intermediate – the “secondary amorphous phase”. In the final stage of synthesis reaction, the

secondary amorphous phase is converted into the crystalline zeolite product. The amorphous materials can be transformed into zeolites with uniform pore dimensions.⁷³

2.2.2 Nucleation

Nucleation is the process that leads to the formation of a stable nucleus. In zeolite synthesis, there is evidence for the participation of (i) the primary nucleation may be homogeneous (for solution) or heterogeneous (induced by foreign particles), and (ii) the secondary nucleation may be considered as a special case of heterogeneous nucleation, in which the nucleating particles are crystals of the same phase. The most common process of zeolite nucleation relies on a primary nucleation mechanism.⁷⁰

2.2.3 Crystal Growth

Crystal growth is the process in which the nucleus grows to a detectable nucleus. In general, the particles may increase in size in two ways: (i) by addition of growth units, and (ii) by aggregation. For zeolite systems, the crystal growth model is based on mass gain from simple species (predominantly monomer) in solution.⁷⁴ Following the nucleation, the crystalline region is extended by the acquisition of growth units from solution. These are supplemented by the adjustment of solution equilibrium and the dissolution of amorphous material.

2.3 Dry-Gel Conversion Technique

Besides the hydrothermal synthesis of zeolite crystals, a method called “dry gel conversion” (DGC) technique has been used to synthesize a variety of zeolites. The DGC method has been developed as an alternative technique to synthesize zeolites with advantages of reduced template consumption and less complicated preparation of zeolites in a convenient way. In this method, a dry gel containing zeolite nutrients is converted into microporous crystals in presence of steam or in a mixed vapor consisting of steam and template. This technique could be described in two methods; one is the “vapor-phase transport” (VPT) method and the other is “steam-assisted conversion” (SAC). Figure 2.2 is the schematic diagram of reactor used for the dry gel conversion method.

The VPT has been first reported by Xu et al.⁷⁵ In this former method, zeolite was crystallized by the transformation of aluminosilicate dry gel under the mixed vapors of water and volatile amines such as triethylamine, ethylenediamine. This technique has also been applied for various types of zeolites such as MFI, MOR,⁷⁶ FER.⁷⁷ On the contrary, in SAC method, some quaternary ammonium compounds, e.g. tetraethylammonium hydroxide, tetraethylammonium bromide are used as non-volatile templates. Matsukata suggested that these compounds must be incorporated in the dry gel and only water is supplied from the gas phase.⁷⁸

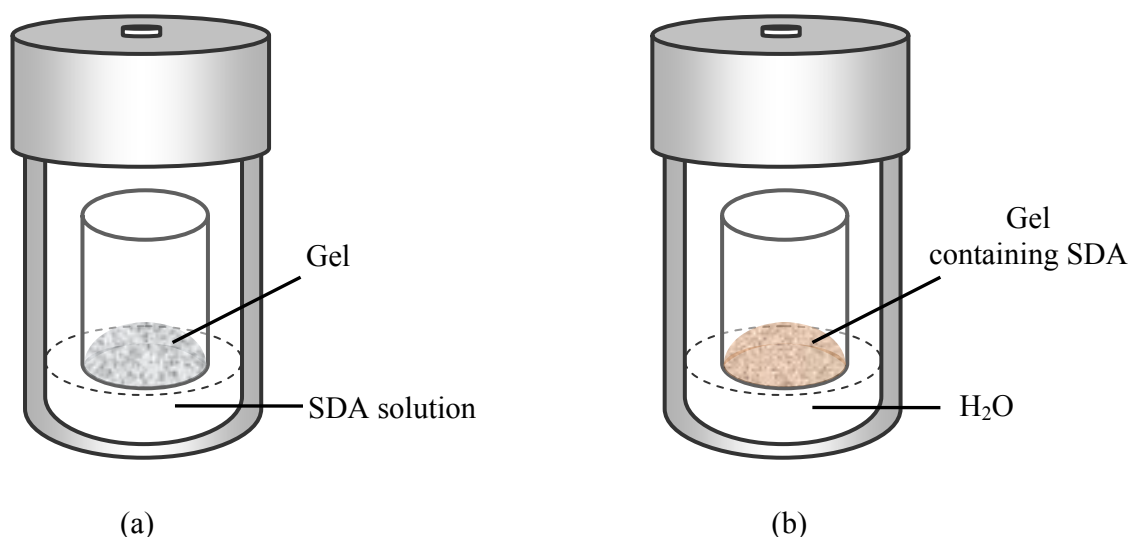


Figure 2.2: Schematic diagram of the dry gel conversion method (a) vapor-phase transport (VPT), (b) steam assisted conversion (SAC)

As the DGC method can yield a high silica zeolite, which cannot be obtained by the hydrothermal method, and a zeolite possessing fewer defect sites, the DGC method is excellent for the synthesis of zeolites having high catalytic activities.

2.4 Post-Synthesis Modification

Besides the direct synthesis methods, post-synthetic methods are also useful for the modification of zeolites. The post-synthesis can alter various properties for applications such

as catalysis, for example to control the stability and activity of zeolite catalysts. In general, there are three major types of post-synthesis to modify zeolites:

- Structural modification: the framework of $\text{SiO}_2 / \text{M}_2\text{O}_3$ (M: Al, B, Ga, Fe) is changed resulting in a change of acid activity.
- Surface modification: the surface of the crystals is modified to change the size of the pore opening.
- Internal pore modification: the structural acid sites are blocked or altered; in addition, the internal pore diameter can be restricted.

Ion exchange is a most common post-synthetic method to modify the selectivity and acidity of zeolites. Following this method, zeolites synthesized by direct synthesis can be treated by the wet impregnation technique or vapor-phase treatment.²¹ In liquid phase treatment, the metal components are dissolved in organic solvent (such as alcohol) or in aqueous solution at about 60°C or room temperature.⁷⁹ By contrast, in the vapor-phase treatment, the metal components are vaporized and passed through zeolite in inert environment.

Borosilicates with flexible property of boron in framework can provide a unique post-synthesis route for preparing aluminosilicates, gallium silicates or other isomorphous substitutions of zeolites. Trivalent metal ions are added that can not be incorporated directly into the framework by direct synthesis.

Chapter

3

Colloidal Zeolite Nanocrystals

The reduction of crystal size from micrometer to nanometers leads to a substantial change in the properties of materials.^{80, 81} Compared to microsized zeolites, nanosized zeolites display a larger surface to volume ratio, therefore they are expected to show a high activity and significant importance in catalytic reactions.^{82, 83} The major application of nanosized zeolite is the preparation of special materials, especially in the fields of films, membranes, chemical sensing, microelectronics and composites.

During the past decades, there has been a growing interest in the reduction of zeolite particle sizes from micrometer to nanometer with the goal to prepare zeolite crystals size of less than 1000 nm.⁸⁴ Special attention is dedicated to stable colloidal suspensions of zeolites with narrow particle size distribution and size of about 200 nm. Various methods were applied to prepare the zeolite nanocrystals.

3.1 Synthesis of Zeolite Nanocrystals

Preparation of zeolite nanocrystals in the form of stable colloidal suspensions was one important achievement in zeolite science. Most zeolite nanocrystal structures can be formed by direct synthesis.

3.1.1 Synthesis of Zeolite Nanocrystals from Clear Solution and Gel

Clear precursor solutions with an excess of organic template are generally used to prepared nanosized zeolite. These zeolites or molecular sieves are often present as discrete particles in solution and they are called as colloidal zeolites or colloidal molecular sieves. This synthesis requires fast nucleation with minimal aggregation of particles during the entire crystallization process.⁸⁵ Most of the syntheses of zeolite nanocrystals have been performed using clear homogeneous solutions, where only sub-colloidal or discrete amorphous particles are present. This synthesis approach provides colloidal suspensions of discrete particles with often narrow particle size distribution of below 100 nm. In order to prepare zeolite nanocrystals, the precursors systems should have a high degree of supersaturation. The high supersaturation tends to result in high nucleation rates, a large number of nuclei and thus in the smallest particle sizes.

Depending on the zeolite structures, the aggregation can be avoided by decreasing the content of alkali cations in the precursor system.⁸⁶ The content of alkali cations, which facilitated the crystals growth, should be minimized to limit the aggregation of the negatively charged alumino and/or silicate sub-colloidal particles. Meanwhile, the quaternary ammonium cations in the OH^- form usually play the structure directing role and provide the high pH value needed for the synthesis.

The synthesis of uniform zeolite nanocrystals requires the homogeneous distribution of the viable nuclei in the system. Therefore, the homogeneity of the starting mixture and the simultaneous sequence of the events leading to the formation of precursor gel particles and their transformation into crystalline zeolitic materials are of primary importance. In order to obtain such homogeneous starting systems, abundant amounts of tetraalkylammonium hydroxides and water were employed in the synthesis of zeolite nanoparticles.^{87, 88} Unfortunately the use of organic templates in the OH^- form makes the synthesis of colloidal

zeolites an expensive process. Moreover, the crystalline yield of zeolite nanoparticles is typically low. As a consequence, a high amount of the initial reactants remains unused in the solutions at the end of the synthesis, including a high fraction of the expensive organic templates, which are lost during the purification stage of the crystalline particles. Therefore, the synthesized zeolite suspensions can be purified by repeated high speed centrifugation and redispersion in a liquid in an ultrasonic bath.⁸⁹

The crystallization temperature has a pronounced effect on the ultimate zeolite crystal size. As a rule, lower temperatures lead to smaller particle sizes. A lower crystallization temperature favors reduced particle sizes due to the nucleation process and crystal growth rate, the main factors for the formation of particular particle size.⁹⁰ Thus, relatively low crystallization temperatures are usually employed to minimize the ultimate crystal sizes. Generally, the zeolite nanocrystal syntheses are performed at temperature of around 100°C for periods of time between several hours or several weeks.^{91, 92} Several research groups suggested that the aging step results in the formation of viable nuclei, which induce crystallization upon raising the temperature.⁹³ Zeolite nuclei can be formed under ambient conditions; there are neither thermodynamic nor chemical constraints that should interfere with the subsequent growth of the crystallites. However, as should be expected, the kinetics of such a crystallization process is relatively slow. Recently, successful attempts to decrease the crystallization temperature in the synthesis of microporous zeolite type material have been made. There are a few examples showing the feasibility of ambient temperature synthesis of nanosized zeolites on a laboratory time scale. For instance, [TPA]-silicate can be formed in high yield at temperature below 35°C over a period of 18 to 24 months.⁹⁴ Zeolite A (LTA) can be obtained with the particle size distribution of 40 to 80 nm at room temperature after 7 days of crystallization.⁹⁵ In practice, the organic template induces the aggregation of primary (5-10 nm) colloidal silica particles leading to the formation of 40-80 nm aggregates. Using a conventional system free of organic template, a colloidal zeolite A with a crystallinity of about 80 % can be obtained after 28 days of crystallization at room temperature.⁹⁶ Recently, FAU-type with a well-crystallized material containing 100-300 nm spherical aggregates consisting of 10-20 nm nanocrystals was obtained after 3 weeks of synthesis at room temperature.⁹⁷ The main stages could be summarized as follows: (i) the system reaches a specific critical level of chemical evolution before the onset of crystallization; (ii) during the first crystallization stage (10-15 % crystallinity), a crystal

growth by propagation through the gel phase dominates; (iii) the second crystallization stage includes spontaneous aggregation of nanoparticles around a crystallization center followed by maturation. The observed events are illustrated in Figure 3.1.

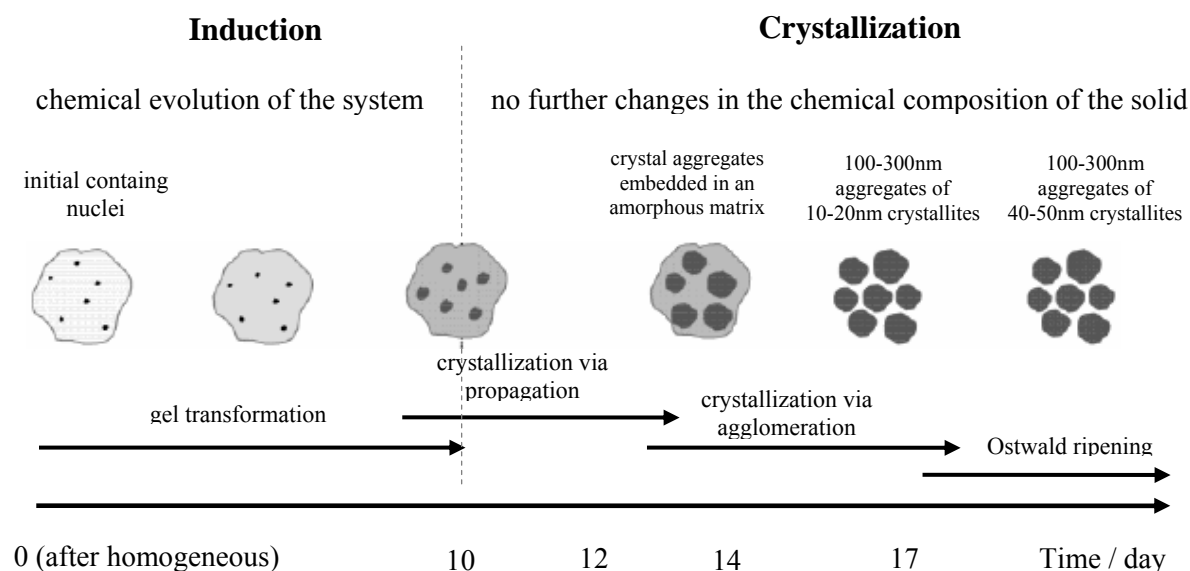


Figure 3.1: Scheme of crystallization mechanism of FAU-type zeolite under ambient conditions.

Besides the temperature and the alkalinity of the reactant mixture, zeolite formation is very sensitive to the nature of the reactants, in particular of the silica source. Thus, a great variety of silica sources, which differ in their specific surface area, impurities, and ability to dissolve in alkaline mixtures have been employed so far in zeolite syntheses. The silica source can influence different aspects of the zeolite crystallization, including the kinetics of crystal growth and the properties of the final product.⁹⁸ Since the crystallization temperature was as low as 25°C, in order to reduce crystallization time special attention was paid to all other factors controlling the kinetics of zeolite growth. A silica source containing low-mass species was employed and further depolymerized by adding sodium hydroxide so as to obtain a completely transparent initial solution. Different silica sources have been employed for the formation of nanosized zeolites. Thus, the silica sources influence the zeolite crystallization and lead to a change in the properties of the final product. Colloidal silica, TEOS and fumed silica can yield zeolite phases, but sodium metasilicate gives a quartz phase.⁹⁹ Some experiments show that nucleation was faster when TEOS was used as a silica source compared to the other amorphous silica sources. The structure of amorphous silica

was of importance for the ultimate crystal size and concentration.¹⁰⁰ The final size of ZSM-5 increased in the following order: TEOS (15 nm) < colloidal silica (25 nm) < fumed silica (50 nm).¹⁰¹ For colloidal Beta zeolite, the size of nanoparticles depends also on the silica sources employed. The main particle size of *BEA crystals formed from TEOS is slightly lower than crystals formed from fumed and colloidal silica.¹⁰²

An initial gel system can also influence to the formation of zeolite nanoparticles. The preparation of nanosized zeolite with narrow particle size distributions from hydrogel precursors requires the utilization of highly reactive and uniform precursors. Thus, initial solutions containing monomeric and/or low mass silica and alumina species are used for the preparation of alumino and/or silicate gels.¹⁰³ These solutions can be prepared as follows: (i) the utilization of easily dissolvable silica and alumina sources; (ii) the application of alkali bases in sufficient amounts to cause complete dissolution of the silica and alumina resources; and (iii) vigorous mixing of the precursor solutions in order to form a synthesis mixture with homogeneous distribution of the components in the starting system. This mixing step often carried out at low temperature close 0°C. Similar to clear solution synthesis, the crystallization temperature is usually moderate to favor the nucleation over the growth in the system.

The colloidal zeolite crystals synthesized via a hydrothermal process using structure directing agents often occludes an organic template in their void spaces. To avoid the aggregation due to the calcination procedure for removing the structure directing agent, several zeolite nanocrystals have been successfully synthesized from SDA-free system. Recently, zeolite A nanocrystals can crystallize within 3 days under room temperature from the SDA-free system.¹⁰⁴

3.1.2 Confined Space Synthesis

Syntheses within an inert matrix providing a confined space for zeolite crystal growth have been developed for preparation of zeolite nanocrystals. The synthesis method involves crystallization of the zeolite within the mesopore system of an inert support material. Figure 3.2 illustrates a scheme of the confined space procedures used for the synthesis of zeolite nanocrystals. The experiments via confined space synthesis using mesoporous carbon black as removable templates were first reported by Jacobsen et al. for the preparation of

ZSM-5.¹⁰⁵ A principle of confined space synthesis is crystallization of the zeolite gel inside the mesopores of inert matrix. The confined space synthesis allows preparation of nanosized zeolite with a controlled crystal size distribution.¹⁰⁶ The crystal size of the zeolite is controlled by the size distribution of the inert mesopore system and does not depend on the gel composition.

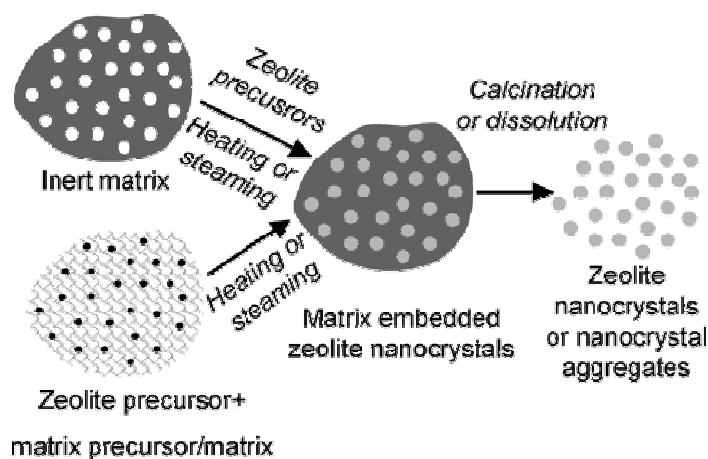


Figure 3.2: Scheme illustrating the confined space syntheses of zeolite nanocrystals .

The synthesis procedure following this method is introduced by sequential incipient wetness impregnations of the inner matrix material with zeolite gel precursor solutions. The precursor solutions should be clear with a low viscosity, which enable them to enter the mesopores of the matrix instead of blocking the pore entrance. Crucial steps in the synthesis were (i) restriction of the crystallization of the zeolite gel within the pore system of the matrix, which was achieved by the incipient wetness impregnation method employed to load the mesopores with a synthesis gel, and (ii) prevention of diffusion of the zeolite gel species from the mesopores, which was ensured by avoiding direct contact between the impregnated contents and the water at the bottom of the autoclave.

Different mesoporous materials were utilized as inert matrices for the preparation of nanosized zeolite particles by confined space synthesis.¹⁰⁷ Mesoporous carbon black was used for synthesis of ZSM-5, zeolite A, and Beta zeolite.^{108, 109} The mesopore volumes of the carbon black templates resulted in more than 10 wt % of zeolite in the final product. However, using carbon black has an intrinsic drawback; for example, this matrix must have a

uniform distribution of mesopores to ensure the narrow size distribution of the product. Careful processing is necessary to impregnate the synthesis solution just inside the mesopores but not outside. Instead of carbon black, a surfactant/precursor composite was used as an inert matrix.¹¹⁰ Mesoporous carbons formed through the carbon replication of mesostructured silica and through the colloid-imprinted carbons with much more uniform pore size distributions can replace carbon black.¹¹¹ These latter carbons should be much more suitable template media for the “nanocasting” of zeolite phases because of the uniform pore sizes.¹¹² Interestingly, Beta zeolite nanocrystals were successfully synthesized under non-hydrothermal conditions using carbon nanotubes as templates.¹¹³ In another experiment, thermo-reversible polymer hydrogels are very effective for controlling zeolite nanocrystals; zeolite A (LTA) and Faujasite (FAU) were observed with methylcellulose as thermo-reversible polymer hydrogels under hydrothermal condition.¹¹⁴ Using starch as additive material, NaY crystals with a narrow size distribution (50-100 nm) were simply isolated from metakaolin and sodium silicate.¹¹⁵

Unlike colloidal zeolites, the recovery of the nanozeolites from confined space can be easily realized by simple calcination, during which both the carbon matrix and the zeolite structure directing templates are removed. When swelling polymers are involved, they can be readily removed after zeolite synthesis by simple washing, and the zeolite nanocrystals obtained are readily redispersed in various solvents. Starch is also easily removed by pyrolysis.

Via confined space synthesis, several nanocrystal zeolites were successfully synthesized with the crystal size tailored in the range of 10 to 100 nm and with very little intergrowth of the individual crystals. The zeolites have an additional inter-crystalline mesopore volume.

3.2 Application of Zeolite Nanocrystals

Zeolites with nanoscale domains in particular have very emerging applications. Besides the benefits of nanoparticle zeolites over conventional zeolites related to their small crystal size, the major interest in colloidal zeolite suspensions is due to their use for preparation of zeolite films, membranes, as well as composites and hierarchical structures.¹¹⁶ The colloidal zeolites employed in such preparation generate unique properties of the structures prepared

and expand the area of zeolite applications, for instance towards optoelectronics, chemical sensing, and biomaterials.^{117, 118}

3.2.1 Preparation of Structure Materials

3.2.1.1 Supported Zeolite Films and Membranes

Preparation of zeolite films and membranes from preformed zeolite nanocrystals is one of the major applications of colloidal zeolites. Generally, the quality of a zeolite coating on various supports is determined by the homogeneity and intactness of the zeolite layer, the number of defects in the film, such as cracks and pinholes. Largely used procedures to produce zeolite supported layers of improved quality comprise a preliminary adsorption of zeolite nanoseeds, which are induced to grow into a dense film by secondary growth. The common method for preparation of films uses seeding. This method includes a preliminary treatment of the support with a cationic polymer in order to reverse the surface charge followed by adsorption of colloidal zeolite crystals on the surface. The second step consists of hydrothermal treatment of the support in a molecular sieve precursor solution resulting in the formation of a continuous molecular sieve film.¹¹⁹ A very important feature of the zeolite film syntheses by seeding is that the preliminary adsorption of seeds may cause a preferred orientation of the growing zeolite crystals. A schematic of these is illustrated in Figure 3.3. In thin films, most of the crystalline material is oriented with the b-axis perpendicular to the substrate surface. In thick films, most of the crystalline material is oriented with the a-axis perpendicular to the support surface. The choice of size and coverage of the support with the seeds can be used to control the preferred orientation of the crystals in a zeolite layer of a given thickness. The zeolite membranes can be obtained by coating of a porous support with a colloidal solution. The usual coating techniques are dip-coating, slip-casting or spin-coating. Dip-coating is the most frequent technique used for membrane preparation.¹²⁰

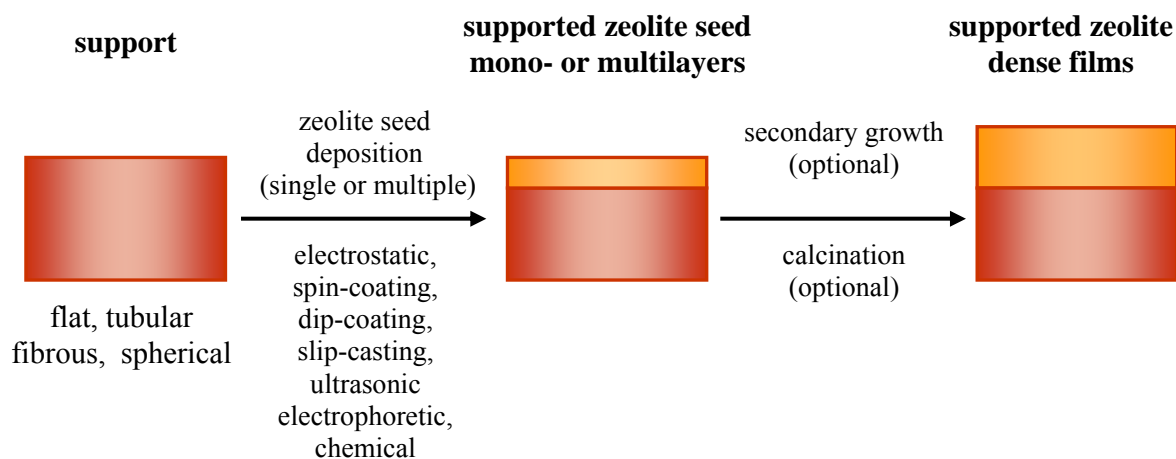


Figure 3.3: Scheme illustrating the methods for preparation of supported zeolite film by seeding

In some cases, the support may be removed after the synthesis by combustion or dissolution and the zeolite structures obtained are self-standing. The self-standing zeolite structures are often characterized by a poor mechanical stability.

Some zeolite films or membranes, for instance MFI-, LTA-, FAU-, *BEA- were successfully prepared and they had some important applications. Among novel applications of zeolite films and layers, chemical sensors have received considerable attention. Issues such as film stability, compatibility with sensor transducers, and novel transduction concepts will very likely play a role in future research. Other demonstrated or potential applications of zeolite films include solar energy conversion, zeolite electrodes, electron relays, zeolite batteries, zeolite fast ion conductors, intrazeolite semiconductors, and zeolite imaging and data storage materials. It is a wide field waiting to be explored.¹²¹

3.2.1.2 Zeolite Structures Synthesized by Application of Zeolite Nanocrystals.

Besides the major application in the preparation of zeolite films and membranes, the zeolite nanoparticles were known as useful materials to prepare macroscopic zeolite structures. The interest in preparing macroscopic zeolite structures is driven by the following: (i) the optimized zeolite performance (no pore blocking and zeolite diluting binding additives are present), easy handling, and attrition resistance; (ii) the presence of secondary larger pores that minimize diffusion limitations; and (iii) possibilities for nonconventional applications, such as guest encapsulation, bioseparation, enzyme

immobilization, etc. Currently, the procedures used to prepare hierarchical zeolite structures use sacrificial macrotemplates, molds, micropatterning, and self-assembly of nanocrystals.

Preparation of hollow zeolite spheres from zeolite nanoparticle is one typical example of these applications. Zeolites are ideal construction materials for the shell of hollow spheres owing to their high thermal stability, large microporosity, high shape-selectivity and intrinsic chemical activity.¹²² Recently, a layer-by-layer (LbL) technique based on electrostatic interaction or hydrogen bonding has been widely adopted to fabricate films on the surfaces of flat and spherical substrates. It has been noticed that colloidal zeolites are negatively charged in basic solution and can aggregate readily to form hierarchical structures such as membranes, fibers and micro/macroporous zeolite monoliths. The electrostatic attraction between a negatively charged nanozeolite and an oppositely charged polymer is an effective driving force for the self-assembly of zeolite polymer multilayers on colloidal templates. Hollow zeolite spheres have been prepared employing polystyrene spheres and the LbL method.¹²³ A schematic illustration of the preparation of hollow zeolite spheres using colloidal zeolite nanoparticles is presented in Figure 3.4. The mechanical stability of hollow zeolite spheres synthesized by the LbL method could be improved by secondary hydrothermal treatment with synthesis gels or solutions of suitable compositions.¹²⁴

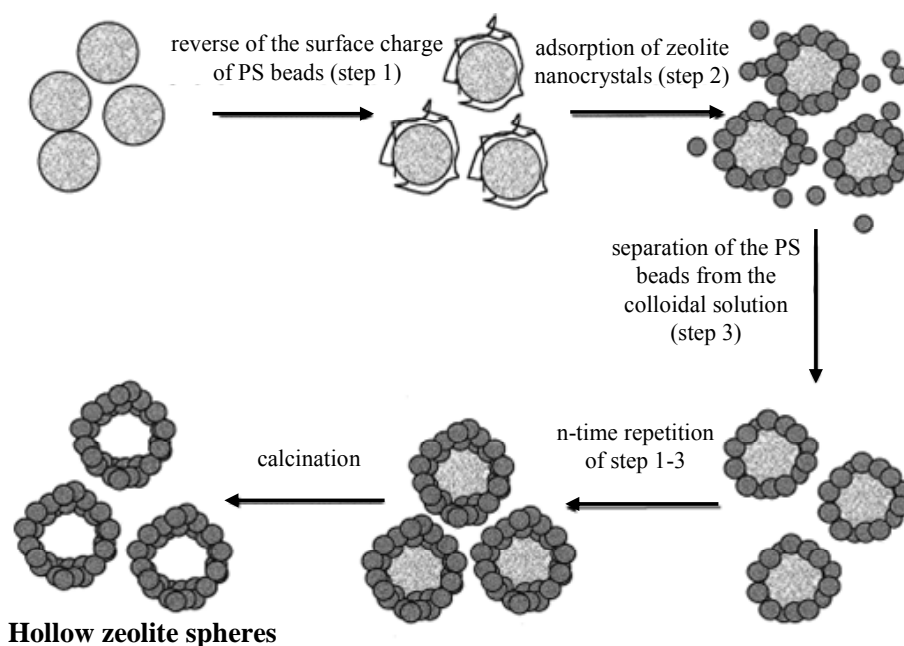


Figure 3.4: Scheme illustrating the Layer-by-Layer technique used for preparation of multilayer zeolite coatings. PS: Polystyrene.

In reality, several microporous materials including LTA, MFI, LTL, *BEA, FAU in the forms of stable colloidal suspension with particle size below 100 nm and narrow particle size distribution have been utilized for preparation of macroscopic zeolite structures.

Preparation of hierarchical structures from colloidal zeolites by macrotemplating is another useful application of zeolite nanoparticles. Biological species are excellent macrotemplates due to some advantageous properties, for instance they are inexpensive and environmentally benign, and provide thousands of possibilities for the synthesis of hierarchical structures. Diatomite as a sedimentary rock, composed of the fossilized skeletons of diatoms, is another macrotemplate that has been used to produce hierarchical zeolite structures. The honeycomb silica structures give diatomite useful characteristics such as high absorptive capacity and surface area, chemical stability, and low bulk density. The approaches used were as follows: (i) diatomite seeding with zeolite nanoparticles by sonication followed by hydrothermal treatment in a synthesis mixture; (ii) diatomite seeding by electrostatic deposition and subsequent vapor-phase transport treatment.¹²⁵ Hierarchical zeolite structures have also been prepared by wood cell templating. Two kinds of tissues, as cedar and bamboo, were covered with a thin layer of zeolite seeds by electrostatic adsorption of colloidal zeolite seeds. Upon secondary hydrothermal treatment and calcinations, a zeolitic tissue faithfully replicating the wood macrocellular structure was obtained.¹²⁶

3.2.2 Tailored Synthesis of Porous Solids

It is well-known that seeding a molecular sieve synthesis mixture frequently has beneficial effects, for example, in controlling the particle size of the product, avoiding the need for an organic template, accelerating the synthesis, and improving the yield of product of the intended structure type. The discrete nature of zeolite nanoparticles and their homogeneous distribution in the colloid make them very convenient for seeding zeolite synthesis gels. Colloidal zeolite seeds have already proven to be especially effective in the zeolite industrial production. Such nanocrystals can also be employed in very specific syntheses like, for instance, BEA-type framework or synthesis of nanosized ZSM-5 crystals.

Besides seeding of synthesis, zeolite nanoparticles have been utilized for preparation of micro-/mesoporous materials. Recently, an approach that has gained much attention is the surfactant-assisted assembly of subcolloidal zeolite precursors. The procedure includes two

stages. During the first stage, a zeolite precursor system is prepared and subjected to aging at room or elevated temperature to promote the formation of zeolite nanocluster precursors. During the second stage these precursors are integrated in the walls of a structured mesoporous material. Thus, different mesoporous materials using zeolite Y, ZSM-5, Beta zeolite, and TS-1 precursors were synthesized via this method.¹²⁷

The use of nanozeolite catalysts could reduce the mass transport limitations since the diffusion path is relatively short and the accessibility of the catalytic sites through the external surface is high. On the other hand, nanosized zeolites cannot be used directly due to the much higher pressure drops in packed-bed reactors. Therefore, micro-/mesoporous composites containing well-defined zeolite nanocrystals are of interest for reactions where bulky molecules are processed. Different approaches have been developed to prepare composites of uniformly distributed zeolite nanocrystals in a mesoporous matrix.

3.2.3 Other Applications of Zeolite Nanocrystals

It is well known that nanosized zeolites prepared in the form of stable colloidal suspensions provide an advantage of a homogeneous initial precursor which can be uniformly distributed in a matrix. Due to the uniformity of distribution and accessibility of the active phase, the nanosized zeolites are expected to result in a better performance of the material in the traditional zeolite applications such as heterogeneous catalysis, molecular separation and ion exchange. Besides the impact on the traditional applications, stable colloidal suspensions of zeolite nanocrystals could open new possibilities for processing these materials and respectively to extend the application of microporous material. The nanosized zeolites are also preferred in all processes requiring a higher reaction rate.

Based on the uniform pores, the hydrophilic/hydrophobic properties and thermal, chemical and attrition stability of stable colloidal zeolite, zeolite nanoparticles are perfect materials for sensing applications.

A new field where the zeolite nanocrystals have made the first encouraging steps is medical diagnostics, in particular, Magnetic Resonance Imaging (MRI).

3.3 Zeolite Nanoparticles Prepared in Organic Solvents

3.3.1 Organic Solvent

Organic solvents have been attracted attention of investigations due to their important features. Because of low boiling point, organic solvents are easily evaporated and removed by distillation, thereby leaving the dissolved compound. Solvents should be inert, and unreactive with the dissolved compound. On the other hand, the solvent could create various weak chemical interactions with the solute. The most common of these interactions are the relatively weak van der Waals interactions, induced dipole interaction, the stronger dipole-dipole interactions and hydrogen bonds. Solvents can also be used to extract soluble compounds from a mixture. There are about three hundred common solvents available; consequently, there is a nearly infinite number of solvent mixtures.¹²⁸ Solvents can be broadly classified into polar and non-polar. The polarity can be measured as the dielectric or the dipole moment of a compound. Some characteristics of several common solvents are displayed in Table 3.1. The polarity of a solvent determines what type of compounds it is able to dissolve and with what other solvents or liquid compounds it is miscible. The solvent polarity can play an important role in chemical reactions, molecular separations and other important chemical technologies.¹²⁹

Table 3.1: Characteristics of several common solvents

solvent	chemical formula	boiling point (°C)	dipole moment (Debye)
Hexane	$\text{CH}_3\text{-CH}_2\text{-CH}_2\text{-CH}_2\text{-CH}_2\text{-CH}_3$	69	0.0
Ethanol	$\text{CH}_3\text{-CH}_2\text{-OH}$	79	1.65
Water	H-O-H	100	1.86
Dimethylformamide (DMF)	$\text{H-C(=O)N(CH}_3)_2$	153	3.81
Dimethylsulfoxide (DMSO)	$\text{CH}_3\text{-S(=O)-CH}_3$	189	4.05

3.3.2 Nanoparticles in Organic Solvents

The treatment of zeolites in organic solvents is a quite common procedure. It is known that, most of zeolite nanocrystals can be stabilized in solvents for further applications.

However, colloidal nanoparticles can be stable in several organic solvents. Manna and Parak et al.¹³⁰ prepared stable colloidal nanoparticles by using polar solvent. In this method named “size-selective precipitation”, if the polar solvent (such as methanol) was added to colloidal nanoparticles in non-polar solvents (such as toluene), the nanoparticles start to precipitate. The larger nanoparticles settle down as a pellet and smaller ones as a supernatant in solution. This step can be repeated in an iterative way with the pellets, so that fractions containing different nanoparticle sizes can be obtained. This procedure is very important to obtain homogeneous products. Casciola et al. prepared the inorganic gel in several organic solvents such as alkanols, dimethylformamide (DMF), 1-methyl-2-pyrrolidone (NMP), tetrahydrofuran (THF). This gel can be supported for preparation of nanocomposites.¹³¹

In this thesis, a novel route for preparation of zeolite nanoparticles from larger particles using organic solvents will be demonstrated. Throughout the experiments, the solvents are not necessarily inert, and even a portion of the crystals can dissolve to colloidal particles. Consequently, the colloidal nanoparticles can be formed in several organic solvents such as DMF, DMSO.

Chapter

4

Nuclear Magnetic Resonance

4.1 Fundamentals of Nuclear Magnetic Resonance

Spectroscopy [132](#), [133](#), [134](#)

The nuclear magnetic resonance (NMR) is based on the interaction between nuclear magnetic moment, applied in external magnetic field and internal local field. All nuclei that have non-zero spin angular momentum quantum numbers are NMR active. The magnetic moment is related to the nuclear spin angular momentum (\vec{J}) according to the equation given below:

$$\vec{\mu} = \gamma \vec{J} \quad (4.1)$$

where γ is magnetogyric ratio, characteristic for each nucleus.

The dimensionless angular momentum operator \hat{I} can be defined by the equation:

$$\hat{J} = \hbar \hat{I} \quad (4.2)$$

Therefore, the nuclear spin angular momentum $\hat{\mu}$ relates to \hat{I} through the expression:

$$\hat{\mu} = \gamma \hbar \hat{I} \quad (4.3)$$

In NMR spectroscopy, the quantization of the eigenstates along the direction of the external magnetic field B_0 is of interest. The usual convention is to let the direction of the externally applied magnetic field B_0 define the z-direction in the laboratory frame. The eigenvalues are labeled with m or the observable state of the \hat{I}_z component can have the $(2I+1)$ discrete values: $-I, -I+1, \dots, +I$.

$$\hat{I}^2 = I(I+1) | I, m \rangle \quad (4.4a)$$

$$\text{and } \hat{I}_z = m | I, m \rangle \quad (4.4b)$$

The meaning of (4.3) is then that:

$$|\mu| = \gamma\hbar\sqrt{I(I+1)} \quad (4.5a)$$

$$\text{and } |\hat{\mu}_z| = \gamma\hbar m \quad (4.5b)$$

When the nucleus is placed in an external magnetic field \vec{B}_0 (in the z direction), there will be an interaction between $\vec{\mu}$ and \vec{B}_0 . The energy of interaction between the magnetic moment and external magnetic field is given by:

$$\hat{H} = -\hat{\mu}B_0 \quad (4.6)$$

In the z direction, $\hat{\mu}_z$ is expressed by \hat{I}_z , so that:

$$\hat{H}_z = -\gamma\hbar B_0 \hat{I}_z \quad (4.7)$$

This is called the Zeeman Hamiltonian. The eigenvalues of \hat{I}_z are m , so the energies of the eigenstates are obtained by:

$$E_m = -\mu_z B_0 = -\gamma\hbar B_0 m \quad (4.8)$$

The energy difference between two adjacent levels m and $(m+1)$ is:

$$\Delta E = \gamma\hbar B_0 = h\omega_0 \quad (4.9)$$

where $\omega_0 = \gamma B_0 / 2\pi$ is the Larmor frequency of nucleus, the frequency of rotation of the magnetic moment around the z-axis.

In the NMR experiments, a large number of nuclei are observed. A spin packet is a group of spins experiencing at the same magnetic field. The nuclear spins will be then distributed between the states with a probability of occupation described by the Boltzmann distribution:

$$\frac{N_+}{N_-} = e^{(-\Delta E/kT)} \approx 1 - \frac{\Delta E}{kT} = 1 - \frac{\gamma \hbar B_0}{kT} \quad (4.10)$$

where N_+ and N_- are the population of the lower and higher energy states, respectively, k is the Boltzmann constant, and T is the absolute temperature.

The net magnetization vector at equilibrium (M_0) lies along the direction of the applied magnetic field B_0 is given by Curie Law:

$$M_0 = \frac{N\gamma^2 \hbar^2 I(I+1)}{3kT} B_0 \quad (4.11)$$

where N is the total number of spins ($N = N_+ + N_-$).

The magnetization vector does not process forever around the magnetic field. In reality, there are tendencies to return to the equilibrium of system that has been slightly perturbed by the imposition of a change in one of the variable of state. Relaxation is a dynamic process that determines how rapidly the thermodynamic equilibrium is achieved between the spin states. There are two relaxation types: (i) the longitudinal (spin lattice) relaxation (T_1): is the characteristic time for exchange of energy between the spin system and the thermal surroundings (the lattice) and (ii) the transverse (spin-spin) relaxation (T_2). In solids, T_1 may be as long as 1000s because of the absence of mechanism for interchanging nuclear spin energy with the rest of the sytem; T_2 is often of the order of microseconds.

4.2 Interactions in Nuclear Magnetic Resonance ^{135, 136, 137}

In the external magnetic field, there are not only the external interactions but also the internal interactions effect on the nucleus. The nuclear Hamiltonian can be written as a sum of internal and external parts:

$$\hat{H} = \hat{H}_{\text{int}} + \hat{H}_{\text{ext}} \quad (4.12)$$

For this separation, the H_{int} includes the intrinsic effects to the spin system while the H_{ext} component involves terms due to the experimental setup.

The external Hamiltonian can usually be separated into Zeeman (\hat{H}_z) and radio frequency (\hat{H}_{RF}) contributions.

$$\hat{H}_{\text{ext}} = \hat{H}_z + \hat{H}_{\text{RF}} \quad (4.13)$$

The internal Hamiltonian can be further subdivided into the basic interactions resulting from the environment of the nucleus:

$$\hat{H}_{\text{int}} = \hat{H}_{\text{CS}} + \hat{H}_J + \hat{H}_D + \hat{H}_Q \quad (4.14)$$

where \hat{H}_{CS} is the chemical shift Hamiltonian, \hat{H}_J is the indirect spin-spin coupling (or J-coupling), \hat{H}_D is the direct dipole-dipole interaction (or dipolar coupling), and \hat{H}_Q is the quadrupole coupling. Each of these interactions is intrinsic to the spin system and primarily depends upon the chemical environment of nucleus. Each component of the internal or the external interactions will be described in more detail below.

4.2.1 The Zeeman Interaction

The Zeeman interaction is the interaction between the magnetic moment of the nucleus and external applied magnetic field. The Zeeman Hamiltonian can be given by:

$$\hat{H}_z = -\gamma\hbar B_0 \hat{I}_z \quad (4.15)$$

where γ is the magnetogyric ratio, B_0 is the magnitude of the external magnetic field, and I_z is the z-component of angular momentum operator.

4.2.2 Radiofrequency Interaction

The other external interaction is radio frequency resulting from the external oscillating magnetic field.

$$\hat{H}_{\text{RF}} = 2\omega_1 \cos(\omega t + \phi) I_x \quad (4.16)$$

The Hamiltonian is utilized to describe the application of RF pulse.

4.2.3 Chemical Shift Interaction

The chemical shift interaction occurs by the presence and motion of electrons around the nucleus. Due to the shielding effect on nucleus of the fields produced by the surrounding electrons, the field experienced at the nucleus generally is not exactly the applied magnetic field. It can be represented by:

$$\vec{B}_{\text{eff}} = (1 - \sigma)\vec{B}_0 \quad (4.17)$$

where B_{eff} is the effective magnetic field, B_0 is the applied magnetic field, and σ is the shielding tensor. The chemical shift is in general an anisotropic interaction depending on the relative orientation of the molecule to the external static field, there is a change in the resonance frequency. The chemical shift Hamiltonian can be written as:

$$\hat{H}_{\text{CS}} = \gamma \hat{I} \sigma B_0 \quad (4.18)$$

In the NMR experiment, the applied field B_0 orientates to the spin vectors (I) and also determines the shielding field from the electrons. Thus, the interaction between spin I and shielding field depends on the relative position of the spin I and the electrons giving the shielding field with respect to B_0 .

4.2.4 Spin-Spin Coupling Interaction

The spin-spin coupling interaction, also called as the J coupling is the interaction between nuclei mediated through the bonding electrons in the molecular. The J coupling interaction can be represented as:

$$\hat{H}_j = \vec{I}_i \cdot \hat{J} \cdot \vec{I}_k \quad (4.19)$$

The interaction is the independent field and usually smaller than the other consideration interaction.

4.2.5 Direct Dipole-Dipole Interaction

The dipole-dipole interaction, also called the dipolar interaction arises from the direct dipole-dipole interaction between nuclei through space. This interaction depends on the internuclear distance and also on the molecular orientation. The dipolar interaction is expressed by the Hamiltonian as:

$$\hat{H}_D = -\frac{\mu_0}{4\pi} \gamma_i \gamma_k \hbar \left[\frac{\hat{I}_i \cdot \hat{I}_k}{r^3} - 3 \frac{(\hat{I}_i \cdot \mathbf{r})(\hat{I}_k \cdot \mathbf{r})}{r^5} \right] \quad (4.20)$$

Using spherical coordinates, the dipolar Hamiltonian can be represented as:

$$\hat{H}_D = -\frac{\mu_0}{4\pi} \frac{\gamma_i \gamma_k \hbar}{r^3} [\hat{A} + \hat{B} + \hat{C} + \hat{D} + \hat{E} + \hat{F}] \quad (4.21)$$

where the terms are:

$$\hat{A} = \hat{I}_z^i \hat{I}_z^k (3 \cos^2 \theta - 1)$$

$$\hat{B} = -\frac{1}{4} [\hat{I}_+^i \hat{I}_-^k + \hat{I}_-^i \hat{I}_+^k] (3 \cos^2 \theta - 1)$$

$$\hat{C} = \frac{3}{2} [\hat{I}_z^i \hat{I}_+^k + \hat{I}_+^i \hat{I}_z^k] \sin \theta \cos \theta e^{-i\varphi}$$

$$\hat{D} = \frac{3}{2} [\hat{I}_z^i \hat{I}_-^k + \hat{I}_-^i \hat{I}_z^k] \sin \theta \cos \theta e^{+i\varphi}$$

$$\hat{E} = \frac{3}{4} [\hat{I}_+^i \hat{I}_+^k] \sin^2 \theta e^{-2i\varphi}$$

$$\hat{F} = \frac{3}{4} [\hat{I}_-^i \hat{I}_-^k] \sin^2 \theta e^{+2i\varphi}$$

where the operators \hat{I}_+, \hat{I}_- are the raising and lowering operator defined as:

$$\hat{I}_\pm = \hat{I}_x \pm \hat{I}_y \quad (4.22)$$

θ and φ are the polar angles, specifying the orientation of the dipolar vector in the laboratory frame. A scheme illustrating the polar angles is shown in Figure 4.1.

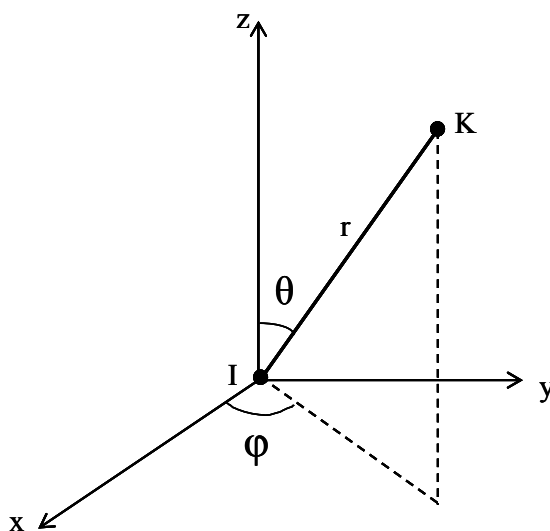


Figure 4.1: The relative orientation of the nuclear distance vector in the laboratory frame is given by angles θ and φ

On the other hand, the dipole Hamiltonian can be expressed in the second-rank Cartesian tensorial form:

$$\hat{H}_D = -2\hat{I} \cdot \mathbf{D} \cdot \hat{I} \quad (4.23)$$

where \mathbf{D} is the dipole-coupling tensor with principal values of $-d/2$, $+d/2$, $+d$ with d is the dipolar coupling constant is given by:

$$d = \frac{\mu_0}{4\pi r^3} \gamma_i \gamma_k \hbar \quad (4.24)$$

The dipolar coupling constant has a strong dependence on the distance between two spins and also dependent on the angle between the internuclear vector and the external magnetic field.

The dipolar interaction between homonuclear spins I_i and I_k is given by:

$$\hat{H}_D^{\text{homo}} = -\frac{\mu_0}{4\pi} \frac{1}{2r_{ik}^3} \gamma^2 \hbar (3 \cos^2 \theta - 1) [3\hat{I}_z^i \hat{I}_z^k - \hat{I}^i \hat{I}^k] \quad (4.25)$$

The heteronuclear dipolar Hamiltonian for spins I and S is given:

$$\hat{H}_D^{\text{hetero}} = -\frac{\mu_0}{4\pi r_{is}^3} \gamma_i \gamma_s \hbar (3 \cos^2 \theta - 1) \hat{I}_z \hat{S}_z \quad (4.26)$$

Both heteronuclear and homonuclear dipolar interactions depend on the γ as well as on the orientation of the internuclear vector and the inverse cube of distance.

4.2.6 Quadrupolar Interaction

The quadrupolar interaction is a result of the interaction between the non-spherical charge distribution of the nucleus (only for $I > 1/2$) and the electric field gradient at the nucleus. The quadrupole Hamiltonian can be expressed as:

$$\hat{H}_Q = \frac{eQ}{2I(2I-1)\hbar} \hat{I} \cdot \mathbf{V} \cdot \hat{I} \quad (4.27)$$

where \hat{I} is the nuclear spin vector and Q is the nuclear quadrupolar moment.

The valuable information of quadrupolar interaction can be described by the quadrupole coupling constant

$$C_Q = \frac{e^2 q Q}{h} \quad (4.28)$$

where eQ is a nuclear quadrupole moment, and $eq = V_{zz}$ is an electric field gradient due to non-spherically symmetric charge distribution.

The quadrupole asymmetric parameter (η_Q) describes the asymmetry of electric field

$$\eta_Q = \frac{V_{xx} - V_{yy}}{V_{zz}} \quad (4.29)$$

A schematic picture for a spin $I = \frac{3}{2}$ is illustrated in Figure 4.2. Placing the nucleus in external magnetic field leads to equal splitting of the energy levels due to the Zeeman interaction. In the first-order quadrupole interaction (H_Q^1), the central transition (CT) ($m = -\frac{1}{2} \leftrightarrow +\frac{1}{2}$) is not perturbed, while the satellite transitions (ST) ($m = \pm\frac{1}{2} \leftrightarrow \pm\frac{3}{2}$ etc.) are affected. A powder sample will provide a sharp central transition unaffected by the anisotropic quadrupole interaction, whereas the satellite transitions give broad powder patterns. The spectra due to large quadrupole interactions can not be precisely described by the first-order energy levels. The second-order quadrupole interaction (H_Q^2) influences all of central and satellite transitions. In practice, only a broad powder pattern is observed for the central transition. For the central transition of non-integer quadrupole nuclei the dominant perturbation is second-order.

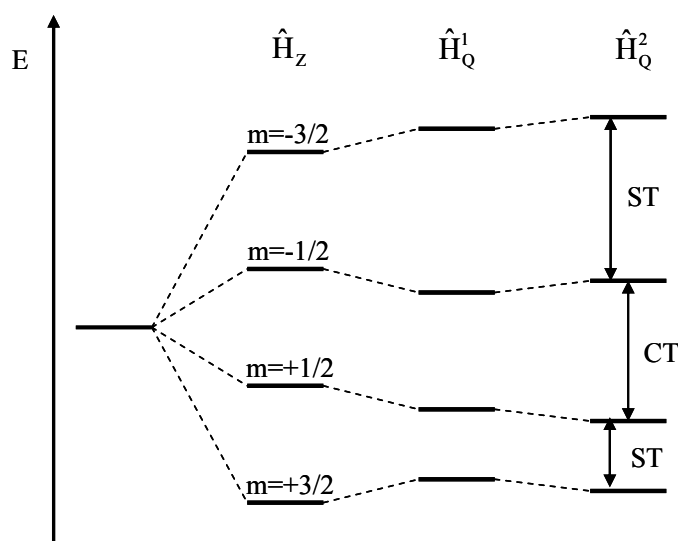


Figure 4.2: Energy level diagram for a spin $\frac{3}{2}$ showing the Zeeman interaction (\hat{H}_Z), the first order (\hat{H}_Q^1) and the second-order (\hat{H}_Q^2) quadrupole perturbation of energy levels

4.3 NMR Techniques

4.3.1 Magic Angle Spinning (MAS)

The Magic Angle Spinning (MAS) technique was discovered by Andrew et al.¹³⁸ and independently by Lowe.¹³⁹ In solid-state NMR, anisotropic interactions such as chemical shielding, dipole-dipole coupling, and quadrupole coupling contribute a broadening line in NMR spectrum. In order to narrow the line, the MAS technique is applied with the rotating sample about a spinning axis, which is inclined at the angle of 54.74° to the direction of the static magnetic field. Under this condition, the second-rank interactions are averaged to zero over the rotor period.

The molecular orientation dependence of the nuclear spin interaction is defined as $(3\cos^2\theta - 1)$, while θ is an angle which depicts to the orientation of the spin interaction tensors respecting to anisotropic interactions. In solid state NMR, the angle θ efficiently takes on all possible values, and then molecular orientations are represented. While the powder sample is spun about axis inclined to the applied magnetic field (B_0) at θ_R angle (Figure 4.3), θ varies with time as the molecule rotates with the samples. Then the average of the orientation dependence of nuclear spin interaction under spinning condition can be presented as:

$$\langle 3\cos^2\theta - 1 \rangle = \frac{1}{2}(3\cos^2\theta_R - 1)(3\cos^2\beta - 1) \quad (4.30)$$

where β is angle between the spinning axis and principal z-axis; θ_R and θ are defined above.

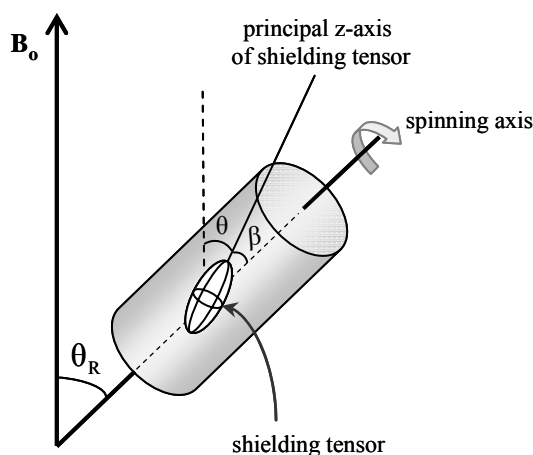


Figure 4.3: The magic angle spinning technique with the sample is spun about spinning axis at the angle 54.74° in related to the applied magnetic field

The angle β is fixed by a given nucleus, the angle θ takes on all possible values; whereas θ_R can be controlled. On the other hand, if the angular dependence $\langle 3 \cos^2 \theta - 1 \rangle$ is zero, the anisotropic parts will disappear, leaving only the isotropic parts, as would be expected. By setting the $\theta_R = 54.74^\circ$, the $(3 \cos^2 \theta_R - 1) = 0$, and then the average $\langle 3 \cos^2 \theta - 1 \rangle$ becomes zero. Therefore, at fast spinning rate, the θ is rapidly averaged in comparison with anisotropy of the interaction, the interaction anisotropy averages to zero. Thus, the angle 54.74° is called the "magic angle".

4.3.2 Multiple Quantum Magic Angle Spinning (MQMAS)

Determination of quadrupole coupling parameters by regular MAS NMR becomes more difficult if multiple lineshapes overlap. In 1995, Frydman and Harwood^{140, 141} proposed a multiple quantum magic angle spinning (MQMAS) NMR technique for achieving high resolution spectra of half-integer quadrupolar nuclei. The MQMAS technique is a two dimensional NMR technique in which one dimension is free of quadrupolar broadening. In this technique, the isotropic dimension is correlated to the anisotropic dimension that gives the second-order broadened effects.

The MQMAS technique utilizes the transitions of the type $|m_s\rangle \leftrightarrow \langle -m_s|$, which are predicted that powder resonances arising from these transitions will be devoid of the first order quadrupole effects. The generalized transition frequency is given below:¹⁴⁰

$$\omega_{-m_1 \leftrightarrow +m_1} = \frac{\omega_Q^2}{\omega_0} \left[A_0 C_0^1(m) + A_2(\alpha, \beta) C_2^1(m) P_2(\cos \theta) + A_4(\alpha, \beta) C_4^1(m) P_4(\cos \theta) \right] \quad (4.31)$$

where ω_Q is the quadrupole coupling constant; ω_0 is the Larmor frequency; A_0 is a constant proportional to the isotropic quadrupole shift; $A_2(\alpha, \beta)$ and $A_4(\alpha, \beta)$ are the orientation dependent functions responsible for the residual broadening that is observed even under spinning conditions; $P_2(\cos \theta)$ and $P_4(\cos \theta)$ are the second- and fourth- order Legendre polynomials; and the $\{C_l^1(m)\}_{l=0-4}$ are coefficients depending on the spinning number l and the Zeeman levels being correlated.

Since symmetric transitions are not affected by the first-order quadrupole effects, all anisotropies will vanish at time (t_1, t_2) fulfilling the following condition¹⁴²

$$C_4^1(m_1)t_1 + C_2^1(m_2)t_2 = 0 \quad (4.32)$$

Under MAS conditions with the selection rules for NMR ($\Delta m = \pm 1$) only the coherence order concerning to the central transition ($m_2 = 1/2$) can be observed during t_2 . The correct t_1 evolution sense is possible chosen, regardless of the relative sign of the $C_4^1(m_1), C_4^1(1/2)$ coefficients, that will lead to the refocusing of the fourth-rank anisotropies. The high resolution echo will form:

$$t_2 = \left| \frac{C_4^1(m_1)}{C_4^1(1/2)} \right| t_1 \quad (4.33)$$

Fourier transforming in the t_1 and t_2 periods produces the 2D spectrum in which the F1 and F2 projections are anisotropic. By applying a shearing transformation, an isotropic spectrum with high resolution along the F1 dimension is found.

For spin $I = 3/2$, the two frequencies resulting after the shearing of the 2D correlation NMR spectrum are given ¹⁴³

$$\omega_{F1} = \frac{34\omega_{CS}^{iso} - 60\omega_Q^{(0)}}{9} \quad (4.34)$$

$$\text{and } \omega_{F2} = \omega_{CS}^{iso} + 3\omega_Q^{(0)} - 21\omega_Q^4(\alpha, \beta) \quad (4.35)$$

Since the center of mass of the $\omega_Q^{(4)}(\alpha, \beta)$ term for randomly distributed powders is zero, a center of mass calculation of the anisotropic line shape along ω_{F2} ends up reflecting only the sum of two isotropic components

$$\langle \omega_{F2} \rangle = \omega_{CS}^{iso} + 3\omega_Q^{(0)} \quad (4.36)$$

By using the center of mass of the signal and the equation above, the isotropic quadrupolar shift can be determined

$$\omega_Q^{(0)} = -\frac{(\text{SOQE})^2}{30\omega_0 [2I(2I-1)]^2} \quad (4.37)$$

where SOQE is the second order quadrupolar effect given by

$$\text{SOQE} = C_Q \sqrt{1 + \frac{1}{3} \eta_Q^2} \quad (4.38)$$

The main drawback of the MQMAS experiment is the rather inefficient excitation and conversion of the multiple quantum transition. To decrease dispersion signals, the z-filtered sequence can be applied.¹⁴⁴ Figure 4.4 shows the z-filter MQMAS pulse sequence.

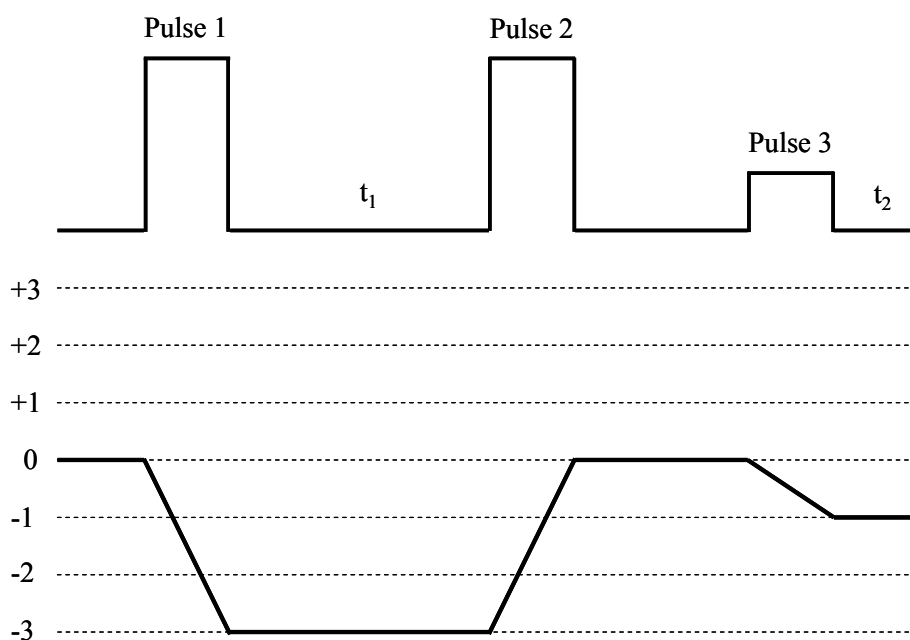


Figure 4.4: Zero quantum filter MQMAS NMR pulse sequence

In such experiment, the first pulse is designed to create the maximum amount of $\pm p$ quantum symmetrical coherences. Both coherences evolve during t_1 and are refocused along $p = 0$ by the second pulse. The time between second and third pulses is called z-filter, in which all components of magnetization perpendicular to the external field dissipate during this period. The final soft pulse transforms the zero quantum coherence into an observable signal.

Chapter

5

Experimental

5.1 Synthesis

Generally, zeolites and molecular sieves are synthesized hydrothermally in autoclaves under autogenously pressure. Besides the hydrothermal synthesis, the dry-gel method can be applied for zeolite and molecular sieve synthesis.

5.1.1 *BEA Hydrothermal Synthesis

5.1.1.1 Beta Borosilicates (B-*BEA)

*BEA borosilicates with sodium or without sodium were synthesized using the gel compositions of $1 \text{ SiO}_2 : 0.033 \text{ B}_2\text{O}_3 : x \text{ Na}_2\text{O} : 0.54 \text{ TEAOH} : 18 \text{ H}_2\text{O}$ ($x = 0.15$ or $x = 0$).

A typical synthesis for B-*BEA is as follows: 1.63 g (0.026 mol) H_3BO_3 (Aldrich) was dissolved in 22.72 g of an aqueous solution TEAOH (35 % w/w, Aldrich) and 68.5 ml de-ionized water. In the case of sodium B-*BEA, 4.82 g (0.12 mol) NaOH was dissolved completely in 2 ml de-ionized water, and the NaOH solution was slowly dropped into the

boron solution. The solutions were stirred for 30 min, and then 24.03 g of Cab-O-Sil M5 (Cabot) was slowly added, the gels were stirred for 2 hours. The aluminum solution was prepared as follows: 0.37 g (0.001 mol) $\text{Al}(\text{NO}_3)_3 \cdot 9\text{H}_2\text{O}$ (Aldrich) was dissolved in 2 ml of de-ionized water and stirred until homogeneous. The $\text{Al}(\text{NO}_3)_3$ solutions were slowly added in the gels and stirring were continued for 4 hours. The final gels were charged in Teflon-lined stainless steel autoclaves and heated at 423 K. The crystallizations were typically completed by heating up to 96 hours without sodium and 72 hours with sodium, and then centrifuged to separate the solid and liquid phases. The collected solids were washed several times with de-ionized water until $\text{pH} \sim 9$ and dried at 323 K overnight.

These samples were utilized for further investigation of boron sites and post synthesis modification with Al^{3+} and Ga^{3+} . A typical preparation of *BEA borosilicate via hydrothermal method is illustrated in Figure 5.1.

5.1.1.2 Aluminum Beta Zeolites (Al-*BEA)

Aluminum beta zeolites with sodium or without sodium were synthesized using the gel compositions of $1 \text{ SiO}_2 : 0.033 \text{ Al}_2\text{O}_3 : x \text{ Na}_2\text{O} : 0.54 \text{ TEAOH} : 18 \text{ H}_2\text{O}$ ($x = 0.1$ or $x = 0$).

The initial gels were prepared by adding 3 g of Cab-O-Sil M5 in 11.22 g of an aqueous solution TEAOH (35 % w/w, Aldrich), the gels were stirred until homogenized for about 2 hours. The aluminum solution was prepared by dissolving 1.25 g (0.003 mol) $\text{Al}(\text{NO}_3)_3 \cdot 9\text{H}_2\text{O}$ (Aldrich) in 9 ml of de-ionized water and stirred until dissolved. In case of sodium beta zeolite, the aluminum source was prepared from sodium aluminate as following: 0.32 g of sodium aluminate (Fluka) and 0.07 g NaOH (Aldrich) were added in 9 ml of de-ionized water, this mixture was stirred until dissolved completely for about 15 minutes. Finally, the Al^{3+} solutions were slowly added in the silica gels and stirred continuously for 4 hours. The gels were charged in Teflon-lined stainless steel autoclaves, heated at 423 K for 72 hours and then centrifuged to separate the solid and liquid phases. The white solids were recovered by centrifugation, then washed several times with de-ionized water until $\text{pH} \sim 9$ and dried at 323 K overnight. These beta zeolites were used for further investigations of nanoparticle formation in organic solvents.

5.1.2 *BEA Dry-Gel Synthesis

Dry-gel *BEA borosilicates with the compositions of $1 \text{ SiO}_2 : 0.033 \text{ B}_2\text{O}_3 : x \text{ Na}_2\text{O} : 0.54 \text{ TEAOH}$ ($x = 0$ or $x = 0.033$) were prepared as dry-gel conversion (DGC). The typical synthesis as follows: 13.36 g (0.032 mol) of an aqueous solution TEAOH (35 % w/w, Aldrich) was mixed with 8.83 g (0.059 mol) of colloidal silica LUDOX AS-40 (Aldrich) and the mixtures were stirred for 15 min. The boron source with 0.24 g (0.002 mol) H_3BO_3 or 0.37 g (0.002 mol) $\text{Na}_2\text{B}_4\text{O}_7$ (Aldrich) was dissolved in 5 ml of de-ionized water and added dropwise to the above mixture. For the aim to prepare the sodium beta borosilicate, the sodium solution was prepared by dissolving 0.16 g (0.04 mol) NaOH in 2 ml of de-ionized water; the sodium source was added to the gel. The final mixtures were further stirred for 2 hours. After aging, the gels were dried at 353 K in an oil bath with continuous stirring, allowing evaporation of water. While the gels became thick and viscous, they were homogenized by hand until dried. Subsequently, these gels were crushed into fine powders. For crystallization, 0.5 g of each gel was poured in small Teflon cup; this cup was located in a Teflon-lined stainless steel autoclave, in which 1 ml of de-ionized water was poured in the bottom. During the crystallization, the dry-gels never came into the direct contact with liquid water. The DGC processes were carried out at 443 K during periods of up to 72 hours in autogeneous pressure. The samples obtained after quenching autoclaves in cold water and separating by centrifugation were washed three times with 30 ml of de-ionized water and dried at 323 K overnight. A typical preparation of *BEA borosilicates via dry-gel method is shown in Figure 5.1.

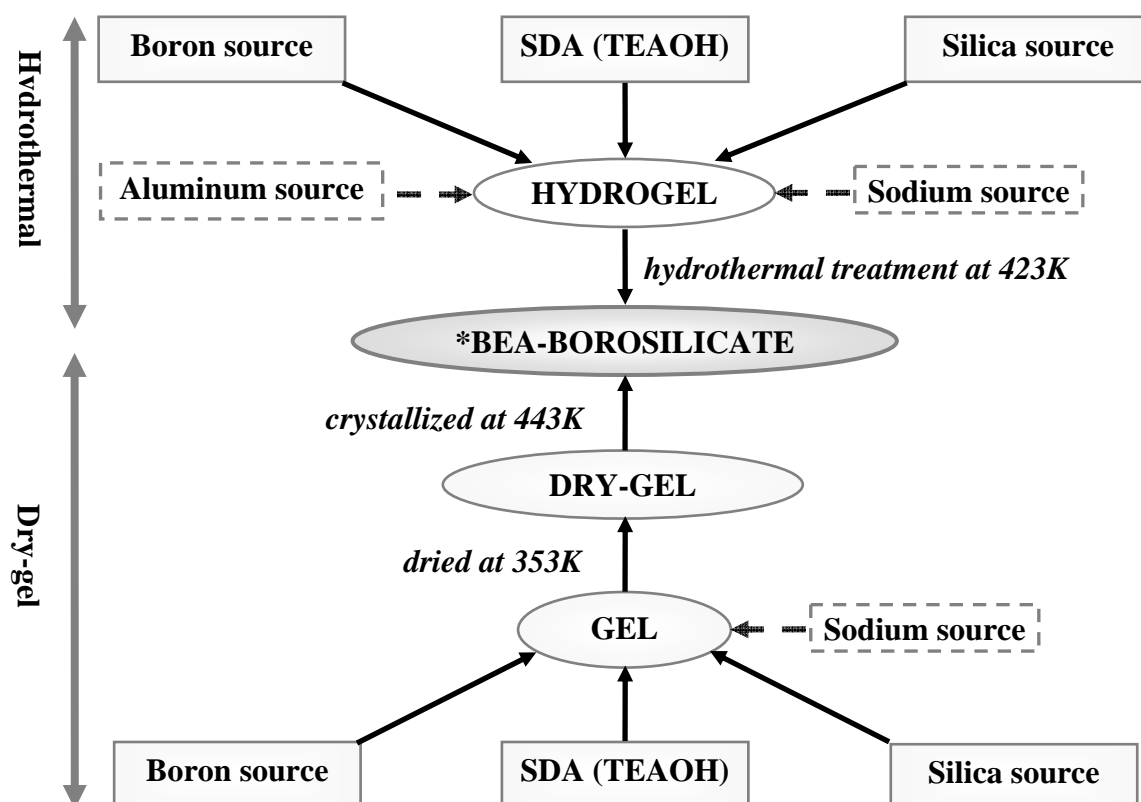


Figure 5.1: Scheme illustrating the synthesis of *BEA-borosilicate via hydrothermal and dry-gel methods

5.1.3 MFI Synthesis

5.1.3.1 B-MFI

MFI borosilicate was synthesized as following the batch composition: 1 SiO₂ : 0.04 B₂O₃ : 0.1 TPAOH : 34 H₂O.

A typical synthesis for B-MFI as follows: 0.31 g (0.01 mol) H₃BO₃ (Aldrich) was dissolved in 6.46 g of an aqueous solution TPAOH (1M aqueous solution, Fluka) and 33.8 ml de-ionized water. After that, 3.82 g of Cab-O-Sil M5 was slowly added, and the gel was stirred for 4 hours. This gel was charged in a Teflon-lined stainless steel autoclave and crystallized in hydrothermal condition at 423 K for 120 hours. After hydrothermal treatment, the autoclave was quenched in cold water. The collected solid after filtration was washed several times with de-ionized water until pH ~ 9 and dried at 323 K overnight.

5.1.3.2 Si-MFI

Si-MFI samples were synthesized according to the work by Koller et al.¹⁴⁵ with the batch compositions: 1 SiO₂ : 0.1 TPAOH : 38 H₂O in basic medium and 1 SiO₂ : 0.1 TPAOH : 0.5 NH₄F : 36 H₂O in fluoride medium.

The initial solution of a typical synthesis for Si-MFI in basic medium was prepared by mixing 13.89 g TEOS (Aldrich) and 6.77 g TPAOH (1M aqueous solution, Fluka) and 40 ml of de-ionized water. This mixture was hydrolyzed under slow stirring for 30 hours at room temperature in an open vessel for evaporating alcohols. The water weight loss due to evaporation process was compensated by adding de-ionized water in the initial solution. The obtained gel was transferred to a Teflon-lined stainless steel autoclave and treated under hydrothermal conditions. The crystallization was performed at 423 K for 6 days. After that, stainless steel autoclave was quenched in cold water. The liquid was removed by filtration and the collected solid was washed several times with de-ionized water until pH ~ 9 and dried at 323 K overnight.

For Si-MFI in fluoride medium, the procedure is as follows: 1.82 g of TPABr (Aldrich) was added in 30 ml of de-ionized water and stirred until dissolved. After that, 4 g of Cab-O-Sil M5 was added slowly in that solution, this gel was stirred for 2 hours. The fluoride solution was prepared from NH₄F (Fluka) by adding 1.26 g NH₄F in 13 ml of de-ionized water, this solution was stirred until dissolved for about 10 minutes. This ammonium fluoride solution was added dropwise into the gel and stirred continuously for 2 hours. The achieved gel was charged in a Teflon-lined stainless steel autoclave and subjected to the hydrothermal treatment at 463 K for 6 days. After the hydrothermal treatment, the solid was selected by filtration and washed several times with de-ionized water until pH ~ 9 and dried at 323 K overnight.

These MFI zeolites were utilized for further investigation of nanoparticle formation in organic solvents.

5.2 Calcination and Dehydration

To remove the SDA occluded in zeolite channels, the as-synthesized B-*BEA zeolites were calcined in air in a muffle furnace at a heating rate of 2 K min⁻¹ from room temperature

(RT) to a final temperature of 923 K. During the heating, the temperature was held constant at two points: 383 K and 693 K for 2 hours of each. The final temperature was maintained for 6 hours.

The calcination of ion-exchanged samples was carried out in vacuum ($< 10^{-4}$ mbar) in glass ampoules with a temperature program as follows: 2 K min^{-1} to 383 K, and held for 2 hours, then 2 K min^{-1} to final temperature of 723 K, and maintained for 6 hours.

Dehydration of the calcined and rehydrated samples was carried out in vacuum ($< 10^{-4}$ mbar) in glass ampoules. The heating rate is 2 K min^{-1} from RT to target temperatures. During the dehydration, the samples were held at 383 K for 2 hours to remove most of water from the framework and then further heating to the target temperatures, which were maintained for 6 hours. After cooling down to the room temperature, the ampoules were sealed for storage and reopened under nitrogen in a glove-box to avoid the introduction of moisture.

5.3 Ion Exchange

5.3.1 Ion Exchange with Na^+ , NH_4^+

Ion exchange experiments were carried out in aqueous solution (1 mol L^{-1}) of the sodium acetate or ammonium acetate. The calcined B-*BEA powders were added to the cation solutions using 50 ml solution per gram of zeolite and stirred slowly for 12 hours. After that, the mixtures were separated by centrifugation and washed thoroughly with de-ionized water and dried at 323 K overnight.

B-*BEA samples which have different sodium/ammonium ratios were obtained by ion exchange in the mixtures of sodium acetate and ammonium acetate solutions with appropriate cation concentrations. For the ammonium exchanges, the pH values of ammonium solution were established at about 8.0 by adding a small amount of aqueous ammonia solution (1 mol L^{-1}) to the ammonium acetate solution.

The $\text{Na}^+/\text{NH}_4^+$ zeolite forms can be transformed to the Na^+/H^+ forms by calcination in vacuum at high temperature.

5.3.2 Post Synthesis Modification

5.3.2.1 Deboronation

Deboronation was carried out with de-ionized water using 100 ml of pure water at pH ~ 7 per gram of the Na^+/H^+ zeolites at room temperature. The mixtures were stirred slowly for 12 hours, separated by centrifugation and dried in air at 323 K overnight. This process was repeated up to four times for complete deboronation.

5.3.2.2 Post-Synthesis Exchange with Al^{3+}

Aluminum modified *BEA samples were prepared in both aqueous (water) and organic (ethyl alcohol) media using aluminum nitrate ($\text{Al}(\text{NO}_3)_3 \cdot 9\text{H}_2\text{O}$, Aldrich) as precursor.

The first series has been treated in aqueous medium. The aluminum solution was prepared by dissolving 0.05 g of aluminum acetate in 20 ml of de-ionized water. Then, NH_4OH was added dropwise to the mixture until pH ~ 10 . The aluminum solution was obtained by centrifugation from the precipitated $\text{Al}(\text{OH})_3$. In this series, 100 mg of deboronated sample was dispersed in a 20 ml of aluminum solution, and stirred for 4 hours at RT. The solid samples were recovered by centrifugation, washed with de-ionized water and air-dried at 323 K overnight.

The second series has been carried out in ethanol containing aluminum nitrate. This solution was prepared by dissolution of 0.5 g of $\text{Al}(\text{NO}_3)_3 \cdot 9\text{H}_2\text{O}$ in 200 ml dried ethanol. In a typical preparation, 100 mg of deboronated sample was dispersed in 20 ml of aluminum nitrate ethanol solution. The mixtures were stirred for 4 hours at room temperature, separated by centrifugation, washed with dried ethanol and then dried at 323 K overnight.

5.3.2.3 Post-Synthesis Exchange with Ga^{3+}

The gallium exchanged samples were performed in ethanol containing gallium nitrate. This solution was prepared by dissolution of 0.35 g of $\text{Ga}(\text{NO}_3)_3 \cdot n\text{H}_2\text{O}$ in 120 ml of dried ethanol. The mixtures were prepared with 20 ml of gallium-ethanol solution per 100 mg of deboronated samples. These mixtures were slowly stirred for 3 hours at 323 K; the solids

were collected by centrifugation, washed thoroughly with cold ethanol and dried at room temperature.

5.4 Zeolite Dissolution

The colloidal zeolites were prepared from powders of zeolite microcrystals. These zeolites were either commercial samples from Degussa (ZSM-5, NaY) or they were hydrothermally synthesized using standard procedures (B-MFI, Beta, B-*BEA). These zeolites were dried at 373 K for 1 day before treatment in DMF. In experiments, 100 mg of zeolite was dispersed in 50 ml of organic solvents (such as DMF, DMSO) and stirred slowly for 6 or 12 hours at room temperature, and then separated by centrifuge (5500 rpm, 10 minutes). This process (Figure 5.2) can be repeated in an iterative way, so that several colloidal zeolite suspensions can be formed.

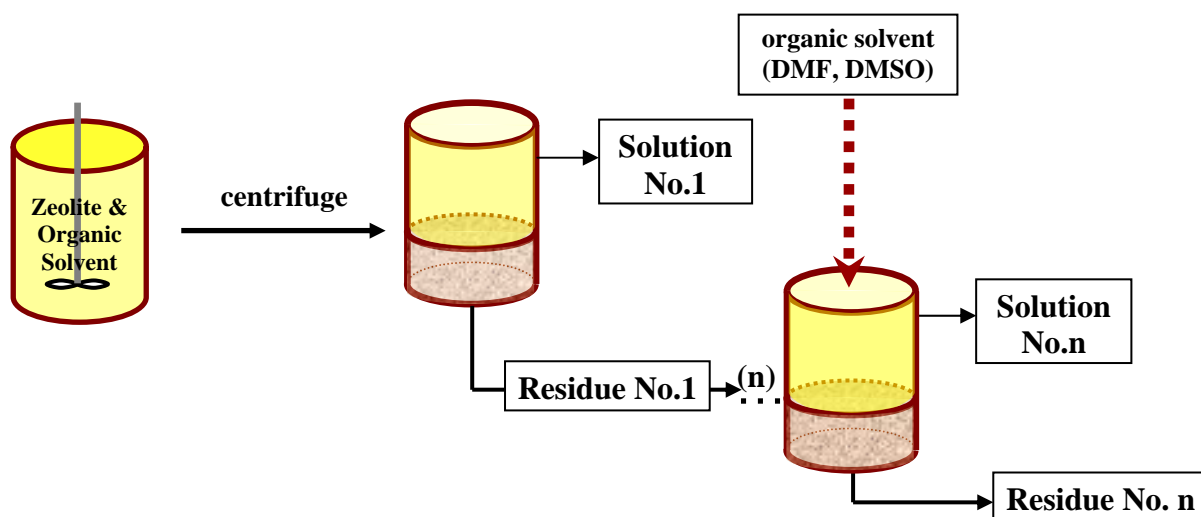


Figure 5.2: Scheme illustrating the preparation of colloidal zeolites in organic solvents

In dissolution series, zeolites were slurried in 10 ml of DMF from Aldrich as received or dried over CaH_2 and stirred for 12 hours at ambient temperature. In the dried DMF series, the processes were performed Argon atmosphere. Clear solutions were obtained by a centrifugation.

The influence of water was studied with 100 mg of zeolite in 10 ml of dried DMF, in which small amounts of de-ionized water were added. These mixtures were stirred for 12

hours at ambient temperature in the Argon line. After that, clear solutions were separated by centrifugation.

The effect of sodium was studied with 100 mg of zeolites treated in 50 ml of DMF. Different amounts of sodium cations as NaCl aqueous solution were added in the mixtures and stirred for 12 hours. Finally, clear solutions are obtained by centrifugation.

5.5 X-Ray Diffraction

The powder X-ray diffraction of zeolite were carried out on Guinier-Camera, using Cu-K α radiation ($\lambda = 1.5406\text{\AA}$). The exposure times were carried out between thirty to forty-five minutes for beta zeolite and between eleven to twenty minutes for the other zeolites. The data were acquired between 7° and 50° (2θ), with 0.025° step. The samples were prepared as thin layers on amorphous scotch tape, prior to scanning.

The relative crystallinities of beta zeolites were determined by a quantitative evaluation of the amplitude of the most intense X-Ray reflection line at $2\theta = 22.4^\circ$.

5.6 Raman Spectroscopy

The Raman spectra were recorded from powdered and liquid samples by Jobin Yvon Horiba HR800 Raman spectrometer. The laser beam (with Nd/YAG laser at 532 nm as the excitation source) was focused through microscope objectives 40x and 50x for liquid and powder samples respectively.

5.7 Scanning Electron Microscopy (SEM)

The SEM images were determined on a LEIKA Cambridge Stereoscan 420 instrument. The samples were loaded on stubs and sputtered with gold film to prevent surface charging and also to protect from thermal damage from the electron beam, prior to scanning. Before the SEM investigations, the samples were dehydrated at room temperature for the pressure $< 10^{-5}$ mbar.

5.8 Atomic Force Microscopy (AFM)

The AFM micrographs were imaged on an AFM Nanoscope IIIa - Controller Digital Instrument (Santa Barbara, CA) DI 3100. For preparation, 100 μl of colloidal zeolites was added dropwise on glass slides with the surface modified by Poly-L-Lysine (0.01 % m/V, $\mu = 150000 - 300000$, Aldrich) and incubation time for 30 seconds at room temperature.

5.9 Thermogravimetric and Differential Thermal Analysis (TGA-DTA)

Thermogravimetric and differential thermal analyses were performed in Netzsch STA 409 C/CD thermal analyzer with about 40 mg of sample with a heating rate at 10 K min^{-1} between 298 K and 1173 K in oxygen flow. The base line correction was made using Al_2O_3 as the reference sample.

5.10 Dynamic Light Scattering (DLS)

The mean particle sizes and zeta potentials of the colloids were measured by ZetaSizer 3000HSA, Malvern Instruments, with a helium-neon laser of 633 nm wavelength and fixed scattering angle of 90° at 25°C . The sizes of particles can be determined with a diameter in the range of 5 to 5000 nm. The colloidal solutions were charged in a glass cuvette 100-OS, Hellma. The particle size distributions are analyzed by Non-Negatively Constrained Least Squares (NNSL) autocorrelation method.

5.11 Nuclear Magnetic Resonance (NMR) Spectroscopy

The solid-state NMR spectra were carried out at ambient temperature on Bruker CXP 300 and Bruker DSX 500 spectrometers at $B_0 = 7.05$ T and 11.7 T respectively. MacNMR and Topspin softwares were applied for the CXP 300 and the DSX 500 spectrometers, respectively. The spectrum lineshape was analyzed by using the DMFIT program. The chemical shifts were referenced with appropriate solutions as summarized in Table 5.1

Table 5.1: *The references for calibration of NMR spectra*

Nuclei	References
^1H	Tetramethylsilane
^{11}B	$\text{BF}_3 \cdot \text{O}(\text{C}_2\text{H}_5)_2$
^{23}Na	NaCl 1 mol L^{-1}
^{27}Al	$\text{Al}(\text{NO}_3)_3$ 1 mol L^{-1}
^{71}Ga	$\text{Ga}(\text{NO}_3)_3$ 1 mol L^{-1}
^{29}Si	Tetramethylsilane

The powder samples were packed in 7 mm ZrO_2 rotor, spun at 4 kHz (CXP 300) and 4 mm ZrO_2 rotor, spun at 10 or 15 kHz (DSX 500) using the Bruker MAS probes (Table 5.2). ^{29}Si -MAS NMR was recorded on Bruker CXP 300 operating at resonance frequency of 59.63 MHz. On Bruker DSX 500, the resonance frequencies were 500.18 MHz for ^1H -, 160.48 MHz for ^{11}B -, 132.31 MHz for ^{23}Na -, 130.33 MHz for ^{27}Al -, and 152.54 MHz for ^{71}Ga -MAS NMR.

Table 5.2: *The probes utilized for NMR measurements with respective nuclei in corresponding magnetic fields*

Nuclei	B_0	Probe
^1H MAS NMR	11.7 T	Bruker HPWB 73B MAS 4BL CP BB WVT
^{11}B MAS NMR	11.7 T	Bruker HPWB 73B MAS 4BL CP BB WVT
^{11}B MAS spin-echo NMR	11.7 T	Bruker HPWB 73B MAS 4BL CP BB WVT
^{11}B MQMAS NMR	11.7 T	Bruker HPWB 73B MAS 4BL CP BB WVT
^{23}Na MAS NMR	11.7 T	Bruker HPWB 73B MAS 4BL CP BB WVT Bruker HPWB 73A MAS 4BL CP BB VTN
^{27}Al MAS NMR	11.7 T	Bruker HPWB 73B MAS 4BL CP BB WVT Bruker HPWB 73A MAS 4BL CP BB VTN
^{71}Ga MAS NMR	11.7 T	Bruker HPWB 73B MAS 4BL CP BB WVT
^{29}Si MAS NMR	7.05 T	Bruker HPWB 73A MAS 7DB CP BB VTN

Typical acquisition parameters for ^{29}Si MAS NMR were pulse length $4.5\ \mu\text{s}$ for flip angle $\pi/2$, and recycle delay of 60 s. ^{11}B MAS NMR spectra were performed after applying a pulse length of $0.7\ \mu\text{s}$, corresponding to a flip angle $\pi/8$ of the liquid reference and a recycle delay of 2 s. The probe background was eliminated by either using a spin-echo sequence, or subtracting the background with an empty rotor. ^1H MAS NMR spectra were recorded using a $\pi/2$ pulse of $2\ \mu\text{s}$ duration and a recycle delay of 2 s. Typical MAS NMR spectra of ^{27}Al , ^{23}Na and ^{71}Ga were recorded after applying a $\pi/8$ pulse of $1\ \mu\text{s}$, $0.7\ \mu\text{s}$, and $1\ \mu\text{s}$ duration and recycle delay of 2 s, 1 s, and 5 s respectively. To compare directly, all spectra were obtained with the same number of transient and the sample weights in NMR measurements.

The ^{11}B 2D MQMAS experiments were performed using the standard z-filtered sequence at 15 kHz spinning. The first two hard pulses were 3.2 and $1.2\ \mu\text{s}$ in length, respectively. The third soft pulse was $12\ \mu\text{s}$ in length. In the t_1 increment, 120 scans were applied.

Chapter

6

Synthesis and Characterization of *BEA-Borosilicate

6.1 Beta Borosilicate Structure

6.1.1 Synthesis Methods

Beta zeolite is a widely used catalyst in various catalytic reactions. Hydrothermal synthesis is the conventional method, and most of zeolites are prepared via this method. However, it is difficult to synthesize the beta borosilicate in total absence of aluminum or without beta zeolite as a seed during the hydrothermal synthesis. Compared with hydrothermal synthesis, the dry-gel synthesis allows solid hydrogel transformation of the borosilicate gel with high yield without seeds or aluminum. On the other hand, the uniform crystals with smaller particle size could be obtained by this method.^{146, 147}

Beta borosilicate samples were prepared with sodium or without sodium via hydrothermal and dry-gel methods. The batch compositions of borosilicate gels are summarized in Table 6.1.

Table 6.1: The bath composition of *BEA-borosilicates synthesized vial hydrothermal and dry-gel synthesis

Sample	Method	Batch composition
$ \text{TEA}^+ [\text{B,Si-*BEA}]_{\text{HYD}}$	Hydrothermal	1SiO ₂ : 0.033B ₂ O ₃ : 0.54TEAOH: 18H ₂ O
$ \text{TEA}^+,\text{Na}^+ [\text{B,Si-*BEA}]_{\text{HYD}}$	Hydrothermal	1SiO ₂ : 0.033B ₂ O ₃ : 0.15Na ₂ O: 0.54TEAOH: 18H ₂ O
$ \text{TEA}^+ [\text{B,Si-*BEA}]_{\text{DRY}}$	Dry-gel	1SiO ₂ : 0.033B ₂ O ₃ : 0.54TEAOH
$ \text{TEA}^+,\text{Na}^+ [\text{B,Si-*BEA}]_{\text{DRY}}$	Dry-gel	1SiO ₂ : 0.033B ₂ O ₃ : 0.033Na ₂ O: 0.54TEAOH

The lattice geometries of *BEA borosilicate were established from X-Ray diffraction. The XRD powder patterns of borosilicate materials as-synthesized and after calcination are illustrated in Figure 6.1 and 6.2 respectively.

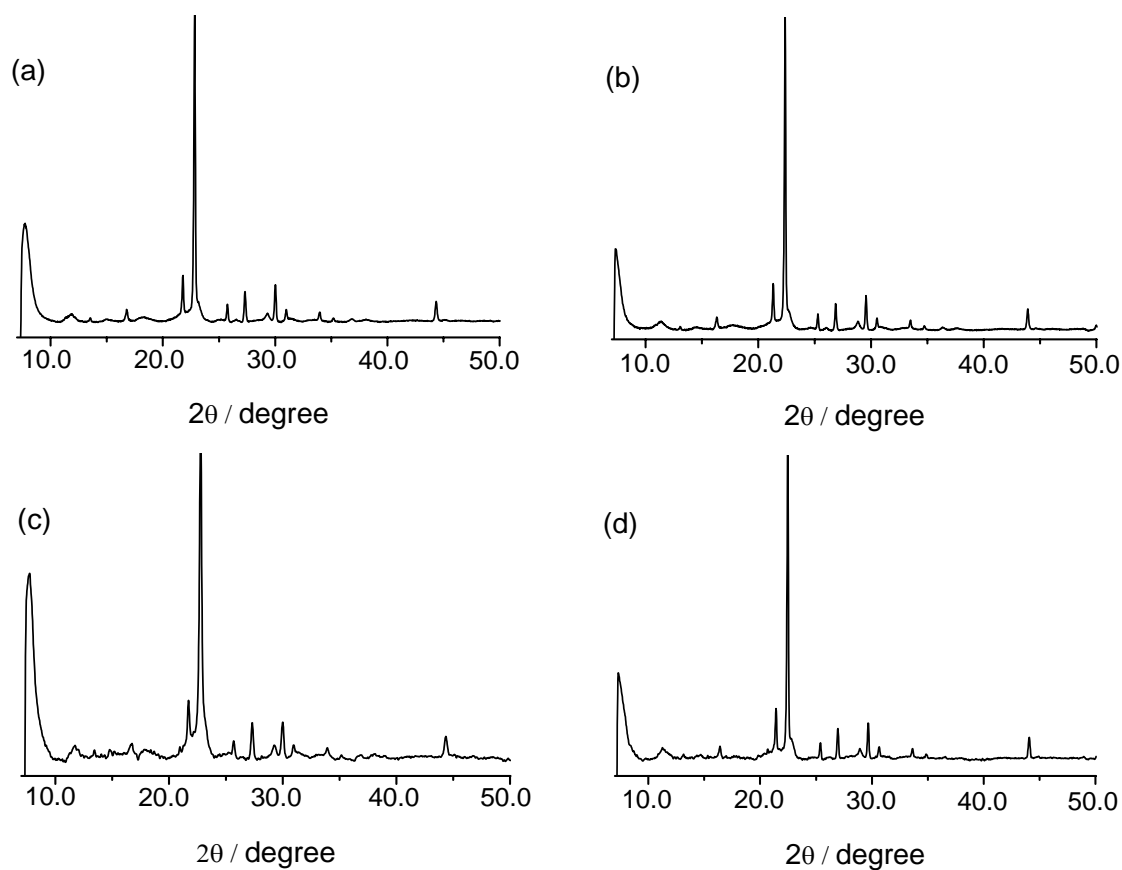


Figure 6.1: XRD powder patterns of beta borosilicates as-synthesized (a): $|\text{TEA}^+|[\text{B,Si-*BEA}]_{\text{HYD}}$, (b): $|\text{TEA}^+,\text{Na}^+|[\text{B,Si-*BEA}]_{\text{HYD}}$, (c): $|\text{TEA}^+|[\text{B,Si-*BEA}]_{\text{DRY}}$, (d): $|\text{TEA}^+,\text{Na}^+|[\text{B,Si-*BEA}]_{\text{DRY}}$

These figures imply that the beta structure is observed in all patterns. As mentioned in Chapter 2, beta zeolite exists as three polytypes: a tetrahedral lattice ($P4_122$) and two different monoclinic lattices ($C2/c$ and $P2$). The highly disordered structure of zeolite Beta produces a sharp peak ($h = 3n, k = 3n$) at $2\theta \sim 22.4^\circ$ and a broad peak at $2\theta \sim 7.5^\circ$ in the XRD patterns, consistent with faulting by $a/3$ and $b/3$ displacements on (001) planes. Thus, the width of sharp ($3n, 3n, l$) reflections will be mainly determined by the crystallite size, while that of the broad reflections is related to faulting.¹⁴⁸ The sharp reflections on the beta zeolite XRD powder patterns are indexed on a tetrahedral and two monoclinic lattices. In comparison between the SDA filled precursor and template free beta borosilicate (Figure 6.1 and 6.2), the changes of crystallinity and line broadening of two main reflections at $2\theta = 7.5^\circ$ and 22.4° are revealed. After calcination, changes of relative intensities are observed due to the removal of organic species and water from the pores.¹⁴⁹

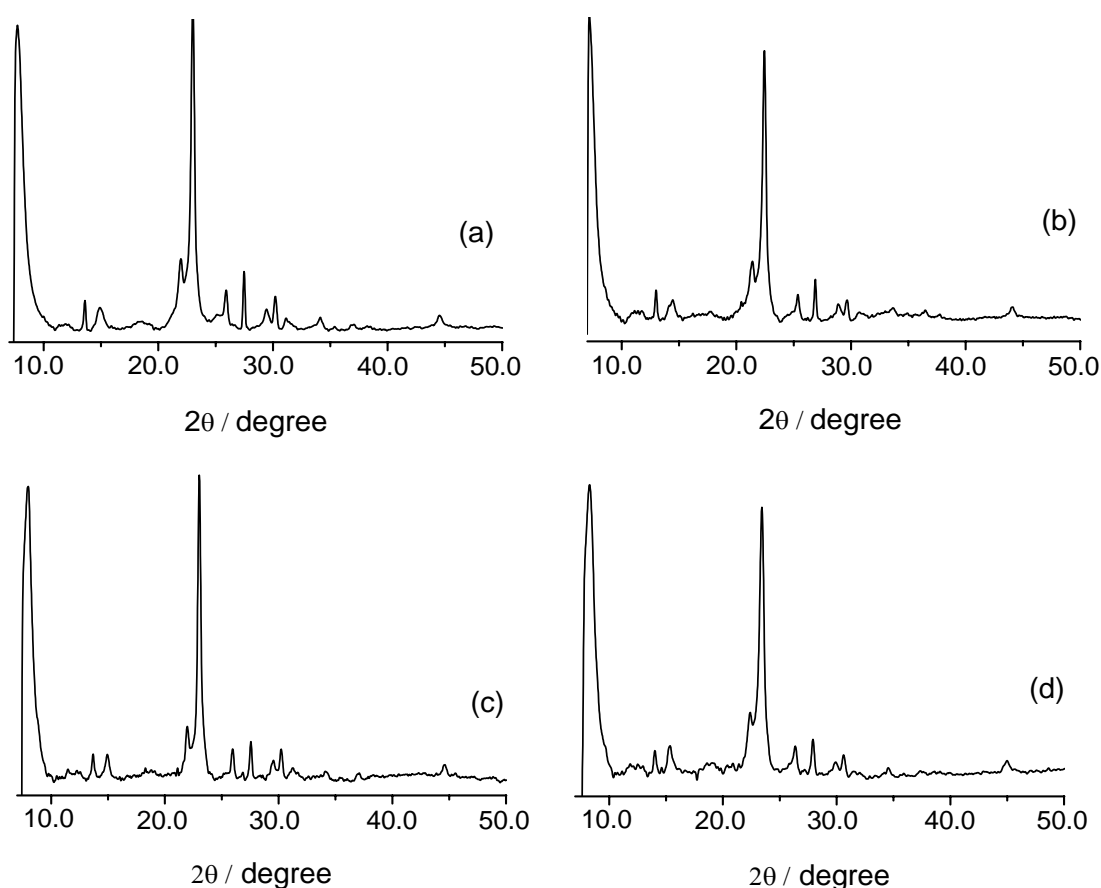


Figure 6.2. The XRD powder patterns of beta borosilicates after calcination (a): $|H^+|[B,Si-*BEA]_{HYD}$, (b): $|H^+,Na^+|[B,Si-*BEA]_{HYD}$, (c): $|H^+|[B,Si-*BEA]_{DRY}$, (d): $|H^+,Na^+|[B,Si-*BEA]_{DRY}$

6.1.2 Crystallization Time

*BEA borosilicates were synthesized via hydrothermal synthesis at different crystallization times. Figures 6.3a and 6.4a show the XRD powder patterns of as-synthesized materials obtained after different crystallization times in the absence and presence of sodium, respectively.

In Figure 6.3a and 6.4a, the patterns obtained after 4 hours of crystallization does not show any reflection, indicating the presences of a totally amorphous material. After 18 hours of crystallization time, the reflections are slightly viable in the absence and presence of sodium borosilicates. A weak increase in the line area of the main positions at $2\theta = 7.5^\circ$ and 22.4° are observed only at longer crystallization times. These reflections in the sodium sample are slightly more intense than without sodium. However, significant changes can be observed for the other weak reflections, i.e., a line area increase and a narrowing of the weak reflections with the ongoing hydrothermal process. This finding indicates that the long range order is essentially established during an initial period of approximately 18 hours, while thereafter only changes in the local structure occur. At about 52 hours of crystallization, all reflections of *BEA structure were recorded in both of XRD patterns of sodium and sodium free borosilicates.

On the other hand, tiny reflections at $2\theta = 21.1^\circ$ and 24.6° which are not characteristic for the *BEA structure are slightly viable in the pattern of the sodium free material after 18 hours of crystallization. Interestingly, these reflections are not growing in the batches at longer crystallization times. In fact, not any reflections at those positions are observed in the patterns of materials crystallized at longer times (Figure 6.3a).

The relative crystallinities of the absence and presence of sodium borosilicates obtained after different crystallization times were performed in Figure 6.3b and 6.4b, respectively. As a reference, the amplitude of the main line at $2\theta = 22.4^\circ$ in the powder pattern of *BEA borosilicate without sodium obtained after a crystallization time of 96 hours was used also for samples without sodium. The crystallization time of sodium beta borosilicate can be decreased by adding sodium to the initial gel. A crystallization time of 72 hours can be achieved for the synthesis of *BEA borosilicate in presence of sodium with the gel ratio: 1 SiO₂ : 0.033 B₂O₃ : 0.15 Na₂O : 0.54 TEAOH : 18H₂O.

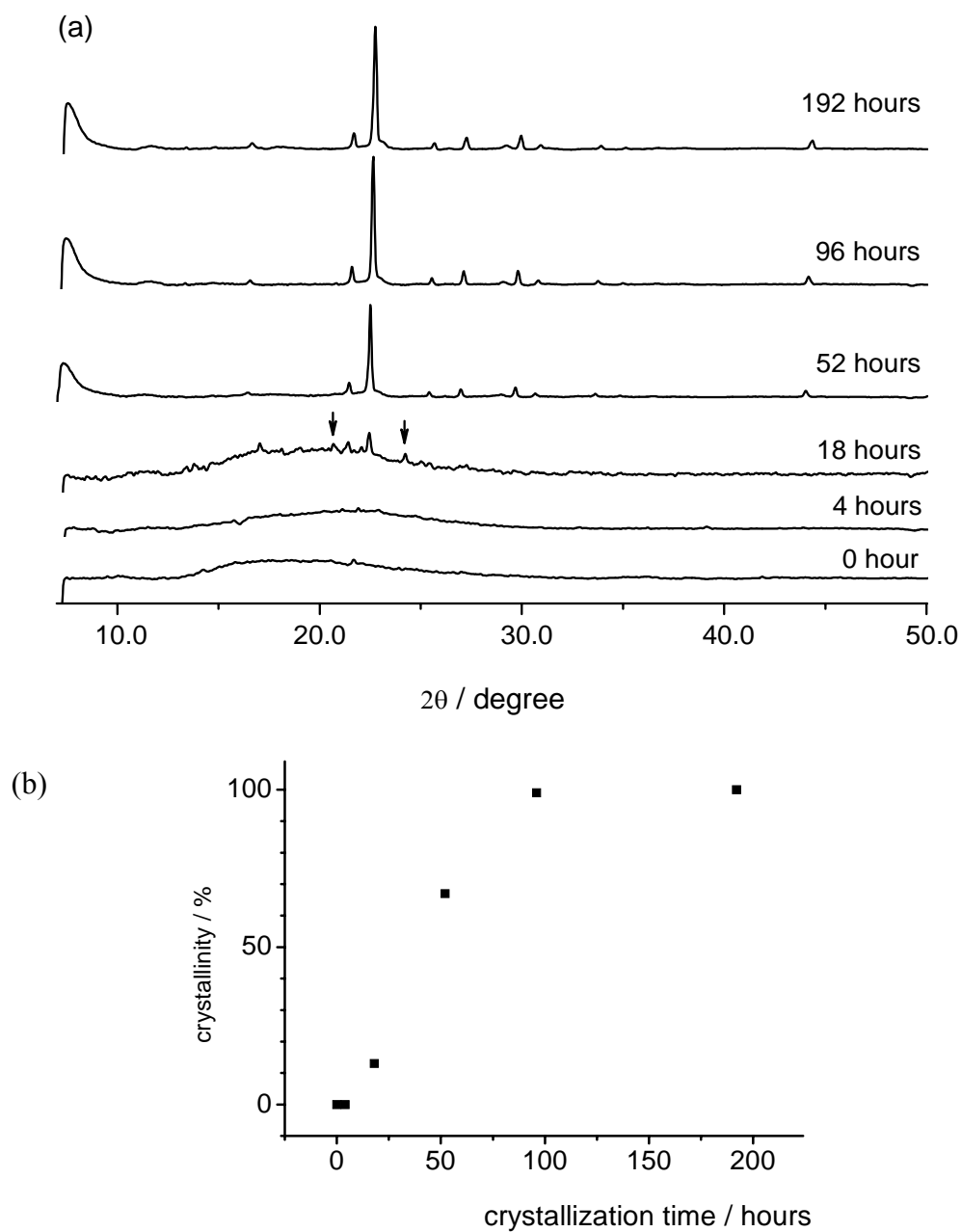


Figure 6.3: (a) XRD powder patterns of as-synthesized borosilicate materials in absence sodium obtained after different crystallization times of 0 hours (bottom) to 192 hours (top), (b) crystallinities

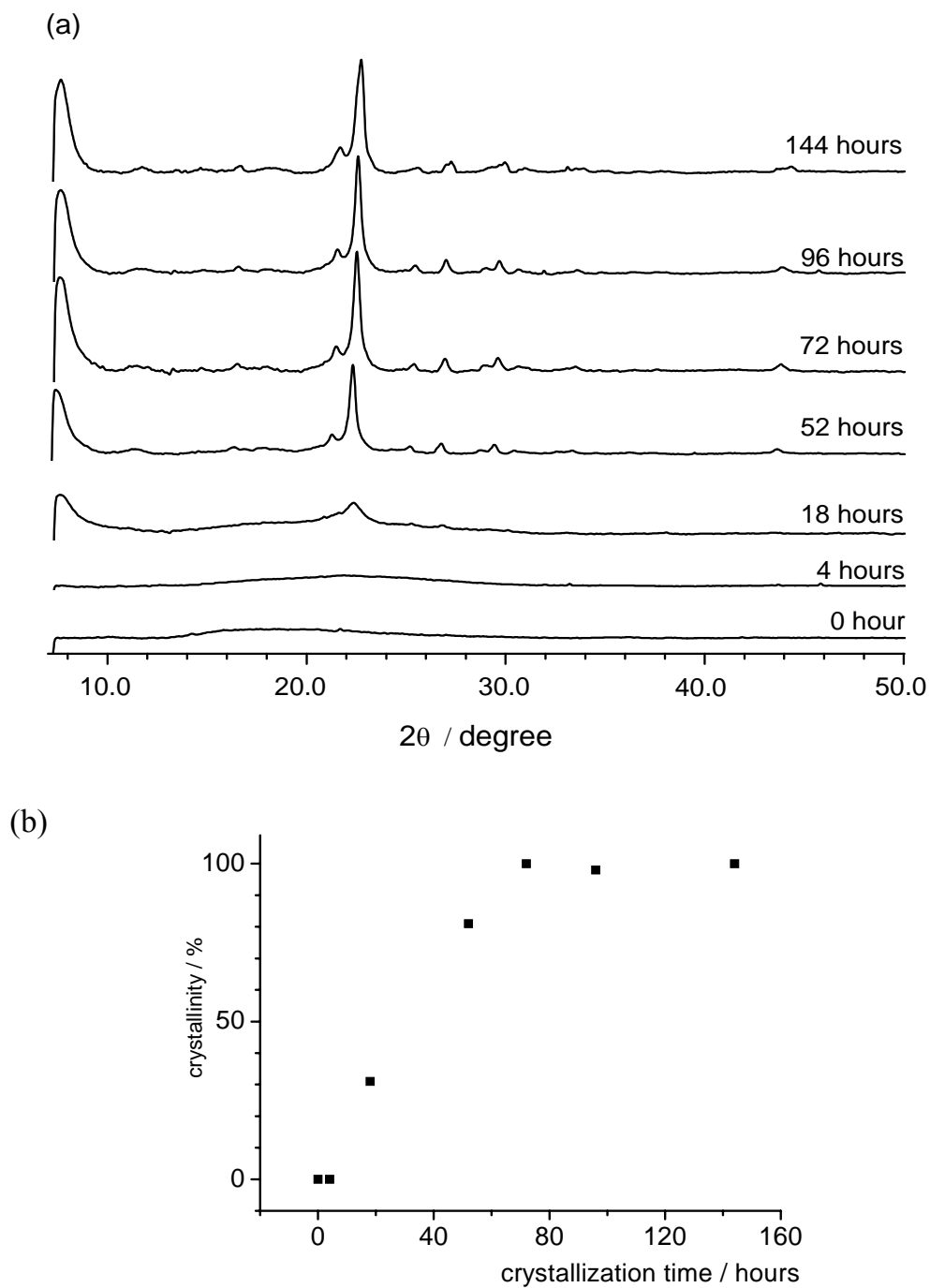


Figure 6.4: (a) XRD powder patterns of as-synthesized borosilicate materials in presence of sodium obtained after different crystallization times of 0 hours (bottom) to 144 hours (top), (b) crystallinities

6.2 Thermal Analysis

The TG and DTA curves of as-synthesized beta borosilicate from hydrothermal and dry-gel methods are illustrated in Figure 6.5.

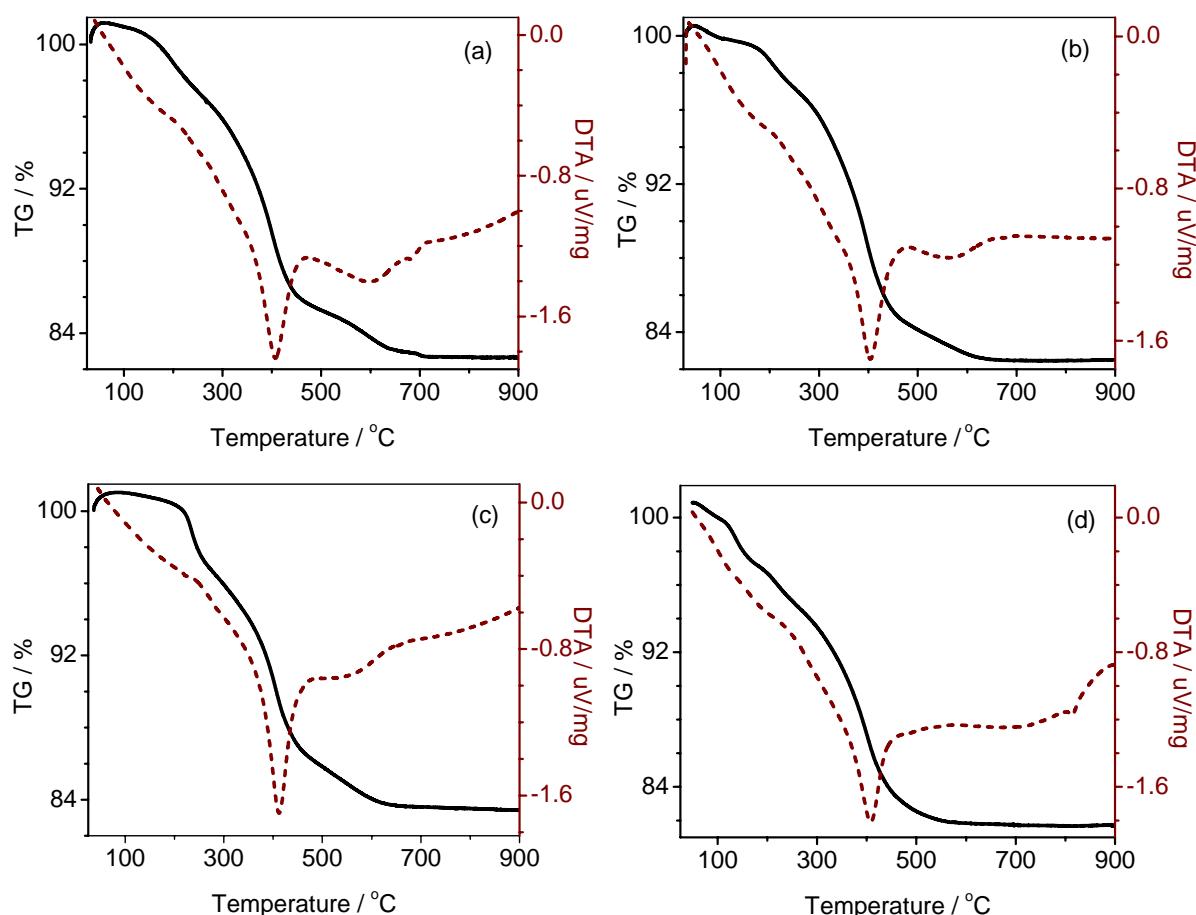


Figure 6.5: Thermogravimetric and differential thermal data of as-synthesized beta borosilicates (a) $|\text{TEA}^+|[\text{B}, \text{Si}-*\text{BEA}]_{\text{HYD}}$, (b) $|\text{TEA}^+, \text{Na}^+|[\text{B}, \text{Si}-*\text{BEA}]_{\text{HYD}}$, (c) $|\text{TEA}^+|[\text{B}, \text{Si}-*\text{BEA}]_{\text{DRY}}$, and (d) $|\text{TEA}^+, \text{Na}^+|[\text{B}, \text{Si}-*\text{BEA}]_{\text{DRY}}$

The calcination of beta borosilicate under flowing oxygen produces weight losses associated with four major temperature steps: (I) RT–150°C, (II) 150–320°C, (III) 320–470°C and (IV) 470–750°C (Figure 6.5).

In the step (I), there is an endothermic process assigned to desorption of occluded water.^{150, 151} The step II can be assigned to TEA^+ cations balancing the charge of Si—O—

groups in connectivity defects. In experiments with different Si/Al ratio beta zeolites, Cambor et al.¹⁵² proposed that this process is more intense the higher the Si/Al ratio. Indeed, as the Si/T (T is trivalent element such as Al, B, Ga etc.) increases, the number of Si—O—groups must increase to achieve full balance of the organic cations. On the contrary, for zeolites with much higher T content, TEA⁺ cations are mainly balanced by framework T and there is no need for framework defects and thus process II does not exist. This process could be primarily assigned to the degradation of TEA⁺ through a Hofmann elimination reaction:¹⁵³



The step (III) is characterized by an intense exothermic peak and a significant weight loss could be attributed to TEA⁺ cations balancing framework B(OSi)₄⁻ species. During the exothermic process (III), the combustion of TEA⁺ produces locally a large amount of heat and local oxygen depletion. The incomplete combustion and pyrolysis of a fraction of the TEA⁺ may yield species amenable to polymerization to form coke. This coke will be finally burned during the next process. In the final step (IV), the thermogravimetric display an exothermic peak, which is less intense (Figure 6.5c,d) but broader than the previous one. This corresponds to the complete oxidation of the residual organics.¹⁵⁴ The weight losses corresponding to four processes of hydrothermal and dry-gel method samples are presented in Table 6.2.

Table 6.2: *Thermal analysis of beta borosilicates under air atmosphere via hydrothermal and dry-gel synthesis*

Samples	Weight loss (%)			
	RT – 150°C	150 – 320°C	320 – 470°C	470 – 750°C
TEA ⁺ [B,Si-*BEA] _{HYD}	2	3.8	10	2.6
TEA ⁺ ,Na ⁺ [B,Si-*BEA] _{HYD}	1.1	3.9	11.2	1.8
TEA ⁺ [B,Si-*BEA] _{DRY}	1	4.2	9.6	2.8
TEA ⁺ ,Na ⁺ [B, Si-*BEA] _{DRY}	2.8	4.4	11.1	0.9

6.3 NMR Spectroscopy

Multinuclear NMR spectroscopy represents an important characterization tool to determine the number and nature of active sites in zeolites and molecular sieves. The generation of the borosilicate structure implies that boron atoms are inserted into the framework by formation of Si—O—B bridges. The environment of the T atoms in the various solids is studied by ^{29}Si and ^{11}B MAS NMR spectroscopy. In addition, some results concerning the characterization of Brønsted acid sites in zeolites are illustrated through ^1H MAS NMR spectra.

6.3.1 ^{29}Si MAS NMR Spectroscopy

The local structure of silicon atoms was studied by ^{29}Si MAS NMR spectroscopy. *BEA zeolite contains nine crystallographic non-equivalent T sites, therefore a rather complex ^{29}Si MAS NMR spectrum is expected. ^{29}Si MAS NMR spectra of as-synthesized and calcined beta borosilicates are presented in Figure 6.6 and Figure 6.7, respectively. Three main components at around -100 to -104 ppm (line II), -109 to -110 ppm (line III) and around -114 ppm (line IV) can be distinguished in ^{29}Si NMR spectra of as-synthesized of $[\text{TEA}^+][\text{B},\text{Si}-*\text{BEA}]_{\text{HYD}}$, $[\text{TEA}^+,\text{Na}^+][\text{B},\text{Si}-*\text{BEA}]_{\text{HYD}}$, $[\text{TEA}^+][\text{B},\text{Si}-*\text{BEA}]_{\text{DRY}}$, and $[\text{TEA}^+,\text{Na}^+][\text{B},\text{Si}-*\text{BEA}]_{\text{DRY}}$ samples (Figure 6.6). In addition, the signal that is centered at around -92 ppm (line I) is observed in ^{29}Si NMR spectra of $[\text{TEA}^+][\text{B},\text{Si}-*\text{BEA}]_{\text{HYD}}$ (Figure 6.6c).

Signals at -110 and -114 ppm can be attributed to silicon atoms, surrounded by four silicons (Q^4 group) in different crystallographic sites. The signal at -104 ppm could be assigned to Q^3 groups and the signal at -92 ppm to Q^2 groups.¹⁵⁵

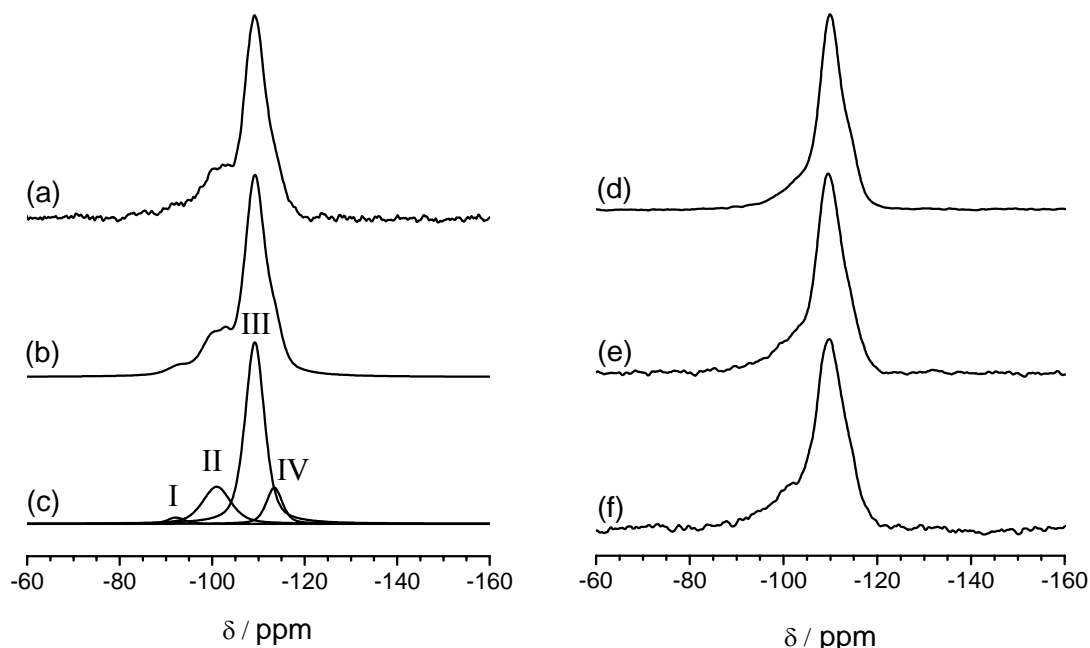


Figure 6.6: ^{29}Si MAS NMR spectra at $B_0 = 7.05\text{ T}$ of *BEA borosilicates as-synthesized (a) $|\text{TEA}^+|[\text{B,Si-*BEA}]_{\text{HYD}}$ experimental, (b) $|\text{TEA}^+|[\text{B,Si-*BEA}]_{\text{HYD}}$ as simulated, (c) $|\text{TEA}^+|[\text{B,Si-*BEA}]_{\text{HYD}}$ components (d) $|\text{TEA}^+,\text{Na}^+|[\text{B,Si-*BEA}]_{\text{HYD}}$, (e) $|\text{TEA}^+|[\text{B,Si-*BEA}]_{\text{DRY}}$, and (f) $|\text{TEA}^+,\text{Na}^+|[\text{B,Si-*BEA}]_{\text{DRY}}$

After calcination, the signals of components II, III and IV are detected (Figure 6.7), but several changes can be observed in ^{29}Si MAS NMR spectra. In comparison to the spectra of the as-synthesized samples, the line area of the broad signals at -100 to -104 ppm appears smaller in the corresponding spectra of the calcined *BEA borosilicate. These changes might be due to a decrease of the line area of the peak corresponding to $\text{Q}^3[1\text{B}]$ and $\text{Q}^3[1\text{OH}]$. The resonance at -92 ppm corresponding to Q^2 group (not only for $\text{Si}(2\text{Si}, 2\text{B})$ but also to $\text{Si}(2\text{Si}, 1\text{B}, 1\text{OH})$ and/or $\text{Si}(2\text{Si}, 2\text{OH})$) disappears in comparison with ^{29}Si MAS NMR spectrum of $|\text{TEA}^+|[\text{B,Si-*BEA}]_{\text{HYD}}$ sample.¹⁵⁶ On the other hand, the resolution of component at -114 ppm is improved, especially in the spectrum of $|\text{H}^+|[\text{B,Si-*BEA}]_{\text{DRY}}$ (Figure 6.7e). This signal and the signal at -110 ppm correspond to the Q^4 groups.¹⁵⁷

The changes of line area and resolution of components in comparison between as-made and calcined B-*BEA zeolites might be due to the removal of the template.¹⁵⁸ The assignment of components in the ^{29}Si MAS NMR spectra of $|\text{TEA}^+|[\text{B,Si-*BEA}]$ to specific

environment is difficult because of the interaction of organic molecules with tetrahedral network.¹⁵⁹

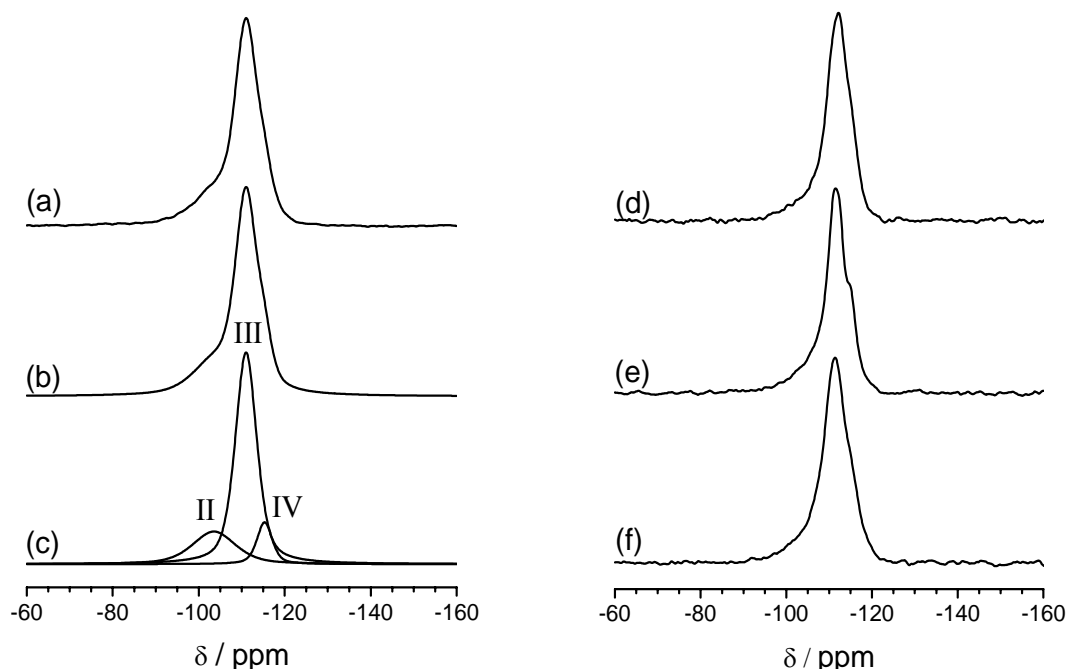


Figure 6.7: ^{29}Si MAS NMR spectra at $B_0 = 7.05$ T of *BEA borosilicates after calcinations (a) $|\text{H}^+|[\text{B,Si-*BEA}]_{\text{HYD}}$ experimental, (b) $|\text{H}^+|[\text{B,Si-*BEA}]_{\text{HYD}}$ as simulated, (c) $|\text{H}^+|[\text{B,Si-*BEA}]_{\text{HYD}}$ components (d) $|\text{Na}^+, \text{H}^+|[\text{B,Si-*BEA}]_{\text{HYD}}$, (e) $|\text{H}|[\text{B,Si-*BEA}]_{\text{DRY}}$, and (f) $|\text{Na}^+, \text{H}^+|[\text{B,Si-*BEA}]_{\text{DRY}}$

6.3.2 ^1H MAS NMR Spectroscopy

The characterization of hydroxyl groups in zeolites is important, because they may act as proton donor sites (Brønsted acid sites), which are responsible for the ability of zeolites to catalyze chemical reactions.¹⁶⁰ MAS NMR spectroscopy possesses the benefit of providing detailed information on Brønsted acid sites in zeolites and molecular sieves.¹⁶¹ ^1H MAS NMR spectra of as-synthesized and calcined beta borosilicates are performed in Figure 6.8 and 6.9, respectively.

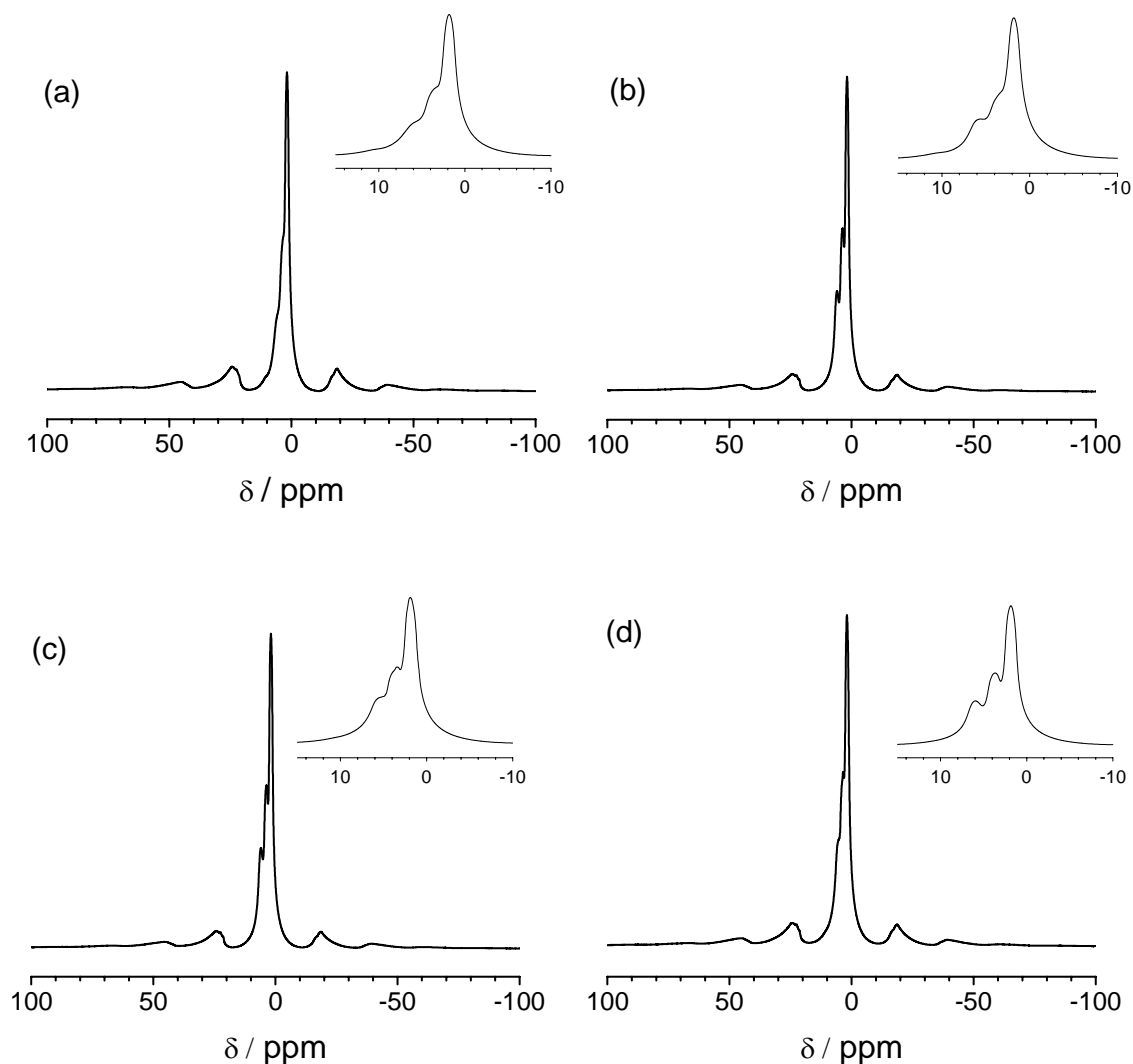


Figure 6.8: ^1H MAS NMR spectra at $B_0 = 11.7\text{ T}$ of $^*\text{BEA}$ borosilicates as-synthesized (a) $|\text{TEA}^+|[\text{B},\text{Si}-^*\text{BEA}]_{\text{HYD}}$, (b) $|\text{TEA}^+,\text{Na}^+|[\text{B},\text{Si}-^*\text{BEA}]_{\text{HYD}}$, (c) $|\text{TEA}^+|[\text{B},\text{Si}-^*\text{BEA}]_{\text{DRY}}$, and (e) $|\text{TEA}^+,\text{Na}^+|[\text{B},\text{Si}-^*\text{BEA}]_{\text{DRY}}$

The ^1H MAS NMR spectra of as-synthesized samples prepared via hydrothermal and dry-gel methods (Figure 6.8) show the main intensity that are centered at 1.8 ppm. The shoulder at about 3.6 ppm is observed in all spectra. These two lines are dominated by the resonance of organic quaternary ammonium cations.¹⁶² In addition, another line determined at 6.2 ppm can be assigned to silanol groups or H_2O forming weak hydrogen bonds.¹⁶³ Typically, the resonances from the SDA show strong spinning sidebands that are mainly due to the dipole interaction between protons. None of the as-made sample shows the signal at 10 ppm which was observed for connectivity defects in pure-silica zeolites.

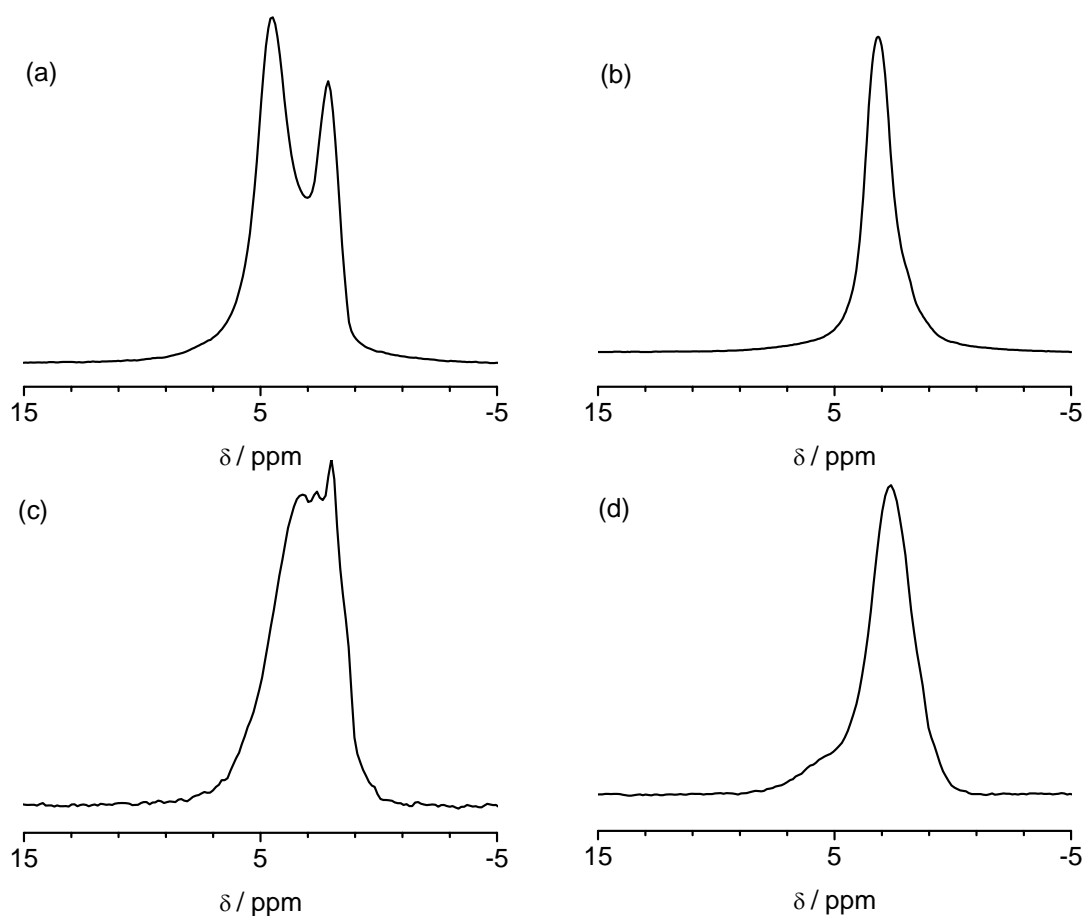


Figure 6.9: ^1H MAS NMR spectra at $B_0 = 11.7$ T of *BEA borosilicates after calcination (a) $|\text{H}^+|[\text{B},\text{Si}-*\text{BEA}]_{\text{HYD}}$ experimental, (b) $|\text{Na}^+, \text{H}^+|[\text{B},\text{Si}-*\text{BEA}]_{\text{HYD}}$, (c) $|\text{H}^+|[\text{B},\text{Si}-*\text{BEA}]_{\text{DRY}}$, and (d) $|\text{Na}^+, \text{H}^+|[\text{B},\text{Si}-*\text{BEA}]_{\text{DRY}}$

After removal of the organic compound, the ^1H MAS NMR spectra (Figure 6.8) show the presence of mainly two classes of hydroxyl groups: bridging hydroxyls that are responsible for the Brønsted acid sites and isolated silanol groups. Koller et al. suggested that at least five components can be simulated in ^1H MAS NMR spectra of borosilicates.¹⁶⁴ The line at -1.7 ppm could be assigned to the isolated SiOH groups. Three lines centered in the range 2 to 3 ppm might be referred to different types of hydroxyl groups located around the trigonal boron sites (i.e. $\text{B}[3]\cdots\text{O}(\text{H})\text{Si}$ groups). The line at around 5 ppm is characterized by strongly adsorbed surface water. More details of these lines in ^1H MAS NMR spectra of *BEA borosilicates will be discussed in Chapter 7.

6.3.3 ^{11}B MAS NMR Spectroscopy

The coordination of boron atoms in *BEA borosilicate were investigated by solid state NMR. ^{11}B MAS NMR spectra of as-synthesized and calcined samples prepared via hydrothermal and dry-gel methods are depicted in Figure 6.10 and 6.11, respectively.

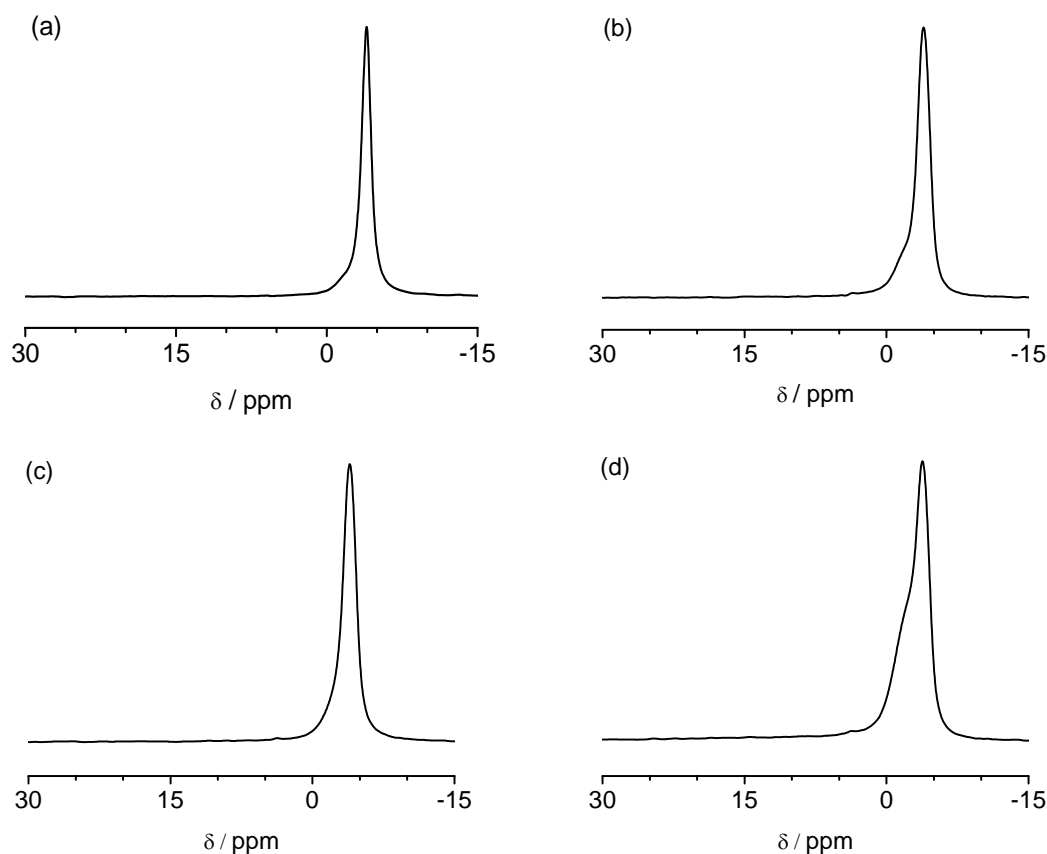


Figure 6.10: ^{11}B MAS NMR spectra at $B_0 = 11.7\text{ T}$ of as-made *BEA borosilicates (a) $|\text{TEA}^+|[\text{B},\text{Si}-*\text{BEA}]_{\text{HYD}}$, (b) $|\text{TEA}^+, \text{Na}^+|[\text{B},\text{Si}-*\text{BEA}]_{\text{HYD}}$, (c) $|\text{TEA}^+|[\text{B},\text{Si}-*\text{BEA}]_{\text{DRY}}$, and (d) $|\text{TEA}^+, \text{Na}^+|[\text{B},\text{Si}-*\text{BEA}]_{\text{DRY}}$

In both of hydrothermal and dry-gel as-synthesized samples, the spectra of samples in the absence of sodium show a signal at around -4 ppm (Figure 6.10a and 6.10c), whereas the sodium as-made samples in hydrothermal and dry-gel samples show an extra signal at -2.5 ppm (Figure 6.10b and 6.10c). The line at around -4 ppm is assigned to boron in tetrahedral framework position $[\text{B}(\text{OSi})_4]$,^{165, 166} whereas the shoulder at -2.5 ppm can be described to tetrahedral non-framework boron. Gabelica et al. observed a ^{11}B MAS NMR line at -0.5 ppm that was attributed to an amorphous borosilicate material.¹⁶⁷ To explain the position of

different lines in ^{11}B MAS NMR spectra, Ruite et al. suggest that the incorporation behavior of boron in silicate frameworks depends on the specific synthesis conditions.

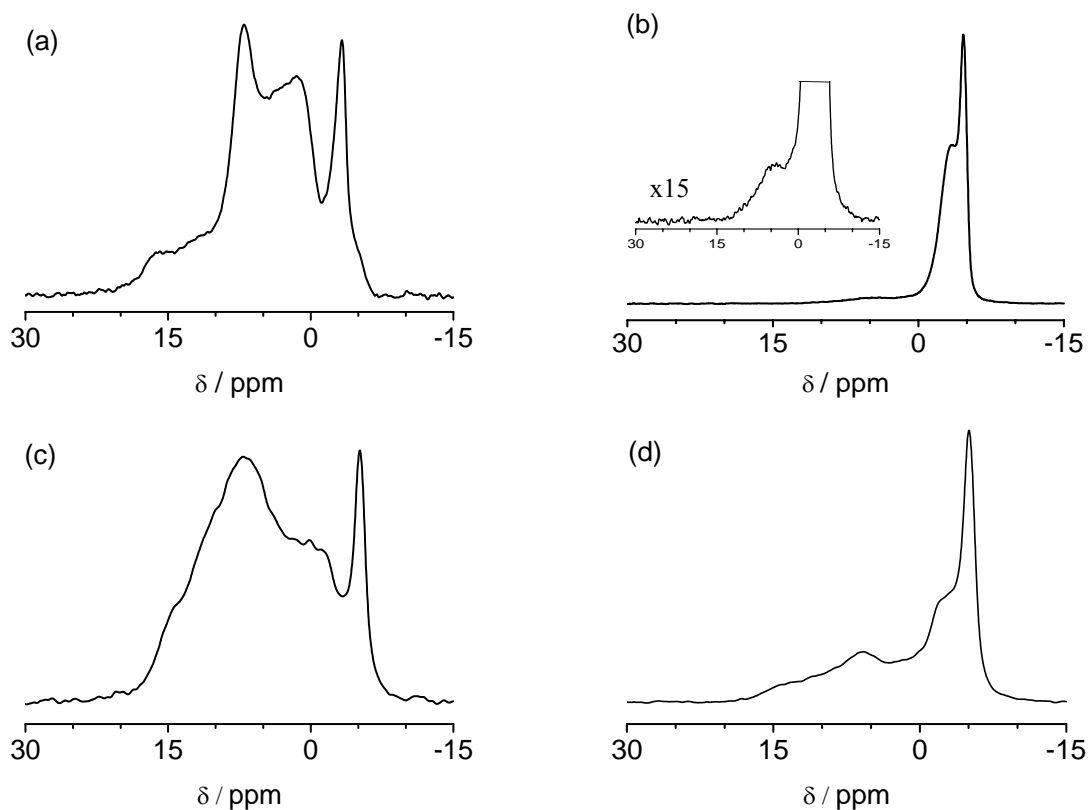


Figure 6.11: ^{11}B MAS NMR at $B_0 = 11.7\text{ T}$ of calcined *BEA borosilicate synthesized by hydrothermal method (a) $|\text{H}^+|[\text{B},\text{Si}-*\text{BEA}]_{\text{HYD}}$, (b) $|\text{Na}^+,\text{H}^+|[\text{B},\text{Si}-*\text{BEA}]_{\text{HYD}}$, (c) $|\text{H}^+|[\text{B},\text{Si}-*\text{BEA}]_{\text{DRY}}$, and (d) $|\text{Na}^+,\text{H}^+|[\text{B},\text{Si}-*\text{BEA}]_{\text{DRY}}$

After calcination at 923 K, some new lines appear in ^{11}B MAS NMR spectra. In $|\text{H}^+|[\text{B},\text{Si}-*\text{BEA}]_{\text{HYD}}$ and $|\text{H}^+|[\text{B},\text{Si}-*\text{BEA}]_{\text{DRY}}$ borosilicates (Figure 6.11a and 6.11c), new broad lines centered at around 10.5, 15.5 and 18.5 ppm are visible. These signals are broadened by second order quadrupole interactions. ^{11}B MAS NMR spectra of $|\text{Na}^+,\text{H}^+|[\text{B},\text{Si}-*\text{BEA}]_{\text{HYD}}$ and $|\text{Na}^+,\text{H}^+|[\text{B},\text{Si}-*\text{BEA}]_{\text{DRY}}$ (Figure 6.11b and 6.11d) also show a small broad signals in the range 5 to 18 ppm. These new lines could be ascribed to trigonal boron in framework or non-framework positions.^{166, 167} The trigonal boron can be interpreted by the interaction between proton and borosilicate framework.¹⁶⁸ They also found that upon dehydration of $|\text{H}^+|[\text{B}-*\text{BEA}]$, the line at around -3.5 ppm disappears and simultaneously two components with quadrupolar lineshape and isotropic chemical shifts of 10.5 and 15.4

ppm appear. These lines can be attributed to $\text{SiOH}\cdots\text{B}(\text{OSi})_3$ and $\text{Si}(\text{OH})\cdots\text{B}(\text{OSi})(\text{OH})_2$ respectively.

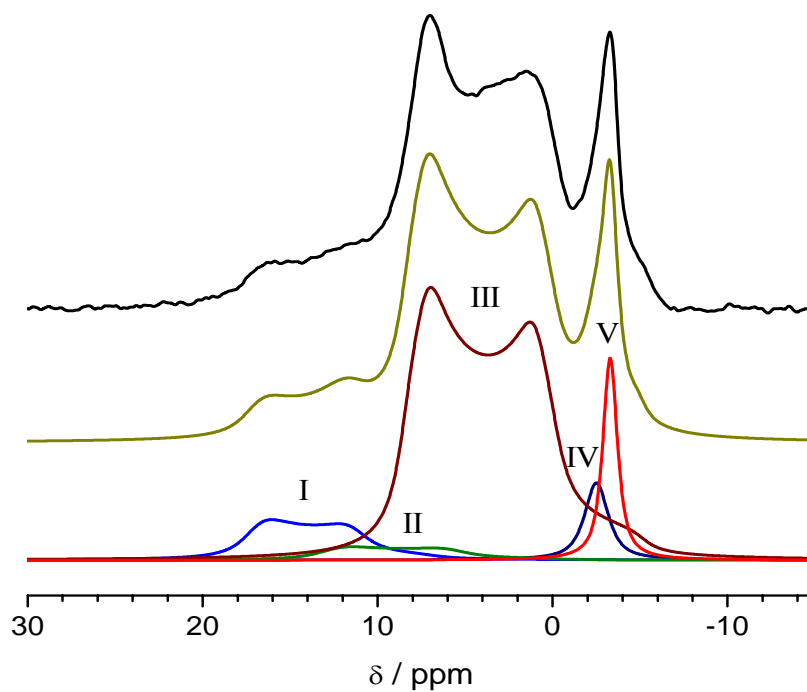


Figure 6.12: ^{11}B MAS NMR at $B_0 = 11.7$ T of calcined *BEA borosilicate synthesized by hydrothermal method, (a) experimental spectrum, (b) simulated spectrum, (c) components

Figure 6.12 shows the components of the $|\text{H}^+|[\text{B},\text{Si}-*\text{BEA}]_{\text{HYD}}$ spectrum. Besides the sharp line at around -3 ppm and -3.5 ppm (component IV and V) assigned to tetrahedral boron, the components affected by second-order quadrupole interaction are distinguished: component III: $C_q = 2.5$ MHz, $\eta = 0.15$, $\delta_{\text{cs}} = 10.1$ ppm; component II: $C_q = 2.3$ MHz, $\eta = 0.16$, $\delta_{\text{cs}} = 14.8$ ppm and component I: $C_q = 2.2$ MHz, $\eta = 0.15$, $\delta_{\text{cs}} = 18.0$ ppm. Components II and III are assigned to trigonal boron in the framework, whereas component I is appointed to trigonal boron in non-framework positions. Scholle et al. reported that the tetrahedral boron can be transformed to trigonal boron coordination upon calcination as evidenced by i) the appearance of a component whose lineshape is dominated by second-order quadrupole interaction and ii) the concomitant disappearance of the line typical for $\text{B}(\text{OSi})_4$ units at around -3.5 ppm.¹⁶⁹

On the other hand, the relative line area of trigonal boron in sodium calcined B-*BEA (Figure. 6.11b and 6.11d) is much smaller than without sodium calcined samples (Figure 6.11a and 6.11c). During template removal at high temperature, the boron coordination can be converted from tetrahedral to trigonal. In the sodium samples, Na^+ stabilizes boron in tetrahedral coordination. As H^+ binds strongly to a framework oxygen atom, this leads to the cleavage of the bond between boron and the protonated oxygen, thus creating trigonal boron.

Chapter

7

Boron Coordination of *BEA-Borosilicate

In recent years, borosilicates have attracted much attention due to their weak acidity that is suitable for certain catalytic reactions.¹⁷⁰ The incorporation of boron inside the zeolite framework has always been a curious question. The transformation of boron coordination and subsequent variation of local geometry are important points that characterize borosilicates.

In this chapter, the change of coordination geometry at boron centers upon hydration and dehydration treatments of borosilicates will be elaborated in more detail with the beta borosilicates synthesized under hydrothermal conditions in the presence of sodium or without sodium.

7.1 Dehydration of *BEA-Borosilicate

7.1.1 ^{11}B NMR Spectroscopy

The influence of dehydration conditions to the boron coordination was investigated. The spectra in Figure 7.1 present the local structure of boron atoms in dehydrated beta borosilicates in the presence of sodium (right) and without sodium (left). As can be seen in the Figure 7.1a and 7.1e, the as-made beta borosilicate spectra merely show sharp resonance lines at about -3.7 ppm or -4.2 ppm in presence of sodium and without sodium borosilicates, respectively. In addition, the shoulder at -2.5 ppm is clearly observed for the sodium borosilicate. These resonances could be assigned to the tetrahedral boron in *BEA-borosilicates. The resonances in the range of -3.7 to -4.2 ppm are assigned to tetrahedral $\text{BO}_{4/2}^-$ groups. In as-synthesized samples, the negative charge of these groups is balanced by structure directing agent cations or sodium cations in case of sodium samples.

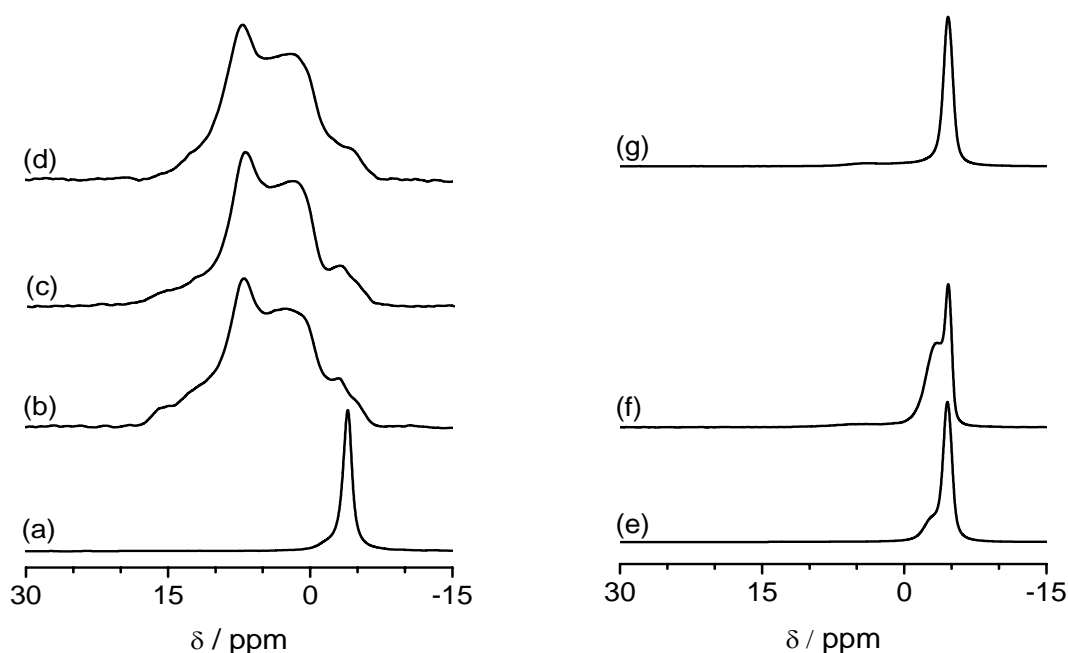


Figure 7.1: ^{11}B MAS spin echo NMR spectra at $B_0 = 11.7\text{ T}$ of (a) $[\text{TPA}^+][\text{B},\text{Si}-*\text{BEA}]$ as-synthesized, (b) $[\text{H}^+][\text{B},\text{Si}-*\text{BEA}]$ freshly calcined at 923 K, (c) $[\text{H}^+][\text{B},\text{Si}-*\text{BEA}]$ dehydrated in vacuum at room temperature, (d) $[\text{H}^+][\text{B},\text{Si}-*\text{BEA}]$ dehydrated in vacuum at 673 K; (e) $[\text{TPA}^+,\text{Na}^+][\text{B},\text{Si}-*\text{BEA}]$ as-synthesized, (f) $[\text{Na}^+,\text{H}^+][\text{B},\text{Si}-*\text{BEA}]$ freshly calcined at 923 K, (g): $[\text{Na}^+,\text{H}^+][\text{B},\text{Si}-*\text{BEA}]$ dehydrated in vacuum at 673 K.

After calcination, the *BEA-borosilicate containing sodium still presents the sharp line corresponding to tetrahedral boron (Figure 7.1f). On the contrary, in the borosilicate proton form, the sharp line at -3.7 ppm almost disappears and a new resonance dominates with second-order quadrupole interaction (Figure 7.1b).

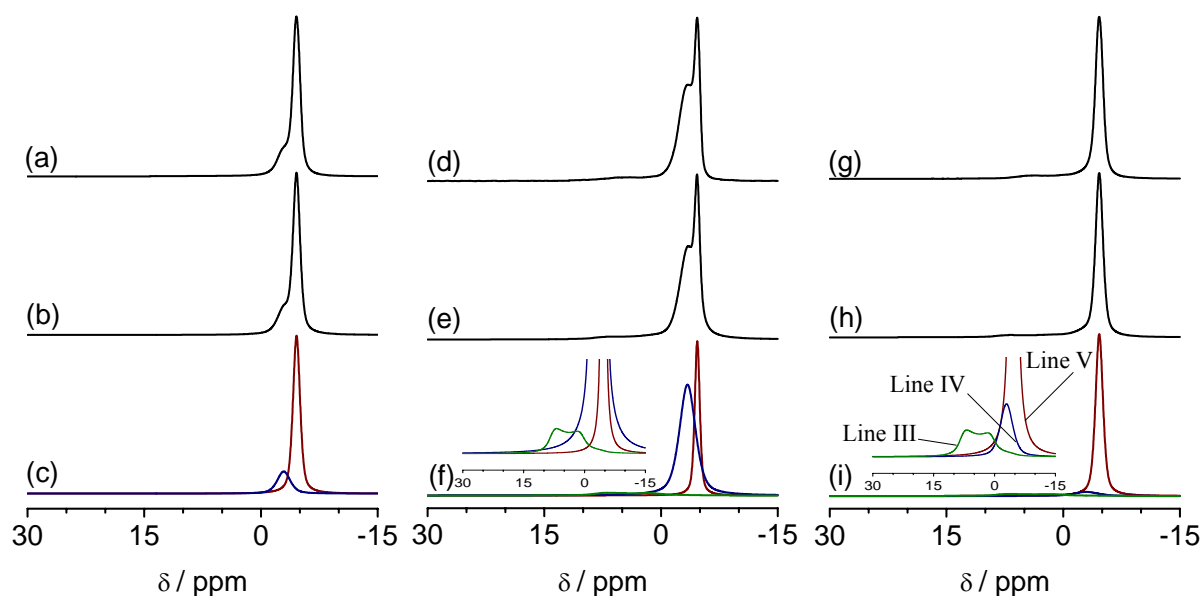


Figure 7.2: ^{11}B MAS spin echo NMR spectra at $B_0 = 11.7\text{ T}$ of *BEA-borosilicate containing sodium (a) as-synthesized spectrum, (b) simulation, (c) components (d) freshly calcined at 923 K spectrum, (e) simulation, (f) components (g) dehydrated at 623 K spectrum, (h) simulation (i) components.

When the samples are dehydrated in vacuum at room temperature or 637 K, the distinct resonance at about -4.6 ppm (component V) and -2.9 to -3.4 ppm (component IV) for tetrahedral boron always is obtained in B-*BEA zeolite containing sodium (Figure 7.1g), but this peak remains small in the proton form. In Table 7.1, the total relative line area of components IV and V is 100 % for as-made *BEA-borosilicate containing sodium. This value is 95 % for freshly calcined sample and 92 % for *BEA-borosilicate dehydrated at 673 K in vacuum (Table 7.1). Interestingly, component IV at -2.9 ppm considerably decreases upon dehydration and almost disappears at dehydration temperatures of 673 K. On the other hand, the tiny resonance (component III) with $C_q = 2.5\text{ MHz}$, $\eta = 0.15$ and $\delta_{cs} = 10.1\text{ ppm}$ is also observed in borosilicates after heating treatment (Figure 7.2d-f and

7.2g-i). This component has 5 % and 8 % of relative area for borosilicates freshly calcined and dehydrated at 673 K, respectively.

Table 7.1: ^{11}B MAS spin echo NMR line assignment of *BEA-borosilicates in the presence of sodium as-synthesized, freshly calcined and dehydrated in vacuum at high temperature

	NMR line for B[3]			NMR line for B[4]	
	Line I	Line II	Line III	Line IV	LineV
[TEA⁺,Na⁺][B,Si-*BEA]					
δ_{cs} / ppm				-2.9	-4.5
relative line area / %				20	80
[Na⁺,H⁺][B,Si-*BEA] freshly calcined in air at 923 K					
δ_{cs} / ppm			10.1	-3.4	-4.6
C_{q} / MHz			2.5	-	-
relative line area / %			5	66	29
[Na⁺,H⁺][B,Si-*BEA] dehydrated in vacuum at 673 K					
δ_{cs} / ppm			10.1	-2.9	-4.6
C_{q} / MHz			2.5	-	-
relative line area / %			8	7	85

In the proton form, in analogy to the freshly calcinated borosilicate, the broad line indicating trigonal boron is always dominant upon dehydration (Figure 7.1c and 7.1d). These lineshapes are comprised of three single resonances (Figure 7.3d-f, 7.3g-i and 7.3j-l). The main resonances (component III) with quadrupole coupling $C_{\text{q}} = 2.5\text{-}2.6$ MHz, $\eta = 0.1\text{-}0.15$ and $\delta_{\text{cs}} = 10.1\text{-}10.5$ ppm are always observed in the dehydrated proton form. Another resonance (component II) with the $C_{\text{q}} = 2.4$ MHz, $\eta = 0.15$ and $\delta_{\text{cs}} = 14.6\text{-}14.9$ ppm is also presents in all dehydrated and freshly calcined borosilicates without sodium. The relative area of these components slightly increases when dehydration conditions are stronger. In Table 7.2, the total relative areas of components II and III are 92 % for the freshly calcined *BEA-borosilicate, 93 % for dehydration in vacuum at room temperature and 97 % in case of further dehydration at 673 K. Besides the components II and III, another resonance (component I) with $C_{\text{q}} = 2.2\text{-}2.3$ MHz, $\eta = 0.15$ and $\delta_{\text{cs}} = 18.0\text{-}18.1$ ppm is also observed.

This component has chemical shift very close to the B(OH)_3 isotropic chemical shift in the solution, therefore it has been assigned to B(OH)_3 .¹⁷¹ In contrast to components II and III, the relative area of component I decreases with increase of dehydration conditions. As shown in Table 7.2, this relative area is 5 % in freshly calcined sample and dehydrated material at room temperature of the proton form.

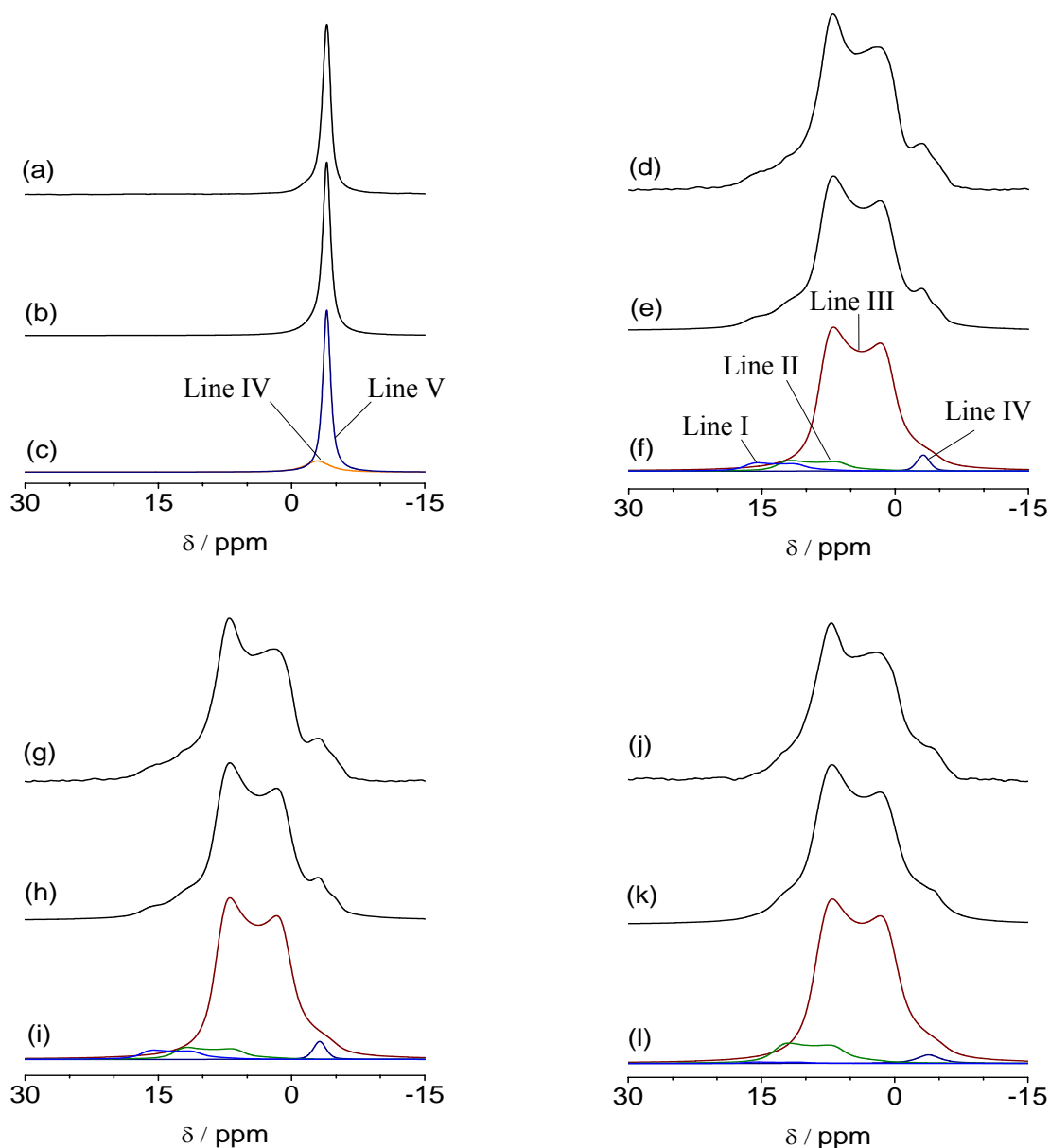


Figure 7.3: ^{11}B MAS spin echo NMR spectra at $B_0 = 11.7\text{ T}$ of *BEA-borosilicate without sodium (a) as-synthesized spectrum, (b) simulation, (c) components (d) freshly calcined at 923 K spectrum, (e) simulation, (f) components (g) dehydrated at room temperature spectrum, (h) simulation (i) components, (j) dehydrated at 673 K spectrum, (k) simulation, (l) components.

As shown above, the relative area of components IV and V assigned to tetrahedral boron significantly decreases when the borosilicate without sodium was dehydrated. In Table 7.2, the total relative areas of these components is 100 % for as-synthesized borosilicate, but almost disappears in case of calcined and dehydrated *BEA-borosilicates. The resonance was observed in the range of -3.2 to -3.5 ppm with low relative area at about 3 % or 2 % in B-*BEA freshly calcined and dehydrated at room temperature and 673 K.

Table 7.2: ^{11}B MAS spin echo NMR line assignment of *BEA-borosilicates without sodium as-synthesized, freshly calcined and dehydrated in vacuum at different temperatures.

	NMR line for B[3]			NMR line for B[4]	
	Line I	Line II	Line III	Line IV	Line V
 TEA⁺ [B,Si-*BEA]					
δ_{cs} / ppm				-2.8	-3.8
relative line area / %				18	82
 H⁺ [B,Si-*BEA] freshly calcined in air at 923 K					
δ_{cs} / ppm	18	14.8	10.1		-3.2
C_{q} / MHz	2.2	2.4	2.6		-
relative line area / %	5	11	81		3
absolute line area / a.u.	4.8	10.7	77		3
 H⁺ [B,Si-*BEA] dehydrated in vacuum at 298 K					
δ_{cs} / ppm	18.1	14.6	10.1		-3.2
C_{q} / MHz	2.2	2.4	2.5		-
relative line area / %	5	6	87		2
absolute line area / a.u.	4.8	5.7	83		2
 H⁺ [B,Si-*BEA] dehydrated in vacuum at 673 K					
δ_{cs} / ppm	18.1	14.9	10.5		-3.5
C_{q} / MHz	2.3	2.4	2.6		-
relative line area / %	1	9	88		2
absolute line area / a.u.	1	8.7	83		2

Figure 7.4 shows the ^{11}B 2D MQMAS spectrum of the proton form after dehydration at 673 K. In this spectrum, $\text{B}^{[4]}$ and non-framework $\text{B}^{[3]}$ appear with small signals.

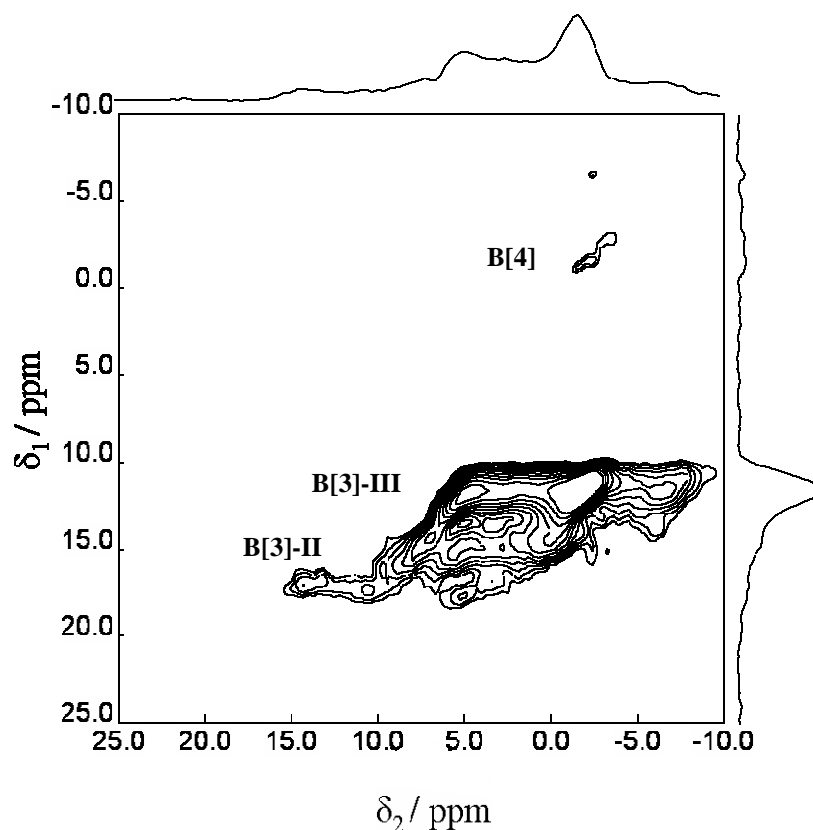


Figure 7.4: ^{11}B 2D MQMAS spectrum at $B_0 = 11.7 \text{ T}$ of $|\text{H}^+|[\text{B},\text{Si}-*\text{BEA}]$ dehydrated in vacuum at 673 K.

7.1.2 ^1H MAS NMR Spectroscopy

Figure 7.5 shows the ^1H MAS NMR spectra of *BEA-borosilicates in presence of sodium (right) and without sodium (left) after calcination and dehydration at different temperatures. In this figure, most of spectra show the lineshape with chemical shift in the range of 1.7 to 5.5 ppm.

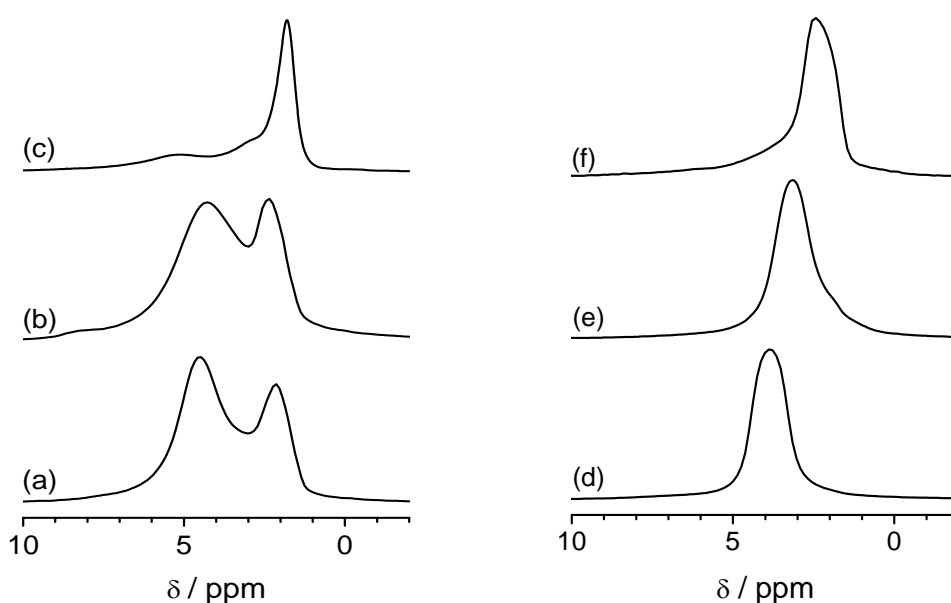


Figure 7.5: ^1H MAS NMR spectra at $B_0 = 11.7$ T of (a) $|\text{H}^+|[\text{B},\text{Si}-*\text{BEA}]$ freshly calcined at 923 K, (b) $|\text{H}^+|[\text{B},\text{Si}-*\text{BEA}]$ dehydrated in vacuum at room temperature, (c) $|\text{H}^+|[\text{B},\text{Si}-*\text{BEA}]$ dehydrated in vacuum at 673 K; (d) $|\text{Na}^+, \text{H}^+|[\text{B},\text{Si}-*\text{BEA}]$ freshly calcined at 923 K, (e) $|\text{Na}^+, \text{H}^+|[\text{B},\text{Si}-*\text{BEA}]$ dehydrated in vacuum at room temperature, (f): $|\text{Na}^+, \text{H}^+|[\text{B},\text{Si}-*\text{BEA}]$ dehydrated in vacuum at 673 K.

As shown in Chapter 6, these ^1H MAS NMR spectra could be composed of at least 5 components. The simulation of these spectra with 5 components is illustrated in Figure 7.6. The line centered at 1.7-1.8 ppm (component V) is assigned to the isolated SiOH groups. The other lines at 2.3-2.4 ppm and 2 ppm (component III, IV) could be referred to the weak hydrogen bonds of different types of hydroxyl groups located around the trigonal boron. The final lines at 2.9-3.0 ppm and 4.3-4.6 ppm (component II and I) are assigned to strongly hydrogen bonds, especially the line I could be assigned to strong dipole interaction of the extra-framework boron.¹⁶⁴

As illustrated in Figure 7.5, both of sodium and without sodium beta borosilicates show the reduction of surface adsorbed water while the dehydration conditions increase. Besides the alteration of this line during dehydration, the spectra also show the various changes of surface hydroxyl groups. The relative areas of simulated components corresponding to the surface adsorbed water and the other hydroxyl groups in dehydrated series are collected in Table 7.3.

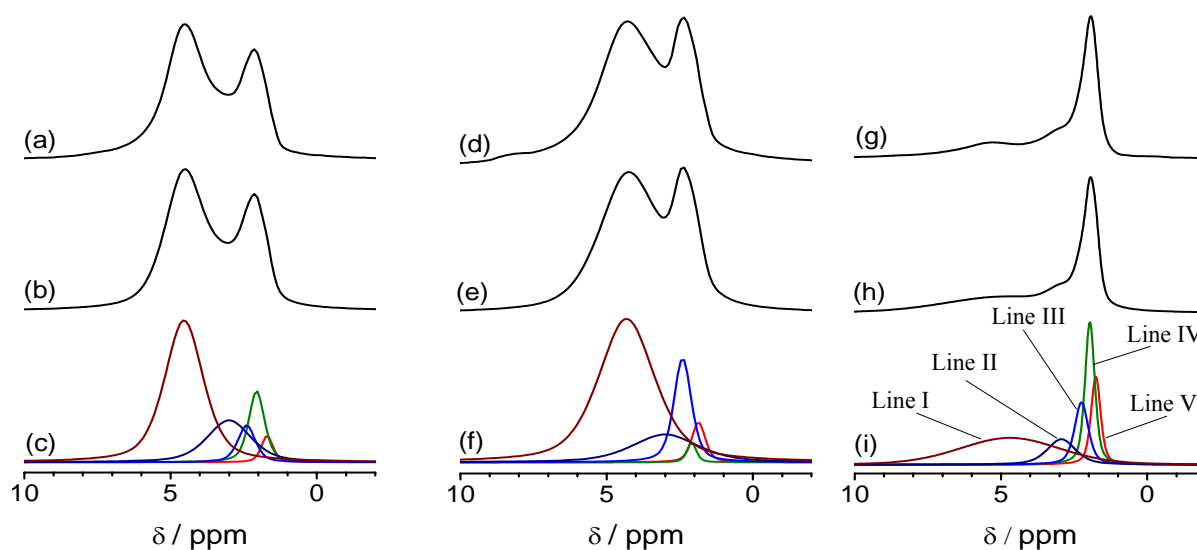


Figure 7.6: ^1H MAS NMR spectra at $B_0 = 11.7$ T of $[\text{H}^+][\text{B,Si-}^*\text{BEA}]$ (a) freshly calcined at 923 K spectrum, (b) simulation, (c) components (d) dehydrated at room temperature spectrum, (e) simulation, (f) components, (g) dehydrated at 673K spectrum, (h) simulation, (i) components.

Table 7.3: ^1H MAS NMR line assignment of *BEA-borosilicate proton forms freshly calcined and dehydrated in vacuum at different temperatures.

$[\text{H}^+][\text{B,Si-}^*\text{BEA}]$	Line I	Line II	Line III	Line IV	Line V
calcined at 923K					
$\delta_{\text{cs}} / \text{ppm}$	4.5	3.0	2.4	2.0	1.7
relative line area / %	58	20	7	12	3
dehydrated in vacuum at 298 K					
$\delta_{\text{cs}} / \text{ppm}$	4.3	3.0	2.4	2.1	1.8
relative line area / %	64	15	15	2	4
dehydrated in vacuum at 673 K					
$\delta_{\text{cs}} / \text{ppm}$	4.6	2.9	2.3	2.0	1.8
relative line area / %	47	10	12	19	12

When dehydration temperature increases from 298 K to 673 K, the relative areas of components I and II reduce mainly from 64 % to 47 % and 15 % to 10 %, respectively. The relative area of component V increases at higher dehydration temperature, this area is 3 % after calcinations, 4 % after dehydration at room temperature and rises to 12 % after

dehydration at 673 K. On the other hand, the areas of components III and IV increase at higher dehydration temperature (Table 7.3). In particular, the relative area of component IV significantly increases from 2 % to 19 % in the temperature variation from 298 K to 673 K. This striking observation could be due to the framework disruption by the interaction with water at high temperature.¹⁶⁴

7.2 Hydration of *BEA-Borosilicate

7.2.1 ¹¹B NMR Spectroscopy

To further investigate the boron coordinations in beta borosilicates, the MAS NMR technique has also been applied to characterize the *BEA-borosilicates at different hydration levels. Figure 7.7 illustrates the ¹¹B NMR spectra of hydration series for beta borosilicates in presence of sodium (right) and without sodium (left).

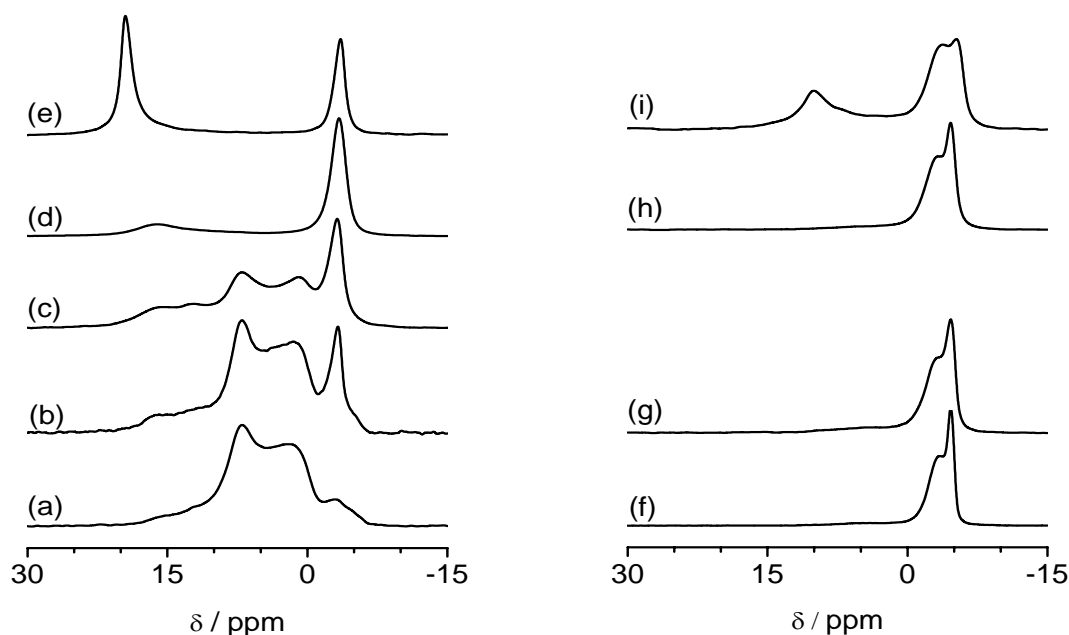


Figure 7.7: ¹¹B MAS spin echo NMR spectra at $B_0 = 11.7$ T of (a) $|H^+|[B,Si-*BEA]$ freshly calcined at 923 K, (b) $|H^+|[B,Si-*BEA]$ stored for 1 month in closed vial, (c) $|H^+|[B,Si-*BEA]$ stored for 1 year in closed vial but not absolutely tight (d) $|H^+|[B,Si-*BEA]$ exposed in air overnight, (e) $|H^+|[B,Si-*BEA]$ further hydrated by soaking water; (f) $|Na^+,H^+|[B,Si-*BEA]$ freshly calcined at 923 K, (g) $|Na^+,H^+|[B,Si-*BEA]$ stored for 1 month in closed vial, (h) $|Na^+,H^+|[B,Si-*BEA]$ exposed in air overnight, (i) $|Na^+,H^+|[B,Si-*BEA]$ further hydrated by soaking in water.

All ^{11}B NMR spectra show the resonance assigned to tetrahedral boron at around -3.2 ppm for the proton forms and around -4.6 ppm for the samples in presence of sodium. During the hydration process, this resonance obviously increases, when more water is adsorbed in the powder samples. On the other hand, the broad line which was clearly obtained after calcination of proton form is almost disappeared when the sample is further hydrated (Figure 7.7d). In particular, the new lines that resonance centered at 18 ppm and 21 ppm are obviously observed (Figure 7.7d,e). These phenomena are also achieved with the sodium *BEA-borosilicates. The broad line almost disappears, and new line at 14 ppm is evidently observed (Figure 7.7h,i respectively).

More details on the components simulated in ^{11}B NMR spectra of the sodium and proton forms are illustrated in Figure 7.8 and 7.10, respectively. The assignments of these components are collected in Table 7.4 for samples in the presence of sodium and Table 7.5 for the proton form.

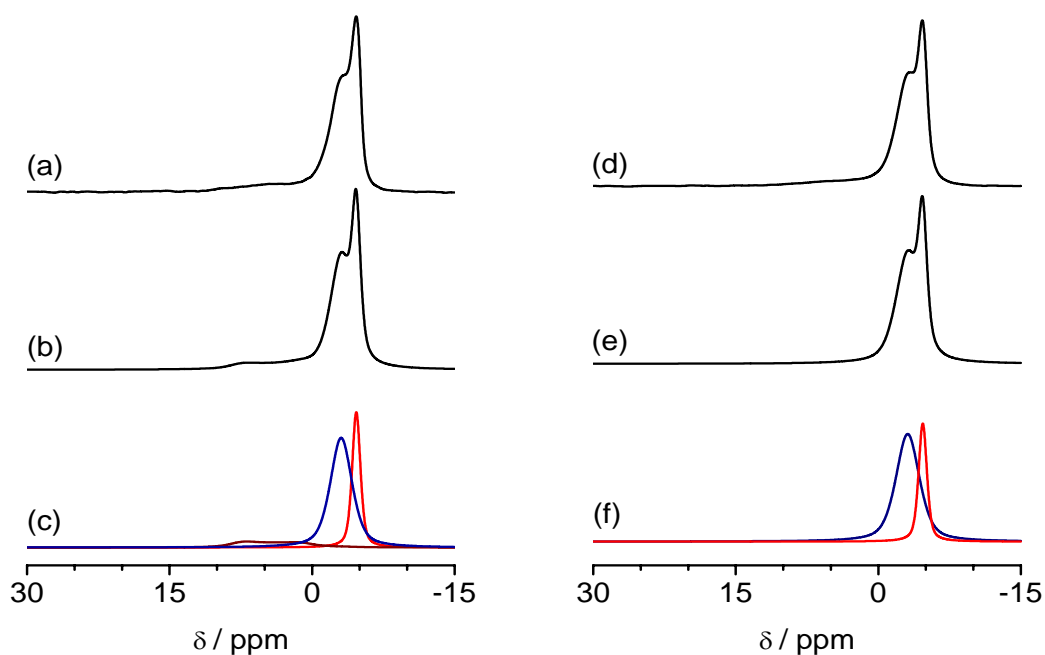


Figure 7.8: ^{11}B MAS spin echo NMR spectra at $B_0 = 11.7\text{ T}$ of $[\text{Na}^+, \text{H}^+][\text{B}, \text{Si}-*\text{BEA}]$ after calcination then (a) stored in closed vial for 1 month, (b) simulation, (c) components (d) exposed in air overnight, (e) simulation, (f) components

In Figure 7.8, the sharp line assigned to tetrahedral boron is always observed in all ^{11}B NMR spectra of the hydration series. This line probably includes at least two components:

component IV at about -3.4 ppm and component V at about -4.6 ppm. However, the relative areas of these components are not the same in all spectra. When the level of hydration increases, the relative area of components IV slightly grows. This value is 64 % for the freshly calcined sample, 66 % after 1 month in a closed vial and 72 % upon further hydration by exposing in air overnight (Table 7.4).

Table 7.4: ^{11}B MAS spin echo NMR line assignment of *BEA-borosilicates in presence of sodium at various hydration levels.

[Na ⁺ ,H ⁺]/[B,Si-*BEA]	NMR line for B[3]			NMR line for B[4]	
	Line I	Line II	Line III	Line IV	LineV
freshly calcined in air at 923 K					
δ_{cs} / ppm			10.1	-3.4	-4.6
C_{q} / MHz			2.5	-	-
relative line area / %			5	64	31
calcined, then stored in closed vial for 1 month					
δ_{cs} / ppm			10.1	-3.1	-4.6
C_{q} / MHz			2.5	-	-
relative line area / %			4	66	30
exposed in air overnight					
δ_{cs} / ppm				-3.1	-4.7
relative line area / %				72	28

Another phenomenon in these spectra is a disappearance of the broad line characterizing trigonal boron after hydration. The tiny resonances which are present in samples freshly calcined or stored 1 month in closed vial (Figure 7.2d-f and 7.8a-c) with the relative area of 5 % or 4 % respectively (Table 7.4) have completely disappeared at further hydration (Fig 7.8d-f).

Figure 7.9 illustrates the ^{11}B 2D MQMAS spectrum of the sodium form after exposing in air overnight. Two separated B^[4] components are clearly observed in this sample.

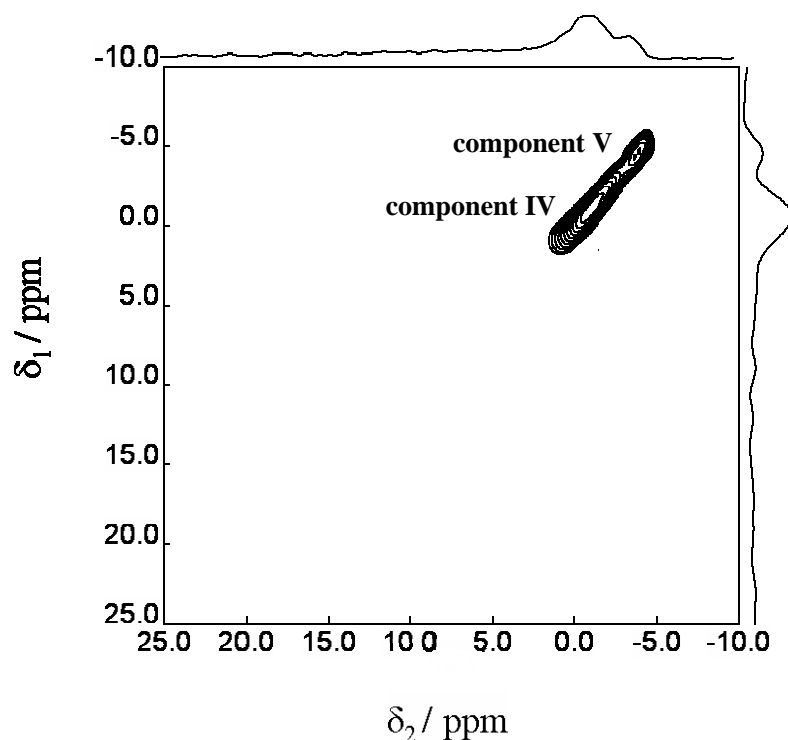


Figure 7.9: ^{11}B 2D MQMAS spectrum at $B_0 = 11.7 \text{ T}$ of $[\text{Na}^+, \text{H}^+][\text{B}, \text{Si}-* \text{BEA}]$ exposed in air overnight

In the proton form, the line assigned to tetrahedral boron also includes at least two components at around -2.4 (component IV) and -3.2 ppm (component V) (Figure 7.10c,f). The total line area of tetrahedral components considerably increases at longer hydration time. The freshly calcined sample shows only 3 %, but after storing in the closed vial at ambient environment, the total value of tetrahedral boron increases to 14 % after 1 month and 27 % after 1 year (Table 7.5).

Besides the components assigned to tetrahedral boron as presented above, the broad line obtained in Figure 7.10a-c; 7.10d-f and 7.3d-f could be formed at least from 3 components, which are affected by second-order quadrupole interaction. These components have similar interaction values (C_q in the range of 2.2-2.6 MHz and $\eta = 0.1-0.15$) but the chemical shifts are different. As shown in Section 7.1, the components II and III indicating trigonal boron in the framework have the chemical shifts at around 10.1 ppm and 14.8 ppm, respectively. Whereas, component I is referred to trigonal non-framework boron.

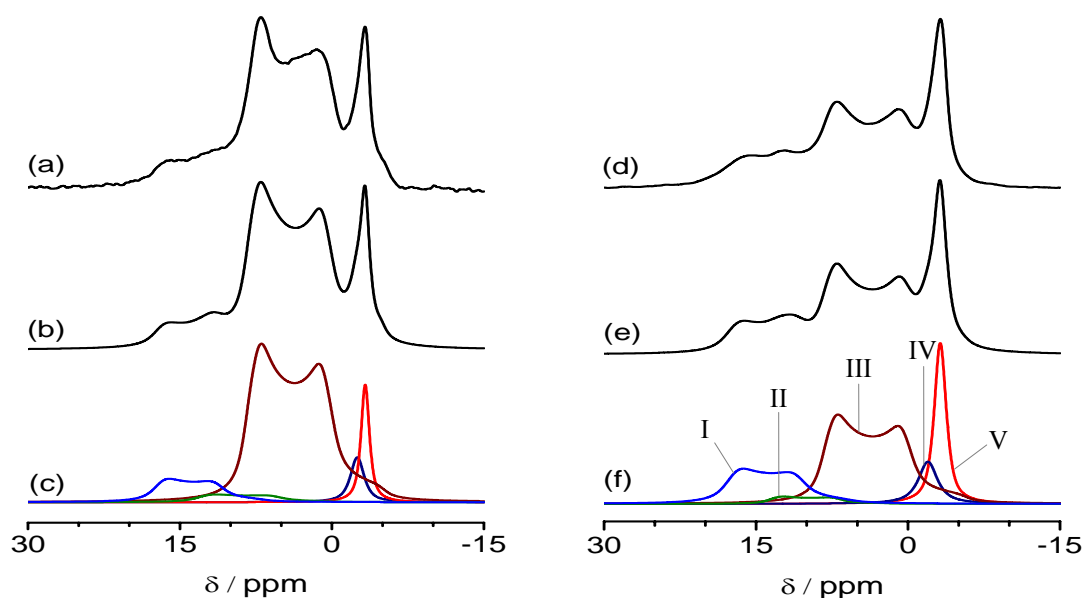


Figure 7.10: ^{11}B MAS spin echo NMR spectra at $B_0 = 11.7\text{ T}$ of $|\text{H}^+|[\text{B},\text{Si}-^*\text{BEA}]$ after calcination then (a) stored in closed vial for 1 month spectrum, (b) simulation, (c) components (d) stored in closed vial for 1 year spectrum, (e) simulation, (f) components

Table 7.5: ^{11}B MAS spin echo NMR line assignment of $^*\text{BEA}$ -borosilicate proton form at various hydration levels.

$ \text{H}^+ [\text{B},\text{Si}-^*\text{BEA}]$	NMR line for B[3]			NMR line for B[4]	
	Line I	Line II	Line III	Line IV	Line V
freshly calcined in air at 923 K					
$\delta_{\text{cs}} / \text{ppm}$	18	14.8	10.1	-3.2	
$C_{\text{q}} / \text{MHz}$	2.2	2.4	2.6	-	
relative line area / %	5	11	81	3	
calcined, then stored in closed vial for 1 month					
$\delta_{\text{cs}} / \text{ppm}$	18.6	14.7	10.0	-2.5	-3.3
$C_{\text{q}} / \text{MHz}$	2.2	2.4	2.5	-	-
relative line area / %	10	4	72	5	9
calcined, then stored in closed vial for 1 year					
$\delta_{\text{cs}} / \text{ppm}$	19.2	14.9	10.0	-2.1	-3.2
$C_{\text{q}} / \text{MHz}$	2.4	2.3	2.5	-	-
relative line area / %	20	4	49	8	19

Interestingly, the chemical shift of the non-framework component is shifted while borosilicates are further hydrated. This line appears at 18 ppm in the freshly calcined sample and increases to 18.6 ppm and 19.2 ppm when the samples are stored in closed vial for 1 month or 1 year, respectively (Table 7.5). When the borosilicates are exposed in ambient air, a broad line at around 18 ppm can be clearly observed. In addition, after hydration by soaking in water, a significant sharp line at 21 ppm is clearly obtained. Hwang et al. claimed the lineshape presented at 18 ppm in the exposed sample could be characterized by Gaussian type lineshapes.¹⁷² The relative areas of quadrupolar resonances have changed as a function of water adsorbed in the samples with different trends. In fact, at further hydration, the total area of components assigned to trigonal boron in framework (components II and III) decreases, whereas the relative area of trigonal non-framework boron (component I) considerably increases. The total area of components II and III is 92 % in the freshly calcined sample, 76 % for 1 month storing in closed vial and obviously decreases to 53 % after 1 year storage. In contrast, the relative area of component I is 5 %, 10 % and 20 % in the samples freshly calcined, stored for 1 month and 1 year in closed vials, respectively (Table 7.5).

Figure 7.11 illustrates the ^{11}B 2D MQMAS spectra of the proton form after 1 year storage and exposing in air overnight.

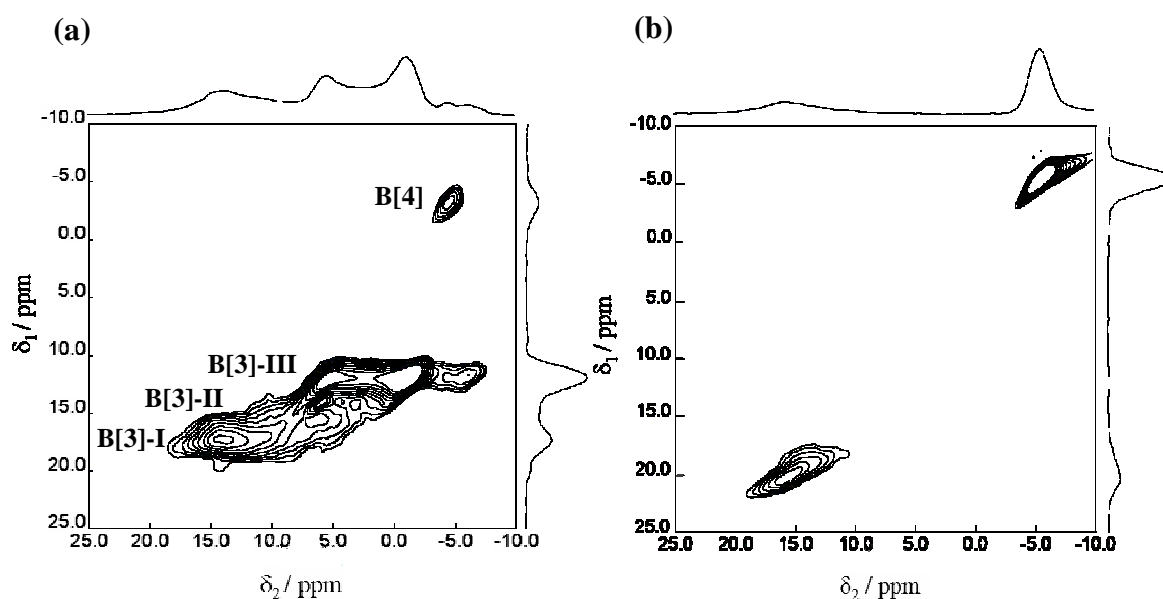


Figure 7.11: ^{11}B 2D MQMAS spectra at $B_0 = 11.7\text{ T}$ of calcined $[\text{H}^+][\text{B,Si-*BEA}]$ (a) stored in closed vial for 1 month, (b) exposed in ambient air overnight

In spectrum of sample after 1 year storage, all trigonal components are clearly observed (Figure 7.11a). Components assigned to tetragonal and non-framework trigonal borons are observed in spectrum of sample after exposing in air overnight (Figure 7.11b).

7.2.2 ^1H MAS NMR Spectroscopy

The ^1H MAS NMR spectra of *BEA borosilicates of the hydration series are summarized in Figure 7.12. As can be seen, the lineshape of ^1H MAS NMR spectra is in the range of 1.6-6 ppm in both, proton and sodium forms. The lines at around 1.8 ppm, 2 ppm or 2.3 ppm, which are assigned to silanol groups or hydrogen bonded hydroxyl groups located around boron can be observed in borosilicates freshly calcined or stored for 1 month in closed vial (Figure 7.12a,b and 7.12e,f). In particular, these lines are apparently present in spectra of the proton forms. At further hydration by exposing in air or soaking in water, these lines have disappeared. On the other hand, when more water molecules are adsorbed in the samples, the line at around 5.5 ppm is obtained (Figure 7.12c,d and 7.12h). This line is attributed to the surface adsorbed water.

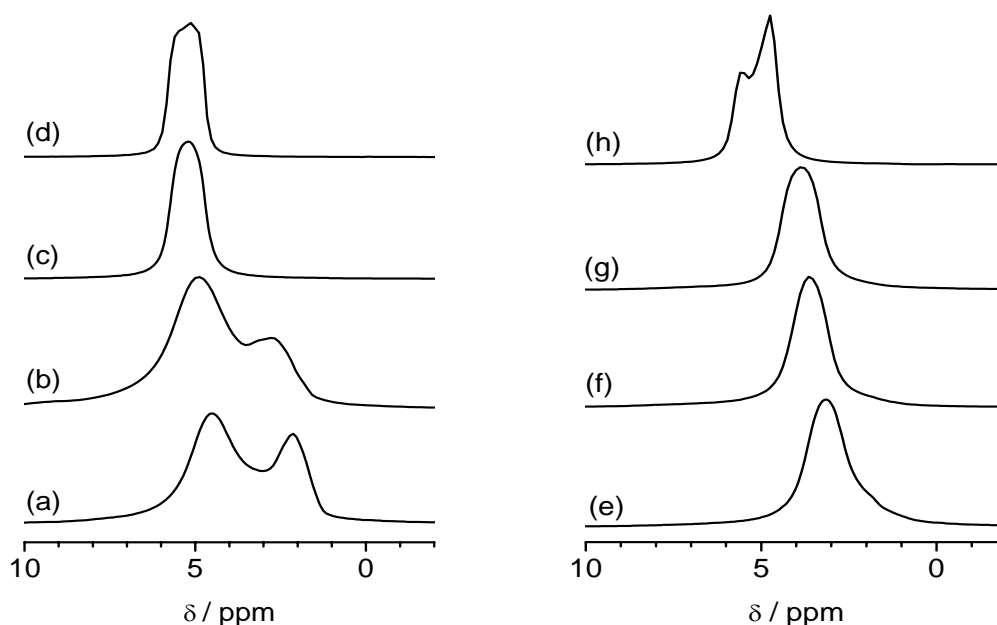


Figure 7.12: ^1H MAS NMR spectra at $B_0 = 11.7\text{ T}$ of (a) $|\text{H}^+|[\text{B,Si-*BEA}]$ freshly calcined at 923 K, (b) $|\text{H}^+|[\text{B,Si-*BEA}]$ stored for 1 month in closed vial, (c) $|\text{H}^+|[\text{B,Si-*BEA}]$ exposed in air overnight, (d): $|\text{H}^+|[\text{B,Si-*BEA}]$ further hydrated by soaking in water; (e) $|\text{Na}^+, \text{H}^+|[\text{B,Si-*BEA}]$ freshly calcined at 923 K, (f) $|\text{Na}^+, \text{H}^+|[\text{B,Si-*BEA}]$ stored for 1 month in closed vial, (g) $|\text{Na}^+, \text{H}^+|[\text{B,Si-*BEA}]$ exposed in air overnight, (h) $|\text{Na}^+, \text{H}^+|[\text{B,Si-*BEA}]$ further hydrated by soaking in water.

7.2.3 ^{29}Si MAS NMR Spectroscopy

The ^{29}Si MAS NMR measurements of the hydrated borosilicates are shown in Figure 7.13. The spectra of borosilicates in presence of sodium do not show any change of the lineshape (Figure 7.13e-g), whereas the proton forms displays a noticeable distortion of the lineshape (Figure 7.13a-d).

The freshly calcined *BEA-borosilicate proton form shows the major silicon signal at around -111 ppm, with a minor line at -102 ppm (Figure 7.13a). These resonances are assigned to $\text{Si}-(\text{OSi})_4$ (Q^4) and the silanol group $\text{HO}-\text{Si}-(\text{OSi})_3$ (Q^3) associated with the trigonal boron units and/or isolated to silanol groups. The resonance at -102 ppm increases upon hydration.

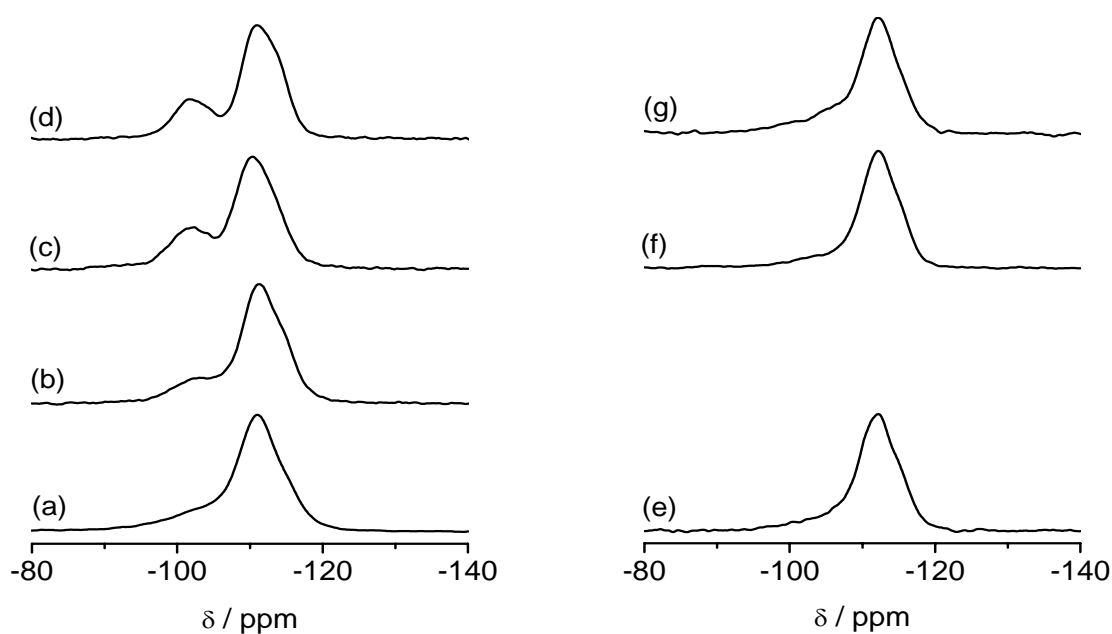


Figure 7.13: ^{29}Si MAS NMR spectra at $B_0 = 7.05$ T of (a) $|\text{H}^+|[\text{B},\text{Si}-*\text{BEA}]$ freshly calcined at 923 K, (b) $|\text{H}^+|[\text{B},\text{Si}-*\text{BEA}]$ stored for 1 month in closed vial, (c) $|\text{H}^+|[\text{B},\text{Si}-*\text{BEA}]$ exposed in air overnight, (d): $|\text{H}^+|[\text{B},\text{Si}-*\text{BEA}]$ further hydrated by soaking in water; (e) $|\text{Na}^+, \text{H}^+|[\text{B},\text{Si}-*\text{BEA}]$ freshly calcined at 923 K, (f) $|\text{Na}^+, \text{H}^+|[\text{B},\text{Si}-*\text{BEA}]$ exposed in air overnight, (g) $|\text{Na}^+, \text{H}^+|[\text{B},\text{Si}-*\text{BEA}]$ further hydrated by soaking in water.

7.3 Dehydration of Borosilicate after Hydration

7.3.1 ^{11}B NMR Spectroscopy

With the aim for further investigate the structural changes of the boron sites after being subjected to such severe hydration, the hydrated *BEA-borosilicates were employed for the following dehydration. The beta borosilicates in the proton and sodium forms after hydration in Section 7.2 were calcined at 923 K and dehydrated in vacuum at 323 K. The ^{11}B NMR spectra of these powder samples are revealed in Figure 7.14.

After re-calcination, the sharp line at 21 ppm in the soaked proton form (Figure 7.14b) and 14 ppm in the soaked sodium form (Figure 7.14f) disappear. On the other hand, the lineshapes of the re-calcined (Figure 7.14c,g) and re-dehydrated sample (Figure 7.14d,h) are similar to the freshly calcined *BEA-borosilicates (Figure 7.14a,e) in the proton and the sodium forms.

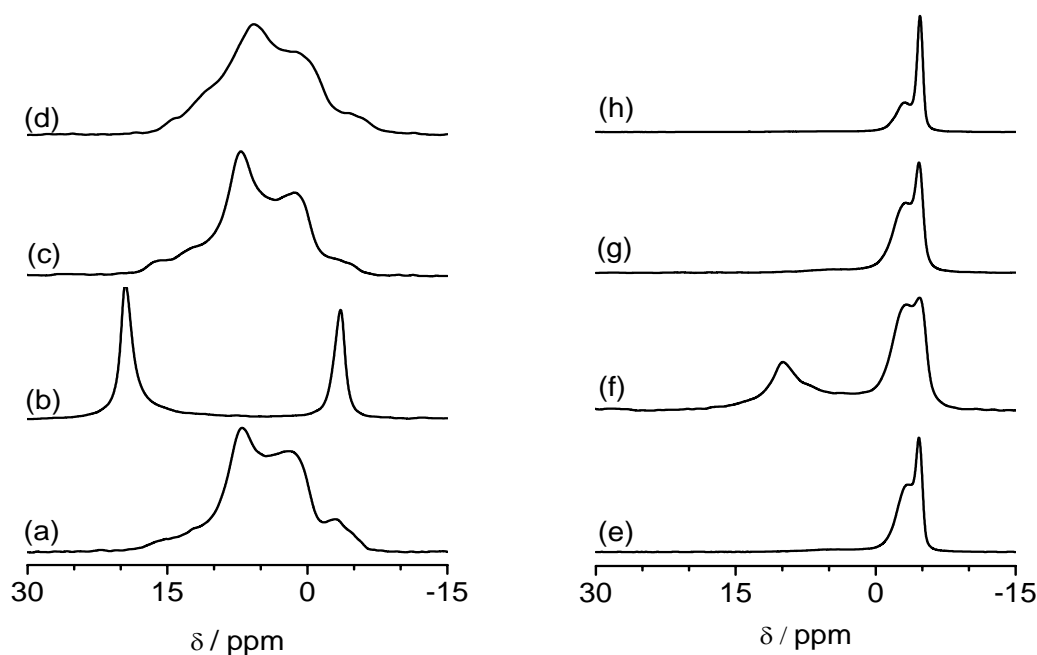


Figure 7.14: ^{11}B MAS spin echo NMR spectra at $B_0 = 11.7\text{ T}$ of (a) sample A: $|\text{H}^+|[\text{B},\text{Si}-*\text{BEA}]$ freshly calcined at 923 K, (b) sample B: $|\text{H}^+|[\text{B},\text{Si}-*\text{BEA}]$ hydrated by soaking in water, (c) sample C: sample B calcined at 923 K, (d): sample D: sample B dehydrated in vacuum at 393 K; (e) sample E: $|\text{Na}^+,\text{H}^+|[\text{B},\text{Si}-*\text{BEA}]$ freshly calcined at 923 K, (f) sample F: $|\text{Na}^+,\text{H}^+|[\text{B},\text{Si}-*\text{BEA}]$ hydrated by soaking in water, (g) sample G: sample F calcined at 923 K, (h) sample H: sample F dehydrated in vacuum at 393 K.

Figure 7.15 shows the simulated spectra of re-calcined and re-dehydrated proton forms. The line assignment of these samples is collected in Table 7.6. The relative area of trigonal components is not much changing much in comparison with the freshly calcined sample. The relative area of component I at 18.3 ppm of trigonal non-framework boron is 5 %, 6 % and 1% for the freshly calcined, re-calcined and re-dehydrated samples, respectively. The total relative areas of the components II at about 14.8 ppm and III at 10.1 ppm, which are attributed to the trigonal boron in the framework, are 92 %, 90 % and 98 % in the samples after fresh calcinations, re-calcination and re-dehydration, respectively. The tetragonal boron is observed after re-dehydration with the relative area not changing compared to the freshly calcined sample.

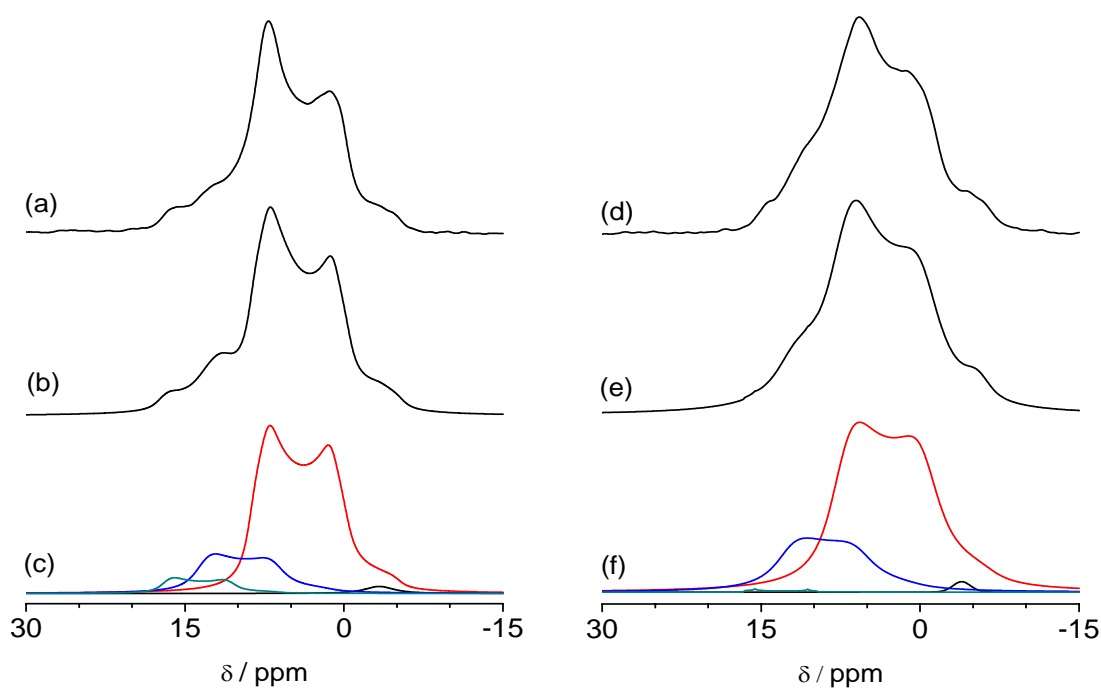


Figure 7.15: ^{11}B MAS spin echo NMR spectra at $B_0 = 11.7\text{ T}$ of $[\text{H}^+]/[\text{B,Si-*BEA}]$ (a) after re-calcination at 923 K, (b) simulation, (c) components (d) after re-dehydration at 393 K, (e) simulation, (f) components

Table 7.6: ^{11}B MAS spin echo NMR line assignment of $^*\text{BEA}$ -borosilicate proton form dehydrated after hydration

$[\text{H}^+][\text{B},\text{Si}-^*\text{BEA}]$	NMR line for B[3]			NMR line for B[4]	
	Line I	Line II	Line III	Line IV	Line V
freshly calcined in air at 923 K					
δ_{cs} / ppm	18.0	14.8	10.1		-3.2
C_{q} / MHz	2.2	2.4	2.6		-
relative line area / %	5	11	81		3
soaked and then calcined at 923 K					
δ_{cs} / ppm	18.5	15.1	10.2		-3.6
C_{q} / MHz	2.2	2.4	2.5		-
relative line area / %	6	18	72		4
soaked and then dehydrated in vacuum at 393 K					
δ_{cs} / ppm	18.0	14.4	9.9		-3.7
C_{q} / MHz	2.3	2.4	2.6		-
relative line area / %	1	23	75		1

The simulated spectra of re-calcined and re-dehydrated sodium form are shown in Figure 7.16. The line assignment of these samples is summarized in Table 7.7. In Figure 7.16, the re-calcination and re-dehydration sodium borosilicates show the main components of tetrahedral boron with a slight change of these components. The relative areas of component IV at -3.2 ppm (about 65%) are the same for the freshly calcined and re-calcined beta borosilicates. But this value considerably decreases to 42 %, when the sample is re-dehydrated in vacuum. Besides the tetragonal components, the quadrupolar resonance at 10.1 ppm assigned to trigonal boron is always observed in both re-calcined and re-dehydrated samples with small relative area about 5 %.

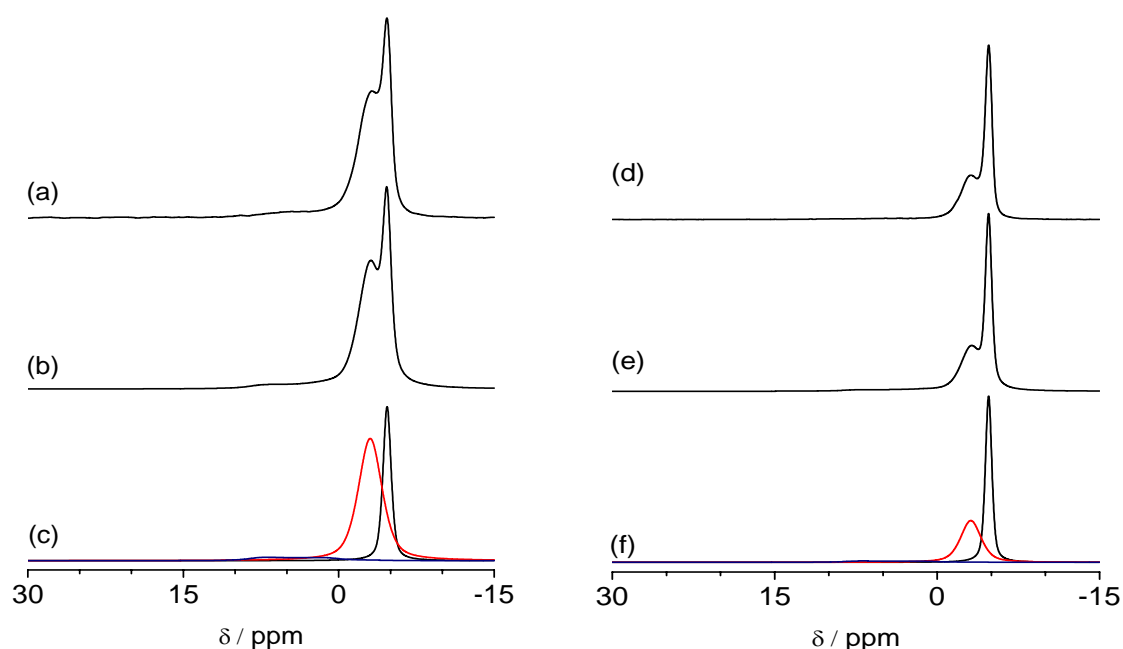


Figure 7.16: ^{11}B MAS spin echo NMR spectra at $B_0 = 11.7\text{ T}$ of $[\text{Na}^+, \text{H}^+][\text{B}, \text{Si}-*\text{BEA}]$ (a) after re-calcination at 923 K, (b) simulation, (c) components (d) after re-dehydration at 393 K, (e) simulation, (f) components

Table 7.7: ^{11}B MAS spin echo NMR line assignment of *BEA-borosilicates in presence of sodium dehydrated after hydration

$[\text{Na}^+, \text{H}^+][\text{B}, \text{Si}-*\text{BEA}]$	NMR line for B[3]			NMR line for B[4]	
	Line I	Line II	Line III	Line IV	Line V
freshly calcined in air at 923 K					
$\delta_{\text{cs}} / \text{ppm}$			10.1	-3.4	-4.6
$C_{\text{q}} / \text{MHz}$			2.5	-	-
relative line area / %			5	64	31
soaked and then calcined at 923 K					
$\delta_{\text{cs}} / \text{ppm}$			10.1	-3.1	-4.7
$C_{\text{q}} / \text{MHz}$			2.5	-	-
relative line area / %			6	65	27
soaked and then dehydrated in vacuum at 393 K					
$\delta_{\text{cs}} / \text{ppm}$			10.1	-3.1	-4.7
$C_{\text{q}} / \text{MHz}$			2.5	-	-
relative line area / %			5	42	53

7.3.2 ^1H MAS NMR Spectroscopy

The ^1H MAS NMR spectra of the proton form (left) and sodium form (right) after re-calcination and re-dehydration are shown in Figure 7.17. The lineshape of re-calcined and re-dehydrated samples are similar to the freshly calcined samples in both the proton and sodium forms. However, in the sodium form, the lineshape of the re-dehydrated sample is narrower than the re-calcined sample.

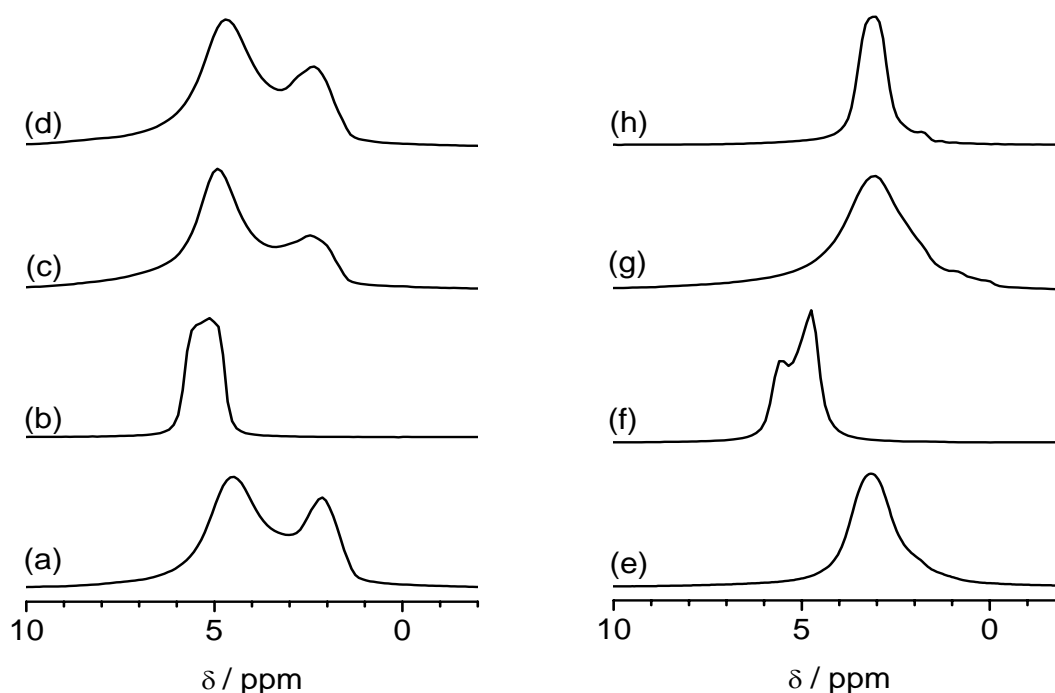


Figure 7.17: ^1H MAS NMR spectra at $B_0 = 11.7$ T of (a) sample A: $|\text{H}^+|[\text{B},\text{Si}-*\text{BEA}]$ freshly calcined at 923 K, (b) sample B: $|\text{H}^+|[\text{B},\text{Si}-*\text{BEA}]$ hydrated by soaking in water, (c) sample C: sample B calcined at 923 K, (d): sample D: sample B dehydrated in vacuum at 393 K; (e) sample E: $|\text{Na},\text{H}|[\text{B},\text{Si}-*\text{BEA}]$ freshly calcined at 923 K, (f) sample F: $|\text{Na}^+,\text{H}^+|[\text{B},\text{Si}-*\text{BEA}]$ hydrated by soaking in water, (g) sample G: sample F calcined at 923 K, (h) sample H: sample F dehydrated in vacuum at 393 K.

7.3.3 ^{29}Si MAS NMR Spectroscopy

In agreement with the trend of ^1H and ^{11}B MAS NMR spectra, the ^{29}Si MAS NMR of re-calcinated samples also shows the return of the lineshape to the freshly calcined samples (Figure 7.18). Apparently, the resonance appearing for the soaked proton form at about

-102 ppm (Figure 7.18b) almost disappears, and the majority of resonance at -111 ppm is clearly observed for the re-calcined sample (Figure 7.18c). Unlike the change of the lineshape of the proton form, the sodium form does not show any alteration of the lineshape before and after re-calcination (Figure 7.18d-f). The main resonance ascribed to Q⁴ is always achieved in all ²⁹Si MAS NMR spectra.

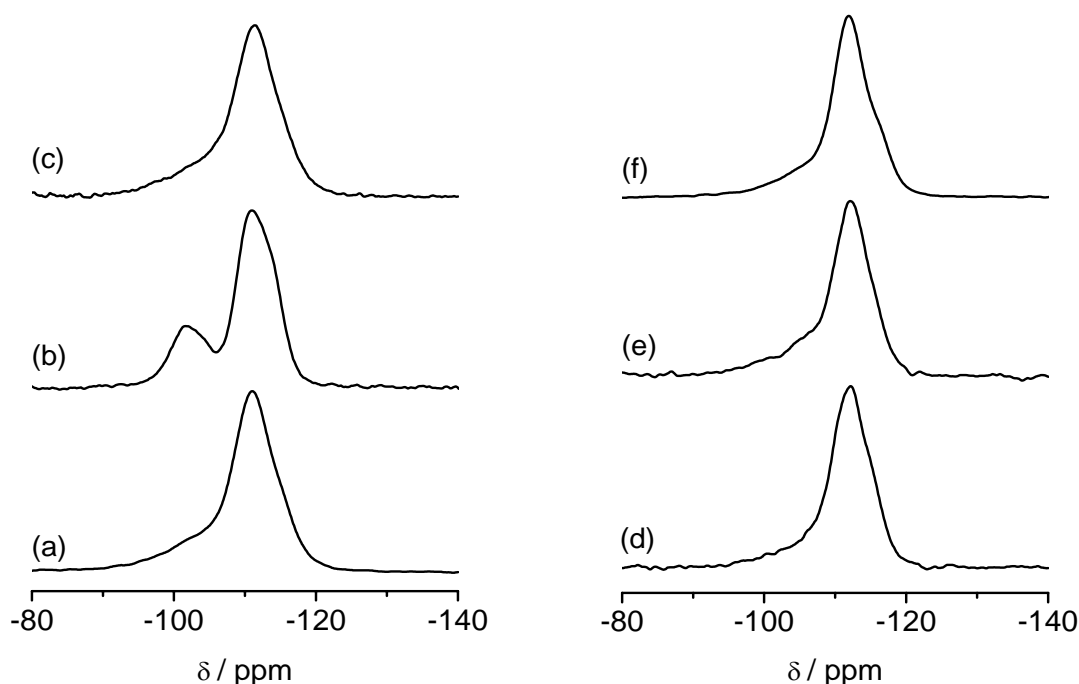


Figure 7.18: ²⁹Si MAS NMR spectra at $B_0 = 7.05$ T of (a) $|H^+|[B,Si-*BEA]$ freshly calcined at 923 K, (b) $|H^+|[B,Si-*BEA]$ hydrated by soaking in water, (c) $|H^+|[B,Si-*BEA]$ subsequently calcined at 923 K; (d) $|Na^+,H^+|[B,Si-*BEA]$ freshly calcined at 923 K, (e) $|Na^+,H^+|[B,Si-*BEA]$ further hydrated by soaking in water, (f) $|Na^+,H^+|[B,Si-*BEA]$ subsequently calcined at 923 K.

7.4 Discussion

The boron coordinations in beta borosilicates are very flexible. Unlike aluminosilicate zeolites, the boron coordinations in *BEA-borosilicates can be transformed from B^[3] to B^[4] or vice versa upon hydration/dehydration processes. The ¹¹B NMR spectra of the as-synthesized beta borosilicates always show only the tetrahedral boron. The negative charge of BO_{4/2}⁻ is compensated by TEA⁺. However, different lineshapes with broad line characterized by second-order quadrupole interactions under magic angle spinning

conditions, particularly in the proton form, are observed for the dehydrated and calcined samples. Partially hydrolysis of trigonal boron $B(OSi)_x(OH)_{3-x}$ ($x = 1, 2, 3$) was suggested by Martens et al.¹⁷³ The resonances shift to lower field while the number of hydrolyzed bonds increase.¹⁶⁴ These components have an isotropic chemical shift that varies depending on the environment. The components at 10.5 ± 0.7 ppm (component III) or 15.4 ± 0.5 ppm (component II) are referred to $B^{[3]}$ in framework $B(OSi)_3$ or $B(OH)_2(OSi)$, respectively. Another line at 18.5 ± 0.5 (component I) is assigned to non-framework $B^{[3]}$. Further information about these resonances can be obtained in ^{11}B 2D MQMAS NMR spectra. In the resolution aspect, the 2D MQMAS spectrum (Figure 7.11a) shows all the components that were mentioned in 1D MAS NMR spectra. The trigonal boron components are broad along the anisotropic axis in agreement with the quadrupolar parameters reported above. In addition, the conversion of boron coordinations during dehydration is also verified in 2D MQMAS spectra. The non-framework site $B^{[3]}$ almost disappears in the 2D MQMAS spectrum of the proton form which was dehydrated in vacuum at 673 K (Figure 7.4). In addition, comparing the two 2D MQMAS spectra in Figure 7.4 and 7.11a, tetrahedral boron decreases under dehydration at high temperature.

The scheme illustrating the conversion between trigonal and tetrahedral boron is presented in Figure 7.19. The number of B—O—Si bridge increases with more severe dehydration conditions, which is illustrated by the increase of the relative line area of trigonal boron in framework and the decrease of component non-framework in ^{11}B NMR spectra.

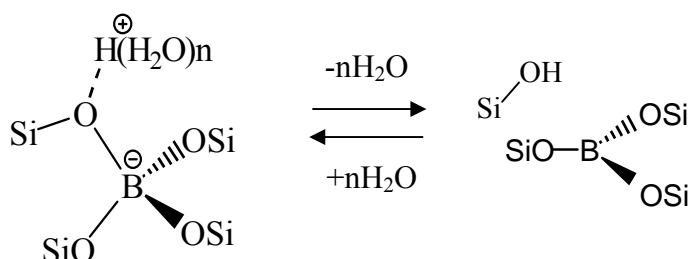


Figure 7.19: Scheme illustrating the conversion between tetrahedral and trigonal boron upon dehydration/hydration processes

The trigonal boron sites that formed via dehydration can be tightly anchored with the framework through three B—O—Si bridges in dehydrated environment. However, the trigonal boron sites are very sensitive to nucleophilic attack by water molecules, when the beta borosilicates become hydrated. This attack creates B—O—H groups in a partially trigonal boron and tetrahedral boron, which is portrayed by an increase of both non-framework trigonal boron and tetrahedral boron (components I and IV), when the beta-borosilicates are hydrated. Acquisition of 2D MQMAS NMR spectrum (Figure 7.11b) allows us to unveil more clearly the spectroscopic lineshape of these resonances. Following this trend, when more water is adsorbed in B-*BEA by soaking in water, most of B—O—Si bridges are hydrolyzed and a sharp line at 21 ppm appears. A tentative interpretation is that the line broadening for trigonal boron is averaged out by mobile $B(OH)_3$ within the zeolite channels. Low temperature experiments to verify this hypothesis have not been carried out.

In agreement with the ^{11}B NMR spectra, the 1H and ^{29}Si MAS NMR spectra also show the same trend of lineshapes during dehydration/hydration processes. At high dehydration temperature, most of the mobile water molecules are readily removed; the 1H components at about 2.0 and 2.3 ppm corresponding to $Si-OH \cdots B^{[3]}$ sites and weakly hydrogen bonded $Si-OH$ and $B-OH$ groups are clearly observed. In contrast to dehydration, adsorbed water leads to hydrolysis, and B—O—H groups were formed from B—O—Si bridges. Therefore, after hydration, the 1H MAS NMR spectra of hydrated beta borosilicates show the lineshape with major resonances at around 5.5 ± 0.5 ppm, which corresponds to hydrogen bonded BOH, SiOH and mobile water, particularly in soaked samples.

The formation of SiOH groups due to the hydrolysis of B—O—Si groups during the hydration process makes the Q^3 resonance increase in the ^{29}Si MAS NMR spectra. Indeed, the Q^4/Q^3 ratio slightly decreases while the proton form was hydrated.

Besides the changes of trigonal boron positions, the tetrahedral boron coordinations also show alteration in at least two main components. Especially in beta borosilicate with sodium, two resonances at about -3.2 ± 0.2 ppm (component IV) and -4.5 ± 0.1 ppm (component V) can be observed in all spectra, except for samples dehydrated at 673 K. Careful simulation of these spectra points out that the ratio between these components alters upon hydration/dehydration. The hydration leads to an increase of component IV. On the contrary, dehydration makes this component decrease. This trend is also obtained in the

proton form. Detailed information of these tetrahedral resonances can be obtained by the ^{11}B 2D MQMAS spectra (Figure 7.9). The tetrahedral sites show rather circular components with minor extension along the chemical shift axis because of weak quadrupole interactions. These resonances could be assigned to partially extra-framework and in tetrahedral framework boron.

Under re-dehydration and re-calcination, the corresponding ^1H MAS NMR as well as ^{11}B NMR spectra have lineshapes similar to the freshly calcined samples. The ^{11}B NMR spectra strongly suggest that boron atoms were partially incorporated back into the framework, which is illustrated by the reappearance of the broad line assigned to $\text{B}^{[3]}$ in the framework and extra-framework.

In conclusion, the sensitivity of boron coordination in beta borosilicates was investigated with NMR techniques. The conversion of boron coordinations not only appears from tetrahedral to trigonal boron under dehydration conditions, but also from trigonal to tetrahedral boron under hydration conditions. As presented in the works of Ruite et al. and Koller et al. the suggested scheme for these conversions is illustrated in Figure 7.20. With the highest degree of hydration, most of the trigonal boron in the framework can transform to tetrahedral boron and non-framework trigonal borons. Especially, the mobile $\text{B}(\text{OH})_3$ within the zeolite channels can be obtained at 21 ppm in ^{11}B MAS NMR, when the borosilicate proton form was soaked in water. Thus, boron can be removed from the framework of the proton form via hydration. Interestingly, these boron sites can reoccupy the framework through re-dehydration treatment. Under re-dehydration conditions, the non-framework and tetrahedral borons can transform to trigonal boron in the framework.

The MQMAS is an effective technique to study the boron positions in borosilicates. All the trigonal boron components were clearly observed in the ^{11}B MQMAS spectra of proton form. Two tetrahedral boron components at -3.2 and -4.5 ppm were also observed, especially in the spectra of the sodium form. Component at -4.5 ppm is assigned to the tetrahedral boron in the framework, whereas the component at -3.2 ppm could be assigned to tetrahedral boron in which parts of B—O—Si bridges were replaced by B—O—H .

In addition, as previously shown by the work of Fild et al. the conversion between trigonal and tetrahedral boron is favourably obtained in the proton form. However, this phenomenon does not appear in the sodium form. The flexible characteristics of boron

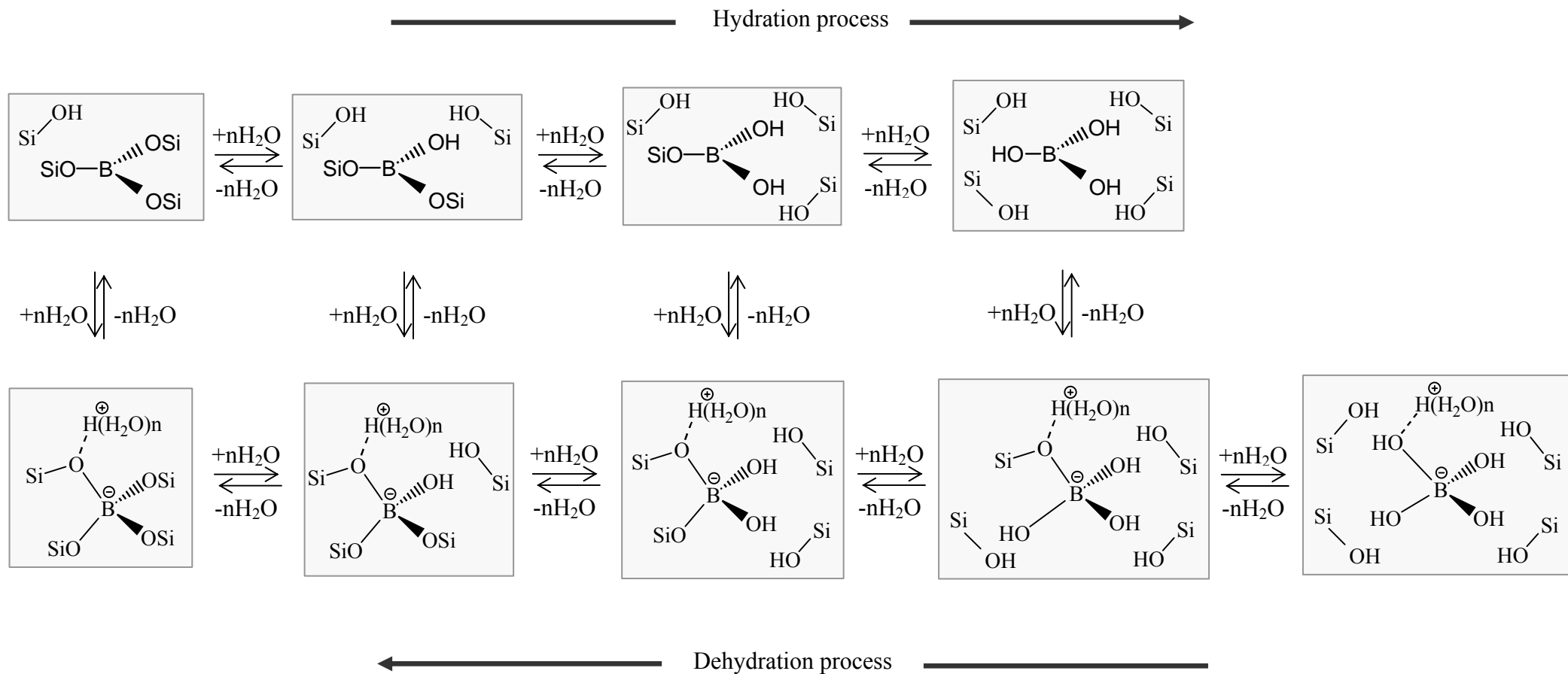


Figure 7.20: Suggested scheme illustrating the conversion between trigonal boron and tetrahedral boron coordinations

coordinations, which are associated with protons has been effectively utilized to extract the boron from the framework and applied to the post-synthetic modification from borosilicates.

Chapter

8

Post-Synthesis of *BEA-Borosilicate

Under mild conditions, boron can be easily removed from the zeolite lattice. This special property of borosilicates is very useful for post-synthetic modification.

In this chapter, the post-synthetic modification is composed of two steps. First, deboronation is carried out to create defect sites. The cations which balanced the charge can influence the deboronation procedure, therefore beta borosilicates with different Na^+/H^+ ratios can be applied for the initial step. In a second step, aluminum or gallium is introduced to the framework in water or ethanol mediums.

Besides the post-synthetic studies on the beta borosilicates, the characteristics of boron sites in beta borosilicates are further clarified in this chapter.

8.1 Deboronation of *BEA-Borosilicate

8.1.1 Ion Exchange

As shown in Chapter 7, the cations balancing the charge of the boron zeolite framework influences the boron coordination. Therefore, to study the influence of these cations on deboronation, beta borosilicates with different $\text{Na}^+/\text{NH}_4^+$ ratios were prepared by ion exchange. Details on the preparation of the ion-exchanged B-*BEA were described in Chapter 5. Based on the $\text{Na}^+ / (\text{Na}^+ + \text{NH}_4^+)$ ratios in the exchange solution, the ion-exchanged beta borosilicates are named as $[\text{Na}^+_x, \text{NH}_4^{+(1-x)}][\text{B}, \text{Si}-*\text{BEA}]$ with $x = 0, 0.2, 0.4, 0.6, 0.8$ and 1.0 . As can be seen in Figure 8.1a, all ^{11}B MAS NMR spectra show the sharp line at -3.7 ppm and the shoulder at -2 ppm that are assigned to tetrahedral boron. The boron content has been verified by quantitative line analyses and the results shown in Figure 8.1b. The figure implies that the boron content increases with increasing sodium content in the samples. This means that boron has been extracted in the solutions depending on the NH_4^+ content.

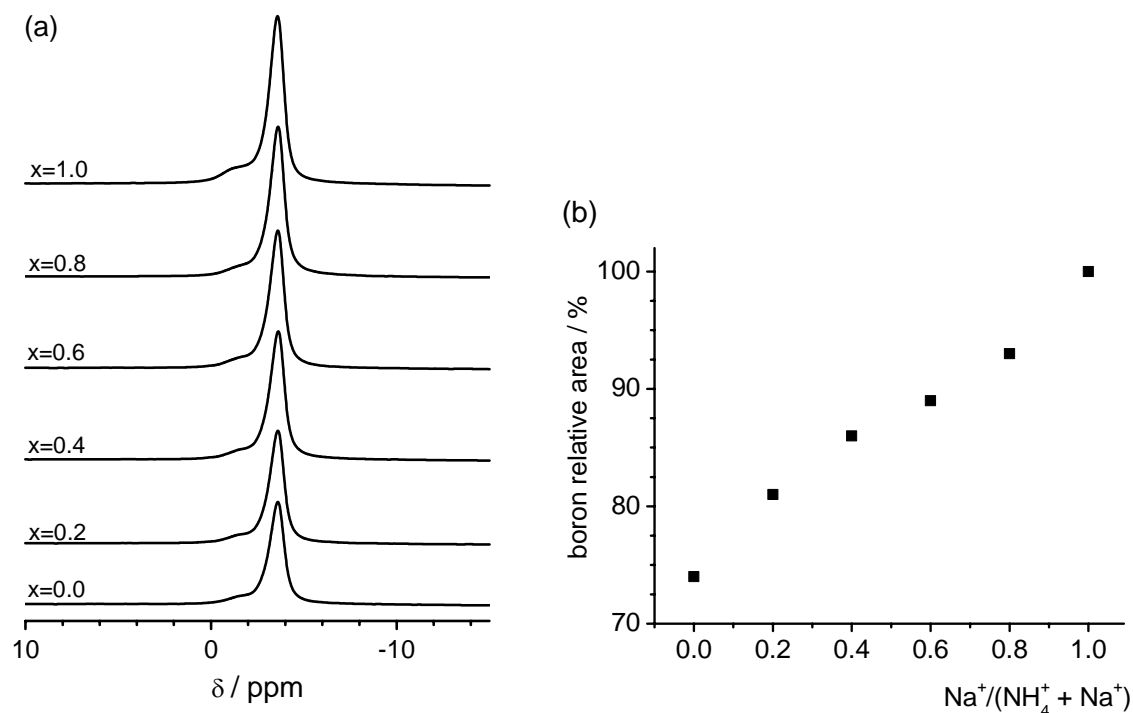


Figure 8.1: (a) ^{11}B MAS NMR spectra at $B_0 = 11.7$ T of $[\text{Na}^+_x \text{NH}_4^{+(1-x)}][\text{B}, \text{Si}-*\text{BEA}]$ ion-exchanged with $x = 0; 0.2; 0.4; 0.6; 0.8; 1.0$; (b) relative areas

To obtain the Na^+/H^+ forms, the ion-exchanged *BEA borosilicates were calcined at 723 K in vacuum. The boron coordination in these samples is studied by ^{11}B MAS NMR in Figure 8.2. As expected, the sodium form ($x = 1$) shows only a sharp line with resonance at -3.9 ppm indicated to tetrahedral boron. On the contrary, in the proton form ($x = 0$), the sharp line almost disappears, whereas broad lines II and III ($C_q = 2.4 \pm 0.2$ MHz, $\eta = 0.15\text{-}0.18$, and $\delta_{\text{cs}} = 10.3 \pm 0.3$ or 12.4 ± 0.3 ppm) are observed. In addition, the broad lines are also obtained in the other spectra of $[\text{Na}^+_x, \text{H}^{1-x}][\text{B}, \text{Si}-*\text{BEA}]$ with $x = 0.2, 0.4, 0.6$ and even 0.8 but have less relative line areas than the fully protonated sample.

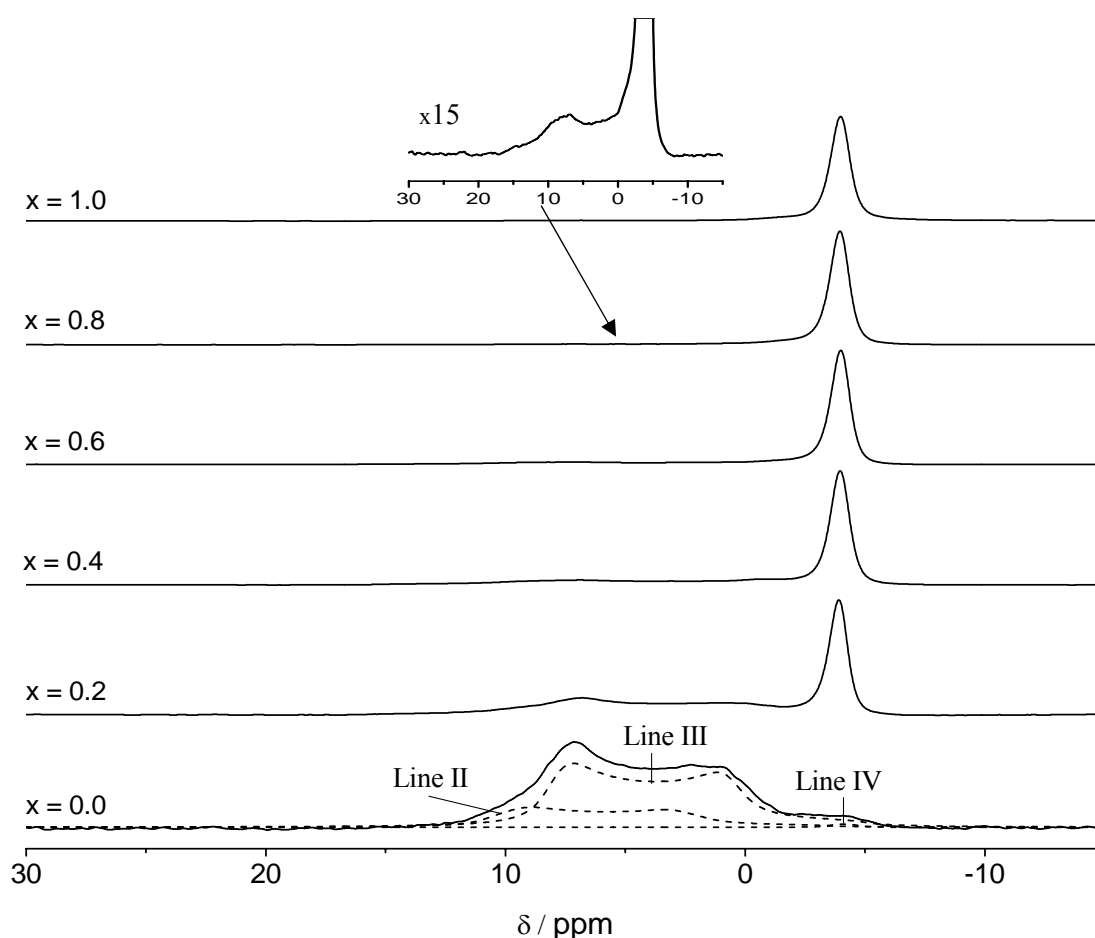


Figure 8.2: ^{11}B MAS NMR spectra at $B_0 = 11.7$ T of $[\text{Na}^+_x, \text{H}^{1-x}][\text{B}, \text{Si}-*\text{BEA}]$ dehydrated in vacuum at 723 K with $x = 0; 0.2; 0.4; 0.6; 0.8; 1.0$

Careful simulation of these spectra indicates that the boron relative line area of trigonal boron decreases when the sodium content increases. Table 8.1 summarizes the ^{11}B MAS NMR line simulations of $[\text{Na}^+_x, \text{H}^+_{1-x}][\text{B}, \text{Si}-*\text{BEA}]$.

Table 8.1: ^{11}B MAS NMR line assignment of $[\text{Na}^+_x, \text{H}^+_{1-x}][\text{B}, \text{Si}-*\text{BEA}]$ dehydrated in vacuum at 723 K

$[\text{Na}^+_x, \text{H}^+_{1-x}][\text{B}, \text{Si}-*\text{BEA}]$	NMR line for B[3]			NMR line for B[4]	
	Line I	Line II	Line III	Line IV	Line V
$x = 0.0$					
$\delta_{\text{cs}} / \text{ppm}$		12.1	10.0		-4.1
$C_{\text{q}} / \text{MHz}$		2.5	2.5		-
relative line area / %		25	74		1
$x = 0.2$					
$\delta_{\text{cs}} / \text{ppm}$		12.3	9.8	-2.7	-3.9
$C_{\text{q}} / \text{MHz}$		2.4	2.6	-	-
relative line area / %		12	40	4	44
$x = 0.4$					
$\delta_{\text{cs}} / \text{ppm}$		12.7	10.7	-1.9	-3.9
$C_{\text{q}} / \text{MHz}$		2.5	2.6		
relative line area / %		10	16	6	68
$x = 0.6$					
$\delta_{\text{cs}} / \text{ppm}$		12.4	10.2	-2.6	-4.1
$C_{\text{q}} / \text{MHz}$		2.5	2.6	-	-
relative line area / %		7	5	7	81
$x = 0.8$					
$\delta_{\text{cs}} / \text{ppm}$		12.3	10.3	-2.2	-4.0
$C_{\text{q}} / \text{MHz}$		2.2	2.6	-	-
relative line area / %		1	3	4	92
$x = 1.0$					
$\delta_{\text{cs}} / \text{ppm}$				-2.4	-3.9
relative line area / %				6	94

Figure 8.3 displays the ^1H MAS NMR of beta borosilicates after ion-exchange in $\text{Na}^+/\text{NH}_4^+$ forms (left) and dehydrated Na^+/H^+ forms (right). All the spectra of the $\text{Na}^+/\text{NH}_4^+$ samples are characterized by an intense and sharp line at about 5.5 ppm (Figure 8.3a). These lines are overlap of several components, which are attributed to adsorbed water and NH_4^+ . In addition, the other line at about 2.7 ppm is always presented in all spectra with a less relative area. As discussed in the last chapter, this line is assigned to hydrogen bonds of hydroxyl groups located around boron. Another observation in these spectra is that the relative area of these signals changes at different $\text{Na}^+/\text{NH}_4^+$ ratios. Indeed, the line area of these resonances increases with increasing sodium content in the samples.

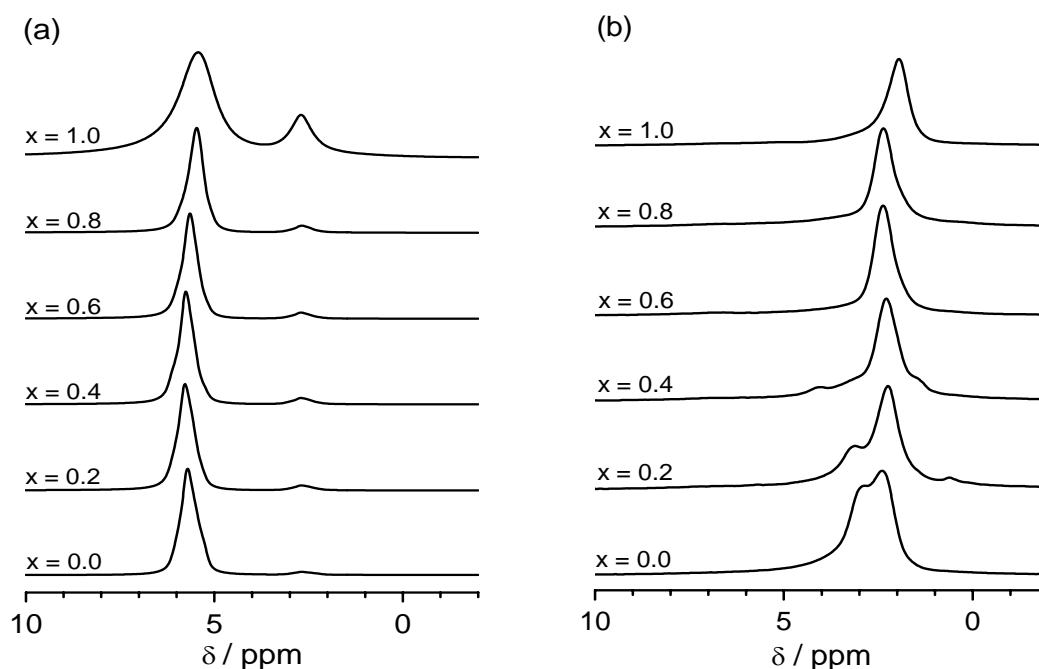


Figure 8.3: ^1H MAS NMR spectra at $B_0 = 11.7\text{ T}$ of (a) $[\text{Na}_x, \text{NH}_4^{(1-x)}][\text{B}, \text{Si}-*\text{BEA}]$ ion-exchanged (b) $[\text{Na}_x, \text{H}^{(1-x)}][\text{B}, \text{Si}-*\text{BEA}]$ dehydrated in vacuum at 673 K

The ^1H MAS NMR spectra of Na^+/H^+ dehydrated beta borosilicates show lines between 1.6 to 4.5 ppm (Figure 8.3b). This lineshape could be included several single components overlapping which characterize to the silanol groups or the hydrogen bonds of hydroxyl groups located around boron. Interestingly, throughout the spectra, the lineshape becomes narrower and shifts to 1.8 ppm while the sodium content increases.

8.1.2 Deboronation

To prepare the samples for Al or Ga implanting, beta borosilicates were deboronated by deionized water at pH ~ 7 . Deboronation procedures were already reported in Chapter 5. The quantitative ^{11}B NMR analyses of deboronated beta borosilicates are shown in Figure 8.4. Apparently, the boron content increases when the sodium content for charge balance increases, as expected. No boron signals are observed in the spectrum of the proton form after 48 hours of deboronation. However, a minor boron line still appears in proton form after 24 hours of deboronated treatment (the spectrum is not shown in this chapter). On the other hand, no change of the boron content is observed in the sodium form.

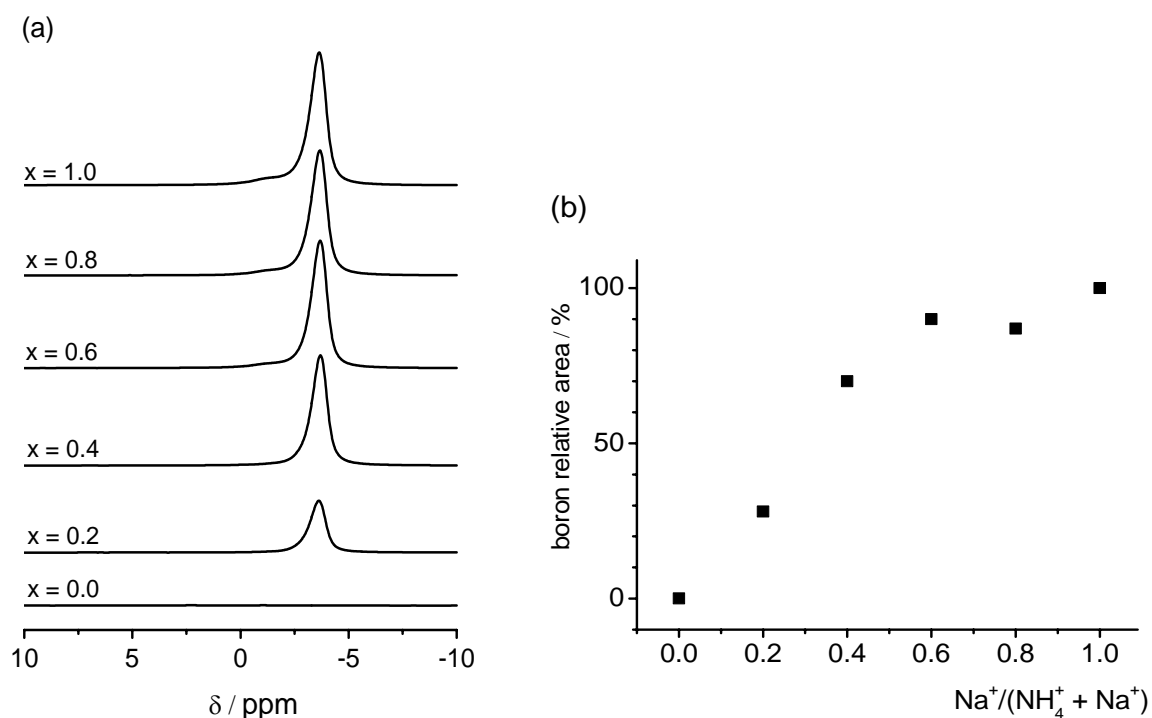


Figure 8.4: (a) ^{11}B MAS NMR spectra at $B_0 = 11.7\text{ T}$ of $[\text{Na}^+_x, \text{H}^+_{1-x}][\text{B}, \text{Si}^* \text{BEA}]$ deboronated in water for 48 hours with $x = 0; 0.2; 0.4; 0.6; 0.8; 1.0$; (b) relative areas

The presence of sodium in beta borosilicates after deboronation was confirmed by ^{23}Na MAS NMR spectra (Figure 8.5a). All spectra have revealed the ^{23}Na NMR broad resonance centered at around -7 ppm. Moreover, the relative intensities (Figure 8.5b) imply that the variation of the relative sodium content in the zeolites is in good agreement with initial preparation experiment.

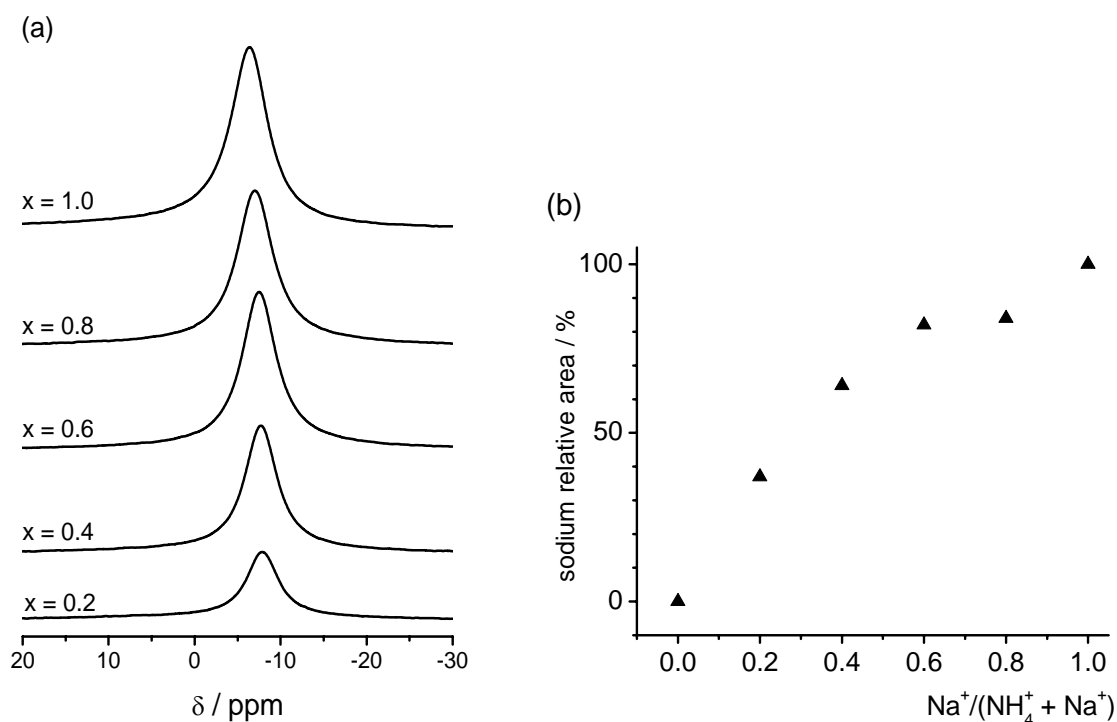


Figure 8.5: (a): ^{23}Na MAS NMR spectra at $B_0 = 11.7$ T of $[\text{Na}^+_x\text{H}^{+}_{1-x}][\text{B},\text{Si}-*\text{BEA}]$ deboronated in water for 48 hours with $x = 0; 0.2; 0.4; 0.6; 0.8; 1.0$; (b) relative areas

Besides the characteristics of deboronated samples which are obtained by the ^{11}B MAS NMR and the ^1H MAS NMR spectra, ^{29}Si MAS NMR spectra also present a different change in the lineshape of $[\text{Na}^+_x\text{H}^{+}_{1-x}][\text{B},\text{Si}-*\text{BEA}]$ spectra during deboronation. Figure 8.6 illustrates the alternation in the ^{29}Si MAS NMR spectra of $[\text{Na}^+_x\text{H}^{+}_{1-x}][\text{B},\text{Si}-*\text{BEA}]$ with $x = 0, 0.5$ and 1 . In Figure 8.6a-c, the proton form ($x = 0$) shows an increase of the component at around -102 ppm at longer deboronation time. This trend is also observed for $x = 0.5$ but with less relative area changes (Figure 8.6d-f). On the contrary, the sodium form ($x = 1$) does not display any change during the deboronation process (Figure 8.6g-i).

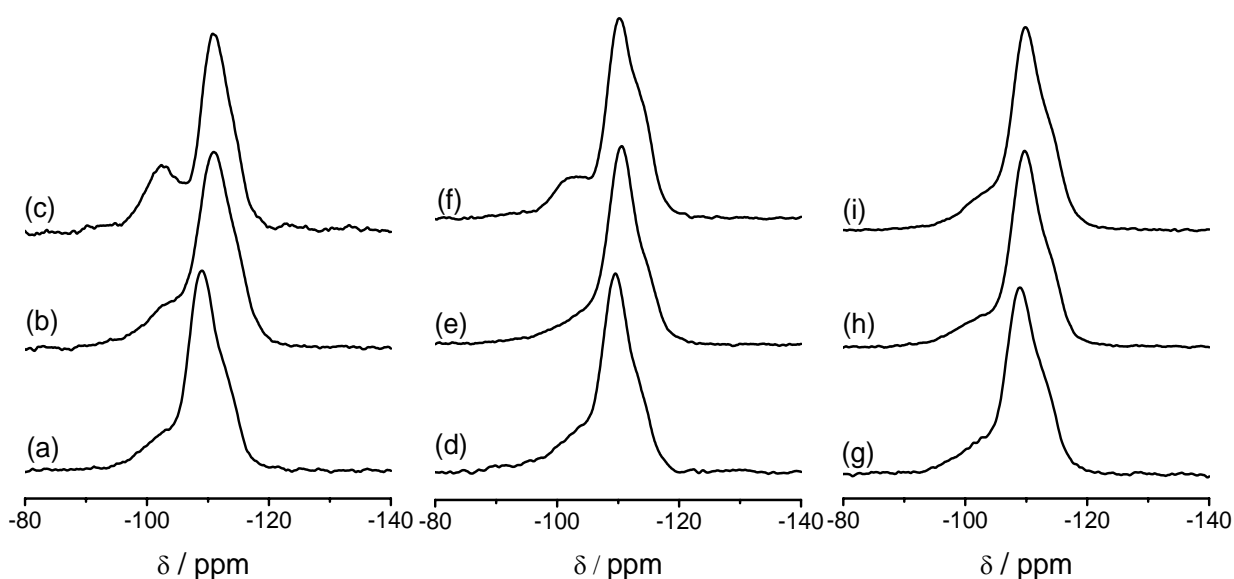


Figure 8.6: ^{29}Si MAS NMR spectra at $B_0 = 7.05$ T of: Left: $|\text{H}^+|[\text{B},\text{Si}-*\text{BEA}]$ with (a) ion-exchange, (b) deboronated in water for 24 hours, (c) deboronated in water for 48 hours. Middle: $|\text{Na}^{+0.5},\text{H}^{+0.5}|[\text{B},\text{Si}-*\text{BEA}]$ with (d) ion-exchange, (e) deboronated in water for 24 hours, (f) deboronated in water for 48 hours. Right: $|\text{Na}^+|[\text{B},\text{Si}-*\text{BEA}]$ with (g) ion-exchange, (h) deboronated in water for 24 hours, (i) deboronated in water for 48 hours

8.1.3 Discussion

Boron was found to be partially removed from the beta borosilicate framework by deboronation at mild conditions (washing in water). Deboronation depends on the counter ions compensating the change of the beta borosilicate framework. Tetrahedral boron which is balanced by a hydrated proton easily converts to trigonal boron through the dehydration process. By contrast, the tetrahedral boron which is compensated by a sodium cation is rather stable upon dehydration and even hydrolysis processes under mild conditions. Indeed, under severe dehydration conditions such as at 923 K in vacuum, most of tetrahedral boron sites in the proton form have transformed to trigonal boron components, whereas the relative line area of these sites does not change in the sodium form. Thus, the stability of tetrahedral boron depends on the cations balancing the charge of the framework. Tetrahedral boron is stable when Na^+ , Li^+ , NH_4^+ , $\text{H}(\text{H}_2\text{O})^+$ are counterbalancing the framework charge, but it is unstable in the proton form. Pelmentchikov et al. claimed that the stability of tetrahedral boron mainly depends on the energy gain upon establishing the fourth boron-oxygen bond.¹⁷⁴

The trigonal boron sites in the proton form are easily hydrolyzed and finally extracted out of the framework. On the other hand, the tetrahedral boron sites in sodium form are rather stable and hardly removed out of the framework. In particular, the boron components can be completely extracted at long hydrolysis periods of 48 hours by washing the proton form in water.

The hydrolysis process during deboronation creates silanol defect sites as confirmed by the increasing number of Q³ sites in the ²⁹Si MAS NMR spectra. These sites can participate in the post-synthetic incorporation of other elements as shown below in Sections 8.2 and 8.3. However, the formation of Q³ is not observed in the sodium form because of the stability of tetrahedral boron balanced by sodium cations. In good agreement with this observation, the Q³/Q⁴ ratio in |Na⁺_{0.5},H⁺_{0.5}|[B,Si-*BEA] is lower than in |H⁺|[B,Si-*BEA] after deboronation.

In conclusion, through the deboronation leaching, a considerable amount of framework and extra-framework trigonal boron sites are extracted in the proton form, as revealed by ¹¹B MAS NMR spectra. The extraction of boron also depends on the deboronation time. Under the long period such as 48 hour, boron was completely extracted out of the framework.

8.2 Post-Synthesis Exchange with Aluminum

The beta borosilicates after deboronation in water were used as materials for aluminum incorporation. Due to the solubility of aluminum salts in different solvents, water and ethanol were used for these post-synthetic treatments.

8.2.1 Post-Synthesis Exchange in Aqueous Media

8.2.1.1 XRD Powder Patterns

The stability of the *BEA structure has been evaluated by comparing XRD powder patterns of the treated materials with that of the parent *BEA borosilicate. Figure 8.7 summarizes the XRD powder patterns of these materials. Similar XRD powder data have been obtained on the whole series of aluminum modified solids. This means that the *BEA structure is stable during the post-synthetic treatment by aluminum in water.

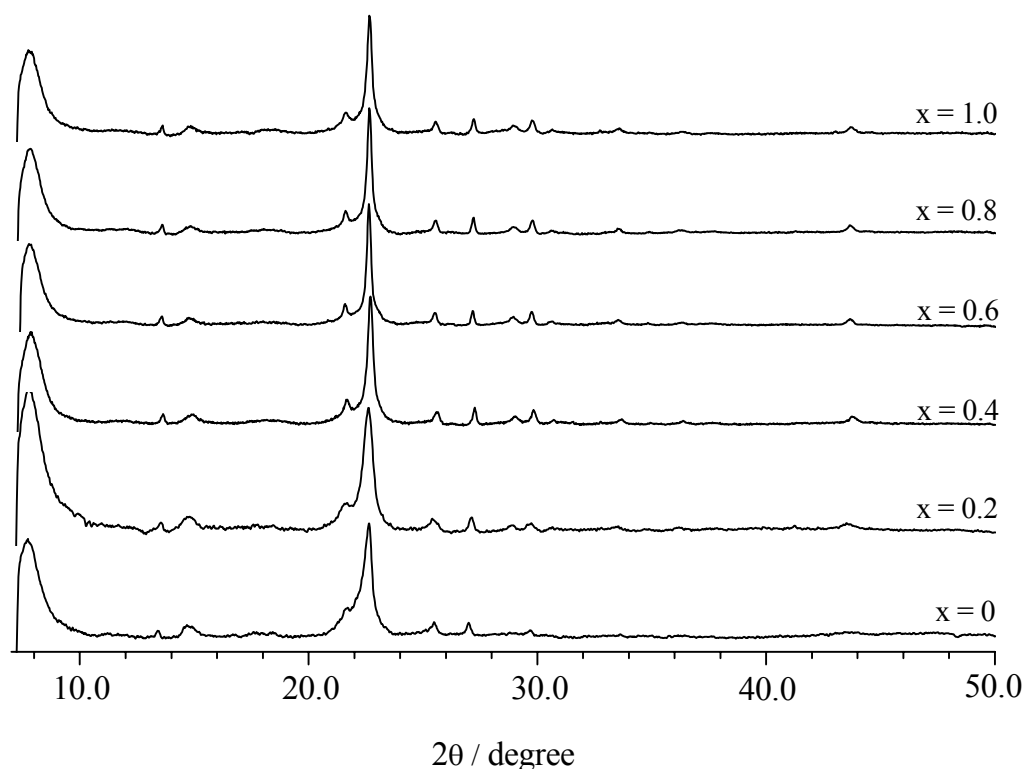


Figure 8.7: XRD powder patterns of $[Na^+_x H^+_{1-x}][Al,B,Si-^*BEA]$ treated with aluminum nitrate in water at $pH \sim 10$

8.2.1.2 MAS NMR Spectroscopy

The local structure of beta zeolite after post-synthetic incorporation of aluminum is studied by MAS NMR spectroscopy. The ^{11}B MAS NMR spectra merely show the sharp line at -3.5 ppm which is ascribed to tetrahedral boron (Figure 8.8). The relative area in the quantitative ^{11}B NMR spectra increases when sample had been ion-exchanged with more sodium cations.

Fig 8.9 shows the ^{23}Na MAS NMR spectra and the relative area of samples after treatment in water. All spectra confirm an appearance of sodium components with broad signals at -7 ppm.

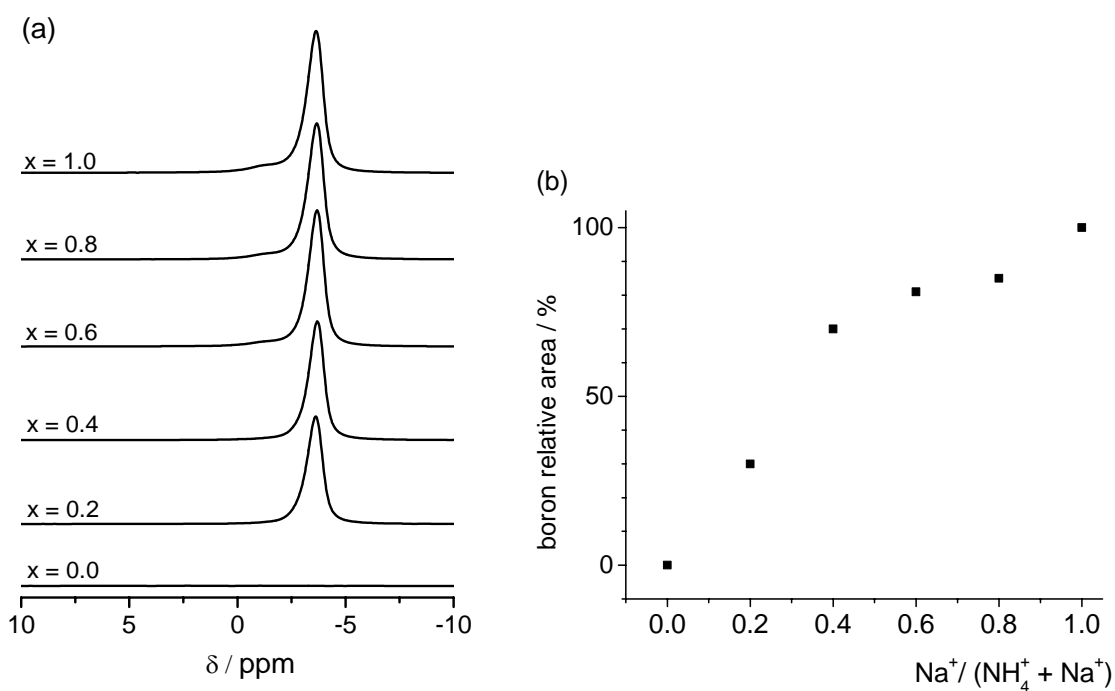


Figure 8.8: (a) ^{11}B MAS NMR spectra at $B_0 = 11.7$ T of $[\text{Na}^+_x\text{H}^{1-x}][\text{Al,B,Si-*BEA}]$ treated with aluminum nitrate in water at $\text{pH} \sim 10$, (b) relative areas

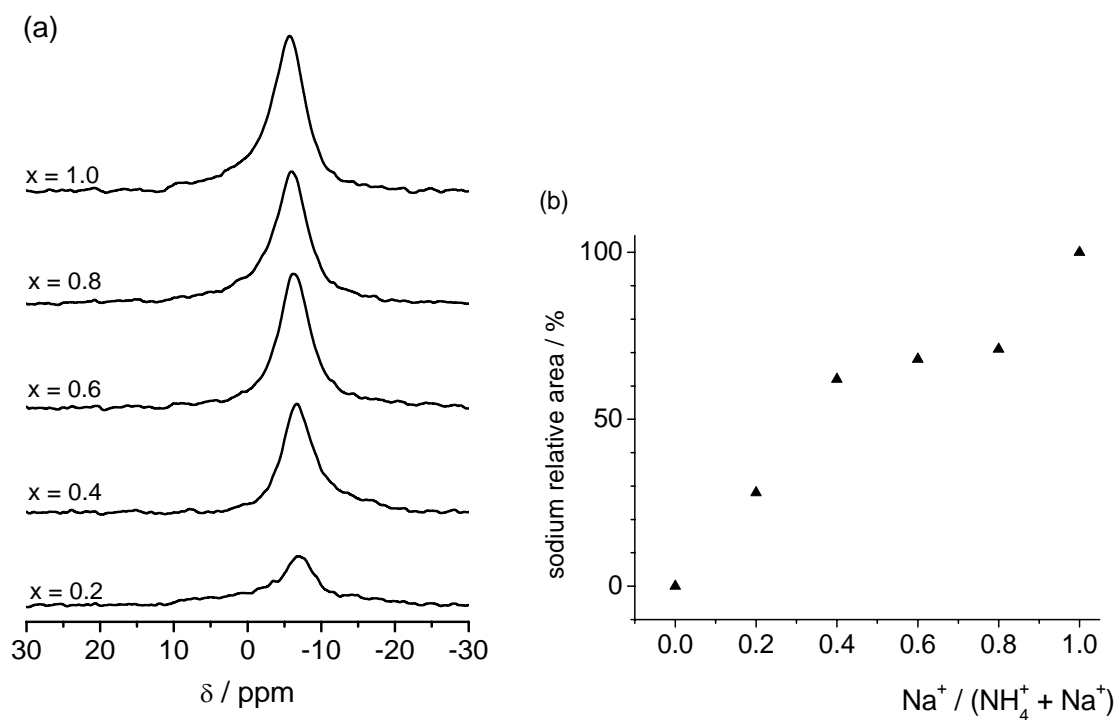


Figure 8.9: ^{23}Na MAS NMR spectra at $B_0 = 11.7$ T of $[\text{Na}^+_x\text{H}^{1-x}][\text{Al,B,Si-*BEA}]$ treated with aluminum nitrate in water at $\text{pH} \sim 10$, (b) relative areas

The ^{27}Al MAS NMR spectra of these materials exhibit an asymmetric resonance at around 56 ppm (Figure 8.10). This indicates that all aluminum atoms in these samples are located in tetrahedral framework sites. As previously suggested by Bokhoven et al., slightly broader signals at about 53 ppm are more observed, when samples are more ion-exchanged with sodium cations. The relative area of the ^{27}Al signals decreases with increasing sodium content in the samples (Figure 8.10b).

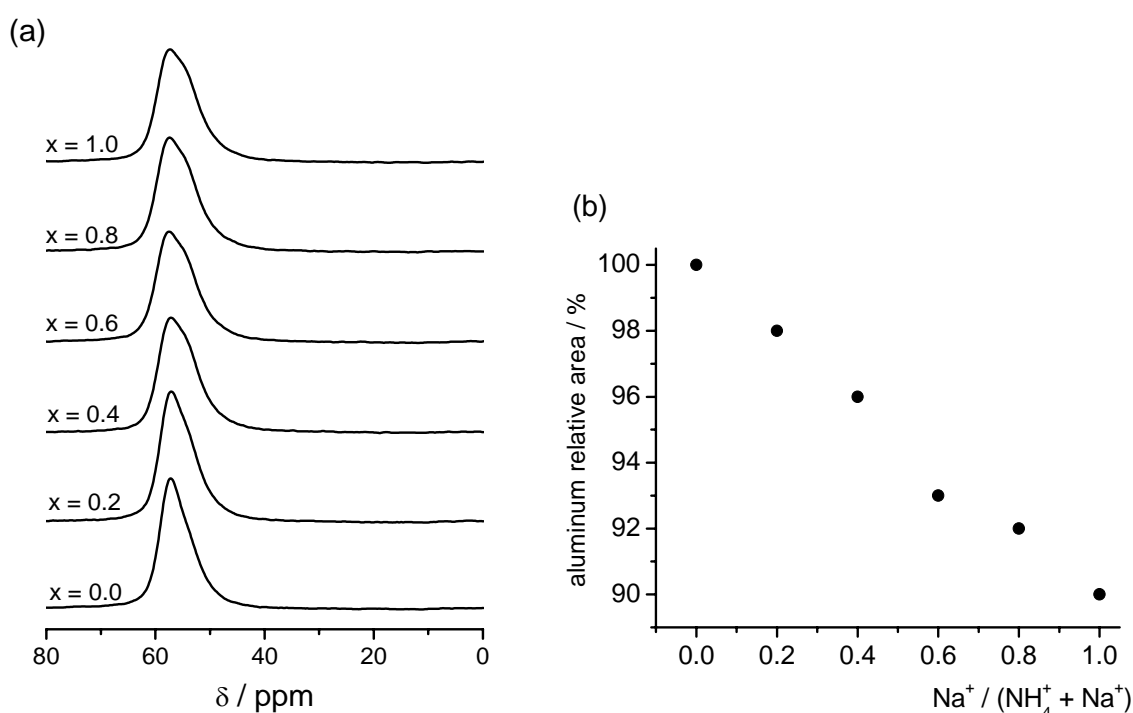


Figure 8.10: (a) ^{27}Al MAS NMR spectra at $B_0 = 11.7\text{ T}$ of $|\text{Na}^+_x, \text{H}^+_{1-x}|[\text{Al}, \text{B}, \text{Si}-*\text{BEA}]$ treated with aluminum nitrate in water at $\text{pH} \sim 10$, (b) relative areas

8.2.2 Post-Synthesis Exchange in Ethanol Solvent

8.2.2.1 XRD Powder Patterns

Figure 8.11 summarizes the XRD patterns of aluminum modified powders obtained after the post-synthetic treatment with aluminum nitrate in ethanol solvent. There are no reflections other than those corresponding to *BEA structure and the intensities of the main signals are almost the same in comparison with the parent beta borosilicate. The structure of beta zeolite is stable throughout the aluminum post-synthetic treatments using ethanol as a solvent.

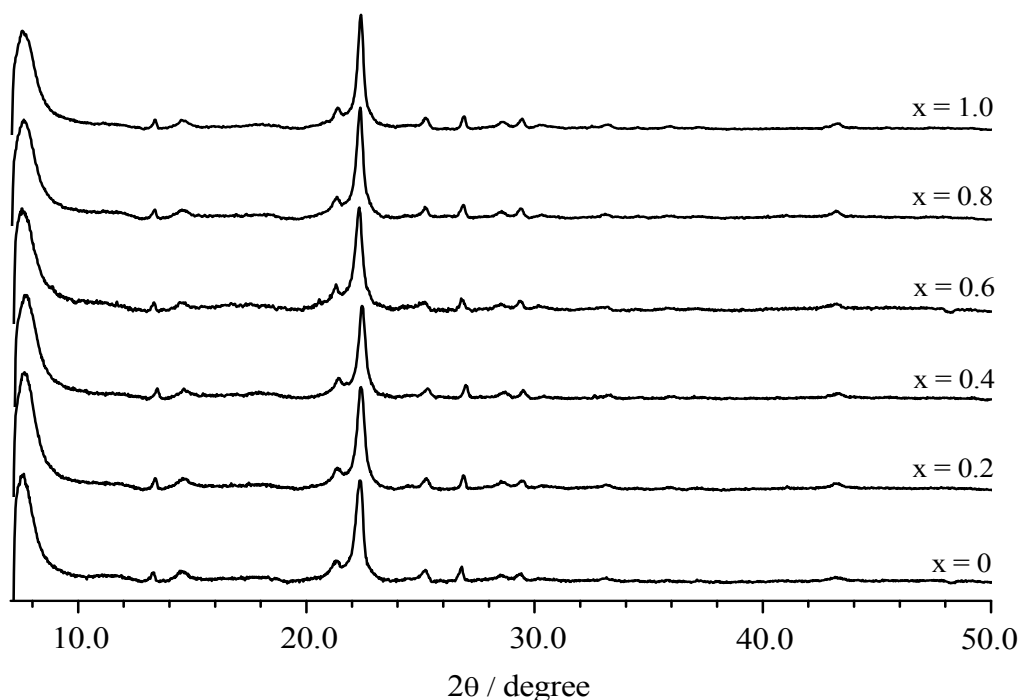


Figure 8.11: XRD powder patterns of $[Na^+_x, H^+_{1-x}][Al, B, Si-*BEA]$ treated with aluminum nitrate in ethanol solvent

8.2.2.2 MAS NMR Spectroscopy

The ^{11}B MAS NMR spectra of the samples treated with aluminum nitrate in ethanol solvent are shown in Figure 8.12. Unlike the water series as presented in last section, these spectra show the narrow resonance at -3.5 ppm and the broad lines in the range between 0 and 19 ppm. This indicates the presence of not only the tetrahedral boron but also of the trigonal boron. As spectrum simulation, the trigonal boron resonances have similar quadrupole coupling constants of 2.3 ± 0.1 MHz, and $\eta = 1.5$ but different chemical shifts at 10.1 ± 0.2 ppm, 14.9 ± 0.1 ppm and at 18.9 ppm. As shown in Chapter 7, these resonances are assigned to trigonal boron coordinations in the framework (10.1 and 14.9 ppm) and extra-framework (18.9 ppm). The total boron relative area increases with increasing sodium content in the samples (Figure 8.12b).

The ^{23}Na MAS NMR spectra present the broad resonance centered at about -5 ppm (Figure 8.13). Figure 8.13b shows a small change of the relative areas of sodium spectra in comparison with the samples after deboronation.

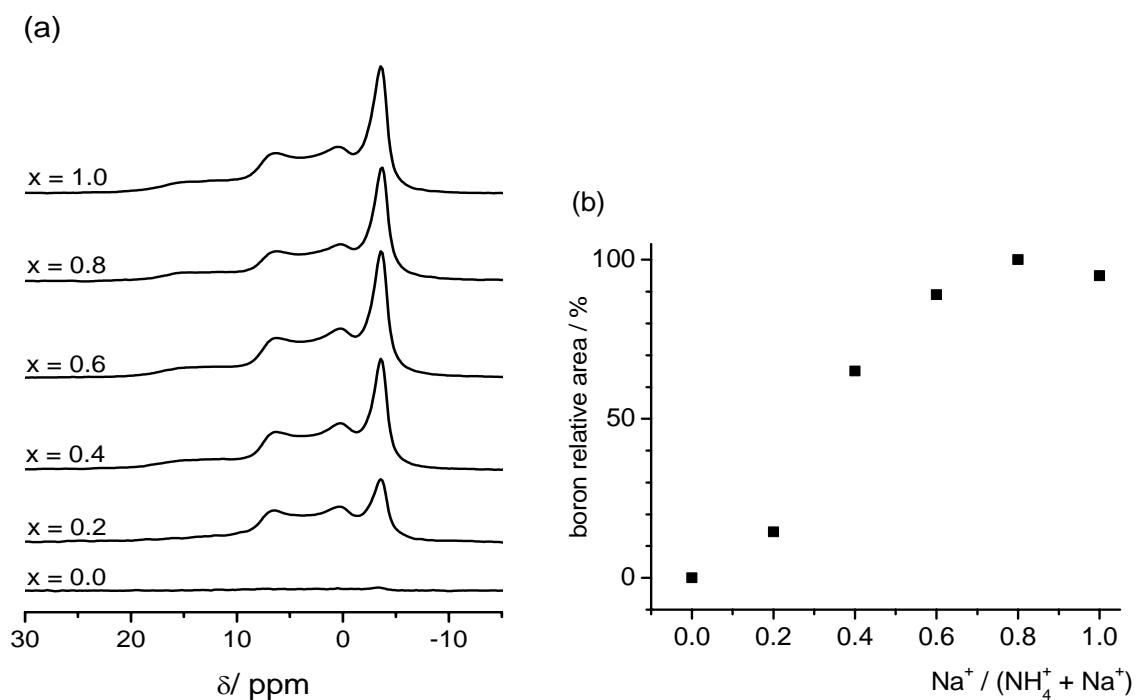


Figure 8.12: (a) ^{11}B MAS NMR spectra at $B_0 = 11.7\text{ T}$ of $[\text{Na}^+_x\text{H}^{1-x}][\text{Al}, \text{B}, \text{Si}-*\text{BEA}]$ treated with aluminum nitrate in ethanol, (b) relative areas

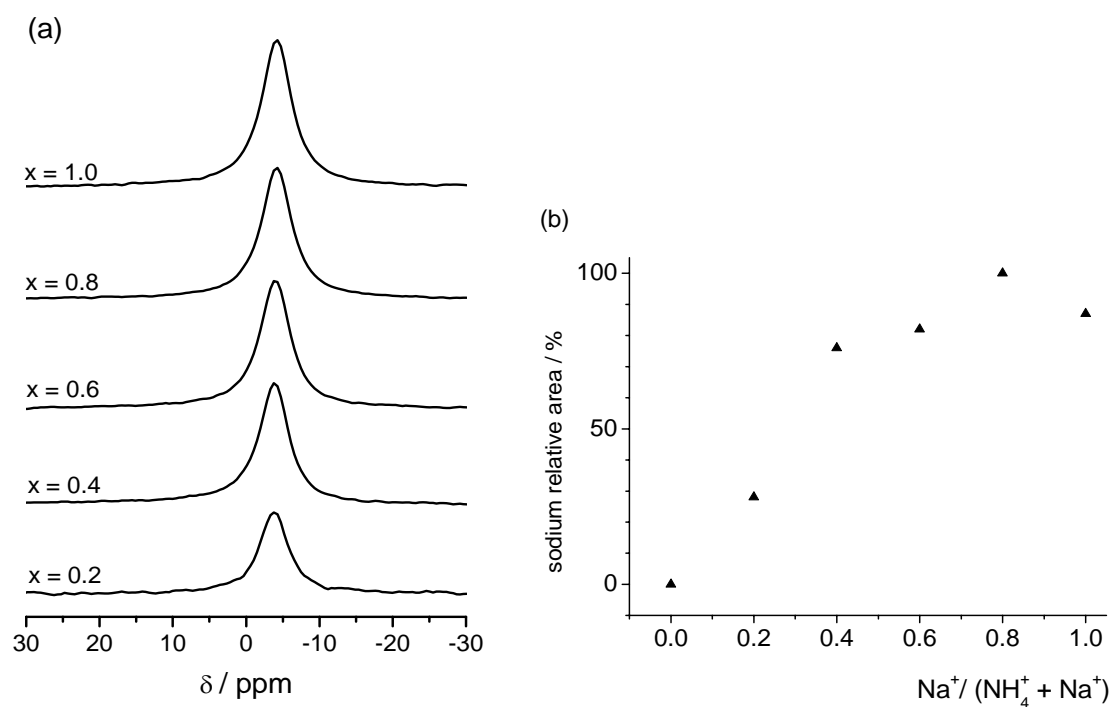


Figure 8.13: ^{23}Na MAS NMR spectra at $B_0 = 11.7\text{ T}$ of $[\text{Na}^+_x\text{H}^{1-x}][\text{Al}, \text{B}, \text{Si}-*\text{BEA}]$ treated with aluminum nitrate in ethanol, (b) relative areas

The local structure of aluminum in these materials is investigated by ^{27}Al MAS NMR spectra in Figure 8.14. The tetrahedral framework aluminum position yielding a resonance at 56 ppm is clearly observed in these spectra. In addition, a small resonance at 0 ppm, which is assigned to octahedral extra-framework aluminum, appears in all spectra. The change of tetrahedral aluminum intensities in comparison with this component in the proton form displays a similar trend as observed in the water series. However, this range is much larger than the post-synthesis in water. This value varies in the range of 35-100 % and decreases when the samples are ion-exchanged with more sodium cations (Figure 8.14b).

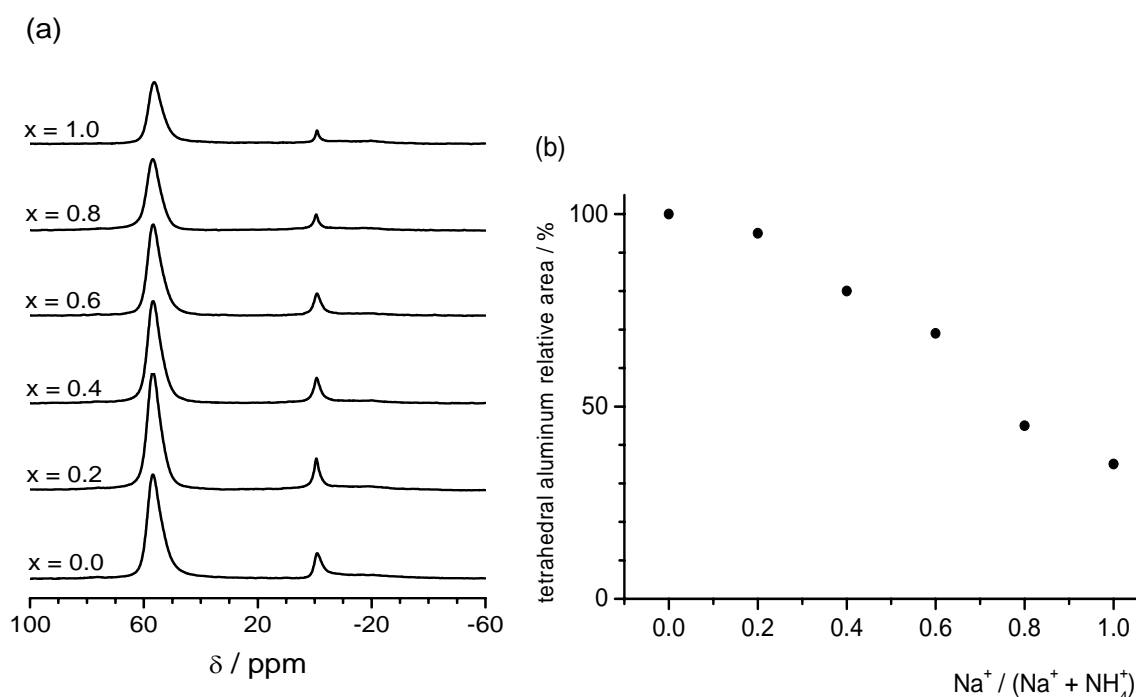


Figure 8.14: (a) ^{27}Al MAS NMR spectra at $B_0 = 11.7$ T of $[\text{Na}^+_x\text{H}^{1-x}][\text{Al},\text{B},\text{Si}-*\text{BEA}]$ treated with aluminum nitrate in ethanol, (b) relative areas

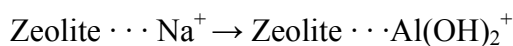
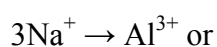
8.2.3 Discussion

After aluminum post-synthetic treatment in water or ethanol solvents, the XRD powder patterns still show the reflections characterizing the beta structure. This indicates that the beta structure is maintained during the post-synthetic treatments.

The local structure and framework modification of these materials is investigated by MAS NMR spectroscopy. The ^{11}B MAS NMR spectra present differences between water

and ethanol series. In the water series, the spectra reveal a symmetric signal due to tetrahedral boron coordinations. The relative line area of ^{11}B in the sodium form after the post-synthetic treatment in water does not change in comparison with the sodium form after deboronation. That means the boron sites which are balanced by sodium cations are stable in water.

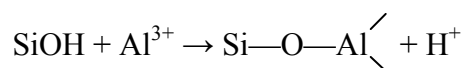
On the contrary, the ethanol series exhibits a combination of trigonal and tetrahedral boron components in spectra. A speculation is a change of extra-framework borosilicates due to the replacement of Na^+ by Al^{3+} :



The aluminum coordinations in the modified beta zeolites were studied by ^{27}Al MAS NMR spectroscopy. All ^{27}Al MAS NMR spectra exhibit the aluminum species in tetrahedral coordination at 57 ppm. This implies that aluminum atoms can be inserted into the framework of beta zeolites through the interaction of Al^{3+} with defect silanol sites, which were created by deboronation. All ^{27}Al MAS NMR spectra show the main asymmetric signal at 57 ppm with a shoulder at around 54 ppm. If the tetrahedral signal is asymmetric, it is because the tetrahedral region consists of at least two components. Bokhoven et al. confirmed an appearance of two components at 57-59 ppm and 53-55 ppm that are well resolved in the isotropic dimension through ^{27}Al MQMAS NMR.¹⁷⁵ Both resonances are due to tetrahedral aluminum incorporation into the framework with low quadrupole coupling constant.¹⁷⁶ These signals are distinguished by aluminum occupying different crystallographic positions in the beta framework, according to Bokhoven. Based on the isotropic chemical shifts, which are related to the Al—O—Si angles, the resonance at lower chemical shift has been assigned to aluminum site at higher average T—O—T angle, whereas the higher chemical shift has attributed to the site at lower T—O—T angles.¹⁷⁷ The resonance at higher chemical shift at about 57 ppm is more populated than another tetrahedral aluminum site at lower chemical shift.

Besides the tetrahedral aluminum sites displayed in all spectra, the ethanol series show a small resonance at 0 ppm corresponding to octahedral aluminum. This resonance is associated to extra-framework aluminum species.

Interestingly, the framework aluminum content increases with decreasing sodium content in both exchange series in water and ethanol. In other words, the quantity of aluminum incorporated in the framework increases, when the sample is more deboronated. As shown in the last section, the deboronation process produces silanol defect sites. During the post-synthetic treatment with Al^{3+} , the hydroxyls in silanol groups easily react with aluminum precursor, creating Si—O—Al bridges:



In summary, aluminum beta zeolites can be prepared from beta borosilicates via the post-synthetic treatments with aluminum nitrate in water or ethanol solvents. As previously shown by Krijnen et al.¹⁷⁸, by means of interaction between silanol defect sites and T precursors (T is element such as Ti, Al...), T can be incorporated into framework. In this work, the exchange of Al for B was carried out by varying the Na^+/H^+ counter ion ratio in beta borosilicates. In addition, the ethanolic solutions allow a higher amount of Al incorporation.

8.3 Post-Synthesis Exchange with Gallium

Gallium modified zeolites has received a great deal of attention due to their importance in catalysis in chemical industry. Catalysis over gallium based zeolites focuses on alkylation, isomerization and disproportionation of aromatics.^{179, 180} Recently, gallium zeolites have known as a high activity catalytic in the reduction of NO_x from engine exhaust gas streams in the presence of excess air.¹⁸¹ Gallium zeolites can be partially achieved by the direct-synthesis via hydrothermal¹⁸² or dry-gel synthesis.¹⁸³ On the other hand, the gallium zeolites can be obtained by post-synthetic treatment. Some post-synthetic methods were applied to prepare the gallium zeolites, such as the Chemical Vapor Deposition (CVD) technique^{184, 185} or impregnation of the aluminum zeolites in $\text{Ga}(\text{NO}_3)_3$ in aqueous solution at low pH.¹⁸⁶ In this section, the post-synthetic treatment in ethanol solvent under mild conditions was performed to obtain gallium beta zeolites from deboronated beta borosilicates deboronated. Details of experimental procedures were presented in Section 5.3. The characteristics of gallium-boron materials are studied by X-Ray diffraction and MAS NMR spectroscopy.

8.3.1 XRD Powder Patterns

The XRD powder patterns of the materials after gallium post-synthetic treatment in ethanol are given in Figure 8.15. All gallium materials present the main reflections at $2\theta = 7.5^\circ$ and 22.4° as similar to the parent sample. In addition, the relative intensities of main reflections are similar in all gallium zeolite patterns and also with the parent beta borosilicate.

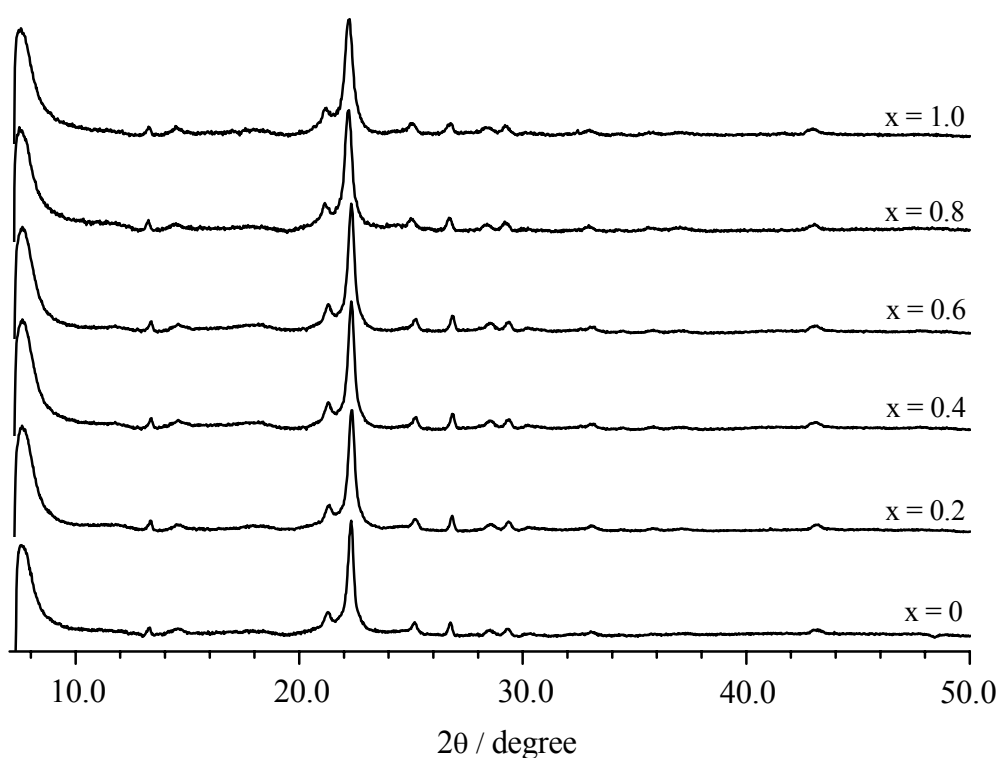


Figure 8.15: XRD powder patterns of $[Na^+_x, H^{+}_{1-x}][Ga, B, Si-*BEA]$ treated with gallium nitrate in ethanol

8.3.2 MAS NMR Spectroscopy

Figure 8.16 shows the ^{11}B MAS NMR spectra of $[Na^+_x, H^{+}_{1-x}][Ga, B, Si-*BEA]$ after treatment with gallium nitrate in ethanol. The sharp line at -4.5 ppm indicates to tetrahedral framework boron in all spectra except for the pure proton sample (Figure 8.16a). Similar to the trend in the aluminum post-synthesis, the quantitative ^{11}B NMR spectra show boron content is following the sodium content (Figure 8.16b).

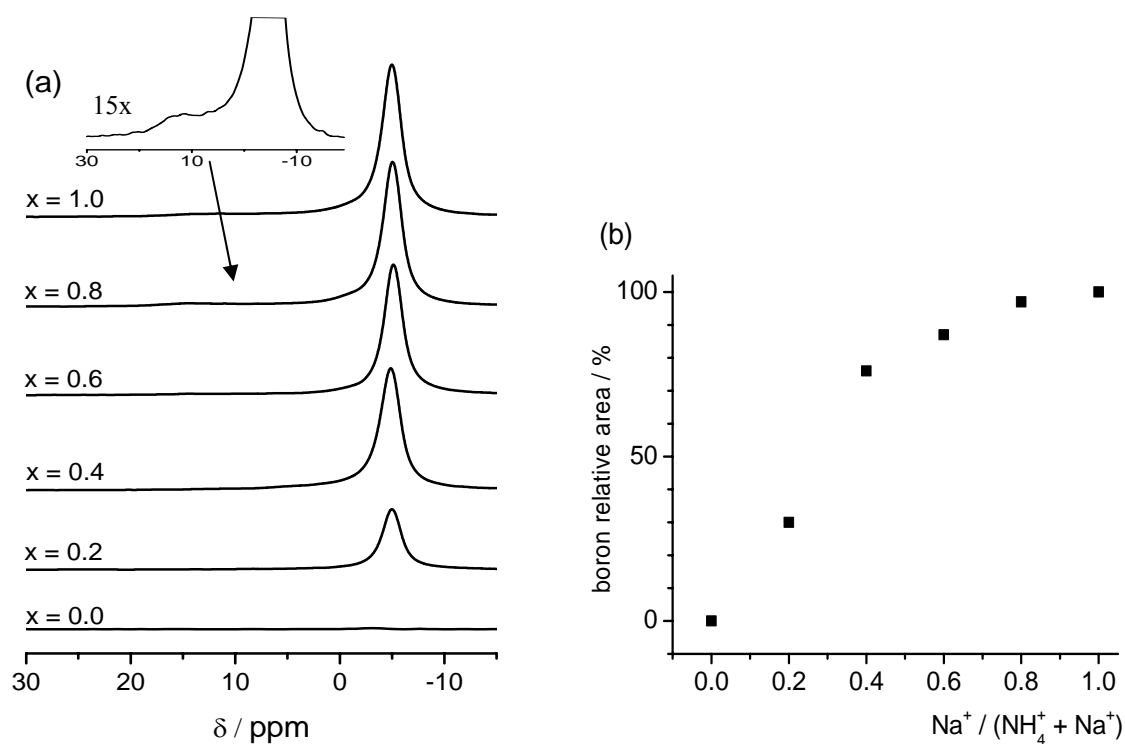


Figure 8.16: (a) ^{11}B MAS NMR spectra at $B_0 = 11.7$ T of $[\text{Na}^+_x\text{H}^{1-x}][\text{Ga},\text{B},\text{Si}-*\text{BEA}]$ treated with gallium nitrate in ethanol, (b) relative areas

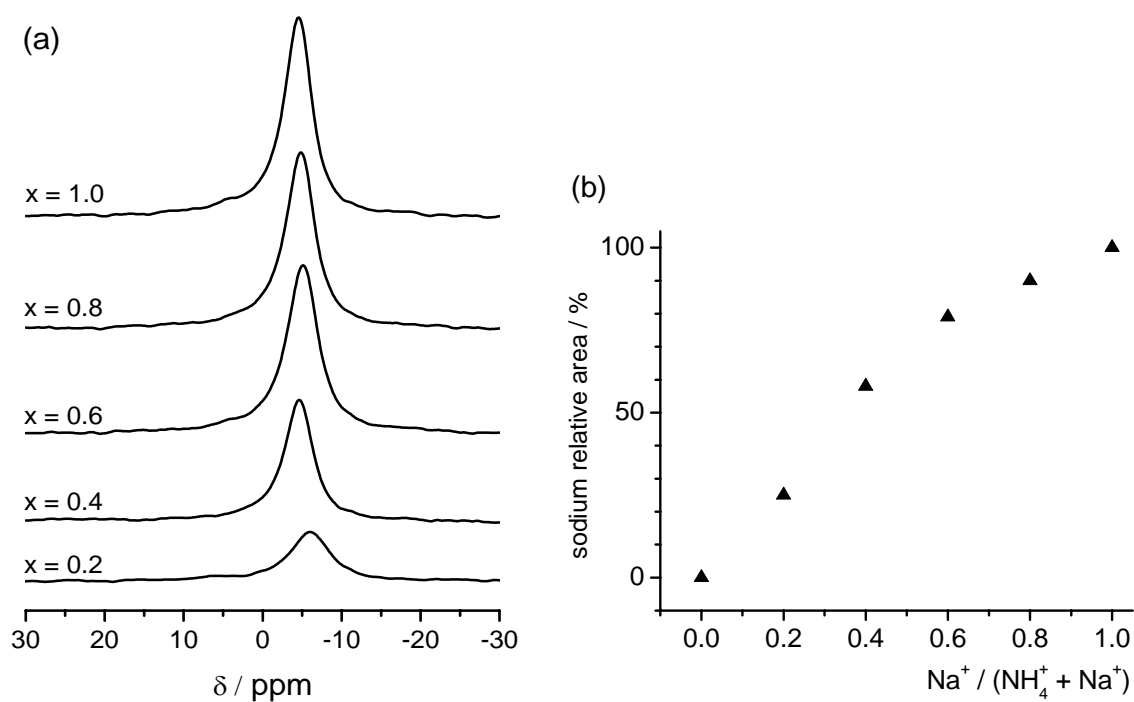


Figure 8.17: (a) ^{23}Na MAS NMR spectra at $B_0 = 11.7$ T of $[\text{Na}^+_x\text{H}^{1-x}][\text{Ga},\text{B},\text{Si}-*\text{BEA}]$ treated with gallium nitrate in ethanol, (b) relative areas

Similar to the aluminum post-synthetic series, sodium components are still viable in gallium zeolites after the post-synthetic treatment. Figure 8.17 illustrates the ^{23}Na MAS NMR spectra with the resonance centered at -5 ppm.

The local environment of gallium species in the gallium zeolites is investigated by ^{71}Ga MAS NMR spectroscopy. Figure 8.18 shows the ^{71}Ga MAS NMR spectra of the gallium zeolites. The broad line in the range -50 ppm to 300 ppm is always observed in all spectra. With the large distribution in the range of chemical shift, this broad line could consist of several components referred to different coordinated gallium species, such as tetrahedral gallium in the framework or octahedral non-framework gallium.^{187, 188}

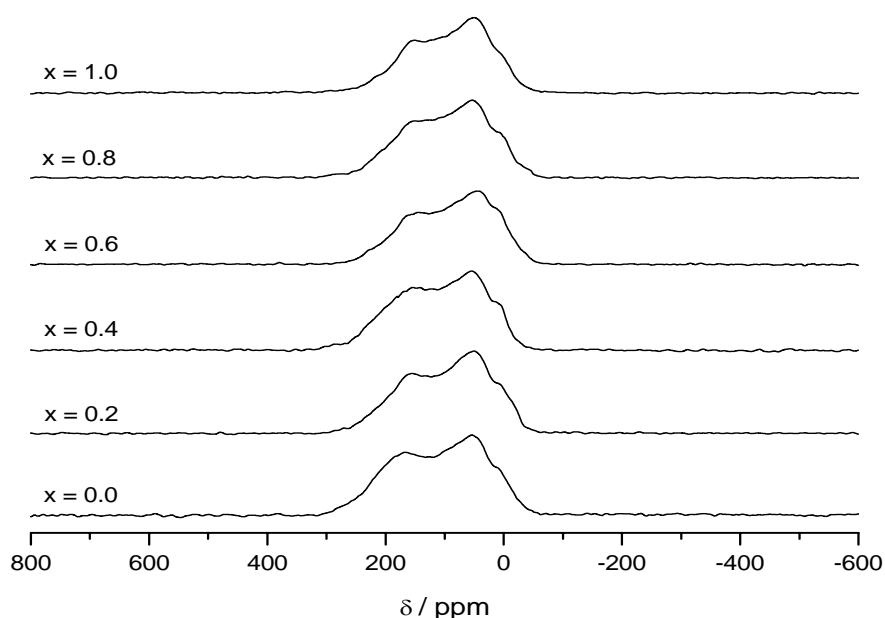


Figure 8.18: ^{71}Ga MAS NMR spectra at $B_0 = 11.7\text{ T}$ of $[\text{Na}^+_x\text{H}^{1-x}][\text{Ga,B,Si-*BEA}]$ treated with gallium nitrate in ethanol with $x = 0.0; 0.2; 0.4; 0.6; 0.8; 1.0$

8.3.3 Discussion

The XRD powder pattern of gallium materials presents a pure beta zeolite structure without other phases. This confirms that the beta structure is essentially retained in comparison with the parent *BEA borosilicate.

Unlike the aluminum post-synthesis in ethanol, the ^{11}B MAS NMR spectra of gallium beta zeolites show the major resonance corresponding to tetrahedral boron only. In fact, a broad line corresponding to trigonal boron is only observed with very low intensity and can be ignored in these spectra. Similar to aluminum post-synthesis in ethanol, the speculation is the change of extra-framework due to the replacement Na^+ by Ga^{3+} : $3\text{Na}^+ \rightarrow \text{Al}^{3+}$ but with smaller amount in comparison with aluminum exchange. The ^{23}Na NMR relative areas also show less change in comparison with with the deboronated samples.

^{71}Ga MAS NMR spectra imply the appearance of gallium species in the framework and in extra-framework positions. The broad lines could indicate an overlap of several resonances due to the different gallium sites. These components have been characterized as tetrahedral and octahedral gallium species.¹⁸⁹ Although the resonance at 160 ppm assigned to tetrahedral gallium coordination is not clearly separated in the spectra, its appearance shows that part of the gallium was incorporated into the framework. The other component at 0-15 ppm is assigned to octahedral non-framework gallium species.¹⁹⁰

In conclusion, beta zeolites with gallium in the framework can be prepared from deboronated borosilicates via the post-synthetic gallation under mild conditions with gallium nitrate in an ethanol exchange solution. Due to the reaction between hydroxyls of defect silanol groups with gallium ions, gallium can be incorporated into the borosilicate frameworks. Although gallium incorporation has been shown to be more difficult than aluminum,¹⁹¹ gallium was partially incorporated into the framework of beta borosilicates.

Chapter

9

Dissolution of Zeolite Nanoparticles in Organic Solvents

Zeolite nanoparticles have received a great deal of attention due to their special applications in industry. Most zeolite nanocrystal structures can be formed by direct synthesis such as from clear solution and gel or confined space methods.

This chapter presents a novel method for the forming of the zeolite nanoparticles from microscale zeolite particles by using organic solvents.

9.1 Zeolite Nanoparticles in Organic Solvents

The colloidal zeolite nanoparticles were prepared from larger zeolite particles through the treatment in dimethylformamide (DMF) or dimethylsulfoxide (DMSO). The particle sizes and the shapes of the colloidal suspensions were investigated by DLS, SEM and AFM.

For clarity, the subsequent colloidal batches after the first, second, third and fourth separations are abbreviated as solution 1, 2, 3, and 4, respectively.

9.1.1 Microscale Zeolites

Microscale zeolites were used as parent zeolites for the preparation of zeolite nanoparticles. These microscale zeolites were either commercial samples such as $[\text{Na}^+][\text{Al,Si-MFI}]$, NaY or they were hydrothermally synthesized using standard procedures, for instance MFI-borosilicates, MFI-silicates, *BEA-borosilicates, and Beta zeolites. Figure 9.1 illustrates the SEM micrographs of several parent MFI zeolites. In this figure, the particles have uniform distributions of microscale crystal sizes. $[\text{Na}^+][\text{Al,Si-MFI}]$ shows the particles about 5 μm , $[\text{Si-MFI}]$ presents the uniform particles ranging from 60-70 μm , and $[\text{H}^+][\text{B,Si-MFI}]$ exhibits homogeneous particles around 20 μm .

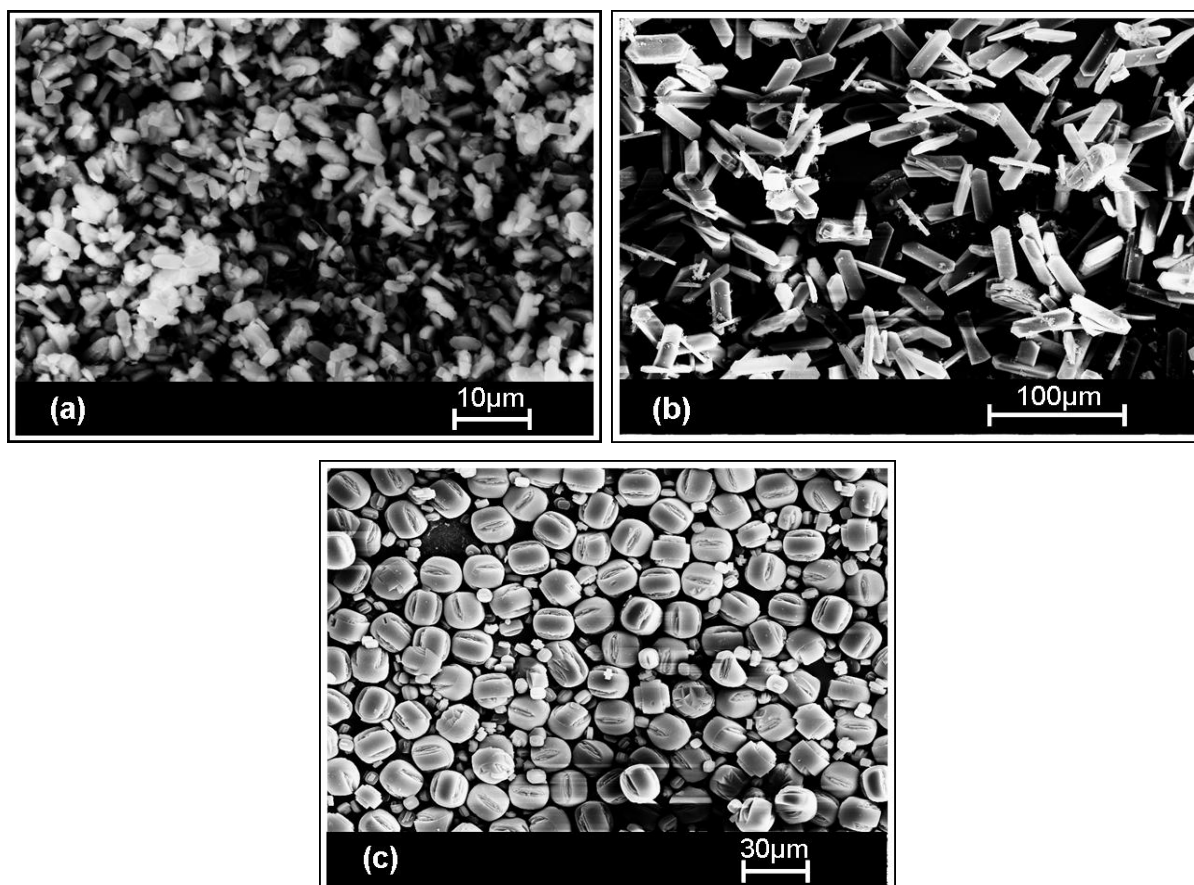


Figure 9.1: SEM micrographs of parent zeolites (a) $[\text{Na}^+][\text{Al,Si-MFI}]$, (b) $[\text{Si-MFI}]$, (c) $[\text{H}^+][\text{B,Si-MFI}]$

9.1.2 Zeolite Nanoparticles in Dimethylformamide (DMF)

The clear zeolite solutions received by centrifugation contain small particles, which do not scatter light to the naked eye. However, the presence of these particles is easily detected with dynamic light scattering techniques. Figure 9.2 demonstrates the particle size distribution curves for the four subsequent solutions of $[\text{Na}^+][\text{Al,Si-MFI}]$ in DMF. The mean particle diameters are rather stable throughout the solutions 1 to 4, and they are centered in the range 190-210 nm. On the other hand, these curves show narrow picks of particle size distributions, which is typical for stable colloidal suspensions.

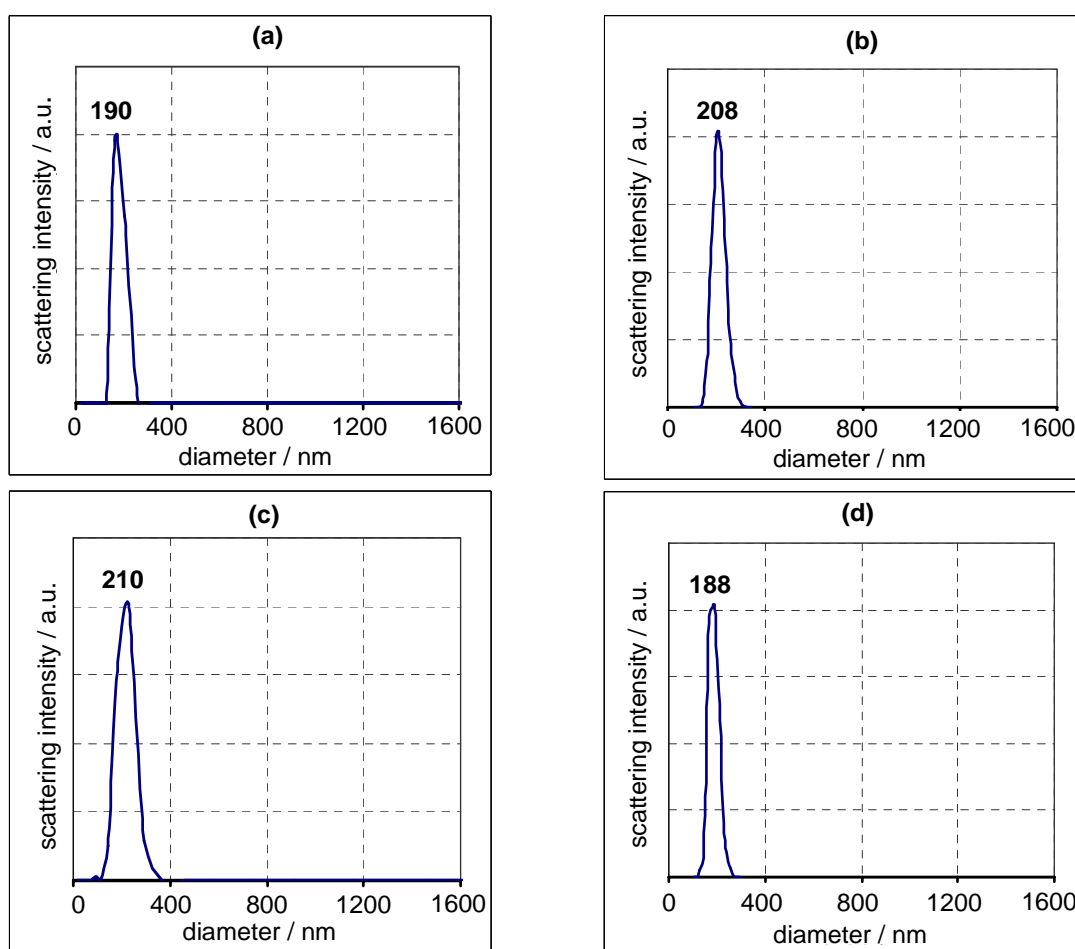


Figure 9.2: DLS data of $[\text{Na}^+][\text{Al,Si-MFI}]$ solutions in DMF (a) solution 1, (b) solution 2, (c) solution 3, (d) solution 4

Similar results are observed for the other MFI zeolite suspensions. The collections of the size distributions and the mean particle sizes of subsequent MFI solutions are summarized in Figure 9.3 and Table 9.1, respectively.

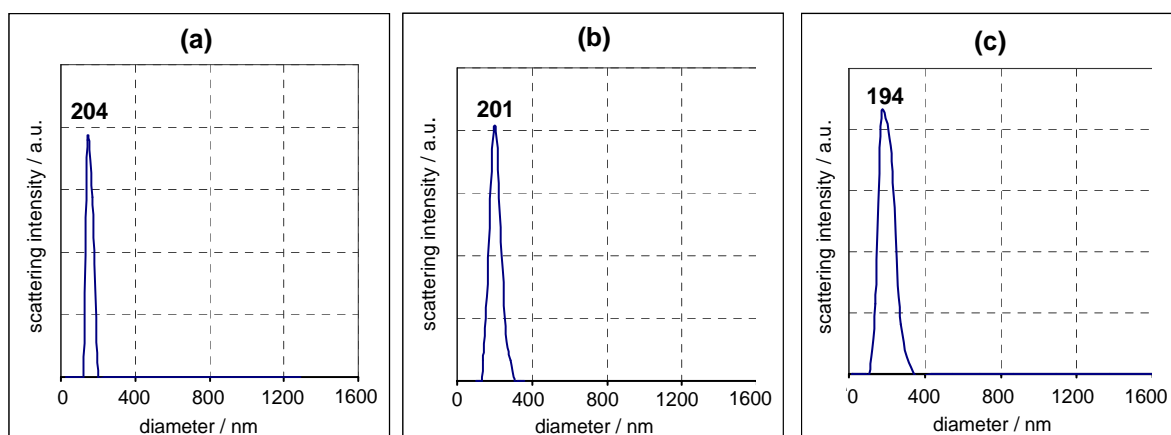


Figure 9.3: DLS data of the first ZSM-5 solutions in DMF (a) $|H^+|[B,Si-MFI]$, (b) $|TPA|[Si-MFI]$, (c) $[Si-MFI]$

Table 9.1: Mean particle sizes, line widths and Poly indexes* of MFI solutions in DMF

	$[Na^+][Al,Si-MFI]$	$ H^+ [B,Si-MFI]$	$ TPA [Si-MFI]$	$[Si-MFI]$
solution 1				
diameter / nm	180	204	201	194
width / nm	75	91	72	100
Poly index	0.05	0.05	0.02	0.09
solution 2				
diameter / nm	208	221	200	217
width / nm	65	48	43	98
Poly index	0.09	0.10	0.09	0.09
solution 3				
diameter / nm	210	175	176	179
width / nm	98	53	53	60
Poly index	0.24	0.12	0.09	0.19
solution 4				
diameter / nm	187	177	178	178
width / nm	53	50	50	65
Poly index	0.03	0.01	0.05	0.07

* Poly index: polydispersity index

Mean particle sizes of four subsequent solutions of MFI-borosilicates, pure silica as-synthesized MFI and also pure silica MFI after calcination are obtained at around 200 nm. Similar to $[\text{Na}^+][\text{Al},\text{Si-MFI}]$ solutions, all the particle size distribution curves show narrow lines implying that stable colloidal suspensions exist. Interestingly, the widths of the size distribution of solution 1 for all MFI samples are slightly larger than the other solutions. These values are observed in the range 75-100 nm. Whereas, the solutions 3 and 4 often show widths of about 50 nm for all MFI solutions except the $[\text{Na}^+][\text{Al},\text{Si-MFI}]$ sample. In agreement with the trend observed for the width of particle size distribution curves, the polydispersity index values, which are dependent on the stability of the colloidal particles, are lower than 0.2 in all DLS measurements except for solution 3 of $[\text{Na}^+][\text{Al},\text{Si-MFI}]$. The low values point out that the colloidal solutions have a mono-modal particle size distribution¹⁹² and stable colloidal suspensions are formed in DMF. The generation of nanoparticles in the subsequent solutions indicates that they are formed from the micro-sized crystals and not a result of impurities on the surface.

Several other zeolites are also treated in DMF. Table 9.2 summarizes the mean particle sizes and the line widths of the first zeolite solutions. These solutions show the mean particle sizes centered at about 200 nm with narrow distributions. That means these colloidal suspensions are also stable in DMF. On the other hand, the mean particle sizes of zeolite proton forms are slightly lower in comparison with corresponding sodium forms. Namely, the mean particle sizes of *BEA-borosilicate and *BEA aluminosilicate proton forms are 174 nm and 201 nm respectively; whereas these values are 205 nm and 218 nm in the sodium forms. The difference of the mean particle sizes in the proton and sodium forms could be explained by the agglomeration of the particles and will be discussed below.

Table 9.2: Mean particle sizes and line widths of the first zeolite solutions in DMF

zeolites	diameter / nm	width / nm
NaY	189	20
$[\text{H}^+][\text{B},\text{Si-MFI}]$	185	50
$[\text{H}^+][\text{B},\text{Si-*BEA}]$	174	55
$[\text{Na}^+][\text{B},\text{Si-*BEA}]$	205	65
$[\text{H}^+][\text{Al},\text{Si-*BEA}]$	201	72
$[\text{Na}^+][\text{Al},\text{Si-*BEA}]$	218	77

Besides the DLS measurements, the SEM technique can assist to study the size and the shape of the particles. Figure 9.4 shows the SEM micrographs of the residue after DMF treatment and the dried clear solution of $[\text{Na}^+][\text{Al,Si-MFI}]$. No change of the size and the shape can be observed in the residue powder. The individual particles with the size of about $5\ \mu\text{m}$ are still viable in the dried residue. However, the dried solution shows a different image. The uniform particles with a size of about $1\ \mu\text{m}$, which is considerable lower than those in the parent sample, can be seen in the SEM image of the dried solution. However, the obtained SEM image still does not correspond to the DLS observations where the main population of crystals is about $200\ \text{nm}$. Clearly, drying of colloidal suspension by evaporation leads to denser packing. In addition, the shapes of these particles are also altered in comparison with the parent sample. In Figure 9.4b, the particles show a more spherical shape, which are really different from the lengthly crystals in the parent sample.

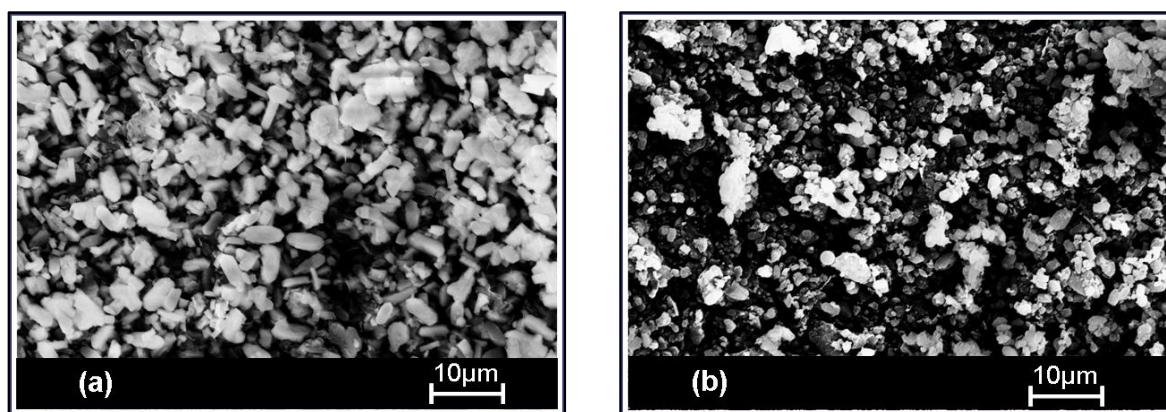


Figure 9.4: SEM micrographs of $[\text{Na}^+][\text{Al,Si-MFI}]$ after DMF treatments (a) dried residue (b) dried solution

Figure 9.5 illustrates the SEM micrographs of the residue and the dried clear solution of $[\text{Si-MFI}]$ after DMF treatment. The residue shows the crystals with particle sizes of $60\text{--}70\ \mu\text{m}$. In addition, some particles with sizes are smaller than those in the parent sample are observed. The uniform particles with a size of about $100\ \text{nm}$ are obtained in the dried solution.

For further study, the AFM technique was used to characterize the particle shape and size of the colloidal suspensions. The nanoparticles are evident, as shown in Figure 9.6 for the $[\text{Si-MFI}]$ solution. In agreement with DLS data, the mean size of the nanoparticles is in the range of $200\text{--}300\ \text{nm}$. The average height of these particles is about $45\ \text{nm}$. In addition,

the AFM image shows a blurred border of the particle that could be a result of aggregation of individual particles forming the larger particles.

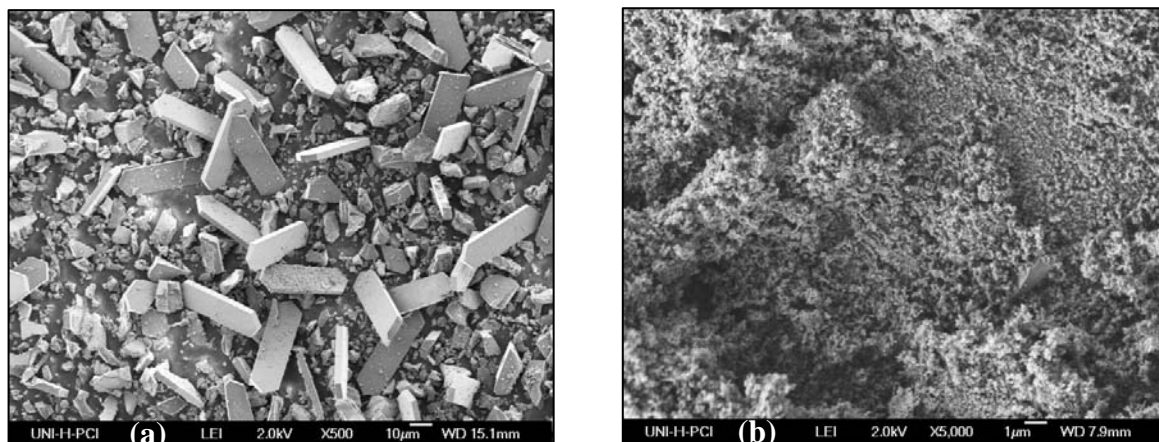


Figure 9.5: SEM micrographs of [Si-MFI] after DMF treatments (a) dried residue (b) dried solution

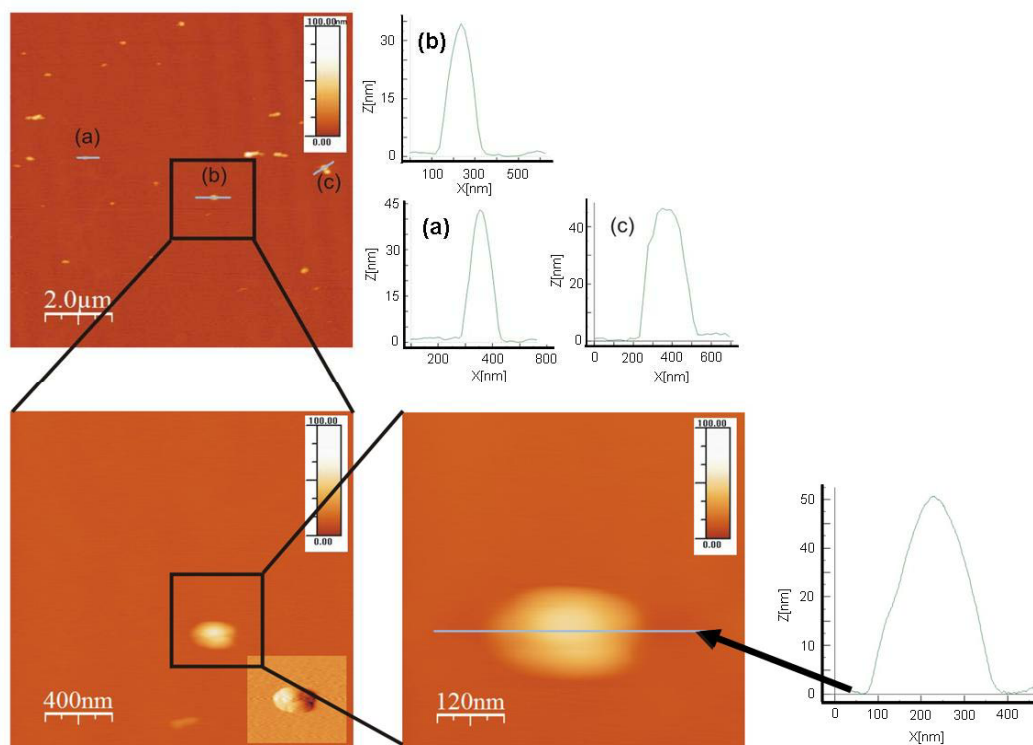


Figure 9.6: AFM micrographs of [Si-MFI] solution in DMF

9.1.3 Nanoparticles in Dimethylsulfoxide (DMSO)

The particle size distribution curves for several MFI zeolites extracted from the first solutions in DMSO solvent are shown in Figure 9.7. The mean particle sizes, the widths and polydispersity indexes of the first and second MFI subsequent solutions in DMSO are collected in Table 9.3. Similar to the zeolite solutions in DMF, nanoparticles can be observed in the colloidal suspensions of DMSO. However, these DLS data show larger mean particle sizes, which are about 400-500 nm. Although the particle size distribution curves present the broader line than those in DMF, the polydispersity index values are still lower than 0.2 except the $[\text{Na}^+][\text{Al,Si-MFI}]$ suspensions. That means most of the zeolite solutions have a mono-modal size distribution in DMSO.

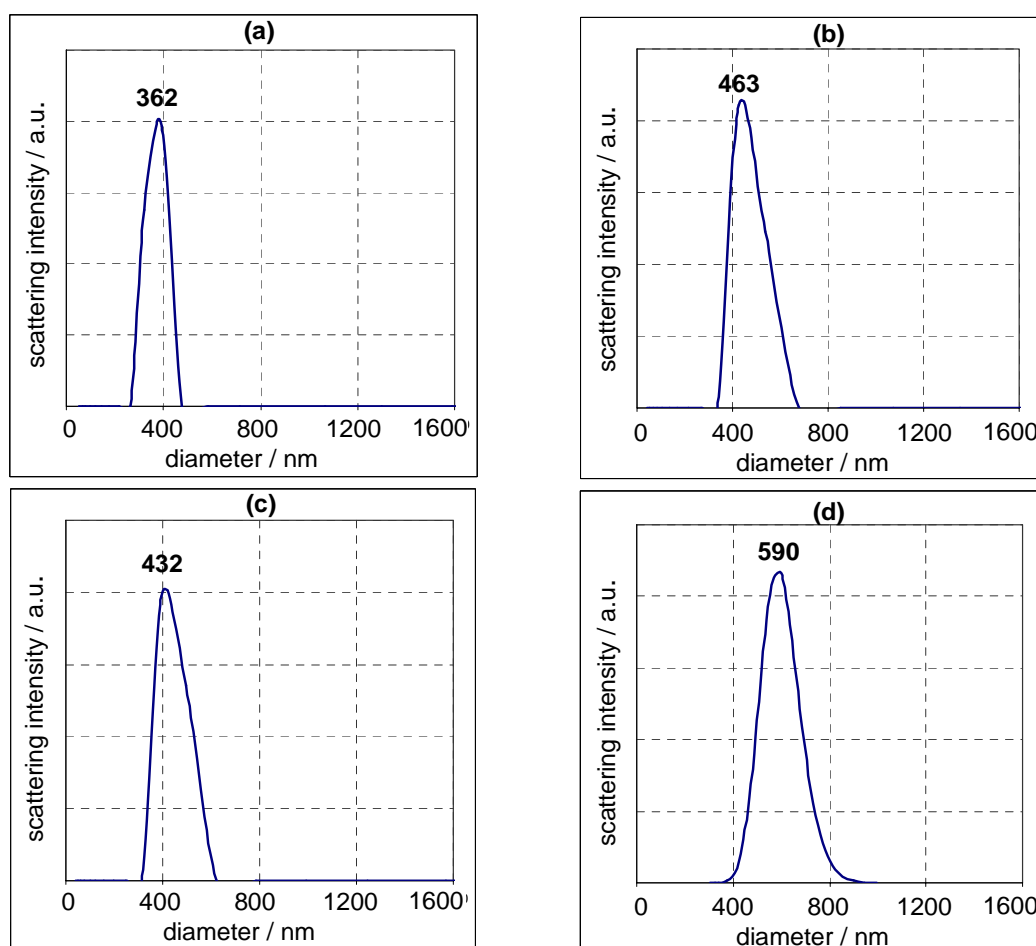


Figure 9.7: DLS data of first ZSM-5 solutions in DMSO (a) $[\text{Na}^+][\text{Al,Si-MFI}]$, (b) $[\text{H}^+][\text{B,Si-MFI}]$, (c) $[\text{TPA}][\text{Si-MFI}]$, (d) $[\text{Si-MFI}]$

Table 9.3: Mean particle sizes, line widths and Poly indexes* of MFI solutions in DMSO

samples	solution 1			solution 2		
	diameter nm	width nm	Poly index	diameter nm	width nm	Poly index
Na ⁺ [Al,Si-MFI]	362	131	0.38	472	139	0.22
H ⁺ [B,Si-MFI]	463	155	0.11	580	93	0.15
TPA [Si-MFI]	432	177	0.11	586	313	0.15
[Si-MFI]	590	192	0.02	660	104	0.08

* Poly index: polydispersity index

9.2 Zeolite Nanoparticle Structure

9.2.1 X-Ray Diffraction

The XRD patterns of solids obtained from the dried solutions of MFI samples treated in DMF are collected in Figure 9.8. The reflections are typical for ZSM-5 crystals, indicating that the ZSM-5 structures are retained in these solutions. In addition, no impurity phases are detected in the solutions dried at room temperature. Thus, the solid structures of nanoparticles obtained after treatment in DMF are maintained in similarity as the parent zeolites.

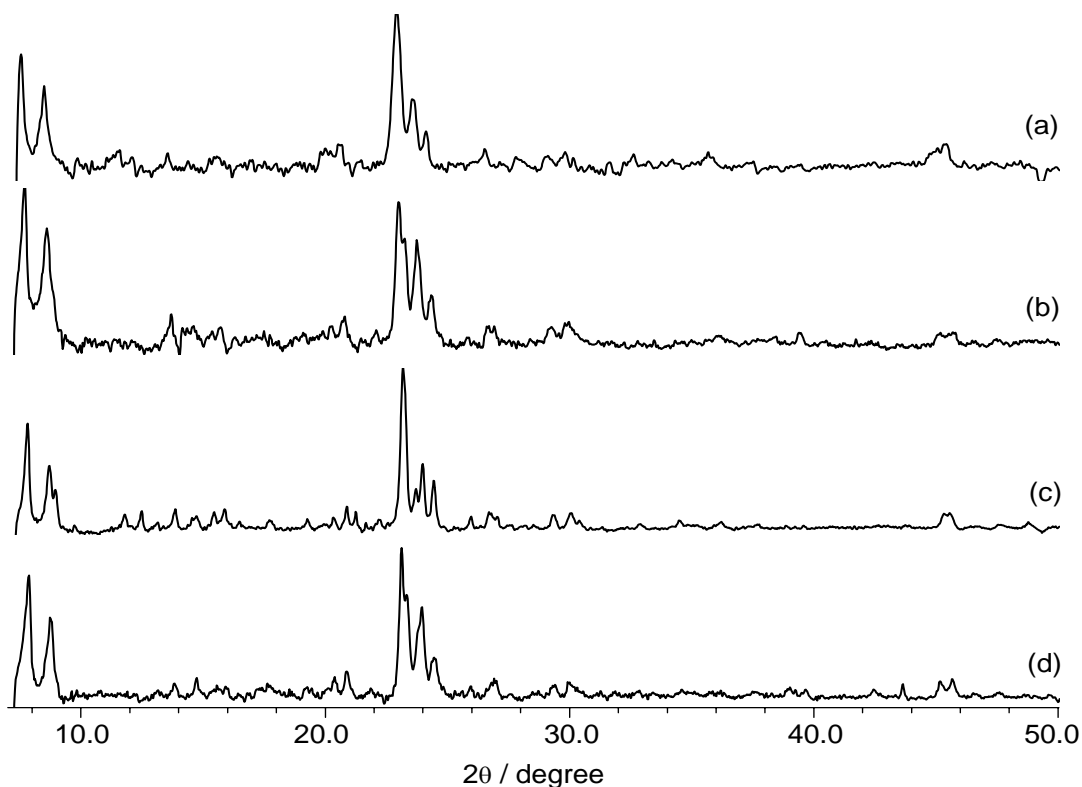


Figure 9.8: XRD powder patterns of dried zeolite solutions after DMF treatments (a) $[\text{Na}^+][\text{Al,Si-MFI}]$, (b) $[\text{H}^+][\text{B,Si-MFI}]$, (c) $[\text{TPA}][\text{Si-MFI}]$, (d) $[\text{Si-MFI}]$

Careful analysis of these patterns indicates that the MFI dried solutions show the orthorhombic MFI structure. However, the orthorhombic phase can transform to the monoclinic phase at high temperatures due to the flexibility of zeolite framework structures upon removal of the pore filling (DMF).¹⁹³ The transitions of these structures are clearly illustrated in Figure 9.9 with the residues of $[\text{Na}^+][\text{Al,Si-MFI}]$. The parent $[\text{Na}^+][\text{Al,Si-MFI}]$ shows the monoclinic structure, whereas the dried residue has orthorhombic structure. During the DMF treatment, the organic molecules can be adsorbed into the MFI pores. At high temperatures of 673 K, the pores which are occupied by the organic molecules become free. Therefore, the calcined residue has monoclinic structure. This behavior is typical for the MFI structure.¹⁹⁴

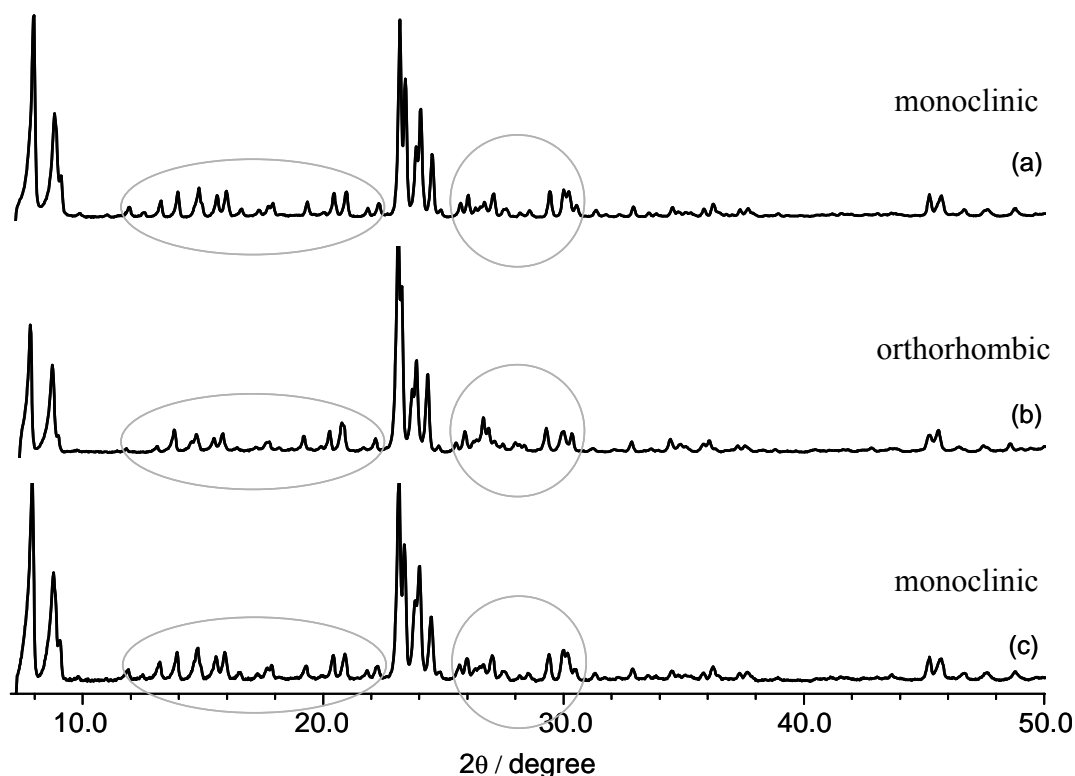


Figure 9.9: XRD powder patterns of $[\text{Na}^+][\text{Al,Si-MFI}]$ (a) parent sample; (b) dried residue at room temperature, (c) calcined residue at 673 K

9.2.2 MAS NMR Spectroscopy

The ^{29}Si MAS NMR spectra of parent $[\text{Na}^+][\text{Al,Si-MFI}]$, dried and calcined residues are shown in Figure 9.10. The parent ZSM-5 sample shows a component at -106 ppm assigned to Si(1Al) (line I) and the main line at about -112 ppm assigned to Si(0Al). This main line (line II) overlaps with a component at -116 ppm (line III) which is also due to Si(0Al). After treatment in DMF, the shoulder at -116 ppm becomes clearer. The spectra simulations indicate that the relative area of line III in dried residue spectrum slightly increases in comparison with the parent sample. Interestingly, when the dried residue is calcined at 673 K, the shoulder disappears and the lineshape is similar with the parent sample.

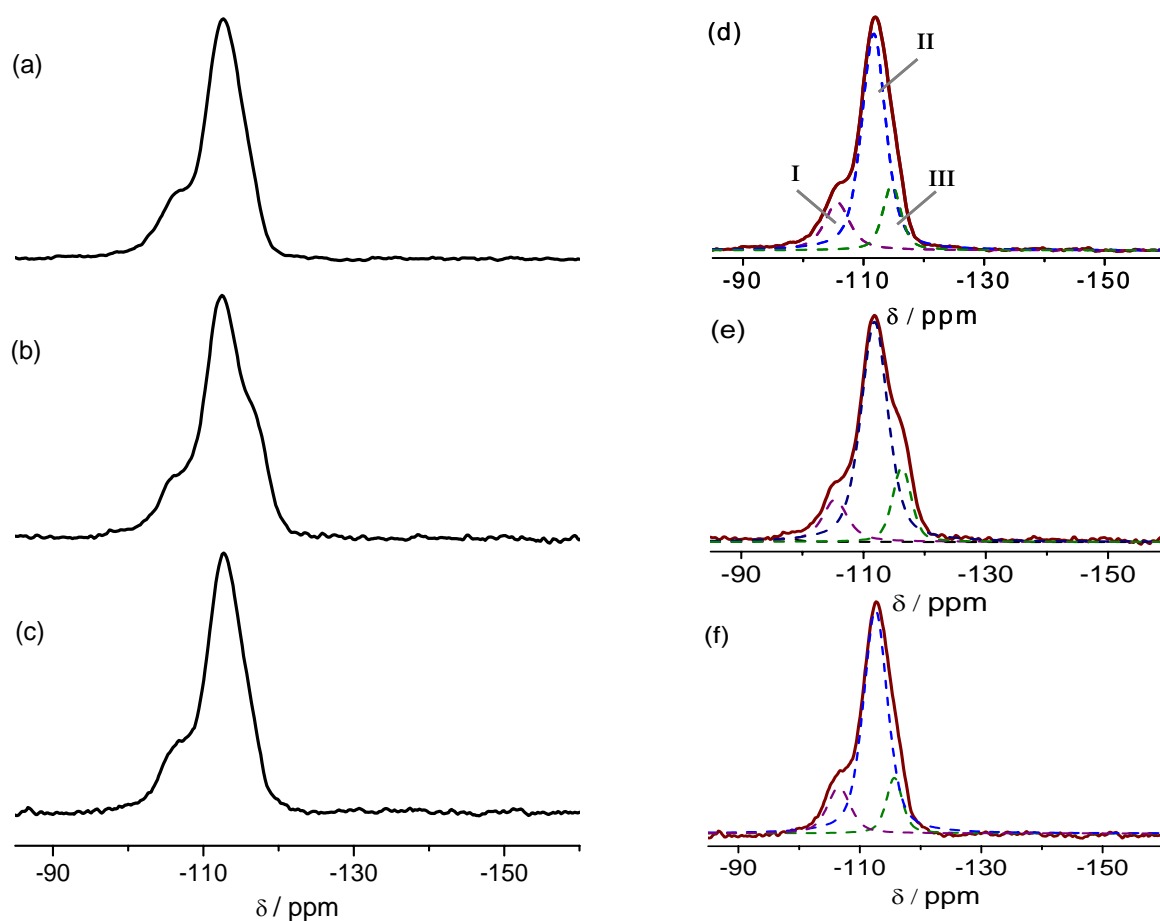


Figure 9.10: ^{29}Si MAS NMR spectra at $B_0 = 7.0\text{ T}$ of $[\text{Na}^+][\text{Al,Si-MFI}]$ (a) parent sample, (b) dried residue at room temperature, (c) calcined residue at 673 K, (d) simulation of parent sample, (e) simulation of dried residue at room temperature, (f) simulation of calcined residue at 673 K

The change in resolution is explained by a different distribution of chemical shifts owing to small differences in the geometry around the distinct Si sites of the framework induced by the guest molecule.¹⁹⁵ As mentioned above in the X-Ray diffraction, the DMF adsorbed into zeolite pores can affect the local framework geometry, i.e. the bond angles and bond lengths of the Si—O—T structural groups. This leads to the change of the ^{29}Si MAS NMR spectra. At high temperature, the DMF molecules are removed out of the framework, leaving the free pores and the Si environment like the parent sample. Therefore the lineshape returns to the parent ZSM-5.

9.2.3 Raman Spectroscopy

The local structure of the zeolite nanoparticles obtained after treatment in DMF is also studied by Raman spectroscopy. Figure 9.11 shows the Raman spectrum of the dried ZSM-5 solution. For convenient comparison, the Raman spectra of parent ZSM-5 and pure DMF solvent are also presented in this figure.

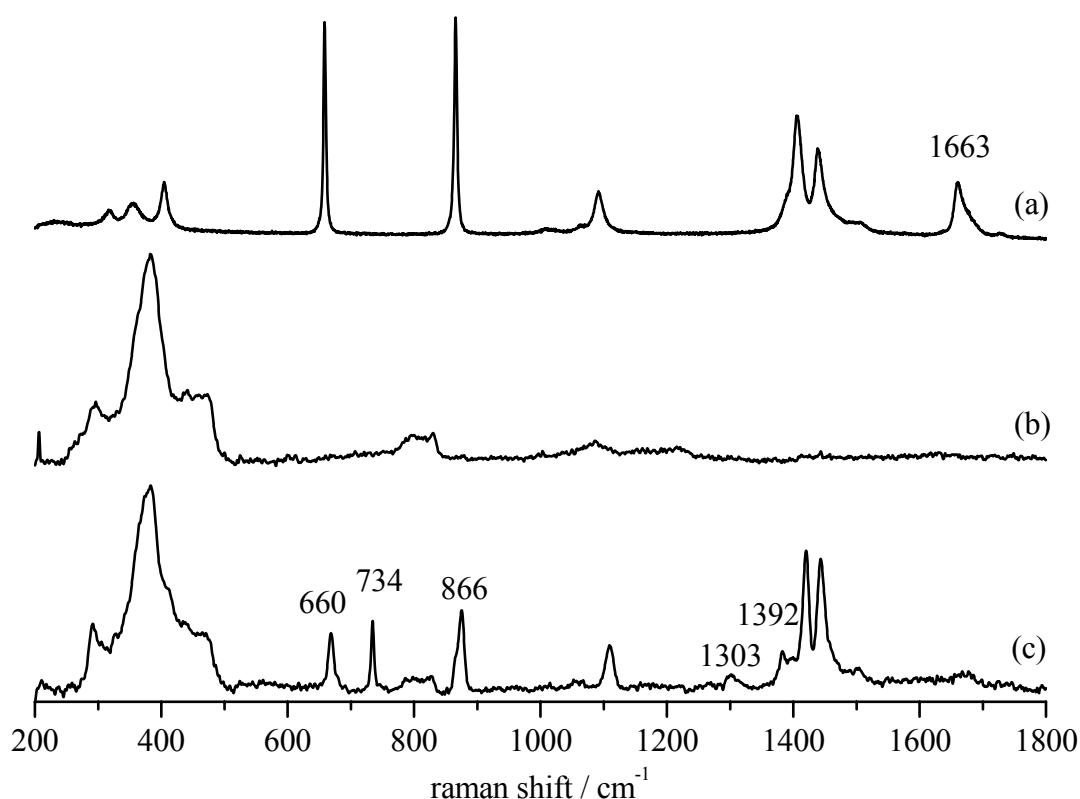


Figure 9.11: Raman spectra of (a) DMF solvent, (b) parent $[\text{Na}^+][\text{Al,Si-MFI}]$, (c) dried solution $[\text{Na}^+][\text{Al,Si-MFI}]$

The dried solution shows the features that are characteristic of the MFI structures. In addition, several vibrations of DMF occluded in the zeolite are also observed in this spectrum. Interestingly, the lines at 660 cm^{-1} assigned to the vibration of $(\text{O}=\text{C}-\text{N})$ and the line at 866 cm^{-1} due to the vibration of $(\text{N}-\text{CH}_3)$ ¹⁹⁶ are visible in the dried solution but significantly lower intensity in comparison with the DMF solvent. Moreover, the line at 1663 cm^{-1} corresponding to the $(\text{C}=\text{O})$ double bond which is clearly observed in DMF, almost disappears in the dried solution, whereas the other lines that are characteristic for

DMF are still visible. In addition, new lines at 1392, 1303 and 734 cm^{-1} appear in this spectrum. The change in the spectrum indicates that an interaction between zeolite surface and DMF molecules occur. This lead the reduction of intensities of vibrations concerning to the (C=O) groups; and the new lines concurrently appear.

9.3 Water and Cation Concentration Effects

The sizes of nanoparticles forming in DMF can be influenced by environment parameters. In this section, the influences of water and cation concentrations to the particle sizes are studied for ZSM-5, pure silica ZSM-5 and beta borosilicates.

9.3.1 Water Effect

To study the effects of water, the experiments were carried out in normal DMF and dried DMF solvents. The dependence of the mean particle sizes on $[\text{Na}^+][\text{Al,Si-MFI}]$ contents is illustrated in Figure 9.12.

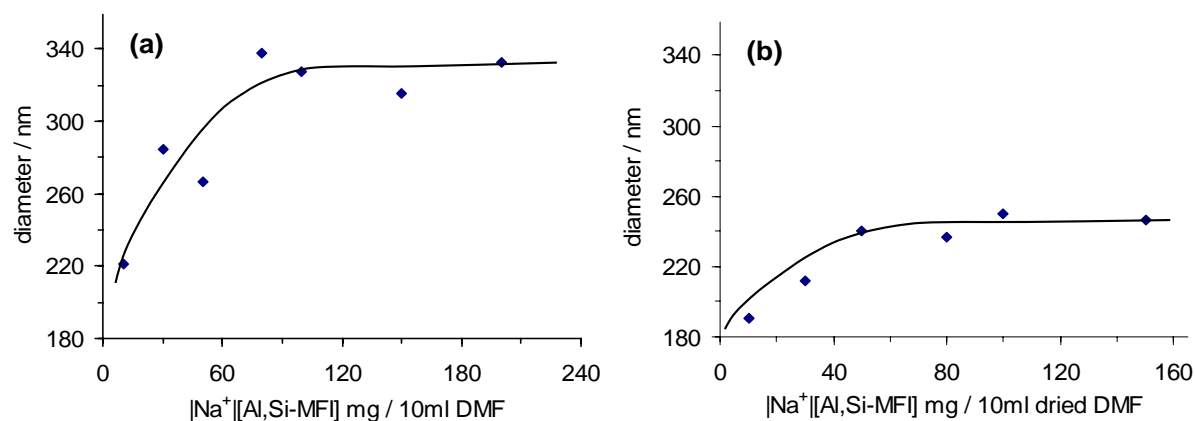


Figure 9.12: Dependence of the mean particle sizes on $[\text{Na}^+][\text{Al,Si-MFI}]$ contents in (a) normal DMF, (b) dried DMF

The diagrams demonstrate that the mean particle sizes in both, normal DMF and dried DMF series increase when the $[\text{Na}^+][\text{Al,Si-MFI}]$ contents in DMF increase. However, these values are limited at about 325 nm in normal DMF, and lower at 245 nm in dried DMF. These results indicate that the water contents in the DMF solvent as well as in the pores of zeolite can affect to the nanoparticle sizes. To clarify the influence of water content to the

particle sizes, a series of experiments was carried out by adding water into the mixture of $[\text{Na}^+][\text{Al,Si-MFI}]$ and DMF solvent. The diagram illustrating the dependence of the mean particle sizes on the supplement water contents is shown in Figure 9.13. With a small amount of water added into the solutions, the mean particle sizes increases. However, these values are also limited at about 320 nm. This could be results by a saturation of water molecules around the nanoparticles, leading the limited particle size.

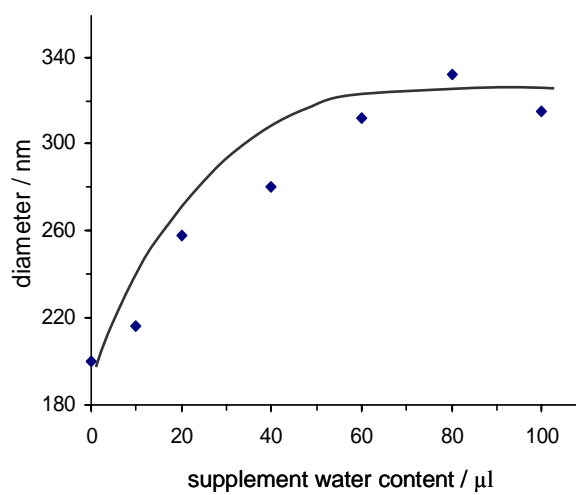


Figure 9.13: Dependence of mean particle sizes on supplement water contents of $[\text{Na}^+][\text{Al,Si-MFI}]$ solutions in DMF

Similar results are also observed in the experiments using $[\text{Si-MFI}]$ as parent sample. The dependence of the mean particle sizes on zeolite concentration and the supplementary water content are illustrated in Figure 9.14. The mean particle sizes increase when the $[\text{Si-MFI}]$ contents in DMF increase and these values are limited at about 215 nm. In addition, the mean particle sizes also shift to the larger radius when the water contents in the $[\text{Si-MFI}]/\text{DMF}$ mixtures increase.

Apparently, the water contents have a certain influence to the nanoparticle sizes in colloidal suspensions. The increase of water contents leads the growth of nanoparticles in the zeolite colloidal suspensions.

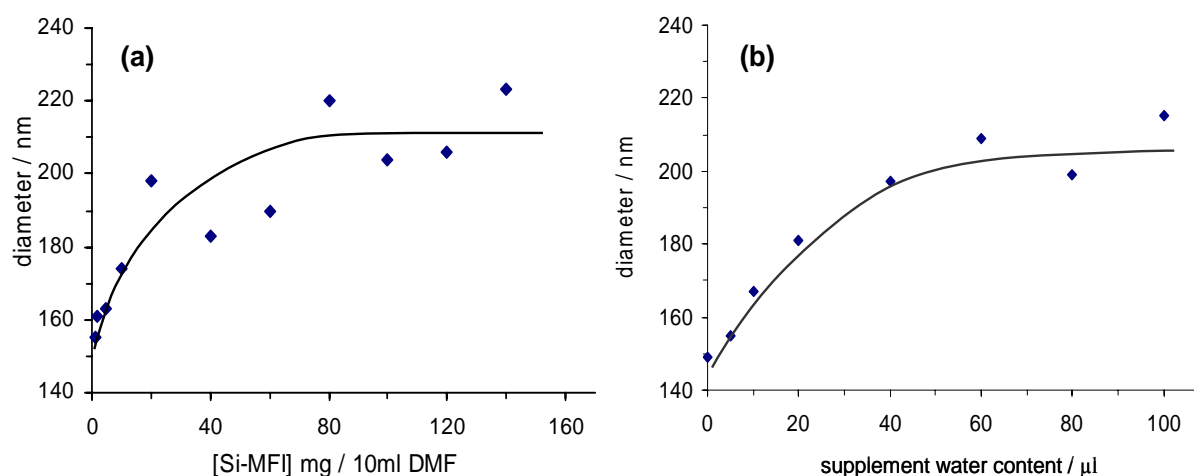


Figure 9.14: Dependence of the mean particle sizes on (a) [Si-MFI] concentrations in normal DMF, (b) supplement water contents of [Si-MFI] solutions in DMF

9.3.2 Sodium Effect

Besides water, sodium concentrations can influence to the zeolite particle sizes in DMF solvent. Experiments were carried out with different commercial ZSM-5 modules, beta borosilicates with different Na^+/H^+ ratios and ZSM-5 (Si/Al = 14) solutions to which NaCl aqueous solution was added.

The mean particle sizes of ZSM-5 modules in DMF are collected in Table 9.4. As shown in Chapter 1, the aluminum charge in the zeolite sodium forms is balanced by sodium cations. Therefore, the increase of aluminum content is synonymous with larger sodium content in zeolites. The results summarized in Table 9.4 indicate that the mean particle sizes of zeolite solutions increases when the Si/Al ratios decrease; that means the particle sizes increase with increasing sodium contents.

Table 9.4: Mean particle sizes of ZSM-5 module solutions in DMF

ZSM-5 solutions	diameter / nm
ZSM-5 module 120 (Si/Al = 60)	148
ZSM-5 module 40 (Si/Al = 20)	170
ZSM-5 module 28 (Si/Al = 14)	198

That trend is also observed in beta borosilicates with different Na^+/H^+ ratios. Table 9.5 summarizes the mean particle sizes of $[\text{Na}^+_x, \text{H}^+_{1-x}][\text{B}, \text{Si}-*\text{BEA}]$ suspensions in DMF. As can be seen, with an increase of the sodium content, the mean particle sizes of beta borosilicate colloidal suspensions also increases.

Table 9.5: Mean particle sizes of $[\text{Na}^+_x, \text{H}^+_{1-x}][\text{B}, \text{Si}-*\text{BEA}]$ solutions in DMF

$[\text{Na}^+_x, \text{H}^+_{1-x}][\text{B}, \text{Si}-*\text{BEA}]$	diameter / nm
x = 0.0	177
x = 0.2	182
x = 0.4	210
x = 0.6	235
x = 0.8	245
x = 1.0	260

Sodium effects are also observed with sodium cations added into the $[\text{Na}^+][\text{Al}, \text{Si}-\text{MFI}]$ solutions as NaCl aqueous salt solution. Figure 9.15 shows the particle size distributions and the mean particle sizes of $[\text{Na}^+][\text{Al}, \text{Si}-\text{MFI}]$ solutions with added NaCl salt. The distribution peaks are shifted to the larger radius when more sodium cations are added into the suspensions. In addition, the lines become broader when the sodium contents increase. In fact, if the sodium concentrations are large enough, the zeolite particles become visible by the naked eye.

Thus, in the colloidal suspensions, zeolite nanoparticles which have a negative surface charge tend to adhere to neighbouring particles under the influence of sodium cations and form larger aggregates. The aggregation ability of zeolite nanoparticles in the presence of sodium cations was also studied by measuring zeta potentials (ξ) of zeolite solutions as shown in Figure 9.16. Once the sodium contents in the zeolite suspensions increase, the particles tends to agglomerate and the negative ξ value approach zero, i.e. the isoelectric point, where the colloidal suspensions are less stable. Hence, the zeolite colloidal suspensions with sodium cations added are unstable; they show an aggregation tendency.

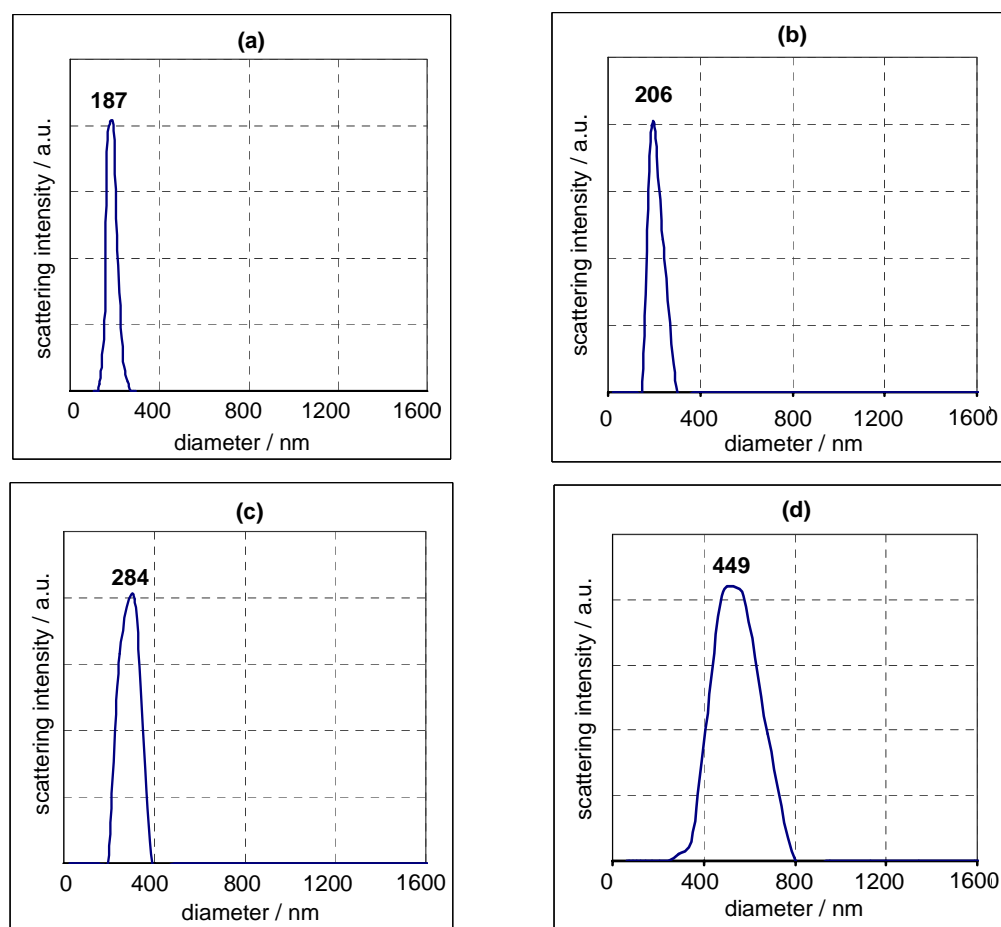


Figure 9.15: DLS data of $[\text{Na}^+][\text{Al,Si-MFI}]$ solutions in DMF of (a) in dried DMF solution, (b) added 5 μl NaCl 0.5M, (c) added 10 μl NaCl 0.5M, (d) added 15 μl NaCl 0.5M

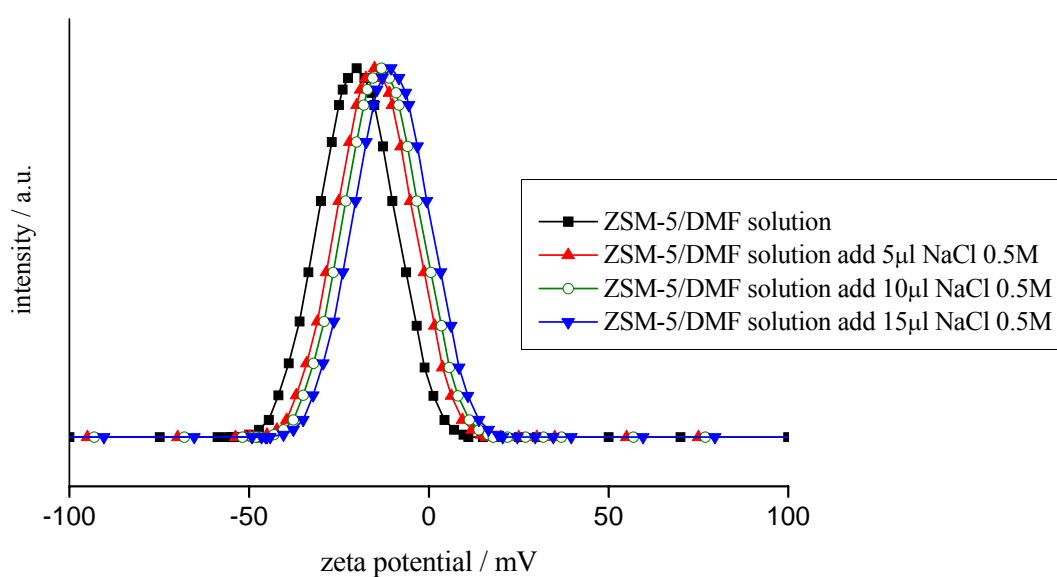


Figure 9.16: Zeta potential of $[\text{Na}^+][\text{Al,Si-MFI}]$ solutions in DMF added Na^+

9.4 Concluding Remarks

It is clear that the nanoparticles are formed in several organic solvents such as DMF and DMSO. The zeolite colloidal suspensions are rather stable in these solvents with the mean particle sizes at about 200 nm in DMF and about 500 nm in DMSO.

The new coordinations between carbonyl group of DMF and zeolite surface are created due to the high polar of DMF molecules. During the DMF treatment, DMF molecules can occupy the pores of zeolite frameworks and lead a slight change of Si environments. However, the zeolite structures are retained throughout the DMF treatment as verified by the XRD patterns of dried solution.

The presence of water molecules and sodium cations has an influence on the particle sizes of the zeolite suspensions. Agglomerations occur in the presence sodium cations. Therefore, higher electrolyte concentrations lead the larger zeolite particles. A proposed model illustrating the formation of zeolite nanoparticles from the zeolite microscale crystals by organic solvents is shown in Figure 9.17. The small primary nanoparticles are formed from the larger zeolite particles; however, they can aggregate to form larger particles. The sizes and shapes of these particles can be observed by several techniques, for instance DLS, AFM and SEM. Up to now, the primary particles have not been observed directly.

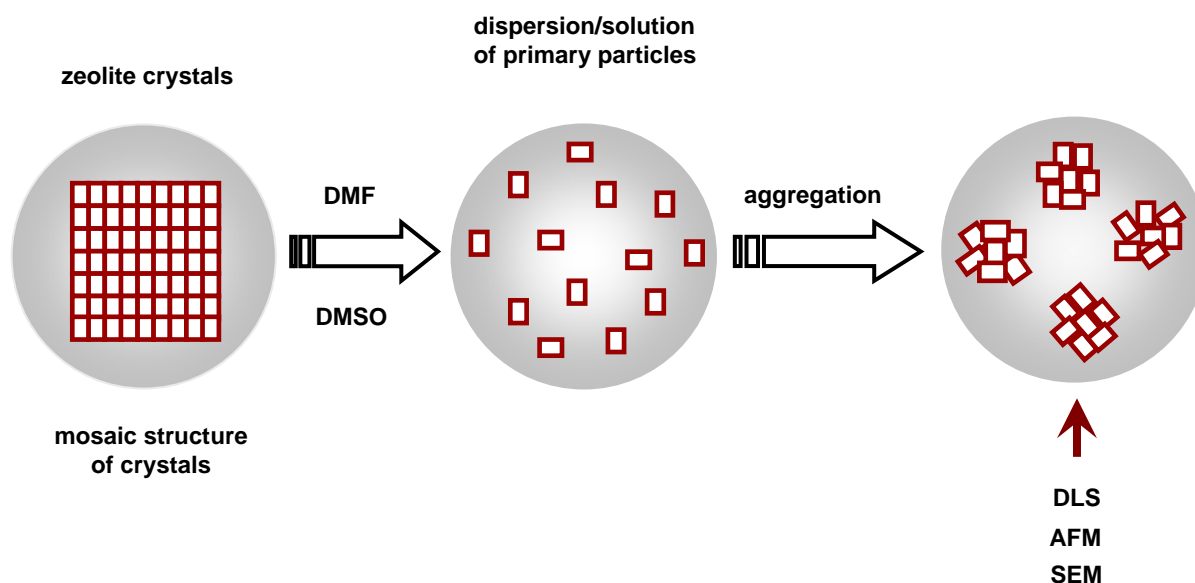


Figure 9.17: Proposed model illustrating the zeolite nanoparticles forming from the larger zeolite crystals in organic solvents

Chapter

10

Summary and Outlook

This thesis is compound of investigations about the boron coordinations in beta zeolite structure as well as the application of beta borosilicate for post-synthetic modification, and the formation of zeolite nanoparticles from the larger zeolite particles in organic solvents. According to the aim of this thesis, the work encompassed:

- The preparation of beta borosilicates via hydrothermal and dry-gel methods.
- Studies of the transformation of boron coordinations in beta borosilicates depending on the environments, for instance humidity, temperature.
- Application of the flexibility of boron coordinations to the post-synthetic exchange with aluminum and gallium.
- Investigations of the formation zeolite nanoparticles from microscale zeolites by using organic solvents such as DMF and DMSO.

***BEA borosilicates and Boron coordinations in beta borosilicates**

Beta borosilicates with sodium or without sodium were synthesized via hydrothermal and dry-gel methods. Unlike aluminosilicates, the hydrothermal process applied for beta

borosilicates required beta zeolite as a seeds or small amount of aluminum. Beta borosilicates were also successfully received from the dry-gel synthesis; however the seed were not necessary for this process. Some parameters have affected to the synthesis procedure such as crystallization time, sodium content, etc. Initial X-Ray reflections characterizing the beta structure were observed after 18 hours of crystallization time.

The formation and the evolution of trigonal and tetrahedral boron coordinations during the hydration and dehydration processes were investigated in this work by employing the MAS and MQMAS solid state NMR techniques. Upon dehydration, tetrahedral boron coordinations have been transformed to trigonal boron sites in the proton form. Trigonal boron in the framework, $B(OSi)_3$, and $B(OSi)_2(OH)$ partially hydrolyzed species, have been observed. Boron also shows a great flexibility in coordination conversion from trigonal to tetrahedral boron depending on the hydration level. At high degree of hydration, the mobil $B(OH)_3$ within the zeolite channels can be obtained in the proton form. In addition, boron can be easily removed from the framework of the proton form even at mild hydration treatment. The flexibility of boron coordinations is also observed upon re-dehydration of samples. The reoccupation of boron into the framework can be achieved by re-dehydration of hydrated samples.

On the other hand, the flexibility of boron coordination depends on the cations that balance the negative framework charge of the tetrahedral boron site in the zeolite. Tetrahedral boron has been stable when Na^+ , NH_4^+ , $H(H_2O)^+$ were counterbalancing cations, but unstable in the proton form. In fact, tetrahedral boron which was balanced by proton has easily converted to trigonal boron through the dehydration process. On the contrary, the tetrahedral boron which was compensated by sodium cations has been rather stable at dehydration and even hydrolysis processes at mild conditions.

Post-synthesis modification to form aluminum and gallium beta zeolites from beta borosilicates

Due to the ability of deboronation at the mild conditions, beta zeolites with aluminum and gallium in the framework were prepared from beta borosilicates. The exchange of aluminum or gallium for boron was carried out by varying the Na^+/H^+ counter ion ratio in beta borosilicates. By using of aluminum nitrate or gallium nitrate as an aluminum/gallium

precursor, water and ethanol were used for the mild exchange in the post-synthetic treatment. However, the method with ethanol has achieved the higher yield.

Zeolite nanoparticles forming in organic solvents

Using the polar solvents, such as DMF and DMSO, zeolite nanoparticles were formed from the zeolite microparticles. Under ambient conditions, the zeolite colloidal suspensions have been stable in these solvents. Zeolite nanoparticles have been shown to retain the structure.

A change of the mean particle sizes of zeolite colloidal suspensions was observed, when the water and sodium concentrations in the sample were altered. The mean particle sizes have increased with increasing water and/or sodium concentrations. An appearance of electrolyte cations in the zeolite suspensions favors aggregation. Under agglomeration, larger particles have been formed in the colloidal suspensions, leading the increase of the mean particle sizes in the zeolite solutions.

Outlook

Beta borosilicates were synthesized via hydrothermal synthesis with high crystallinity after 72 hours or 96 hours of crystallization time. However, small reflections which were not characteristic for the beta structure were observed after 18 hours crystallization time without sodium. These reflections were not observed any longer of after 52 hours. Therefore, more investigations with a shorter variation of crystallization time should be performed to study the growth or disappearance of these reflections during crystallization process. Also further characterization of a possible intermediate phase should be carried out, e.g. with TEM.

The boron coordinations in beta borosilicates are very flexible. Further investigations on the boron coordinations should be carried out with solid state NMR at low temperature. Using this technique, the existence of trigonal extraframework boron should be investigated in view of dynamic properties.

The flexibility of boron coordination has an important application on the post-synthesis modification at mild environment. Using deboronated borosilicates for the post-synthesis exchange with the other ion such as titanium, zirconium, etc. can be a useful tool to form the molecular sieves, which are sometime difficult to synthesize directly.

The formation of zeolite nanoparticles in DMF and DMSO is an initial start for further investigations to form the nanoparticles in polar organic solvents. The zeolites and molecular sieves as well as the different polar solvents can be applied for the investigations. The other parameters that affect the mean particles sizes and the size distributions such as the amount of solvents, the mixture procedures, stirring time, the time to stabilize the suspensions etc. should be performed to understand the formation process of zeolite nanoparticles. So far, only aggregate particles can be observed by the DLS, SEM techniques. Moreover, primary particles should be further studied by the other techniques, for instance TEM.

Appendix A

The DLS Data

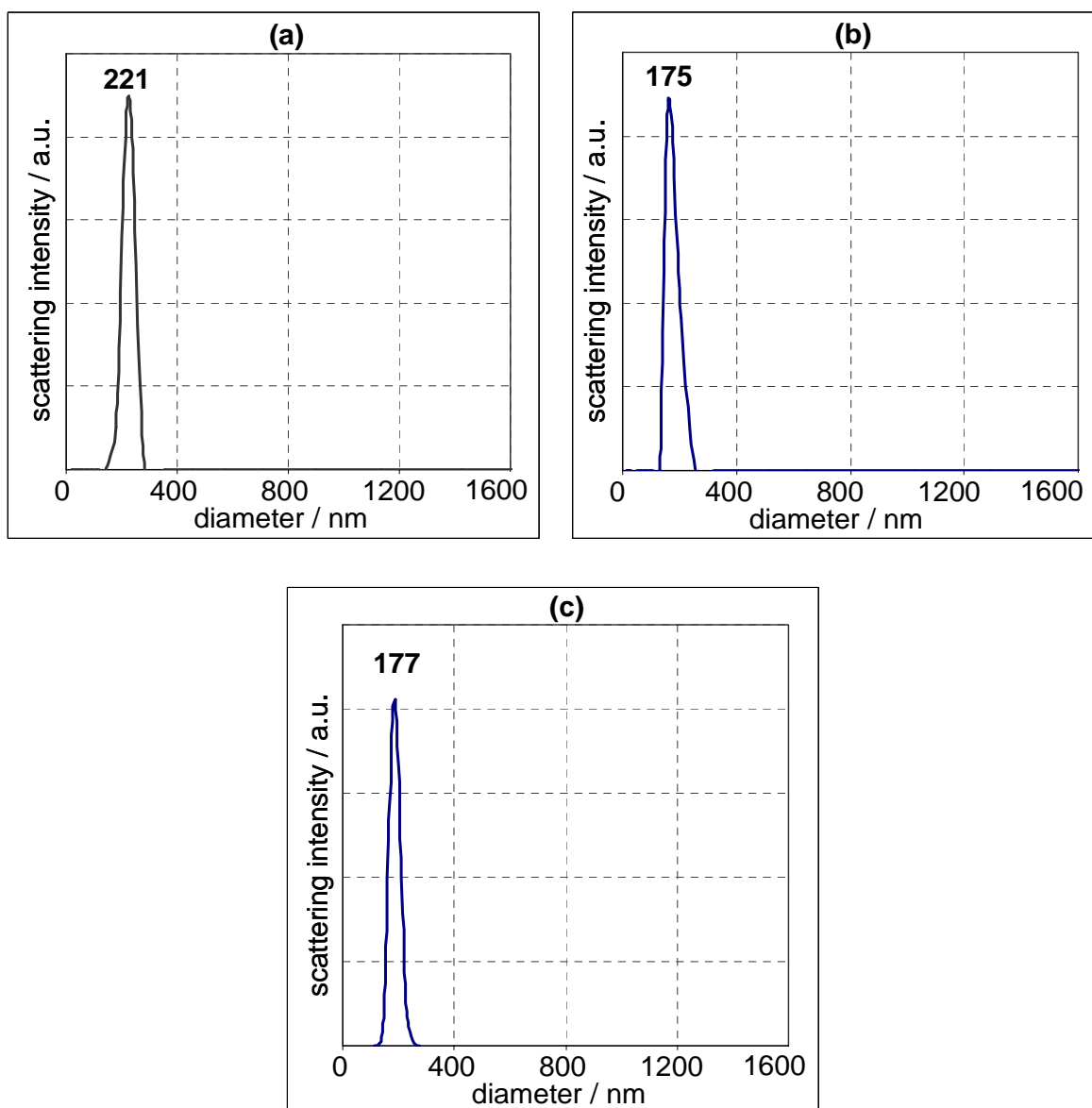


Figure A1: DLS data of $[H^+][B,Si-MFI]$ solutions in DMF (a) solution 2, (b) solution 3, (c) solution 4

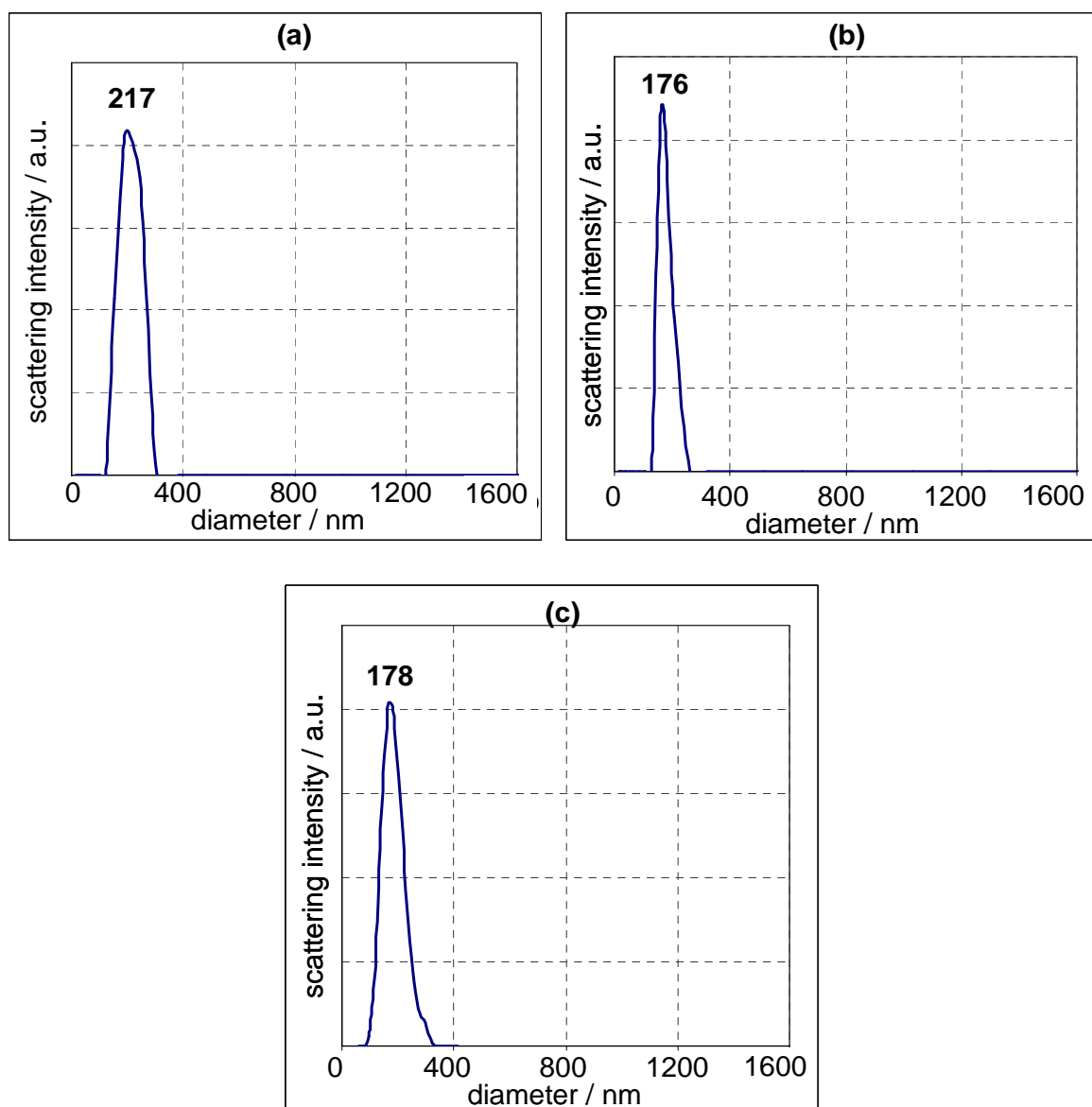


Figure A2: DLS data of $[TPA]/[Si-MFI]$ solutions in DMF (a) solution 2, (b) solution 3, (c) solution 4

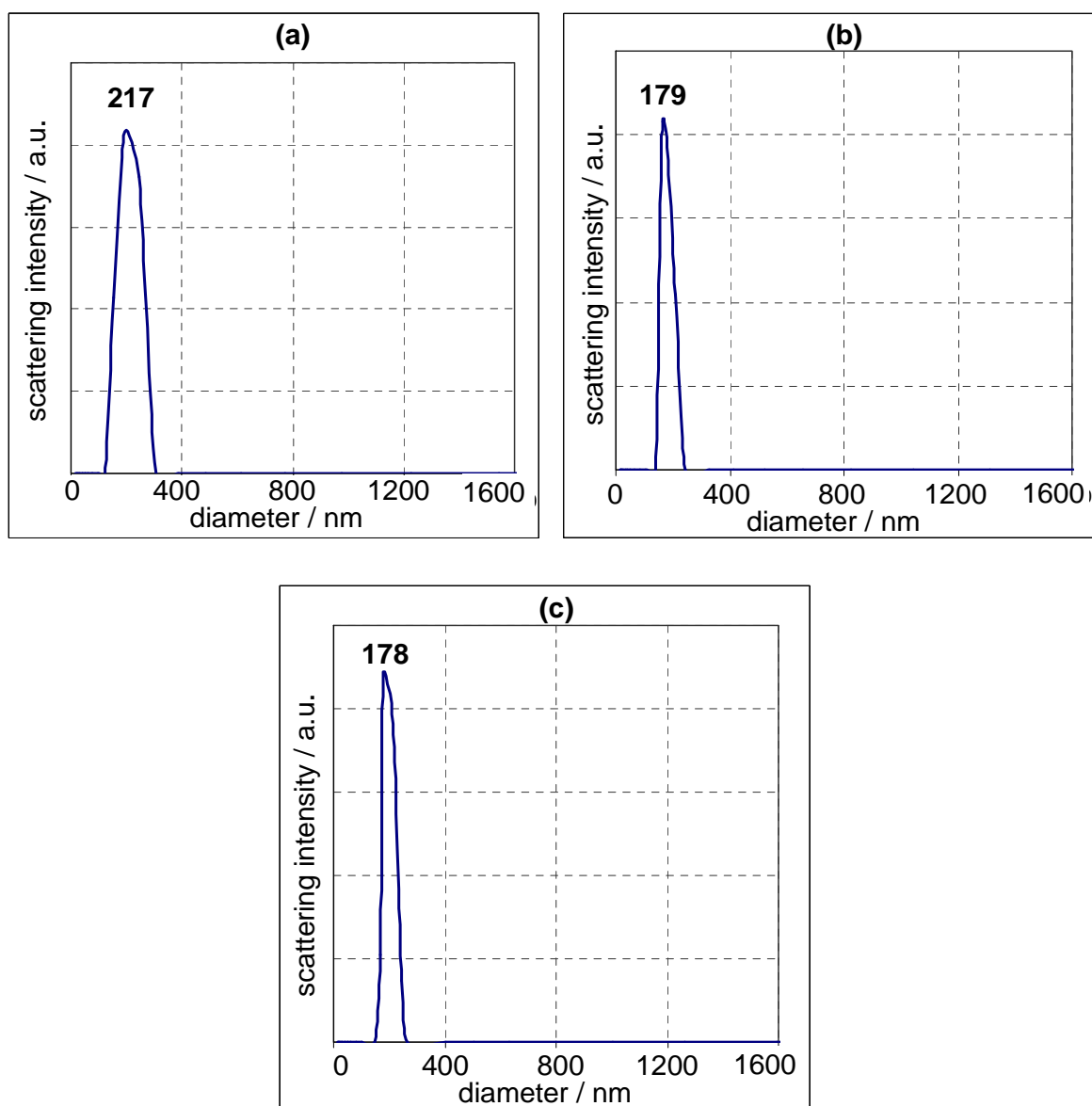


Figure A3: DLS data of [Si-MFI] solutions in DMF (a) solution 2, (b) solution 3, (c) solution 4

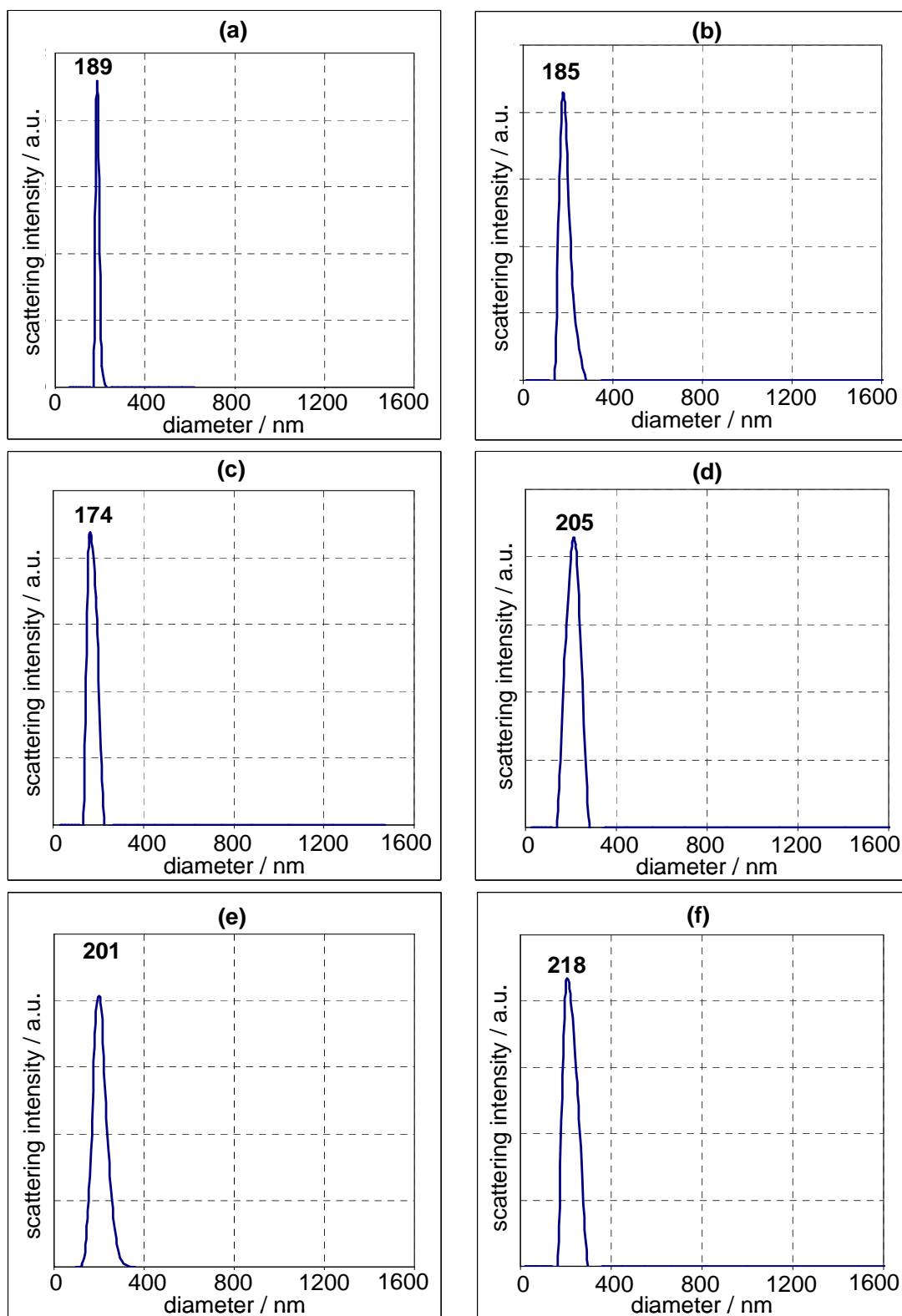


Figure A4: DLS data of first zeolite solutions in DMF (a) NaY, (b) H^+ [B,Si-MFI], (c) H^+ [B,Si-*BEA], (d) Na^+ [B,Si-*BEA], (e) H^+ [Al,Si-*BEA], and (f) Na^+ [Al,Si-*BEA]

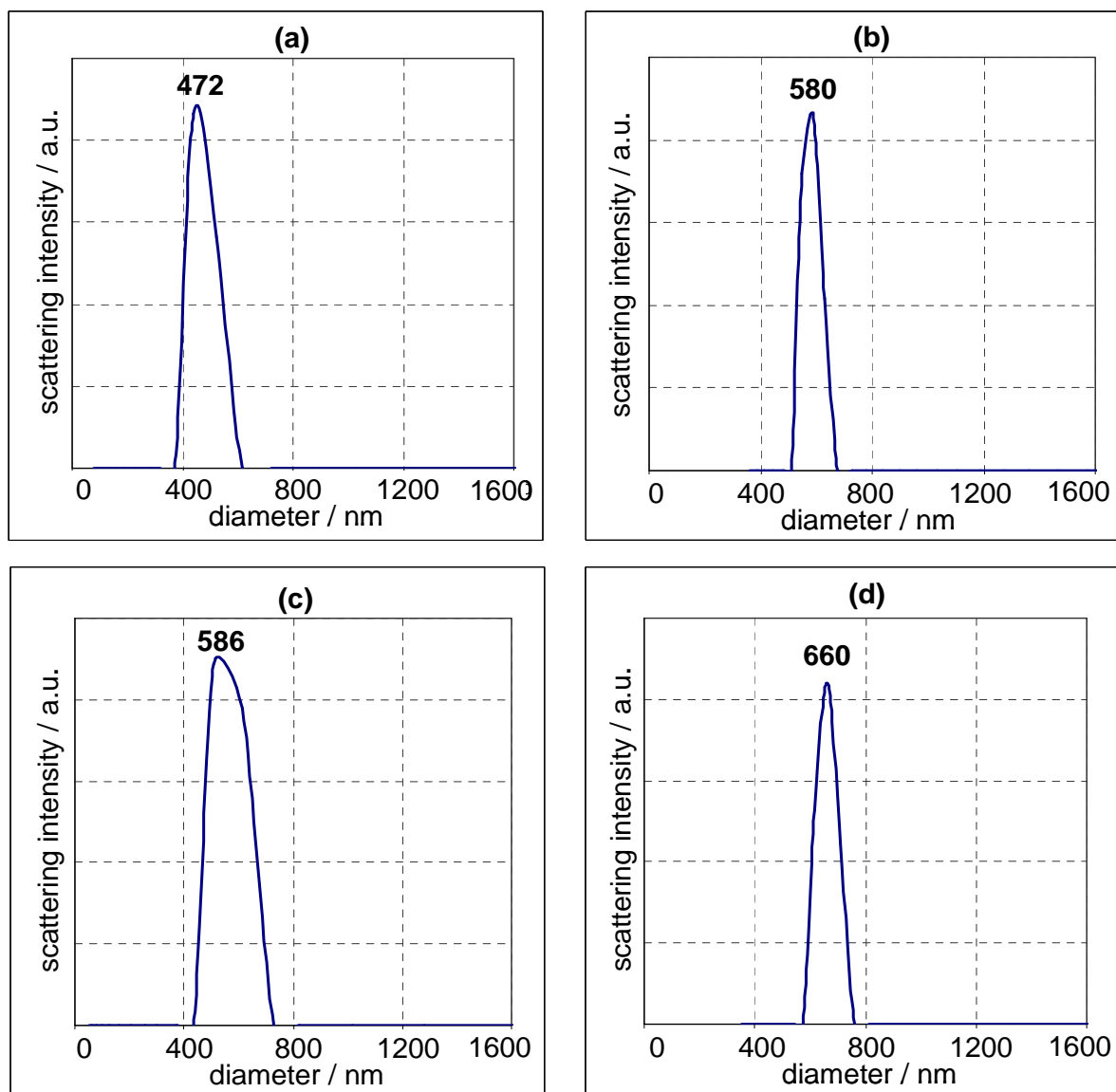


Figure A5: DLS data of second ZSM-5 solutions in DMSO (a) Na^+ /[Al,Si-MFI], (b) H^+ /[B,Si-MFI], (c) TPA/[Si-MFI], (d) [Si-MFI]

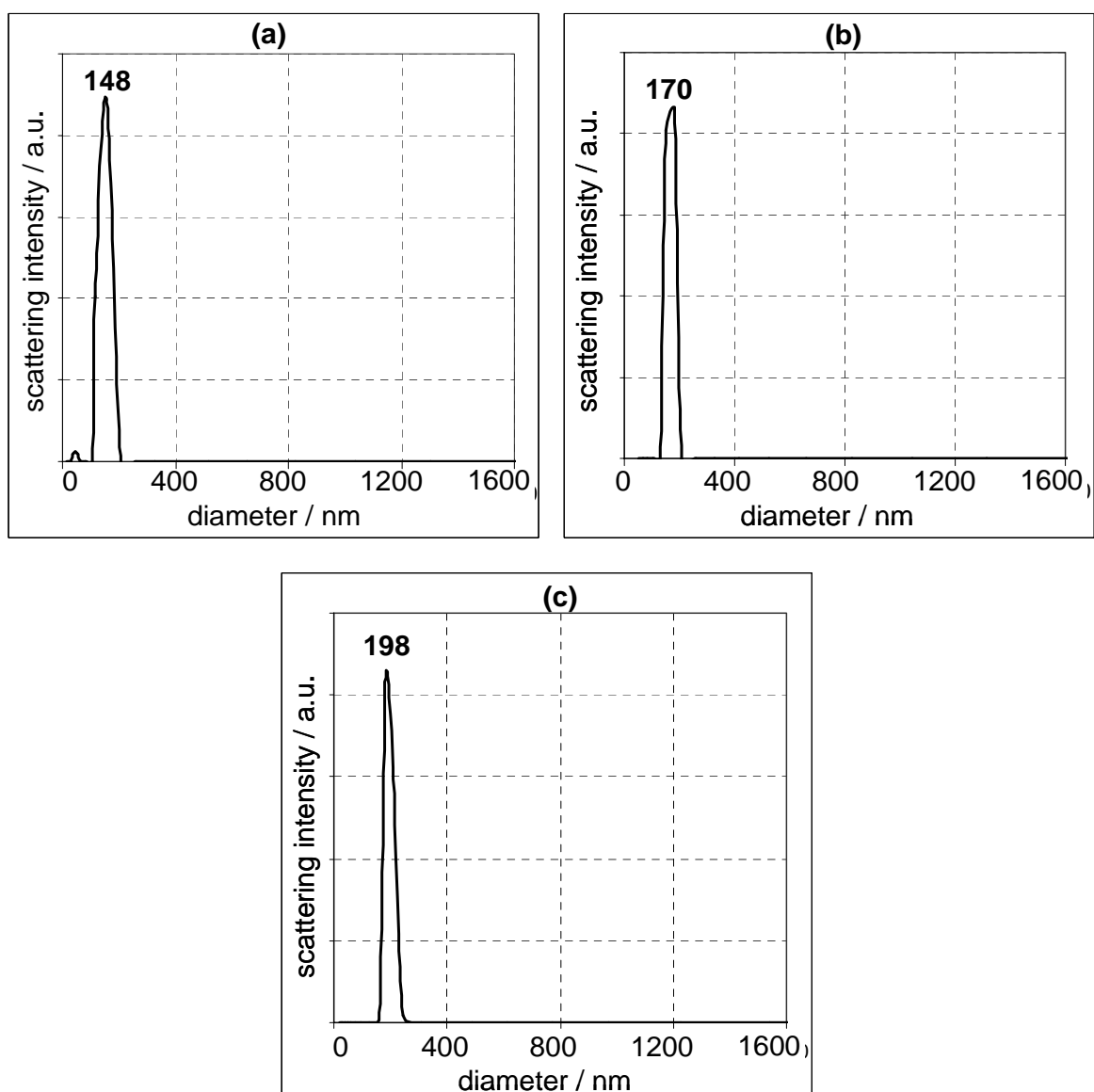


Figure A6: DLS data of different ZSM-5 module solutions in DMF (a) module 120 ($\text{Si}/\text{Al} = 60$) (b) module 40 ($\text{Si}/\text{Al} = 20$), (c) module 28 ($\text{Si}/\text{Al} = 14$)

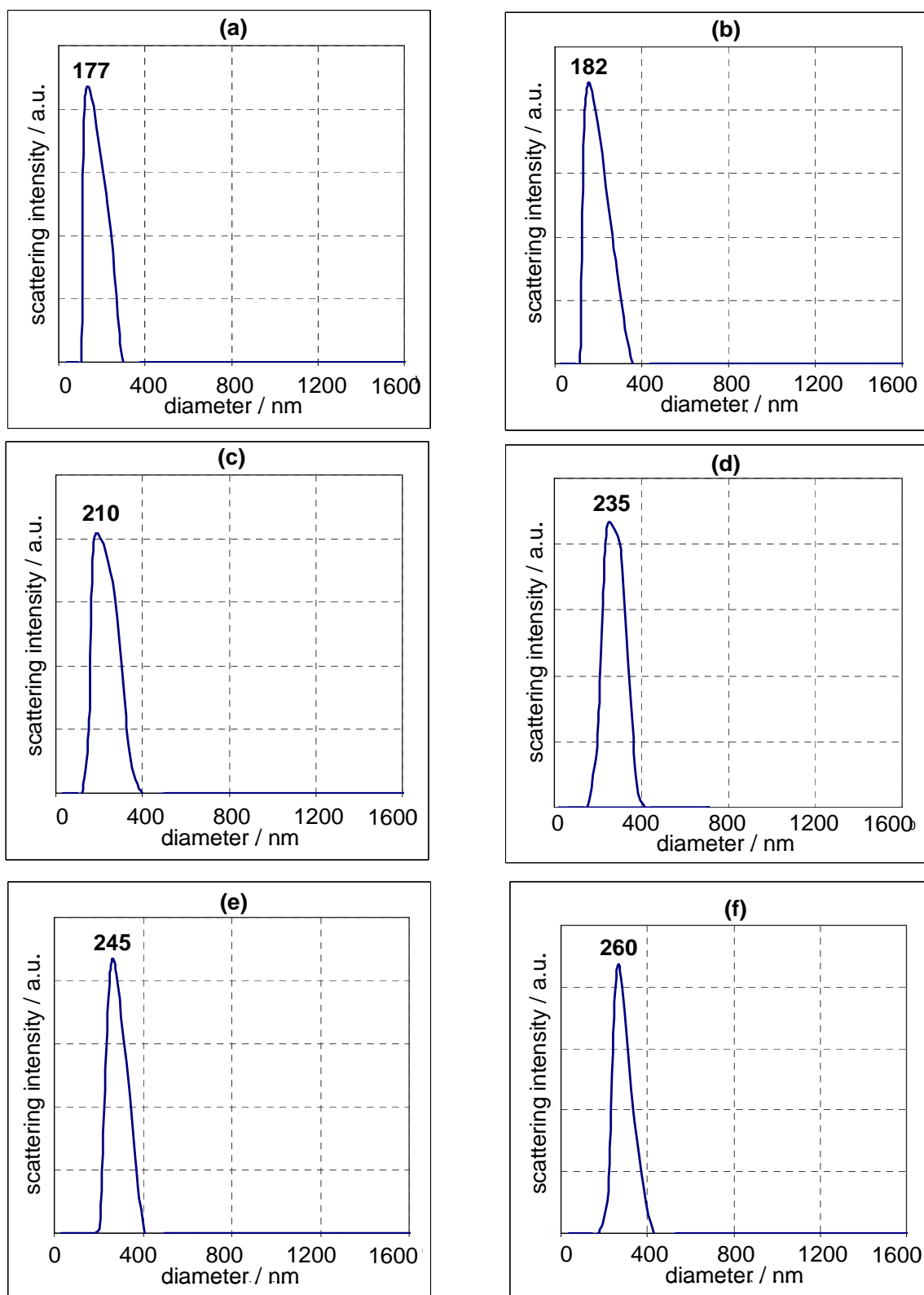


Figure A7: DLS data of first $[Na^+_x H^{+(1-x)}][B, Si^*BEA]$ solutions in DMF (a) $x = 0$, (b) $x = 0.2$, (c) $x = 0.4$, (d) $x = 0.6$, (e) $x = 0.8$, (f) $x = 1.0$

Appendix B

The AFM Micrographs

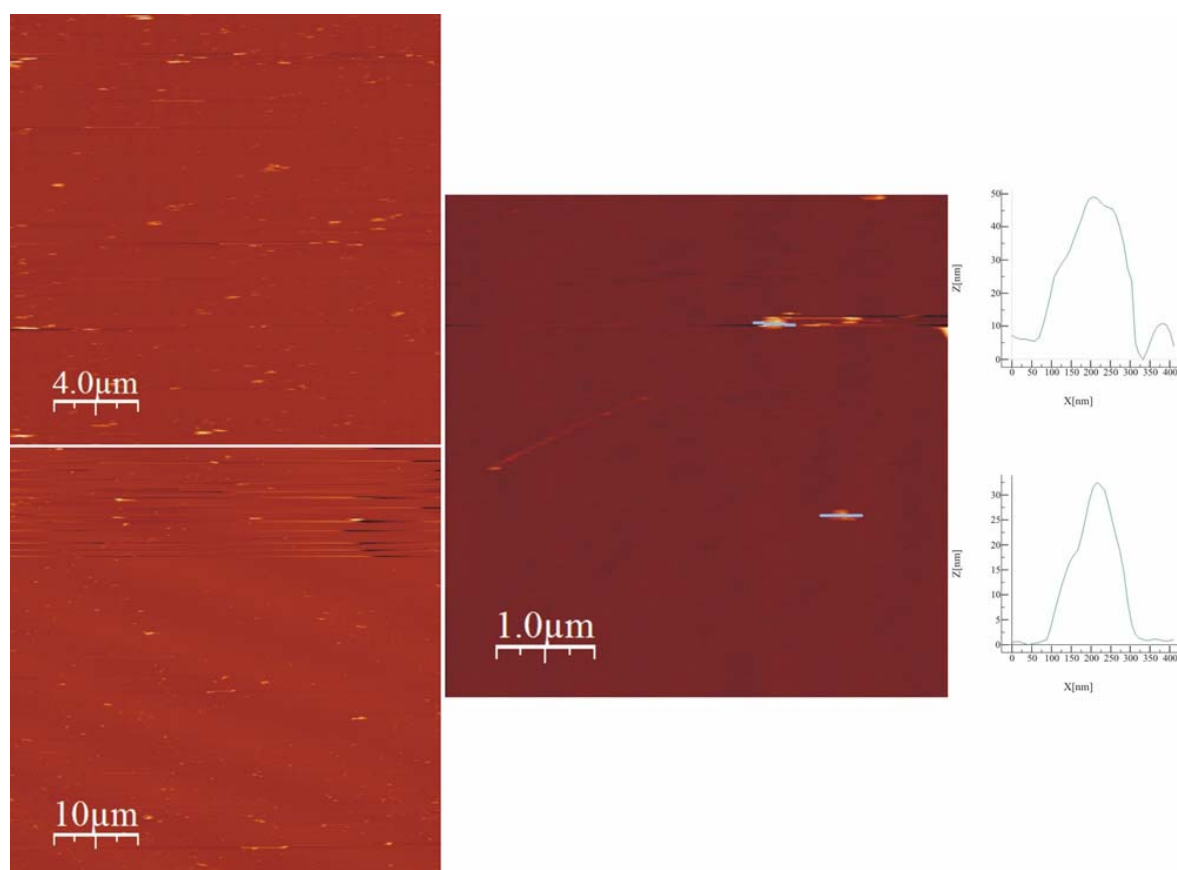


Figure B1: AFM micrographs of $\text{H}^+[\text{B,Si-MFI}]$ solution in DMF

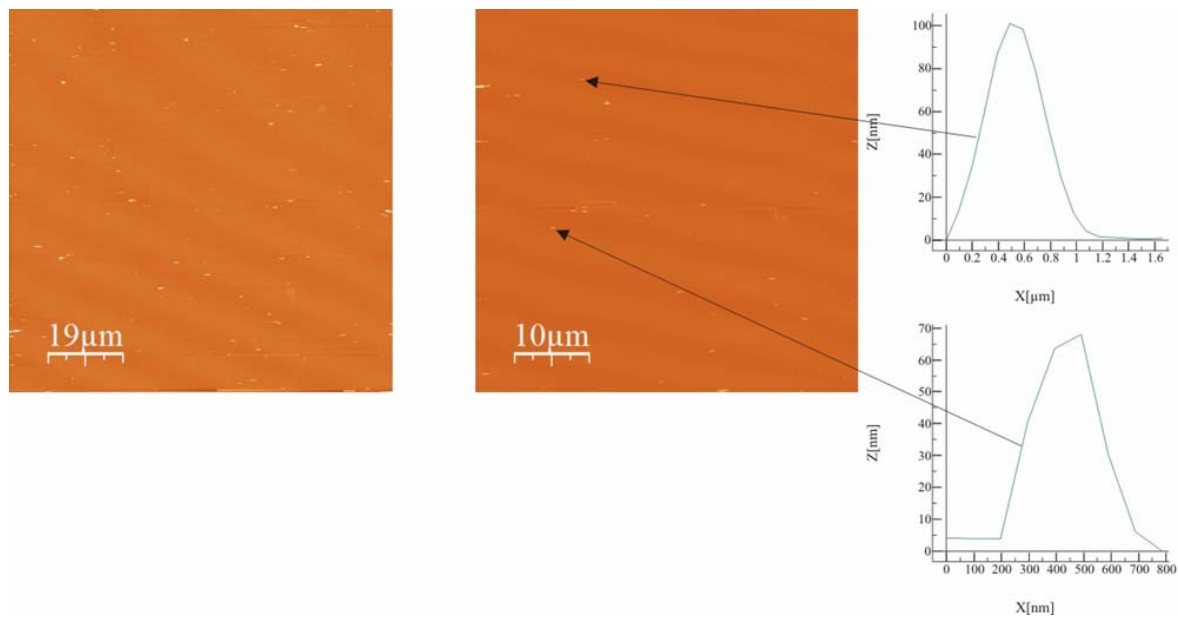


Figure B2: AFM micrographs of $\text{Na}^+[\text{Al,Si-MFI}]$ solution in DMF

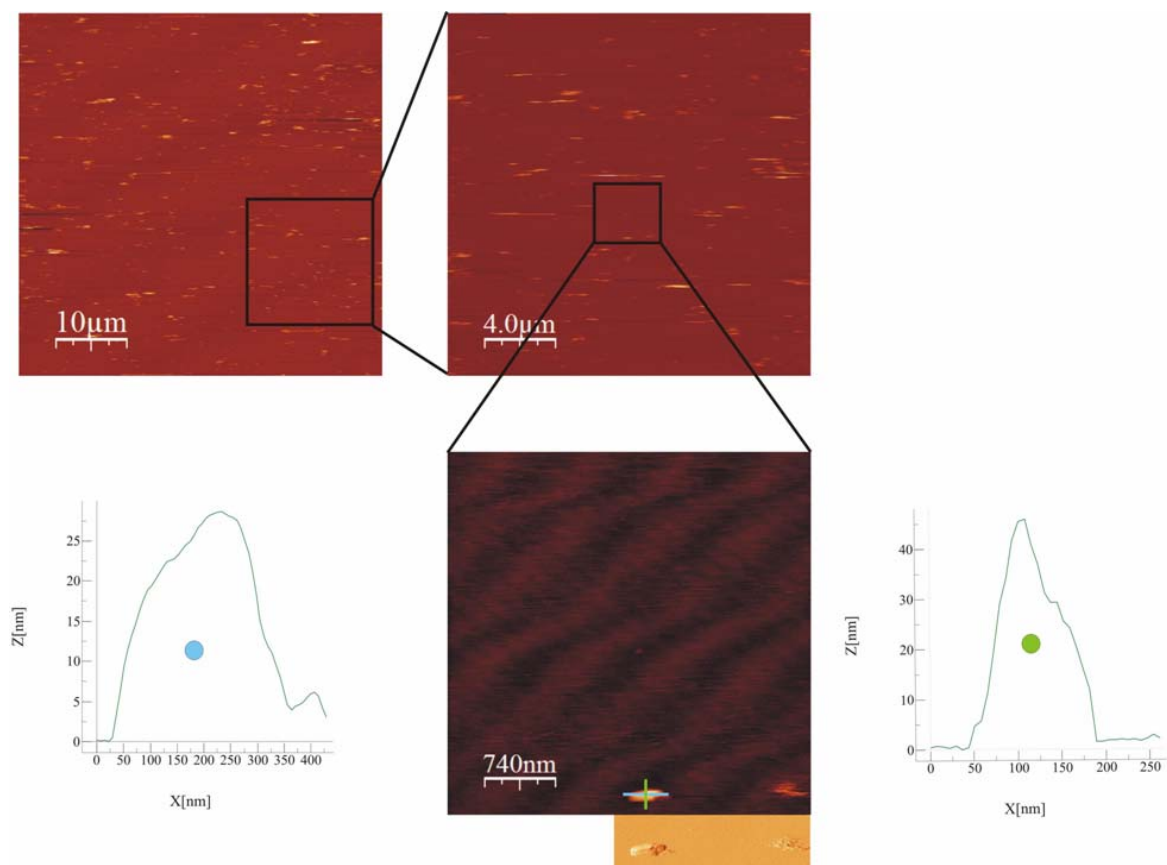


Figure B3: AFM micrographs of $\text{TPA}[\text{Si-MFI}]$ solution in DMF

Bibliography

- ¹ H. van Bekkum, E.M. Flanigen, J.C. Jansen, Introduction to zeolite science and practice, Elsevier: Amsterdam, 1991.
- ² C.S. Cundy and P.A. Cox, Chem. Rev., 2003 (103), 663
- ³ E.M. Flanigen, Pure & Appl. Chem., 52 (1980) 2191.
- ⁴ C. Baerlocher, W.M. Meier, D.H. Olson, Atlas of Zeolite Framework Types, 5th ed., Elsevier: Amsterdam, 2001. <http://topaz.ethz.ch/IZA-SC/StdAtlas.htm>
- ⁵ S. Kallus, J. Patarin, P. Caullet, A.C. Faust, Microporous Materials 10 (1997) 181.
- ⁶ U. Lohse, B. Altrichter, R. Donath, R. Fricke, K. Jancke, B. Parlitz, E. Schreier. J. Chem. Soc. Faraday Trans. 92 (1996) 159.
- ⁷ M.J. Eapen, K.S.N. Reddy, V.P. Shiralkar, Zeolites 14 (1994) 295.
- ⁸ P. Caullet, J. Hazm, J.L. Guth, J.F. Joly, J. Lynch, F. Rantz, Zeolites 12 (1992) 240.
- ⁹ J.C. van der Waal, M.S. Rigutto, H. van Bekkum, Chem. Commun., (1994) 1241.
- ¹⁰ R. de Ruite, K. Pamin, A.P.M. Kentgens, J.C. Jansen, H. van Bekkum, Zeolites 13 (1993) 611.
- ¹¹ J.B. Higgins, R.B. LaPierre, J.L. Schlenker, A.C. Rohrman, J.D. Wood, G.T. Kerr, W.J. Rohrbaugh. , Zeolites 8 (1988) 446.
- ¹² A.P. Stevens, P.A. Cox, Chem. Commun. (1995) 343.
- ¹³ M.A. Camblor, A. Corma, S. Valencia, J. Mater. Chem. 8 (1998) 2137.
- ¹⁴ M.M.J. Treacy, J. M. Newsam, Nature 332 (1988) 249.
- ¹⁵ J.M. Newsam, M.M.J. Treacy, W.T. Koetsier, C.B. de Gruyter, Pro. R. Soc. Lon. A 420 (1988) 375.
- ¹⁶ B. Slater, C.R.A. Catlow, Z. Liu, T. Ohsuna, O. Terasaki, M.A. Camblor, Angew. Chem. Int. Ed. 41 (2002) 1235.
- ¹⁷ Z. Liu, T. Ohsuna, O. Terasaki, M.A. Camblor, M.J.D. Cabañas, K. Hiraga, J. Am. Chem. Soc. 123 (2001) 5370.
- ¹⁸ M.A. Camblor, M. Costantini, A. Corma, L. Gilbert, P. Esteve, A. Martinez, S. Valencia, Chem. Commun. (1996) 1339.

- 19 S.I. Zones, Y. Nakagawa, *Microporous Materials* 2 (1994) 543.
- 20 U. Lohse, B. Altrichter, R. Fricke, W. Pilz, E. Schreier, C. Garkisch, K. Lancke, J. Chem. Soc. Faraday Trans. 93 (1997) 505.
- 21 G.G. Juttu, R.F. Lobo, *Catalysis Letter* 62 (1999) 99.
- 22 M.A. Cambor, J. Pe´rez-Pariente, V. Fornes, *Zeolites* 12 (1992) 280.
- 23 K.J. Chao, S.P. Sheu, L.H. Lin, M.J. Genet, M.H. Feng, *Zeolites* 18 (1997) 18.
- 24 R. Kumar, A. Thangaraj, R.N. Bhat, P. Ratnasamy, *Zeolites* 10 (1990) 85.
- 25 R.B. Borade, A. Clearfield, *Microporous Materials* 2 (1994) 167.
- 26 R. Mostowicz, F. Testa, F. Crea, R. Aiello, A. Fonseca, J.B. Nagy, *Zeolites* 18 (1997) 308.
- 27 J.E. Hazm, P. Caullet, J.L. Paillaud, M. Soulard, L. Delmotte, *Microporous and Mesoporous Materials* 43 (2001) 11.
- 28 R. Millini, G. Perego, G. Bellussi, *Topics in Catalysis* 9 (1999) 13.
- 29 K.F.M.G.J. Scholle, A.P.M. Kentgens, W.S. Veeman, *J. Phys. Chem.* 88 (1984) 5.
- 30 U. Freese, F. Heinrich, F. Roessener, *Catalysis Today* 49 (1999) 237.
- 31 H. Taşkin, C. Kubat, Ö. Uygun, S. Arslankaya, *Computers and Chemical Engineering* 30 (2006) 850.
- 32 L. Bonetto, M.A. Cambor, A. Corma, J.P. Pariente, *Applied Catalysis A* 82 (1992) 37.
- 33 A. Corma, P.J. Miguel, A.V. Orchillés, *Applied Catalysis A* 138 (1996) 57.
- 34 A. Corma, V. González-Alfaro, A.V. Orchillés, *Applied Catalysis A* 187 (1999) 245.
- 35 N. Kubicek, F. Vaudry, B.H. Chiche, P. Hudec, F. Di Renzo, P. Schulz, F. Faujula, *Applied Catalysis A* 175 (1998) 159.
- 36 E. Baburek, J. Novakova, *Collect. Czech. Chem. Commun.* 63 (1998) 42.
- 37 J.G. Goodwin, S. Natesakhawat, A.A. Nikolopoulos, S.Y. Kim, *Catalysis Reviews* 44 (2002) 287.
- 38 G.S. Nyvarthy, A. Feller, K. Seshan, J.A. Lercher, *Microporous and Mesoporous Materials* 35 (2000) 75.
- 39 G. Bellussi, G. Pazzuconi, C. Perego, G. Girotti, G. Terzoni, *Journal of Catalysis* 157 (1995) 227.
- 40 T.C. Tsai, C.L. Ay, I. Wang, *Applied Catalysis* 77 (1991) 199.
- 41 W.H. Chen, A. Pradhan, S.J. Jong, T.Y. Lee, I. Wang, T.C. Tsai, S.B. Liu, *Journal of Catalysis* 163 (1996) 436-446.

- 42 J. Čejka, J. Kotrla, A. Krejčí, *Applied Catalysis A* 277 (2004) 191.
- 43 I. Ferino, D. Meloni, R. Monaci, E. Rombi, V. Solinas, *Journal of Molecular Catalysis A* 192 (2003) 171.
- 44 S. Dzwigaj, A. de Mallmann, D. Barthomeuf, *Journal of Chemical Society, Faraday Transactions* 86 (1990) 431.
- 45 J. Yao, H. Wang, K.R. Ratinac, S.P. Ringer, *Chem. Mater.* 18 (2006) 1394.
- 46 G. Majano, S. Mintova, O. Ovsitser, B. Mihailova, T. Bein, *Microporous and Mesoporous Materials* 80 (2005) 227.
- 47 M. Mihailova, S. Mintova, K. Karaghiosoff, T. Metzger, T. Bein, *J. Phys. Chem. B* 109 (2005) 17060.
- 48 B.Z. Zhan, M.A. White, K.N. Robertson, T.S. Cameron and M. Gharghour, *Chem. Commun.* (2001) 1176.
- 49 V. Mavrodinova, M. Popova, V. Valchev, R. Nickolov, Ch. Minchev, *J. Colloid and Interface Science* 286 (2005) 268.
- 50 P. Prokešová, S. Mintova, J. Čejka, T. Bein, *Microporous and Mesoporous Materials* 64 (2003) 165.
- 51 B.J. Schoeman, K. Higberg, J. Sterte, *Nanostructured Materials* 12 (1999) 49.
- 52 L. Ding, Y. Zheng, *Materials Research Bulletin* 42 (2007) 584.
- 53 J. Sterte, S. Mintova, G. Zhang, B.J. Schoeman, *Zeolites* 18 (1997) 387.
- 54 J.A. Lee, L. Meng, D.J. Noris, L.E. Scriven, M. Tsapatsis, *Langmuir* 22 (2006) 5217.
- 55 M. Stöcker, *Microporous and Mesoporous Materials* 38 (2000) 1.
- 56 C.S. Cundy, P.A. Cox, *Chem. Rev.* 103 (2003) 663.
- 57 F. Liebau, *Structural Chemistry of Silicates*. 1985, Berlin: Springer-Verlag. 242.
- 58 S.I. Zones, Y. Nakagawa, G.S. Lee, C.Y. Chen, L.T. Yuen, *Microporous Mesoporous and Material* 21 (1998) 199.
- 59 Y. Nakagawa, G.S. Lee, T.V. Harris, L.T. Yuen, S.I. Zones, *Microporous Mesoporous and Material* 22 (1998) 69.
- 60 R.F. Lobo, S.I. Zones, M.E. Davis, *Journal of Inclusion Phenomena and Macrocyclic Chemistry* 21 (1995) 47.
- 61 T. Wakihara, S. Yamakita, K. Iezumi, T. Okubo, *J. Am. Chem. Soc.* 125 (2003) 12388.
- 62 H. Lee, S.I. Zones, M.E. Davis, *J. Phys. Chem. B* 109 (2005) 2187.
- 63 J. Patarin, *Angew. Chem. Int. Ed.* 43 (2004) 3878.

- 64 C.W. Jones, K. Tsuji, T. Takewaki, L.W. Beck, M.E. Davis, *Microporous and Mesoporous Materials* 48 (2001) 57.
- 65 H. Lee, S.I. Zones, M.E. Davis, *Nature* 425 (2003) 385.
- 66 K. Tsuji, M.E. Davis, *Microporous Materials* 11 (1997) 53.
- 67 M.A. Camblor, P.A. Barrett, M.J.D. Cabañas, L.A. Villaescusa, M. Puche, T. Boix, E. Pérez, H. Koller, *Microporous and Mesoporous Materials* 48 (2001) 11.
- 68 M.A. Camblor, L.A. Villaescusa, M.J.D. Cabañas, *Topic in Catalysis* 9 (1999) 59.
- 69 P.M. Piccione, S. Yang, A. Navrotsky, M.E. Davis, *J. Phys. Chem. B* 106 (2002) 3629.
- 70 C.S. Cundy, P.A. Cox, *Microporous and Mesoporous Materials* 82 (2005) 1.
- 71 P.P.E.A. de Moor, T.P.M. Beelen, B.U. Komanshek, L.W. Beck, P. Wagner, M.E. Davis, R.A. van Santen, *Chem. Eur. J.* 5 (1999) 2083.
- 72 M.E. Davis, R.F. Lobo, *Chem. Mater.* 7 (1995) 920.
- 73 A. Corma, M.J.D. Cabañas, *Microporous and Mesoporous Materials* 89 (2006) 39.
- 74 C.S. Cundy, B.M. Lowe, D.M. Sinclair, *J. Crystal Growth* 100 (1990) 189.
- 75 W. Xu, J. Dong, W. Li, F. Wu, *J. Chem. Soc., Chem. Commun.* (1990) 755.
- 76 M.H. Kim, H.X. Li, M.E. Davis, *Microporous Material* 1 (1993) 191.
- 77 N. Nishiyama, T. Matsufujy, K. Ueyama, M. Matsukata, *Microporous Material* 12 (1997) 293.
- 78 M. Matsukata, M. Ogura, T. Osaki, P.R.H.P. Rao, M. Nomura, E. Kikuchi, *Topic in Catalysis* 9 (1999) 77.
- 79 N. Lang, P. Delichere, A. Tuel, *Microporous and Mesoporous Materials* 56 (2002) 203.
- 80 M.A. Camblor, A. Corma, A. Martinez, F.A. Mocholi, J.P. Pariente, *Appl. Catal.* 55 (1989) 65.
- 81 M.V. Landau, L. Vradman, V. Valtchev, J. Lezervant, E. Liubich, M. Talianker, *Ind. Eng. Chem. Res.* 42 (2003) 2773.
- 82 M.L. Kantam, B.P.C. Rao, B.M. Choudary, K.K. Rao, B. Sreedhar, Y. Iwasawa, T. Sasaki, *Journal of Molecular Catalysis* 252 (2006) 76.
- 83 C.J.H. Jacobsen, C. Madsen, T.V.W. Janssens, H.J. Jacobsen, J. Skibsted, *Microporous and Mesoporous Materials* 39 (2000) 83.
- 84 F. Schüth, W. Schmidt, *Adv. Mater.* 14 (2002) 629.
- 85 O. Larlus, S. Mintova, T. Bein, *Microporous and Mesoporous Materials* 96 (2006) 405.
- 86 M. Tsapatis, *AIChem. J.* 48 (2002) 654.

- 87 C.E.A. Kirschhock, R. Ravishankar, L. van Looveren, P.A. Jacobs, J.A. Martens, *J. Phys. Chem. B* 103 (1999) 4972.
- 88 B.J. Schoeman, *Microporous and Mesoporous Materials* 22 (1998) 9.
- 89 S. Mintova, M. Hözl, V. Valtchev, B. Mihailova, Y. Bouizi, T. Bein, *Chem. Mater.* 16 (2004) 5452.
- 90 B. Zhan, M.A. White, M. Lumsden, J.M. Neuhaus, K.N. Robertson, T.S. Cameron, M. Gharghoury. *Chem. Mater.* 14 (2002) 3636.
- 91 S. Mintova, N. Petkov, K. Karaghiosoff, T. Bein, *Materials Science and Engineering C* 19 (2002) 111.
- 92 A.E. Persson, B.J. Schoeman, J. Sterte, J.E. Otterstedt, *Zeolites* 15 (1995) 611.
- 93 L. Gora, K. Streltzky, R.W. Thompson, G. D. Phillis, *Zeolites* 18 (1997) 119.
- 94 R.W. Corkery, B.W. Ninham, *Zeolites* 18 (1997) 379.
- 95 S. Mintova, N.H. Olson, V. Valtchev, T. Bein, *Science* 283 (1999) 958.
- 96 L.B. Sand, A. Sacco, R.W. Thompson, A.G. Dixon, *Zeolites* 7 (1987) 387.
- 97 V.P. Valtchev, K.N. Bozhilov, *J. Phys. Chem. B* 108 (2004) 15587.
- 98 J.C. Jansen, *Stud. Surf. Sci. Catal.* 137 (2001) 175.
- 99 R.M. Mohamed, H.M. Aly, M.F.El-Shahat, I.A. Ibrahim, *Microporous and Mesoporous Materials* 79 (2005) 7.
- 100 Q. Li, B. Mihailova, D. Creaser, J. Sterte, *Microporous and Mesoporous Materials* 40 (2000) 53.
- 101 S. Mintova, V. Valtchev, *Microporous and Mesoporous Materials* 55 (2002) 171.
- 102 P. Prokešová, S. Mintova, J. Čejka, T. Bein, *Microporous and Mesoporous Materials* 64 (2003) 165.
- 103 L. Tosheva, V.P. Valtchev, *Chem. Mater.* 17 (2005) 2494.
- 104 V.P. Valtchev, L. Tosheva, K.N. Bozhilov, *Langmuir* 21 (2005) 10724.
- 105 C. Madsena, C.J.H. Jacobsen, *Chem. Commun.* (1999), 673.
- 106 K. Tang, Y.G. Wang, L.J. Song, L.H. Duan, X.T. Zhang, Z.L. Sun, *Materials Letters* 60 (2006) 2158.
- 107 J. Yao, H. Wang, K.R. Ratinac, S.P. Ringer, *Chem. Mater.* 18 (2006), 1394.
- 108 I. Schmidt, C. Madsen, C.J.H. Jacobsen, *Inorg. Chem.* 39 (2000) 2279.
- 109 E.G. Derouane, I. Schmidt, H. Lachas, C.J.H. Christensen, *Catalysis Letters* 95 (2004) 13.

- ¹¹⁰ S.P. Naik, J.C. Chen, A.S.T. Chiang, *Microporous and Mesoporous Materials* 54 (2002) 293.
- ¹¹¹ S.S. Kim, J. Shah, T.J. Pinnavaia, *Chem. Mater.* 15 (2003) 1664.
- ¹¹² F. Schüth, *Chem. Mater.* 13 (2001) 3184.
- ¹¹³ C. Pham-Huu, G. Win, J.P. Tessonier, M.J. Ledoux, S. Rigolet, C. Marichal, *Carbon* 42 (2004) 1941.
- ¹¹⁴ H. Wang, B.A. Holmberg, Y. Yan, *J. Am. Chem. Soc.* 125 (2003) 9928.
- ¹¹⁵ B. Wang, H.Z. Ma, Q. Z. Shi, *Chinese Chemical Letters* 13 (2002) 385.
- ¹¹⁶ S. Mintova, T. Bein, *Microporous and Mesoporous Materials* 50 (2001) 159.
- ¹¹⁷ S. Mintova, V. Valtchev, V. Engström, B.J. Schoeman, J. Sterte, *Microporous Material.* 11 (1997) 149.
- ¹¹⁸ H. Wang, Z. Wang, Y. Yan, *Chem. Commun.* (2000) 2333.
- ¹¹⁹ V. Valtchev, J. Hedlund, B.J. Schoeman, J. Sterte, S. Mintova, *Microporous Materials* 8 (1997) 93.
- ¹²⁰ J. Caro, M. Noak, P. Kölsch, R. Schäfer, *Microporous and Mesoporous Materials* 38 (2000) 3.
- ¹²¹ T. Bein, *Chem. Mater.* 8 (1996) 1636.
- ¹²² X.D. Wang, W.L. Yang, Y. Tang, Y.J. Wang, S.K. Fu, Z. Gao, *Chem. Commun.* (2000) 2161.
- ¹²³ V. Valtchev, S. Mintova, *Microporous and Mesoporous Materials* 43 (2001) 41.
- ¹²⁴ V. Valtchev, *Chem. Mater.* 14 (2002) 4371.
- ¹²⁵ F. Xu, Y. Wang, X. Wang, Y. Zhang, Y. Tang, P. Yang, *Adv. Mater.* 15 (2003) 1751.
- ¹²⁶ A. Dong, Y. Wang, Y. Tang, N. Ren, Y. Zhang, Y. Yue, Z. Gao, *Adv. Mater.* 14 (2002) 926.
- ¹²⁷ Y. Liu, W. Zhang, Y. Han, F.S. Xiao, *Chem. Mater.* 14 (2002) 2536.
- ¹²⁸ C. Reichardt, *Solvent and Solvent Effects in Organic Chemistry, Third Updated and Enlarged Edition*, Wiley-VCH, 2004.
- ¹²⁹ N. Balabai, A. Sukharevsky, I. Read, B. Strasiza, M. Kumikova, R.S. Hartman, R.D. Coalson, D.H. Waldeck, *Journal of Molecular Liquid* 77 (1998) 37.
- ¹³⁰ T. Pellegrino, S. Kudera, T. Liedl, A.M. Javier, L. Manna, W.J. Parak, *Small* 1 (2005) 48.
- ¹³¹ M. Casciola, G. Alberti, A. Donnadio, M. Pica, F. Marmottini, A. Bottino and P. Piaggio, *J. Mater. Chem.* 15 (2005) 4262.

- ¹³² F.A. Rushworth, D.P. Tunstall, *Nuclear Magnetic Resonance*, 1973, Gordon & Breach.
- ¹³³ C.P. Slichter, *Principles of Magnetic Resonance*, 1990, Springer-Verlag.
- ¹³⁴ J.W. Hennel, J. Klinowski, *Fundamentals of Nuclear Magnetic Resonance*, 1993, Longman Scientific & Technical.
- ¹³⁵ M. Mehring, *Principles of High Resolution NMR in Solid*, 1983, Springer-Verlag.
- ¹³⁶ C.A. Fyfe, *Solid State NMR for Chemists*, 1983, C. F. C. Press.
- ¹³⁷ M.J. Duer, *Introduction to Solid-State NMR Spectroscopy*, 2004, Blackwell.
- ¹³⁸ E.R. Andrew, A. Bradbury, R.G. Eades, *Nature* 182 (1958) 1659.
- ¹³⁹ I.J. Lower, *Phys. Rev. Lett.* 2 (1959) 285.
- ¹⁴⁰ L. Frydman, J.S Harwood, *J. Am. Chem. Soc.* 117 (1995) 5367.
- ¹⁴¹ A. Medek, J.S. Harwood, L. Frydman, *J. Am. Chem. Soc.* 117 (1995) 12779.
- ¹⁴² J.P. Amoureux, C. Fernandez, L. Frydman, *Chemical Physics Letters* 259 (1996) 347.
- ¹⁴³ A. Medek, L. Frydman, *J. Braz. Chem. Soc.* 10 (1999) 263.
- ¹⁴⁴ J.P. Amoureux, C. Fernandez, S.J. Steuernagel, *Magn. Reson. A* 123, (1996) 116.
- ¹⁴⁵ H. Koller, R.F. Lobo, S.L. Burkett, M.E. Davis, *J. Phys. Chem* 99 (1995) 12588.
- ¹⁴⁶ P.R.H.P. Rao, M. Matsukata, *Chem. Commun.*, (1996) 1441.
- ¹⁴⁷ R. Bandyopadhyay, Y. Kubota, N.Sugimoto, Y. Fukushima, Y. Sugi, *Microporous and Mesoporous Materials* 32 (1999) 81.
- ¹⁴⁸ J.B. Higgins, R.B. LaPierre, J.L. Schlenker, A.C. Rohrman, J.D. Wood, G.T. Kerr, W.J. Rohrbaugh, *Zeolites* 8 (1988) 446.
- ¹⁴⁹ A. Carati, C. Flego, E.P. Massara, R. Millini, L. Carluccio, W.O. Parker, G. Bellussi, *Microporous and Mesoporous Materials* 30 (1999) 137.
- ¹⁵⁰ J. Perez-Pariente, J.A. Martens, P.A. Jacobs, *Appl. Catal.* 32 (1987) 35.
- ¹⁵¹ R.B. Borade, A. Clearfield, *Microporous Materials* 2 (1994) 167.
- ¹⁵² M.A. Camblor, A. Corma, S. Valencia, *Microporous and Mesoporous Materials* 25 (1998) 59.
- ¹⁵³ J.E. Hazm, P. Caullet, J.L. Paillaud, M. Soulard, L. Delmotte, *Microporous and Mesoporous Materials* 43 (2001) 11.
- ¹⁵⁴ R.B. Borade, A. Clearfield, *Microporous Materials* 5 (1996) 289.
- ¹⁵⁵ G. Engelhardt, H. Koller, *NMR Basic Principles and Progress* 31, Springer Verlag, Berlin, 1994.

- ¹⁵⁶ E. Lippmaa, M. Magi, A. Samoson, M. Tarmak, G. Engelhardt, *J. Am. Chem. Soc.* 103 (1980) 4889.
- ¹⁵⁷ M.A. Camblor, A. Corma, S. Valencia, *Chem. Commun.* (1996) 2365.
- ¹⁵⁸ J.E. Hazm, P. Caullet, J.L. Paillaud, M. Soulard, L. Delmotte, *Microporous and Mesoporous Materials* 43 (2002) 11.
- ¹⁵⁹ J.P. Pariente, J. Sanz, V. Fornes, A. Corma, *Journal of Catalysis* 124 (1990) 217.
- ¹⁶⁰ M. Stocker, *Microporous Mesoporous Material* 29 (1999) 3.
- ¹⁶¹ M. Hunger, *Catal. Rev. Sci. Eng.*, 39 (4) (1997) 345.
- ¹⁶² H. Koller, R.F. Lobo, S.L. Burkett, M.E. Davis, *J. Phys. Chem.* 99 (1995) 12588.
- ¹⁶³ D.F. Shantz, J.S. Gunne, H. Koller, R.F. Lobo, *J. Am. Chem. Soc.* 122 (2000) 6659.
- ¹⁶⁴ H. Koller, C. Fild, R.F. Lobo, *Microporous and Mesoporous Materials* 79 (2005) 215.
- ¹⁶⁵ G. Coudurier, A. Auroux, J.C. Vedin, R.D. Farlee, L. Abrams, R.D. Shannon, *J. Catal.* 108 (1987) 1.
- ¹⁶⁶ E. Brunner, D. Freude, M. Hunger, H. Pfeifer, W. Reschtilowski, *Chem. Phys. Lett.* 148 (1988) 226.
- ¹⁶⁷ Z. Gabelica, J.B. Nagy, P. Bodart, G. Debras, *Chem. Lett.* (1984) 1059.
- ¹⁶⁸ C. Fild, D.F. Shantz, R.F. Lobo, H. Koller, *Phys. Chem. Chem. Phys.* 2 (2000) 3091.
- ¹⁶⁹ K.F.M.G.J. Scholle, W.S. Veeman, *Zeolites* 5 (1985) 118.
- ¹⁷⁰ R. Millini, G. Perego, G. Bellussi, *Top. Catal.* 9 (1999) 13.
- ¹⁷¹ H. Koller, *Studies in Surface Science and Catalysis* 149 (2004) 105.
- ¹⁷² S.J. Hwang, C.Y. Chen, S.I. Zones, *J. Phys. Chem. B* 108 (2004) 18535.
- ¹⁷³ R. Martens, W. Müller-Warmuth, *J. Non-Cryst. Solids* 265 (2000) 167.
- ¹⁷⁴ A.G. Pelmentschikov, G.M. Zhidomirov, D.V. Kuroshvili, G.V. Tsitsishvili, *Stud. Surf. Sci. Catal.* 18 (1984) 85.
- ¹⁷⁵ A. Abraham, S.H. Lee, C.H. Shin, S.B. Hong, R. Prins, J.A. van Bokhoven, *Phys. Chem. Chem. Phys.* 6 (2004) 3031.
- ¹⁷⁶ A. Omega, M. Vasic, J.A. van Bokhoven, G. Pirngruber, R. Prins, *Phys. Chem. Phys. Chem.* 6 (2004) 447.
- ¹⁷⁷ J.A. van Bokhoven, D.C. Koningsberger, P. Kunkeler, H. van Bekkum, A.P.M. Kentgens, *J. Am. Chem. Soc.* 122 (2000) 12842.
- ¹⁷⁸ S. Krijnen, P.S. Sánchez, B.T.F. Jakobs, J.H.C. van Hooff, *Microporous and Mesoporous Materials* 31 (1999) 163.

- ¹⁷⁹ R. Fricke, H. Kosslick, G. Lischke, M. Richter, *Chem. Rev.* 100 (2000) 2303.
- ¹⁸⁰ N.O. Gonzales, A.K. Chakraborty, A.T. Bell, *Topics in Catalysis* 9 (1999) 207.
- ¹⁸¹ L. Brabec, M. Jeschke, R. Klik, J. Nováková, L. Kubelková, D. Freude, V. Bosáček, J. Meusinger, *Applied Catalysis A: General* 167 (1998) 309.
- ¹⁸² C. Prieto, T. Blasco, M. Cambor, J. Pérez-Pariente, *J. Mater. Chem.* 10 (2000) 1383.
- ¹⁸³ A. Arnold, S. Steuernagel, M. Hunger, J. Weitkamp, *Microporous and Mesoporous Materials* 62 (2003) 97.
- ¹⁸⁴ El-M. El-Malki, R.A. van Santen, W.M.H. Sachtler, *J. Phys. Chem. B* 103 (1999) 4611
- ¹⁸⁵ M. García-Sánchez, P.C.M.M. Magusin, E.J.M. Hensen, P.C. Thüne, X. Rozanska, R.A. van Santen, *Journal of Catalysis* 219 (2003) 352.
- ¹⁸⁶ K.J. Chao, S.P. Sheu, L.H. Lin, M.J. Genet, M.H. Feng, *Zeolites* 18 (1997) 18.
- ¹⁸⁷ C.R. Bayense, J.H.C. van Hooff, J.W. de Haan, L.J.M. van de Ven, A.P.M. Kentgens, *Catalysis Letters* 17 (1993) 349.
- ¹⁸⁸ H.K.C. Timken, E. Oldfield, *J. A. Chem. Soc.* 109 (1987) 7669.
- ¹⁸⁹ J.E. Hazm, P. Caultet, J.L. Paillaud, M. Soulard, L. Delmotte, *Microporous and Mesoporous Materials* 43 (2001) 11.
- ¹⁹⁰ M.S. Bradley, R.F. Howe, *Microporous Mater.* 4 (1995) 131.
- ¹⁹¹ Y. Oumi, I. Jintsugawa, S. Kikuchi, S. Nawata, T. Fukushima, T. Teranishi, T. Sano, *Microporous and Mesoporous Materials* 66 (2003) 109.
- ¹⁹² S. Mintova, N. Petkov, K. Karaghiosoff, T. Bein, *Microporous and Mesoporous Materials* 50 (2001) 121.
- ¹⁹³ E. de Vos Burchant, H. van Bekkum, B. van de Graaf, *Zeolites* 13 (1993) 212.
- ¹⁹⁴ C.A. Fyfe, G.J. Kennedy, C.T. DeSchutter, G.T. Kokotailo, *Chem. Commun.* (1984) 541.
- ¹⁹⁵ G. Engelhardt, H. van Koningsveld, *Zeolites* 10 (1990) 650.
- ¹⁹⁶ I.S. Kislina, N.B. Librovich, V.D. Maiorov, *Russian Chemical Bulletin* 43 (1999) 1505.

Lebenslauf

PERSÖNLICHE ANGABEN

Name	Huong Thi Thanh Tong
Geburtsdatum	18.02.1974
Geburtsort	Hai Hung, Vietnam
Staatsangehörigkeit	Vietnamese
Familienstand	verheiratet
Eltern	Prof. Dr. Thanh Dzuy Tong Xuan Thi Nguyen

SCHULAUSBILDUNG

1979-1987	Kim Giang High School, Hanoi, Vietnam
1987-1990	Nguyen Hue High School, Hadong, Vietnam

STUDIUM

1990-1994	Studium der Chemie an der Hanoi Universität, Vietnam
July 1994	Bachelor of Science in Chemie
1995-1997	Master in Chemie, University of Science, Vietnam National University, Hanoi, Vietnam
July 2003	Beginn der Dissertation am Institut für Physikalische Chemie, Westfälische Wilhelms-Universität Münster unter der Betreuung von PD Dr. Hubert Koller

STIPENDIEN

1990-1994	Bachelorstipendium, Hanoi University, Vietnam
2003-2007	Ministry of Education and Training (MOET)

BERUFSTÄTIGKEIT

1995-2003	Wissenschaftlicher Mitarbeiter, University of Mining and Geology, Hanoi, Vietnam
-----------	---